



2013

STRUCTURES AND REACTIONS OF BIOMOLECULES AT INTERFACES

Xiaoning Zhang

University of Kentucky, xzh239@uky.edu

[Right click to open a feedback form in a new tab to let us know how this document benefits you.](#)

Recommended Citation

Zhang, Xiaoning, "STRUCTURES AND REACTIONS OF BIOMOLECULES AT INTERFACES" (2013). *Theses and Dissertations--Chemistry*. 16.

https://uknowledge.uky.edu/chemistry_etds/16

This Doctoral Dissertation is brought to you for free and open access by the Chemistry at UKnowledge. It has been accepted for inclusion in Theses and Dissertations--Chemistry by an authorized administrator of UKnowledge. For more information, please contact UKnowledge@lsv.uky.edu.

STUDENT AGREEMENT:

I represent that my thesis or dissertation and abstract are my original work. Proper attribution has been given to all outside sources. I understand that I am solely responsible for obtaining any needed copyright permissions. I have obtained and attached hereto needed written permission statements(s) from the owner(s) of each third-party copyrighted matter to be included in my work, allowing electronic distribution (if such use is not permitted by the fair use doctrine).

I hereby grant to The University of Kentucky and its agents the non-exclusive license to archive and make accessible my work in whole or in part in all forms of media, now or hereafter known. I agree that the document mentioned above may be made available immediately for worldwide access unless a preapproved embargo applies.

I retain all other ownership rights to the copyright of my work. I also retain the right to use in future works (such as articles or books) all or part of my work. I understand that I am free to register the copyright to my work.

REVIEW, APPROVAL AND ACCEPTANCE

The document mentioned above has been reviewed and accepted by the student's advisor, on behalf of the advisory committee, and by the Director of Graduate Studies (DGS), on behalf of the program; we verify that this is the final, approved version of the student's dissertation including all changes required by the advisory committee. The undersigned agree to abide by the statements above.

Xiaoning Zhang, Student

Dr. Yuguang Cai, Major Professor

Dr. John E. Anthony, Director of Graduate Studies

STRUCTURES AND REACTIONS OF BIOMOLECULES AT INTERFACES

DISSERTATION

A dissertation submitted in partial fulfillment of the
requirements for the degree of Doctor of Philosophy in the
College of Arts and Sciences
at the University of Kentucky

By
Xiaoning Zhang

Lexington, Kentucky

Director: Dr. Yuguang Cai, Professor of Department of Chemistry

Lexington, Kentucky

2013

Copyright © Xiaoning Zhang 2013

ABSTRACT OF DISSERTATION

STRUCTURES AND REACTIONS OF BIOMOLECULES AT INTERFACES

This dissertation serves to study a protein's conformation-function relationship since immobilized proteins often behave differently from their solution-state counterparts. Therefore, this study is important to the application of protein-based biodevices. Another aim of this dissertation is to explore a new approach to realize low voltage electrowetting without the help of oil bath. Utilizing this approach, a protein micro-separation was realized. Additionally, the interfacial properties of ionic liquid (IL) solid-like layer, which played a key role in electrowetting, was studied for further developments of IL-based applications.

Atomic Force Microscopy (AFM) was utilized in the study and played multiple roles in this dissertation. First, AFM was used as a fabrication tool. In the contact mode, conductive AFM tip was used to conduct the electrochemical oxidation to create a chemical pattern or to conduct an electrowetting experiment. Subsequently, AFM was used as a characterization tool in the tapping mode to characterize the surface structure, the thickness, and the surface potential. Furthermore, AFM in the contact mode was used as a measurement tool to measure the tribological force properties of sample.

The results of the study concerning the conformational change in immobilized calmodulin showed that the immobilized CaM retained its activity. Additionally, the immobilization of CaM on a solid support did not interfere with the ability of the protein to bind calcium, as well as CaM kinase binding domain. For the electrowetting experiment, our data suggested that the ultra-high capacitance density of the IL dielectric layer leads to the low voltage electrowetting. We also successfully demonstrated the streptavidin and GFP proteins separation by Electrowetting-on-Dielectric (EWOD) force. The results of the surface properties study indicated that the charge and dipole of the substrate can influence the structures and properties of the IL interfacial layer.

Our study would be beneficial in research and assay work involving engineered proteins, as well as the study and development of electrowetting applications.

KEYWORDS: Atomic Force Microscopy (AFM), Calmodulin,
Ionic Liquid, Electrowetting, Micro-separation

Xiaoning Zhang

04-20-2013

STRUCTURES AND REACTIONS OF BIOMOLECULES AT INTERFACES

By

Xiaoning Zhang

Dr. Yuquang Cai

Director of Dissertation

Dr. John E. Anthony

Director of Graduate Studies

April 20 , 2013

DEDICATED TO

my beloved parents: Mr. Shunqin Ning and Mrs. Dejuan Zhang

and

all those who gave me support and encouragement

ACKNOWLEDGEMENTS

I sincerely thank Dr. Yuguang Cai, as both a teacher and a mentor, for his guidance and patience during my Ph.D. training. He not only taught me hands-on laboratory techniques but also trained me to become a creative chemist. This dissertation would not be complete without him. I wish to thank him for everything he has done for me.

Words fail to convey my appreciation for my committee members, Dr. Dong-Sheng Yang, Dr. Mark D. Watson, and Dr. J. Zach Hilt. Their valuable discussions and accessibility for our meetings lead me on the right path of Ph.D. study - I not only grew as an experimentalist but also an independent thinker.

I would also like to thank Dr. Yinnan Wei for her assistance and guidance in protein expression and purification. Additionally, I am very grateful for the help from all the members of her research group: Linliang Yu, Dr. Wei Lu, Meng Zhong, Cui Ye, and Qian Chai. They were very supportive for my research in many ways.

The past and present members in Dr. Cai's research group, Dr. Pei Gao and Lingbo Lu, also have contributed to and supported me in my research. I feel very fortunate to work with these two fine chemists.

Particularly, I would like to thank Dr. Guangchu Hu and his wife Mrs. Xulian Yang, who have taken care of me during my study in the U.S.

Finally, but most importantly, I would like to thank my family for their support and love. Throughout my life, my mom and dad have believed me even when I did

not believe in myself. They are always my source of inspiration and the motivation to complete this work.

TABLE OF CONTENTS

ACKNOWLEDGEMENTS.....	III
CHAPTER 1: INTRODUCTION	1
1.1 Nanolithography.....	2
1.1.1 Optical lithography.....	2
1.1.2 Scanning beam lithography	3
1.1.3 Mechanical surface patterning/force lithography	5
1.1.4 Dip-Pen lithography	6
1.1.5 Oxidative probe lithography technique.....	8
1.2 Microreactor	10
1.3 Electrowetting (EW)	11
CHAPTER 2: ATOMIC FORCE MICROSCOPY (AFM)	14
2.1 AFM Operation Principle	14
2.2 Forces.....	18
2.3 Force-Distance Curve	21
2.4 Imaging Modes	23
2.5 AFM Tip Characterization.....	30
2.6 Methodology	33
CHAPTER 3: SELF-ASSEMBLED MONOLAYERS (SAMS) FABRICATION AND AFM LOCAL OXIDATION LITHOGRAPHY	34
3.1 Introduction	34
3.2 Experimental Set-up to Create Chemical Patterns on OTS	37
3.2.1 Instruments.....	37
3.2.2 Chemicals and materials	38
3.2.3 Octadecyltrichlorosilane (OTS) self-assembled monolayer preparation for pattern fabrication.....	38
3.2.4 Fabrication hydrophilic chemical patterns on OTS by using local oxidation lithography.....	40
3.3. Conclusion	44
CHAPTER 4: ATOMIC FORCE MICROSCOPY STUDY OF THE CONFORMATIONAL CHANGE OF IMMOBILIZED CALMODULIN	45
4.1 Introduction	45
4.2 Experimental	47
4.2.1 Instruments.....	47

4.2.2 Chemicals and materials	53
4.2.3 Methods.....	54
4.2.4 Characterization of conformational change of CaM	69
4.2.5 Analysis of the hydration on the exposed protein surface	75
4.2.6 Possible orientations of the adsorbed protein	79
4.2.7 Friction Force Spectroscopy of immobilized CaM and Apo-CaM monolayers	80
4.2.8 Label-free detection of the Ca ²⁺ binding on CaM patterns using Kelvin Probe Force Microscopy (KPFM)	84
4.2.9 CaM orientational difference detected by KPFM.....	87
4.3 Conclusion	95
CHAPTER 5: OCTADECYLTRICHLOROSILANE (OTS)-COATED IONIC LIQUID DROPS: MICRO-REACTORS FOR HOMOGENOUS CATALYTIC REACTIONS AT DESIGNATED INTERFACES.....	97
5.1 Introduction	97
5.2 Experimental.....	101
5.2.1 Instruments.....	101
5.2.2 Chemicals and materials	101
5.2.3 Coating IL on OTSpd patterns	102
5.2.4 AFM and optical microscope characterization.....	104
5.2.5 Reaction of the OTS-coated IL capsules.....	111
5.3 Conclusion	119
CHAPTER 6 SURFACE PROPERTIES OF IONIC LIQUID (IL) ADSORBATE LAYER ON DIFFERENT CHEMICAL PATTERNS.....	120
6.1 Introduction	120
6.2 Experimental.....	122
6.2.1 Instruments and chemicals	122
6.2.2 Coating IL on OTSpd patterns	122
6.2.3. Characterization of IL adsorbed layer on chemical patterns.....	124
6.2.4 Surface properties of IL adsorbate layers depend on the surface dipole of the underneath chemical pattern	131
6.3 Discussion	140
6.4 Conclusion.....	146
CHAPTER 7 ULTRA-LOW VOLTAGE ELECTROWETTING ON SOLID-LIKE IONIC LIQUID DIELECTRIC LAYER.....	148
7.1 Introduction	148

7.2 Experimental.....	151
7.2.1 Surface preparation.....	151
7.2.2 Electrowetting setup and measurement of contact angle.....	153
7.3 Low Voltage EW and Its Application.....	154
7.3 Conclusion.....	167
CHAPTER 8 CONCLUSIONS AND FUTURE PROJECTS.....	169
8.1 Summary.....	169
8.2 Future work.....	170
Reference.....	172
VITA.....	182

LIST OF TABLES

Table 1-1 Comparison of various nanolithography techniques.....	10
Table 2-1 Van der Waals interaction laws for most common AFM geometries.....	19
Table 4-1 Height of the surface patterns.....	75
Table 4-2 Phase Signals and Hydrophilicity Factors (H) of the Protein Surfaces in Figure 4-22.....	77
Table 6-1 The surface properties of OTSpd and OTSpd-Zn patterns before and after the IL vapor adsorption.....	125
Table 6-2 The surface properties of OTSpd-APTMS patterns before and after the IL vapor adsorption.....	134
Table 6-3 The surface potentials of OTSpd, OTSpd-Zn and OTSpd-APTMS patterns before and after the IL vapor adsorption.....	140
Table 7-1 Benchmark achievements in EWOD.....	149

LIST OF FIGURES

Figure 1-1 Schematic of a simple optical lithography system.....	3
Figure 1-2 Schematic illustration of the scanning beam lithography.....	4
Figure 1-3 AFM tapping mode topography image of Apo-CaM obtained after the AFM contact mode tip scanning.....	6
Figure 1-4 Schematic representation of dip-pen nanolithography (DPN).	7
Figure 1-5 Schematic representation of the oxidative probe lithography techniques.....	9
Figure 1-6 Picture of aqueous-organic liquid, and gas-liquid reactor system.....	11
Figure 1-7 Schematic of the electrowetting set-up with cross-sectional view..	13
Figure 2-1 Scheme representation of the atomic force microscopy.....	15
Figure 2-2 Top and side view of a piezoelectric tube scanner.....	17
Figure 2-3 Schematic diagram shows the potential energy and force with separation (r) between tip and sample surface as described by the Lennard-Jones functions.	23
Figure 2-4 Approaching and withdrawal force curve.	23
Figure 2-5 AFM and lateral deflection signals of the cantilever.	25
Figure 2-6 AFM topography image of a diluted hydrogel sample.	26
Figure 2-7 Examples of AFM images.....	30
Figure 2-8 Measurement of the AFM tip radius.....	32
Figure 2-9 The flow chart of the methodology in this dissertation.....	33
Figure 3-1 Representation of a SAM structure.....	36
Figure 3-2 The formation of OTS film on Si (100) wafer.....	40
Figure 3-3 AFM (a) topographic and (b) phase image of a homogenous OTS film	40
Figure 3-4 The experimental setup for the AFM probe oxidation lithography on OTS film.	42
Figure 3-5 Measuring the depth of OTSpd pattern.....	43
Figure 3-6 The reaction of PDAM and carboxylic acid-terminated surface.....	44
Figure 4-1 The main chain structure of (a) Ca^{2+} -CaM (PDB accession code 1CLL) and (b) Ca^{2+} -free CaM (Apo-CaM, PDB accession code 1CFD) (b) with respective N-terminal domains on bottom.....	46
Figure 4-2 (a) Energy-level diagram for a fluorescence system and (b) components of a fluorometer.	50
Figure 4-3 Capacitances formed between AFM pyramid-shaped conductive tip and sample surface.	52
Figure 4-4 Scanning electron microscope (SEM) image of Ag_2Ga needle tip, from NaugaNeedles Inc.	53

Figure 4-5 This cartoon depicts a protein (blue line) incubated in the SDS solution.	57
Figure 4-6 SDS gel electrophoresis of one Cys CaM.	58
Figure 4-7 Formation of a disulfide bond.	60
Figure 4-8 Reduction of disulfide bonds by using TCEP.	60
Figure 4-9 Maleimide (MAL) dye is highly specific for cysteine residues.	61
Figure 4-10 Specificity of thiol-reactive dyes for Cys proteins.	61
Figure 4-11 EDTA titrations of ANS labeled CaM monitored by ANS fluorescence emission measurement	63
Figure 4-12 Schematic representation of the construction of a MUTMS monolayer on the OTSpd surface.	65
Figure 4-13 Panel a) is an AFM topography image of the MUTMS pattern. Panel b) is a zoom in view of the region in the cyan box in panel a), figure c) is the histogram corresponding to b).....	65
Figure 4-14 Representative AFM image of dodecanethiol islands on the MUTMS chemical pattern.	67
Figure 4-15 The structure and formation of dodecanethiol (CH ₃ (CH ₂) ₁₁ SH) layers.....	67
Figure 4-16 Experimental scheme	69
Figure 4-17 AFM topography image of the CaM (with Ca ²⁺) coated pattern.....	70
Figure 4-18 AFM topography image of the Apo-CaM (without Ca ²⁺) coated pattern.....	71
Figure 4-19 Fluorescent image of an immobilized ANS-labeled CaM array (a) before and (b) after EDTA incubation	72
Figure 4-20 AFM topography image of the CaM (with Ca ²⁺) coated pattern.....	74
Figure 4-21 AFM topography image of CaM-CaM KI binding domain pattern	75
Figure 4-22 Partially covered protein patterns that reveal different surfaces	77
Figure 4-23 Panel a and panel b are the topography image obtained during the contact mode scanning for the CaM and Apo-CaM patterns with different loading forces respectively	82
Figure 4-24 Comparisons of frictional behavior were made among the following three interfaces: a Si tip sliding on an OTS-coated Si wafer (Si-on-OTS), the same Si tip sliding on CaM (Si-on-CaM) and Apo-CaM (Si-on-Apo-CaM).	83
Figure 4-25 The surface potential (a, b) images of the tightly packed CaM pattern before and after incubation with the EDTA solution.	85
Figure 4-26 Panel a is the KPFM image of a CaM KI binding domain-bound CaM pattern. Panel b is the histogram corresponding to a.....	86
Figure 4-27 (a) The topography image for the tightly packed CaM pattern. (b) The phase image corresponding to the topography image in a). (c) The surface potential map corresponding to the topography image in a). (d) The topography (black line) and	

surface potential (blue line) channel cross-sectional profiles corresponding to the cyan lines shown in a) and c).....	88
Figure 4-28 (a) is the representative AFM topography image of the proteins on the chemical pattern template. (b) and (c) are the phase images of protein pattern before and after EDTA solution incubation, which correspond to the zone of the cyan box in (a). The height cross-sectional profile corresponding to the cyan lines were plotted in (d). ..	92
Figure 4-29 AFM phase images of protein patterns at (a) the first and (b) second time scanning, and (c) an (a)–(b) combined image.....	93
Figure 4-30 The phase image of the same protein pattern (a) before and (b) after the sample was subjected to 3 hours scanning, and (c) is an (a)–(b) combined image.....	94
Figure 4-31 a) AC mode topography image for CaM patch with double layer on it.....	95
Figure 5-1 The structures of a) 1-butyl-3-methylimidazolium chloride ([Bmim]Cl) and b) 1-butyl-3-methyl-imidazolium bis(trifluoromethanesulfonyl)imide ([Bmim]Tf ₂ N).....	100
Figure 5-2 Octadecyltrichlorosilane (OTS)-coated ionic liquid/FeCl ₃ drop.....	101
Figure 5-3 AFM topography images and surface potential images of the ILs droplets on OTSpd pattern.....	103
Figure 5-4 [Bmim]Cl assembles on the OTSpd pattern.....	105
Figure 5-5 Tapping mode image of an representative [Bmim]Cl drop on OTSpd pattern	106
Figure 5-6 a) A representative [Bmim]Cl drop on the OTSpd pattern before OTS coating. Tapping mode phase image. b) The phase (blue line) channel cross-sectional profiles corresponding to the cyan lines shown in a)	107
Figure 5-7 a) A representative OTS-coated [Bmim]Cl drop on the OTSpd pattern. Tapping mode topography image. b) Optical image of OTS-coated [Bmim]Cl drops on the OTSpd disc array. The imaged was acquired under water. c) The phase image corresponding to the topography image in a). d) The topography (black line) and phase (blue line) channel cross-sectional profiles corresponding to the cyan lines shown in a) and c)	109
Figure 5-8 AC mode image of an representative OTS-coated [Bmim]Cl drop	110
Figure 5-9 The molecular structure of (11-mercaptopoundecyl)trimethoxysilane.	112
Figure 5-10 H ₂ O ₂ decomposition reaction catalyzed by FeCl ₃	113
Figure 5-11 OTS-coated capsules after the H ₂ O ₂ decomposition reaction	114
Figure 5-12 Assessment of IL leaking from the OTS-coated capsule.....	116
Figure 5-13 The AFM topography image of OTSpd pattern after a 10 μL drop of water covering the pattern area.....	116
Figure 5-14 No oxygen bubble was observed inside the droplet, when two 30 μl 30% H ₂ O ₂ solution drops were mixed together.	117

Figure 5-15 The OTS coating on the IL drop surface effectively suppressed the diffusion of Fe^{3+} into the external solution.	118
Figure 5-16 The [Bmim]Cl solution was assembled on a 8x8 OTSpd disc array	118
Figure 6-1 AFM topography image of OTSpd-IL disc (left) and OTSpd-Zn-IL disc (right) on OTS film background.	125
Figure 6-2 Surface potentials of the same clean OTSpd and OTSpd-Zn patterns before and after incubation in IL vapor	127
Figure 6-3 Representative AFM force v.s. distance curve for the OTSpd-Zn-IL surface	129
Figure 6-4 The friction v.s. loading curves for OTS surface (black), OTSpd-IL surface (green) and OTSpd-Zn-IL surface (red)	135
Figure 6-5 The surface potential image of adsorbate layer of 1-butyl-3-methylimidazolium bis(trifluoromethylsulfonyl) imide ([Bmim][Tf ₂ N]) on OTSpd (left two discs) and on OTSpd-Zn (right two discs) chemical patterns	137
Figure 6-6 The surface potential image of adsorbate layer of 1-decyl-3-methylimidazolium chloride ([C ₁₀ mim]Cl) on OTSpd (left two discs) and on OTSpd-Zn (right two discs) chemical patterns.....	138
Figure 6-7 The surface potential image of adsorbate layer of 1-butyl-3-methylimidazolium chloride ([Bmim]Cl) on OTSpd (left two discs) and on OTSpd-APTMS (right two discs) chemical patterns.....	139
Figure 6-8 Amplitude-phase-distance curves with AFM probe and OTS coated Si wafer.	142
Figure 6-9 Energy dissipation of a NSC14 tip during one cycle of tapping over different surfaces.....	143
Figure 7-1 (a) A conductive liquid sits on a EWOD surface with and without voltage applying. (b) The boxed drawings enlarged for the contact line region.	149
Figure 7-2 The formation of UTSox film on Si (100) wafer.	152
Figure 7-3 Representative AFM image of a) [Bmim]Cl and b) [Bmim][Tf ₂ N] vapor coated UTSox wafer.....	152
Figure 7-4 Scheme of the experimental setup with cross sectional view.	153
Figure 7-5 Illustration of model for the theoretical calculation.	154
Figure 7-6 Optical microscope images for voltage dependence of the shape of the [Bmim]Cl IL droplet.	155
Figure 7-7 The contact angle of a [Bmim]Cl drop on OTS surface as a function of the applied voltage	156
Figure 7-8 Conceptual description of ac electrowetting.....	157
Figure 7-9 AFM image of the edge of the drop after the IL drop was blasted off	158

Figure 7-10 AFM image of the OTSpd pattern after incubated in [Bmim][Tf₂N] vapor for 2 hours162

Figure 7-11 Schematic diagram of a small satellite droplet connected to the reservoir drop164

Figure 7-12 a) 240 nm nanospheres were distributed through the thin liquid bridge while
b) 500 nm nanospheres maintain within the main droplet165

Figure 7-13 Optical microscope image of protein mixture after the introduction of voltage
.....166

LIST OF SCHEMES

Scheme 6-1 Preparation of different chemical patterns on the OTS surface and subsequent vapor-phase IL adsorption on the chemical patterns	124
Scheme 6-2 Carboxylic acid terminated surface plus (3-Aminopropyl)trimethoxysilane (APTMS) cross linking reaction scheme.	134

CHAPTER 1: INTRODUCTION

In this dissertation, atomic force microscopy (AFM) was used to conduct the research. The goal of this work includes two parts: 1) to develop more applications of the atomic force microscopy (AFM) based on scanning-probe lithography (SPL) technique and 2) to explore a method for generating low voltage electrowetting and its applications by using AFM.

This dissertation is organized as follows. In the present chapter, I am going to give an overview of the early or recent development in nanolithography, microreactor, and electrowetting technique. Chapter 2 is devoted to the introduction of the theoretical principle of atomic force microscopy (AFM). Chapter 3 introduces the principal method to fabricate hydrophilic patterns over an octadecyltrichlorosilane (OTS) film surface with an atomic force microscopy (AFM). The chemical templates fabricated using this method will be used as functionalized nanopatterns and modified with a variety of different materials in later investigation. Chapter 4 introduces our research on protein's conformation–function relationship employing AFM as a tool. In Chapter 5, I describe our studies about the OTS-coated IL drops assembled on chemical patterns, which are created by AFM and, can be used as novel micro-reactors. Chapter 6 deals with the ionic liquid interface properties on surfaces with charge/dipole using experiments via AFM. Finally, before briefly summarizing current and future projects, a method for generating low voltage electrowetting is introduced and its application in bio-molecular sorting is presented in Chapter 7.

1.1 Nanolithography

Lithography means “writing on stone”. The foundation of modern meaning of lithography can be traced back to China’s Tang dynasty (618 - 907AD). The Chinese people used inked blocks to make the patterned textiles.¹ In 1822, modern photolithography was developed by Nicephore Niepce due to an accident.¹ With the development of integrated circuit (IC) chips and their increasing complexity,² nanolithography emerges as the time require to increase the density of chip components and lower the fabrication prices. Basically, the nanometer-scale patterns fabrication with functional structures is concerned as nanolithography.³⁻⁵ It has been widely used for the microelectronic devices fabrication including integrated circuit,⁶ biosensor⁷, et al. Nanolithography techniques can be simply classified as conventional techniques, which are commercially available and widely used in manufacturing, and unconventional techniques, which are often followed in research. These two classifications will be discussed in detail as followings.⁴

1.1.1 Optical lithography

The first conventional nanolithography technique I will briefly review is optical lithography. Optical lithography is one of the widely used lithography techniques, which plays an important role in the integrated circuit production. Figure 1-1 is a schematic of a basic optical lithography system. An optical source shines the light through the mask. The pattern information, which is fabricated on the mask, is projected onto the wafer surface, where a light sensitive photoresist is coated. Once the photoresist is selectively exposed, a chemical process occurs to

transfer the pattern image from the mask to the wafer. Because of the diffraction effects and the imperfections in the optical train, the resolution of the optical lithography is not high enough, which limits its development, especially in the academic field⁸. So far, a sub-50-nm sized pattern can be achieved by using a 193 nm wavelength light.⁹⁻¹⁴ Since the resolution of the optical lithography system is proportional to the wavelength of the optical source, reducing the wavelength can be used to improve the resolution. Currently, excimer lasers are the most widely used optical source.¹⁵ However, a shorter wavelength of light requires not only a sophisticated optical-lens system,¹⁶ but also new photoresists with higher sensitivity, which can increase the cost significantly.¹⁷⁻²⁰ Other drawbacks, like its time-consuming nature, also restrict the development of the optical lithography.⁴

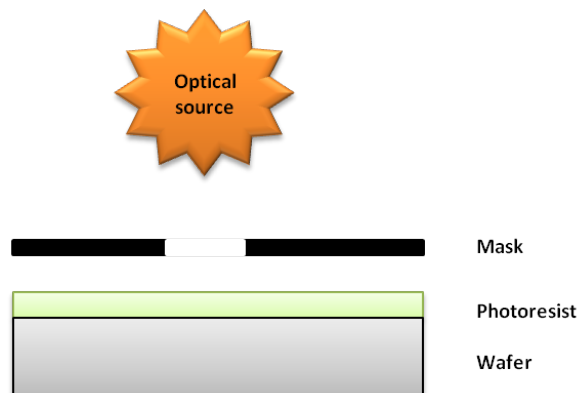


Figure 1-1 Schematic of a simple optical lithography system.

1.1.2 Scanning beam lithography

Another conventional nanolithography technique for patterning nanoscale features is scanning beam lithography. In this technique, a concentrated electron or ion beam is emitted onto the photoresist coated substrate or the substrate

directly.⁴ Those electrons or ions can cause erosion at the surface (subtractive) or substances deposition on the surface (additive). Compared to the photolithography, this process takes longer, but, with higher resolution features (down to ~5 nm)²¹ and maskless²². A notable example is published by Grunze et al., who chemically modify the terminal nitro groups of self-assembled monolayers (SAMs) to amines via an electron beam and then functionalize the surface with carboxylic acid anhydrides.^{23,24} So far, this technique still is not used in the manufacturing process because of the difficulty in developing practical electron beam sources.²⁵

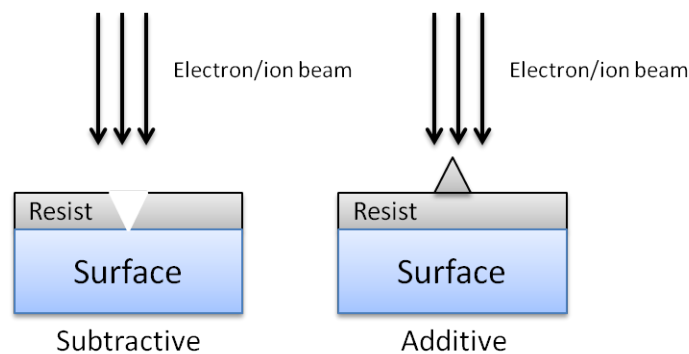


Figure 1-2 Schematic illustration of the scanning beam lithography.

The limitations of these conventional nanolithography techniques, like the resolution limit, hard to apply on nonplanar surfaces, high costs with the decrease of the substrate sizes, and inapplicability to biological and sensitive materials, let researchers to explore some new, unconventional nanolithography techniques. Here, I would like to spend more time on the review of the development of various scanning-probe lithography (SPL) systems, which is one of the unconventional nanolithography techniques, and in which a nano-sized

stylus of scanning probe microscopy (SPM) is used to fabricate a pattern on the surface. I would also like to introduce their applications, since these techniques run through most parts of our research projects.

Scanning tunneling microscopy (STM) and Atomic Force Microscopy (AFM) are well known to effectively identify the structure and nature of surfaces with atomic-scale resolution since 1982.^{2,26} By taking advantage of the interaction between the probe and surface, scanning-probe lithography (SPL) was developed for the pattern creating and modification of substrate.²⁷ Because of the molecular or atomic resolution of STM and AFM, SPL technique can achieve a high resolution with atomic scale.^{28,29} Based on the mechanism of pattern formation, SPL can be used in two areas: physical and chemical surface modification.²

1.1.3 Mechanical surface patterning/force lithography

One of the physical probe lithography techniques is the mechanical surface patterning/force lithography.² As the name of this technique describes, the loading force exerted on the probe was used to remove or move the material on the substrate selectively during the tip scanning, leaving a specific shape or pattern on the surface.³⁰⁻³² During our experiment, it was found that when AFM contact mode tip swiped over a protein pattern with a large loading force, the immobilized protein can be selectively shaved off in a well-defined pattern as Figure 1-3 illustrates. If this technique is conducted in a solution environment with other molecules or nanoparticles, the free place, which is created by the tip, can be replaced by those second materials *in situ*.^{30,33} This substitution makes this technique more interesting since a patterning with multiple types of molecules

can be realized.^{2,4} Liu et al.³⁰ grafted octadecyltrichlorosilane (OTS) into 11-sulfanyl-1-undecanol coated gold substrate successfully by utilizing this method. Gold nanoparticles were also deposited on the nanoshaved SAMs by the same group via the same method.³³ The most attractive form of the modification by using this approach is the atomic manipulation. For example, Eigler and co-workers directly moved adsorbed CO molecules on a Cu(111) substrate and created artificial structures in an ultrahigh vacuum (UHV) at low temperature.^{34,35} The disadvantage of this technique is that the deformation and contamination of the tip can affect the repeatability of the pattern creating since this approach is a tip-induced technique. One of the solutions is using diamond or diamond-coated tip.²

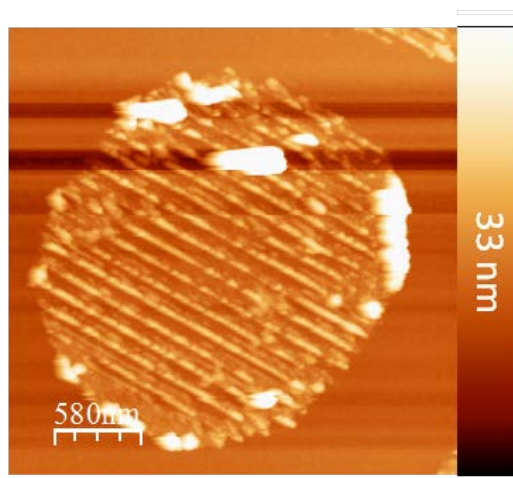


Figure 1-3 AFM tapping mode topography image of Apo-CaM obtained after the AFM contact mode tip scanning.

1.1.4 Dip-Pen lithography

Another physical probe lithography technique that can be used to transfer atoms or molecules to the surface selectively is known as dip-pen nanolithography

(DPN), which was developed by Mirkin's group.^{2,36} During the experiment, an AFM tip works as a "pen" and the interest molecules which are transferred act as "ink", while the substrate acts as a "paper". With the movement of the AFM tip (pen), those materials (inks) can be written on the surface (paper), as Figure 1-4 demonstrates. In this technique, the ink can be the tip itself, like gold, induced by a force or a current, or it can be materials physically adsorbed onto the tip. By switching to another tip, it is possible to create structures with more than one ink.³⁷ Water meniscus between the AFM tip and the sample surface plays an important role in material transportation in this approach.³⁶⁻⁴² Other factors, like the radius of the curvature of the tip, the movement velocity of the tip, as well as the reactivity of the "ink" with the substrate also affect the spreading of the "ink".⁴³⁻⁴⁶ By using DPN, Mirkin et al.⁴⁷ have deposited IgG and Lysozyme on a gold substrate in nanoarrays, whereas David et al.⁴⁸ have patterned silicon substrates with various dyes.

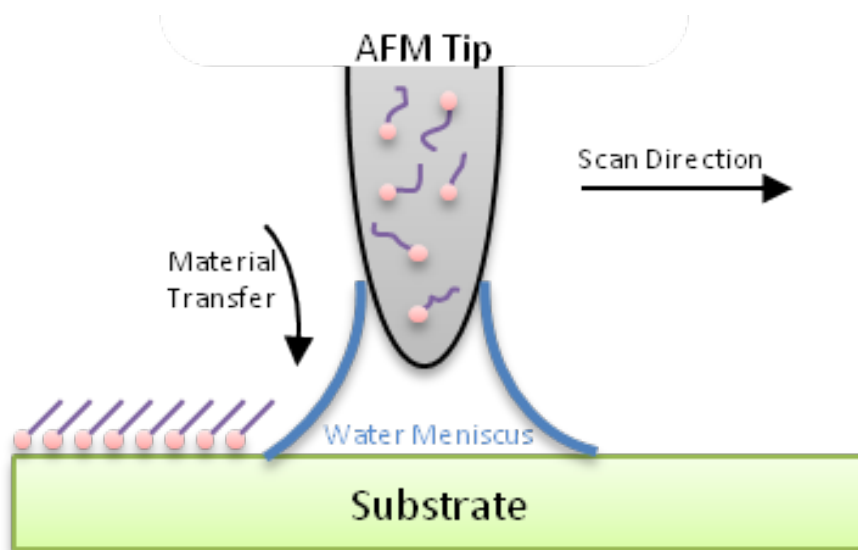
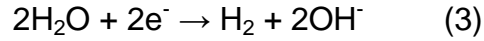
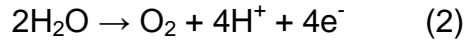
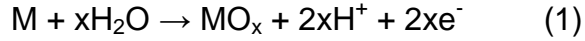


Figure 1-4 Schematic representation of dip-pen nanolithography (DPN).

1.1.5 Oxidative probe lithography technique

Unlike above two techniques, the oxidative probe lithography technique was used to modify surface through an electrochemical reaction. In the experiment, a conductive AFM or STM tip scans over the surface and an electric field is generated between the tip and surface. Typically, the area right under the tip is oxidized by the electric field, while the material between the tip, like oxygen or water, decomposed and the reaction products oxidize the substrate (Figure 1-5). These reactions can be expressed by the following equations (equation 1 to 3).² Since the invention of STM, this electrochemical patterning experiment was used to modify surfaces.²⁷ In the early 1990s, this oxidation technique was firstly transferred to AFM and has been successfully applied to organic resists^{49,50}, SAMs⁵¹, and LB (Langmuir-Blodgett) film⁵². This prominent approach can be conducted on almost any conducting sample and thin organic resists with high resolution. It opens up a new era for the preparation of nanoscale functional architectures, like biomolecules,^{47,53} biominerals,⁵⁴ nanoparticles, and block copolymers^{55,56} on surface. Since this technique can change chemical and physical properties of the sample surface, which can be introduced into biosensor construction,⁵⁷ microfluidic devices,⁵⁸ molecular electronics^{59,60} or special smart coating preparation. For example, our research group fabricated various chemical patterns by AFM local oxidation lithography on octadecyltrichlorosilane (OTS) coated Si wafer from nanometer to sub-millimeter. Then, the functional protein was immobilized on the surface and the activity of the protein was studied.⁶¹⁻⁶³



In summary, SPL is capable of precisely creating patterns on a surface down to the molecular and atomic resolution. However, although it is prominent in the formation of functional nanostructured surfaces, at present, SPL is only used in research since it is not suitable for patterning large areas in manufacturing. In this dissertation, AFM local oxidation, which is one of the oxidative probe lithography techniques and will be discussed in detail in Chapter 3, was used as a basic patterning technique. Then, molecules are selectively anchored or adsorbed to the desired pattern for the further study.

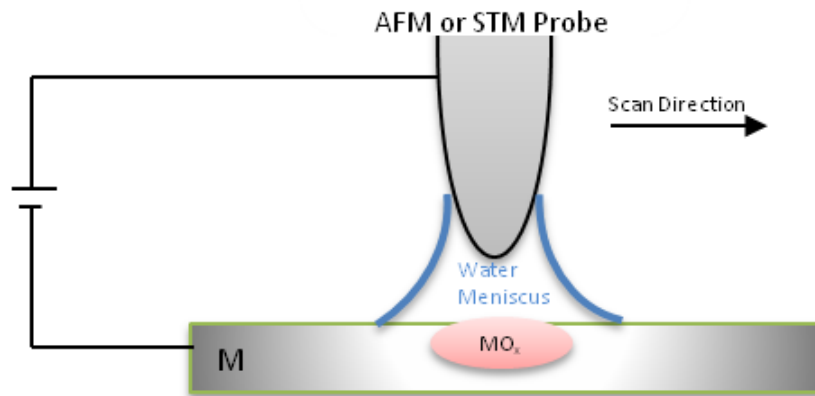


Figure 1-5 Schematic representation of the oxidative probe lithography techniques.

Table 1-1 compares the above methods for nanolithography, which summarizes the minimum feature size, as well as the types of patterns that can be generated by each technique.⁴ As one of the important areas in nanoscience and nanotechnology, it is unquestionable that nanolithography will lead further

advances in the development of microelectronic circuits, biology, materials science, and optics.⁴

Table 1-1 Comparison of various nanolithography techniques.

Technique	Minimum feature ^a	Pattern
Photolithography ⁶	37 nm	Parallel generation of patterns
Scanning beam lithography ⁶⁴	5 nm	Serial writing of patterns
Scanning Probe lithography ^{28,29}	<1 nm	Serial writing of patterns

^a Refers to the minimum demonstrated lateral dimension.

1.2 Microreactor

As I mentioned before, micro- and nanolithography has been one of the key techniques in nanotechnology, which is often used in microreaction system.¹⁶ Such microreactors have become important for analytical and environmental monitoring,⁶⁵⁻⁶⁸ micro fuel cells,⁶⁹ and microorganic synthesis/production in the pharmaceutical industry⁷⁰⁻⁷³. The most striking advantages of microreactor are their high portability because of the small and compact size, reduced reagent consumption and minimization of waste production. In addition, it has efficient heat dissipation owing to the high surface-area-to-volume ratios.⁶⁹ Thus, if there is accident due to the reaction, the impact in the case of micro-reactor will be lower compare to the conventional reactor. Once the procedure is developed, it can be scaled up to the industrial level.

Generally, there are three types of micro-reaction systems which allow diffusion and reaction occur at the interfaces, so that the main product can be removed from one phase to another phase due to the large specific interfacial area and short molecular diffusion distance in the microsystem, they are aqueous-organic liquid⁷⁴⁻⁷⁶, gas-liquid⁷⁷⁻⁷⁹, and gas-liquid-solid^{80,81} system. Obviously, the reagent

phases involved in above systems are immiscible with each other. In Chapter 5 of this dissertation, a novel microreactor was designed, which allows homogenous catalytic reactions to occur at the designated interfaces and separate the subsequent product conveniently.

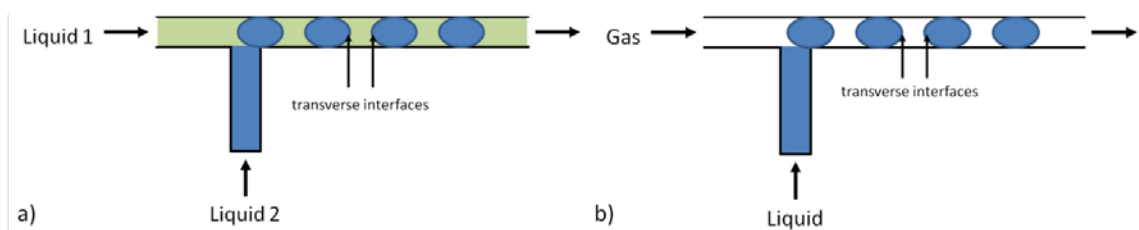


Figure 1-6 Picture of aqueous-organic liquid, and gas-liquid reactor system.

1.3 Electrowetting (EW)

As another approach to miniaturize chemical and biological instrumentation,⁸² electrowetting (EW) was first proposed by Lippmann in 1875⁸³ and had a rapid development over the last 20 years. Basically, EW is the phenomenon for the change of the surface tension caused by the applied voltage between a droplet and the underneath electrode (Figure 1-7). Since EW has been proven very controllable in degree of switchability, the switching speed, the long term reliability, and the compatibility with variable environments,⁸⁴ it has been used in a number of fields, which include biotechnology-related micro-fluidic devices,⁸⁵ display technology,⁸⁶ adjustable lenses,⁸⁷ and so on. For example, Huh et al.⁸⁵ used EW technique to manipulate the air-water two-phase flow on a millisecond timescale for sorting applications. Feenstra and Hayes⁸⁶ presented an electrowetting-based reflective display, which can be used as an electric paper. Peseux and Berge⁸⁷ designed an optical system by using EW technique in which,

an oil droplet was used as lens and operated electrically with variable focal length.

EW originated from the combination of surface chemistry and electrostatics. Basically, the surface tension at a voltage V can be given by Lippmann equation:

$$\gamma_{SL} = \gamma_{SL}^0 - \frac{1}{2} CV^2 \quad (1),$$

where γ_{SL}^0 is the voltage-free solid-liquid interface energy, C is the capacitance between the drop and the solid surface, V is the voltage applied.^{88,89} In the case of electrowetting on dielectrics (EWOD), the capacitance C can be expressed by:

$$C = \frac{\epsilon_0 \epsilon_r A}{d} \quad (2),$$

where ϵ_0 is the permittivity in vacuum, ϵ_r is the dielectric constant, A is the area of the drop on the surface and d is the thickness of the dielectric layer. Since the contact angle (θ) can be expressed according to Young equation:

$$\cos \theta = \frac{\gamma_S - \gamma_{SL}}{\gamma_L} \quad (3),$$

Combining equation (1), (2), and (3), the contact angle can be expressed as a function of voltage applied to the liquid:

$$\theta = \arccos \left(\frac{\gamma_S - \gamma_{SL}^0 + \frac{\epsilon_0 \epsilon_r A}{2d} V^2}{\gamma_L} \right) \quad (4)$$

Where γ_L is the surface tension of liquid, γ_S is the surface tension of solid, γ_{SL} is the surface tension of solid-liquid surfaces.

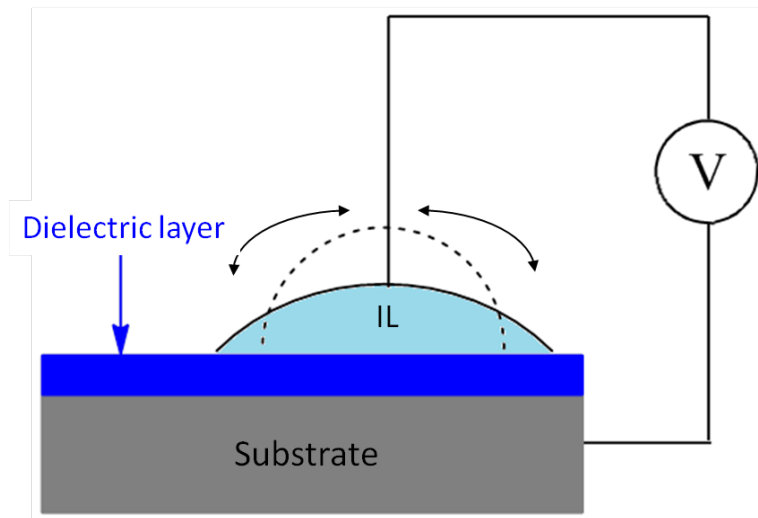


Figure 1-7 Schematic of the electrowetting set-up with a cross-sectional view. Liquid droplet at zero voltage (dash) and at high voltage (solid).

It is always desirable to have a large contact angle change with a smaller applied voltage. However, the high driving voltage is still the main obstacle for further developments and wider applications of electrowetting-based devices currently. Therefore, most recent research has focused on achieving a low voltage operation, in order to conserve power and make electrowetting more practicable for commercial fabrication.

Thus, there is still much room for improvements of EW to make this technique to be achievable for more commercial products. In Chapter 7 of this dissertation, we discovered that it is possible to reduce the driving voltage to 70 mV by using an ionic liquid (IL) film as the dielectric layer without oil bath. We believe our method to realize low voltage electrowetting provides a new approach to simplify the digital micro-fluidic design, and enables new studies on micro-separation, micro-pumps, liquid lens and e-ink display.

CHAPTER 2: ATOMIC FORCE MICROSCOPY (AFM)

2.1 AFM Operation Principle

Atomic Force Microscopy (AFM), invented by Quate and Gerber in 1986,⁹⁰ could provide an atomic resolution on both conducting and insulation surfaces. Basically, AFM images sample by 'feeling' rather than by 'looking'. The scheme in Figure 2-1 demonstrates the main features of an AFM system. A flexible force-sensing cantilever scans in a raster way over the surface of the sample. The motion of the cantilever is manipulated by a piezoelectric tube, that moves the tip in x, y, and z directions. A laser beam is focused onto the end of the cantilever, and then reflects off onto a photodiode detector, which splits into four segments. During scanning, the interaction between the tip and the sample surface causes a deflection of the cantilever. As a result, the angle of the reflected laser beam changes and the moving laser spot which falls onto the photodiode produces changes in intensity in each of photodiode quadrants. The difference in laser intensity between the top two segments and the bottom two segments $((A+B)-(C+D))$ produces an electrical signal which quantifies the vertical motion of the tip, which represents the height of the sample surface, while, the difference of the laser intensity between the left and right pairs of the segments $((A+C)-(B+D))$ quantifies the twisting motion of AFM cantilever.⁹¹ Besides the laser beam deflection, there are still three basic hardware parts in an AFM: the AFM tip, scanner, and feedback electronics.

The AFM tip probes the sample surface during AFM scanning. Generally, the AFM tip is comprised of two major components: a micro-fabricated, extremely

sharp assembly with a cantilever. AFM manipulates the sharp spike through the cantilever and the sharpness of the spike determines the resolution of the AFM. Furthermore, the spring constant of the cantilever is usually low, which enables the AFM to control the force between tip and sample with greater precision. In recent years, it has become possible to functionalize probes by coating biological molecules or other functional layers for special applications. Liu et al. modified AFM tips with self-assembled monolayer, and those tips exhibited a superior wear-resistant behavior in tapping mode scans.⁹² Chen et al. modified the AFM tip to carry antiricin antibodies, and this modified tip was applied to detect trace amounts of ricin for food toxin detection.⁹³

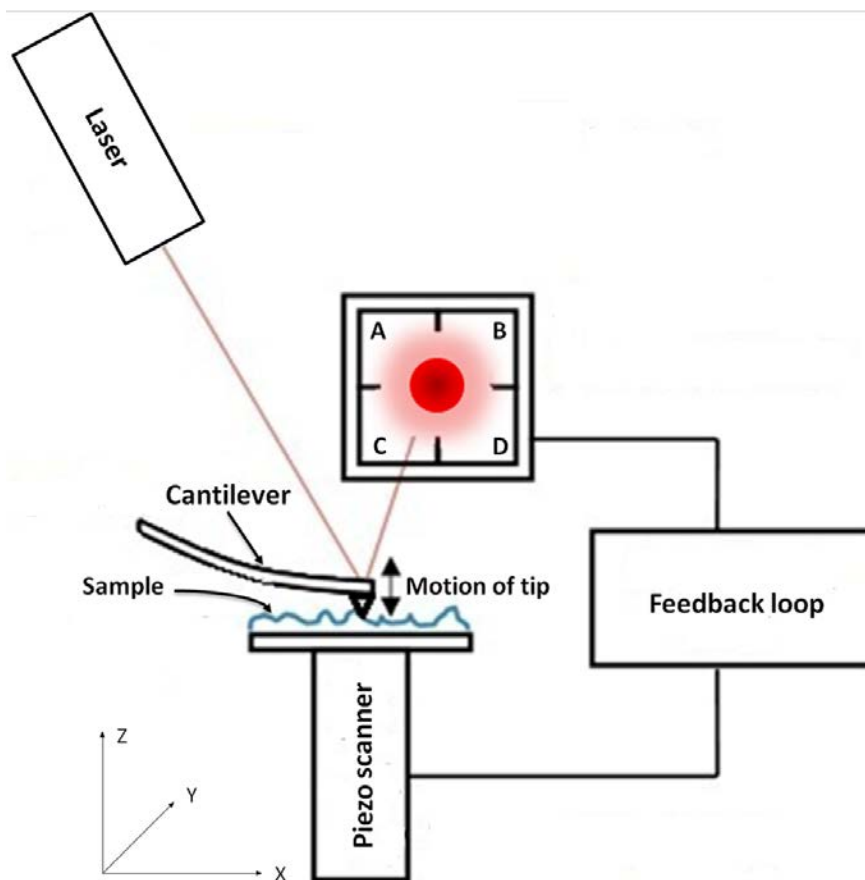


Figure 2-1 Scheme representation of the atomic force microscopy.

To manipulate the tip to scan over the sample surface three dimensionally, the AFM scanner is utilized, which is made of piezo-ceramics. Piezo-ceramics are a type of materials that can expand or contract in the presence of a voltage gradient, which position the tip with high precision based on the piezoelectric effect. The piezoelectric effect was discovered by French physicists Jacques and Pierre Curie in 1880, when the quartz crystals were subjected to a mechanical pressure, from which an electric potential can be generated. Conversely, it is found that an electric field can also cause the distortion of the crystal.

The single-tube AFM scanner consists of five electrodes. Four are external electrodes which are parallel to the axis with opposite polarities (-x, x, -y, y), the inside surface of the AFM tube is the ground electrode (z), used as one whole electrode (Figure 2-2). Silver epoxy is used to connect high voltage wire to these electrodes. If the positive voltage is applied on the +x electrode and negative voltage is applied on the -x electrode, the +x electrode expands while the -x electrode contracts. As a result, the tube will bend to -x direction. In the same way, the tip can move from the center to other three directions (-X, +Y and -Y). If the positive or negative bias voltage is applied on the four outer electrodes at a same time, the tube can extend or contract in z direction. Either the sample or the tip can be manipulated precisely through the combination of the above movements by using piezo.

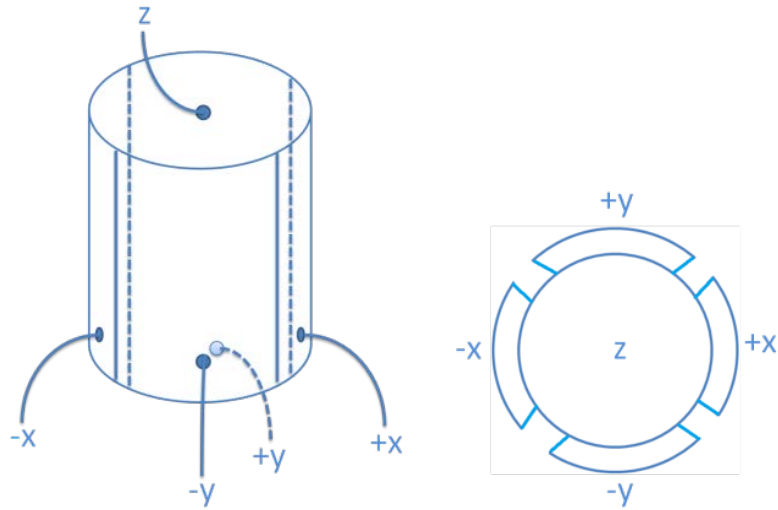


Figure 2-2 Top and side views of a piezoelectric tube scanner. +x, -x, +y, -y and z represent 5 electrodes in three orthogonal directions.

During AFM functioning, the tip tracks the sample surface in a constant force (contact mode) or constant amplitude (tapping mode) by maintaining a predefined level via feedback control system, which is called set-point. The principle of this electronics can be described as follows. The signal from the photodiode is fed back into the piezoelectric transducer, which causes the sample move up and down.⁹¹ If the distance is too large, the feedback system increases the current, and makes the scanner tube to do a z-movement to lower the tip. If the distance is too small, the feedback system decreases the current to raise the tip, preventing the tip from damaging the sample surface.

Compared with other microscopy techniques, AFM has several extra advantages. First, AFM probes the sample surface with a presentation of three-dimensional image. Second, the resolution of an AFM topography image can be 0.1 to 1.0 nm in the x-y plane and 0.01 nm in the z direction, which is an atomic level. Third, no vacuum environment or any special sample treatment is needed before imaging.

Besides, it can be used in either an ambient or liquid environment, so, it is allowed to image bio-sample in real time. On the other hand, the drawbacks of AFM also cannot be neglected. It scans the sample surface line by line and so far, the maximum scanning area is about $150 \times 150 \mu\text{m}^3$. Obviously, other microscopy techniques, like a scanning electron microscope (SEM), can scan a wider area than AFM with a faster speed.

2.2 Forces

AFM captures the image based on monitoring forces between the tip and sample. Basically, there are three different types of forces: van der Waals force, electrostatic force, and capillary force.

Tip and substrate consist of neutral molecules but with imperfect symmetrical electron distribution. This gives rise to subtle charge imbalances known as “dipoles”.⁹⁴ The van der Waals forces are the sum of three different types of forces caused by dipoles. The first type is the orientation or Keesom force, which results from the dipole-dipole interaction between two atoms or molecules; the second one is the Debye force, which results from the dipole-induced dipole interaction between two atoms or molecules; the last one is the London or Dispersion force, which results from the instantaneous dipole-induced dipole interaction and it is the most contribution to the Van der Waals force.⁹⁵ The total Van der Waals potential can be written as:

$$U_{\text{vdW}}(r) = U_{\text{Keesom}}(r) + U_{\text{Debye}}(r) + U_{\text{London}}(r) = -\frac{u_1^2 u_2^2}{3(4\pi\epsilon_0\epsilon)^2 k_B T r^6} - \frac{u_1^2 \alpha_{02} + u_2^2 \alpha_{01}}{(4\pi\epsilon_0\epsilon)^2 r^6} - \frac{3\alpha_{01}\alpha_{02}(h\gamma_1)(h\gamma_2)}{2(4\pi\epsilon_0\epsilon)^2 r^6 (h\gamma_1 + h\gamma_2)} = -\frac{C}{r^6} \quad (1)$$

in which u_1 and u_2 are the dipole moments of the molecules, ϵ_0 is the vacuum permittivity, ϵ is the dielectric constant of the medium, k_B is the Boltzmann constant, T is the temperature, α_{01} and α_{02} are the electronic polarizabilities of the molecules, and h is the Plank constant.⁹⁵

In order to model the interaction between the AFM tip and the sample substrate, it is necessary to consider them as macroscopic bodies rather than individual atoms or molecules. Therefore, based on the tip shape and the geometry feature of the bodies, the approximations of the van der Waals interaction between AFM tip and substrate are listed in Table 2-1.⁹⁶

Table 2-1 Van der Waals interaction laws for most common AFM geometries.⁹⁶

Geometry	Force
Two flat surfaces	$f = -\frac{A_H}{6\pi D^3}$ per unit area
Two spheres	$F = -\frac{A_H}{6D^2} \frac{R_1 R_2}{R_1 + R_2}$
Sphere-flat surface	$F = -\frac{A_H R}{6D^2}$
Cone-flat surface	$F = -\frac{A_H \tan^2 \theta}{6D}$
Paraboloid-flat surface	$F = -\frac{A_H}{12D^2} \frac{l_{xy}^2}{l_z}$
Cylinder-flat surface	$F = -\frac{A_H R^2}{6D^3}$

A_H is the Hamaker constant, D is the distance, R is the radius of the sphere or of the cylinder, θ is the semi-aperture of the cone, l is the semi-axis of the paraboloid. $A_H = \pi^2 C \rho_1 \rho_2$, where C is the constant in the atom-atom pair potential, ρ_1 and ρ_2 are the number of atoms per unit volume.

In this dissertation, the AFM tip and surface interaction was modeled as a spherical surface approaching a flat surface, so the interaction can be described mathematically by function:

$$F = -\frac{A_H R}{6D^2} \quad (2)$$

On the other hand, if the AFM tip and sample surface are charged, the electrostatic/Coulombic force present when they are brought closer together.

This electrostatic force follows the Coulomb force law:⁹⁴

$$F = \frac{1}{4\pi\epsilon_0} \cdot \frac{q_1q_2}{r^2} \quad (3)$$

Where q_1 and q_2 are two charged ions in a vacuum, r is the separation between tip and sample surface, and ϵ_0 is referred to as the “permittivity of free space”.

Besides bearing Van der Waals force and electrostatic force when a AFM tip scan over the sample surface, it also serves as an ideal nucleation site for the condensation of water vapor in the air at normal relative humidity (RH).⁹⁴ A water thin layer adsorbed on the sample surface also contributes to the formation of the meniscus. This means the tip will also bear an attractive force exert by the liquid meniscus, and this force is called “capillary force”. The radius of the meniscus is determined by the function^{97,98}:

$$r = \frac{\gamma V}{[RT \log(p/p_S)]} \quad (4)$$

Where γ is the surface tension of water, p and p_S are the partial vapor pressure and the saturated vapor pressure of water. When the radius of the meniscus bridge is less than 100 Å, the capillary force can be described with the equation^{97,98}:

$$F = \frac{4\pi R \gamma \cos\theta}{(1+D/d)} \quad (5)$$

Where θ is the contact angle between the water-vapor interface and the tip, D is the distance between the tip and the substrate, and d is the distance the tip extends into the water bridge. In fact, it is hard to eliminate capillary force since it is independent of the instrument settings and depends on the circumstances. The most effective way would be keep the AFM in a dry air environment.

2.3 Force-Distance Curve

An AFM force-distance curve is a plot, which describes the relationship between tip-sample interaction forces and tip-sample distance. There are two factors contributing to this curve: the tip-sample interaction $F(D)$ and the elastic force of the cantilever.⁹⁵ Usually, the tip-sample forces can be simply modeled by the interatomic Lennard-Jones forces:

$$F_{LJ} = -24\varepsilon\left[2\left(\frac{\sigma^{12}}{r^{13}}\right) - \left(\frac{\sigma^6}{r^7}\right)\right] \quad (6)$$

Where σ and ε are the specific Lennard-Jones parameters that depend on the material, r is the separation between tip and the surface of the sample.

Then the Lennard-Jones potential can be described by the following equation:

$$V_{LJ} = \oint F_{LJ} dr = 4\varepsilon \left[\left(\frac{\sigma}{r}\right)^{12} - \left(\frac{\sigma}{r}\right)^6 \right] \quad (7)$$

If we plot the above two functions, Lennard-Jones potential is given by the light blue dash line in Figure 2-3. While, the Lennard-Jones force is indicated by the orange line. When the force is 0, the position on the Lennard-Jones force curve is exactly the same position where the minimum of the potential well value is.

As Lennard-Jones force curve shows, at very beginning, when the distance between the tip and sample surface is very large, the attractive force is very small. As the tip is gradually brought close to the sample surface, the attractive force starts to increase and exerts a significant force on the tip. This attractive force increases until the distance between the tip and sample surface are so close that the repulsive force starts forming. The repulsive force rises rapidly with the decrease of the separation and it weakens the attractive force until the force goes to zero. After this point, the total force becomes repulsive if the tip goes further close to the sample surface.

Since the forces on the tip are different when it moves toward or away from the sample surface, the force curve can be divided into approaching and retreat portions. As Figure 2-4 illustrated, there is a hysteresis between the lifting portion of force curve and approaching portion of force curve. The commonly known source of hysteresis is the “adhesive force”, which results from the formation of a capillary bridge, as well as the breaking of bonding between the tip and sample. Therefore, the approaching portion of the force curve is more ideal for the analysis.

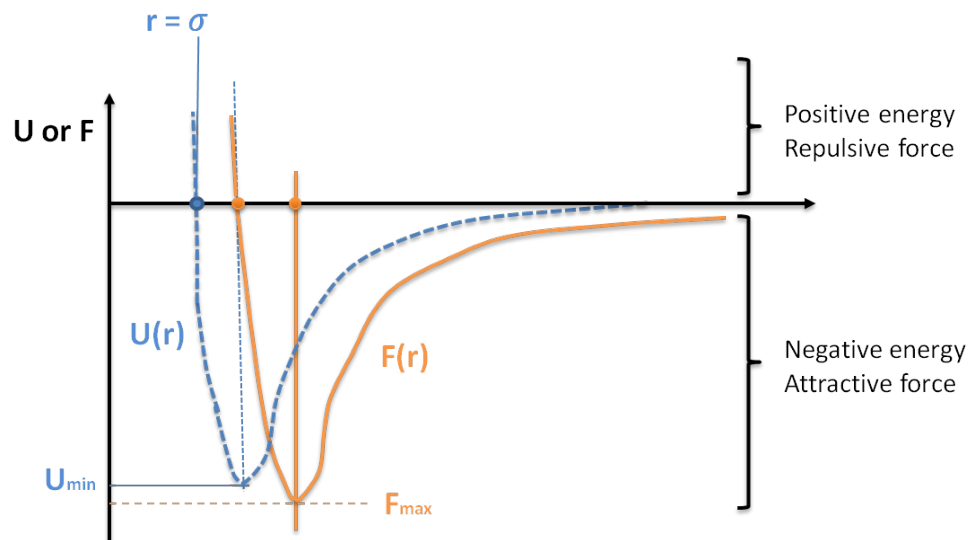


Figure 2-3 Schematic diagram shows the potential energy and force with separation (r) between tip and sample surface as described by the Lennard-Jones functions.

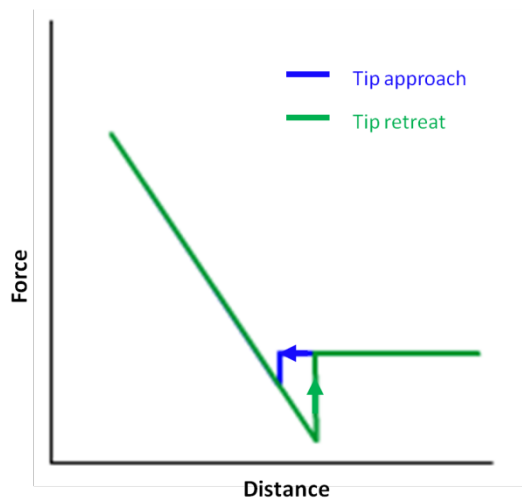


Figure 2-4 Approaching and retreat force curve.

2.4 Imaging Modes

AFM has been widely used to image microscopic features on sample surface. Two modes are used for the surface probing based on the involved force interaction; they are contact mode and non-contact ac modes.

The contact mode is the known the easiest mode for the surface imaging. In this case, the tip scans over the sample by contacting with the surface. During scanning, the piezo crystal pushes the tip against the sample surface with a bend cantilever. It can operate in ambient environment or under liquids.

During contact mode scan, the tip moves across the sample surface, which results in the lateral deflection of the cantilever. Figure 2-5 (b) shows a surface structure with a centrally located step, the lower, smooth areas are located on both side of the central step. The flat part on the left side contains a dashed area with a relatively high frictional coefficient. Figure 2-5 (c) demonstrates the cantilever's deflection when it scans from left to right. Figure 2-5 (d) is an AFM signal of the surface topography. It represents the deflection change in the vertical direction of the cantilever, which does not include the deflection in horizontal direction. Figure 2-5 (e) and Figure 2-5 (f) show the Lateral Force Microscopy (LFM) signal, which indicates the torsion of the cantilever, and during scanning, the step makes the cantilever twist. Also, the area on the sample surface with a different surface frictional coefficient compared to the surrounding area made the cantilever twist. Both result in a lateral force signal.

In summary, the advantage of contact mode AFM is that the capillary force can be eliminated. The disadvantages of contact mode AFM are also obvious. The first one is sample damage at high contact force, especially those vulnerable biological samples. If the applied force is too strong, the sample on the surface might be shaved off during the scanning. The second one is the artificial height signal, when the tip scans over a surface with a high frictional contrast. The high

dragging force can twist the cantilever and make the laser spot to move horizontally on the photodiode. An imperfectly symmetrical lateral torsion of a cantilever or the cantilever is imperfectly aligned vertically to the fast scan direction can also make the laser spot move not only horizontally, but also vertically (Figure 2-5 (a)). Since the vertical movement of the laser spot represents the height of the objects, which means those artificial movements in z direction create artificial topography signals.⁹⁹ In this dissertation, contact mode AFM is used for the local oxidation lithography and friction force microscopy measurement.

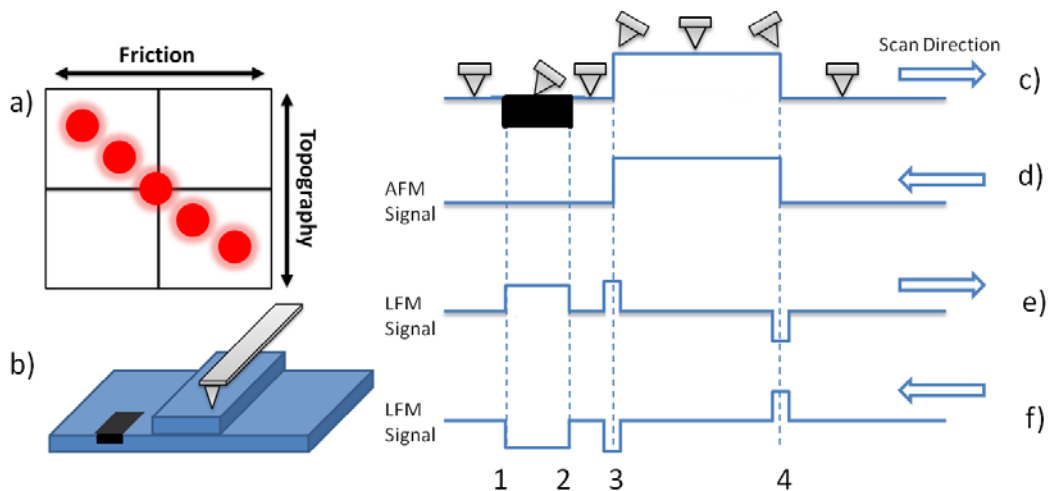


Figure 2-5 AFM and lateral deflection signals of the cantilever.

Though contact mode AFM can apply a very small force on the sample surface, the shear forces and compressive forces created by the tip/sample contact can still generate elastic and/or plastic sample deformation.¹⁰⁰ To avoid these drawbacks of the contact mode AFM, ac modes were used in the image capturing. Therefore, ac mode AFM is better for the sample surface characterization, especially for those samples which are easily deformed or

damaged. However, the resolution of the topographic image captured by the non-contact mode AFM is lower than that captured by the contact mode AFM due to the tiny applied force.

There are two main types of ac mode AFM: Tapping mode and non-contact mode. Tapping mode AFM is a useful assay method, especially in biology since it is capable of achieving high resolution on sample surfaces and biological samples ranging in size from individual molecules to cells. Tissues can also be imaged in their native state. For example, Figure 2-6 is the AFM tapping mode image of YajC-CT hydrogel, after it was dispersed in a dilute water solution and deposited onto mica ($[KAl_2(OH)_2AlSi_3O_{10}]$) surface.

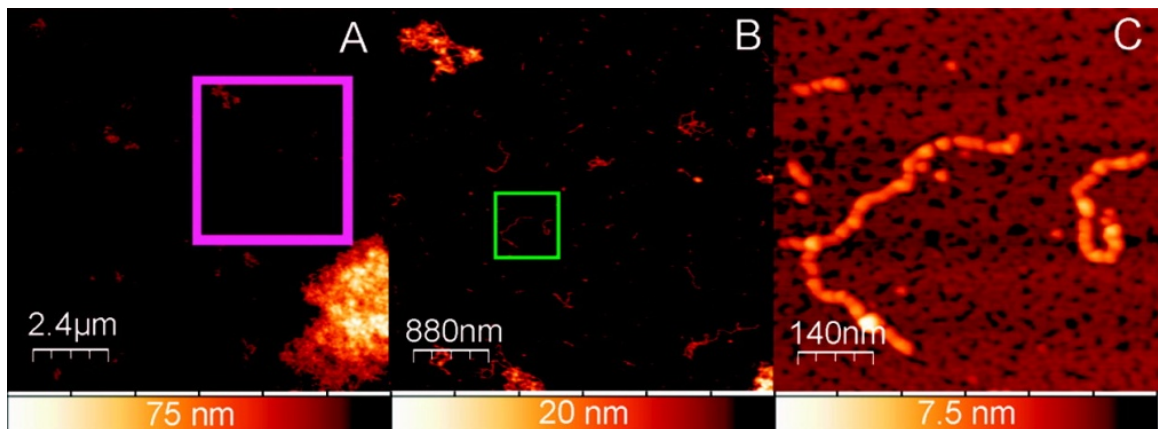


Figure 2-6 AFM topography image of a diluted hydrogel sample. Panel B is a zoom in view of the region in the box in panel A, whereas panel C is a zoom in view of the region in the box in panel B.

For the tapping mode, the cantilever is excited near its resonance frequency by a piezo-element mounted in the AFM tip holder, and constant oscillation amplitude of the AFM tip is maintained through feedback loop during the scanning. The external periodic driving force which acts on the catilever can be expressed by:

$$F = F_0 \sin \omega t \quad (8)$$

Where F is an oscillating driving force, ω is the frequency of driving force and F_0 is the force amplitude. Then, the displacement of the tip from its equilibrium position is defined by the following:

$$\ddot{z} + \omega_0^2 z = A_0 \cos \omega t \quad (9)$$

Where $A_0 = F_0/m$, $\ddot{z} = d\left(\frac{dz}{dt}\right)/dt$, and ω_0 is the natural frequency.

The solution of equation 9 ($\omega_0 \neq \omega$): can be written as

$$z(t) = Z \cos(\omega_0 t + \varphi_0) + Z_0 \cos \omega t \quad (10)$$

Where $Z_0 = \frac{A_0}{\omega_0^2 - \omega^2}$ is the amplitude of the cantilever, $Z = \sqrt{C_1^2 + C_2^2}$ and φ_0 is the phase angle, which can be expressed by: $\varphi_0 = -\arctan(-C_1/C_2)$;

$$C_1 = x_0 - \frac{F_0}{m(\omega_0^2 - \omega^2)}; \quad C_2 = v_0/\omega_0; \quad v_0 = dz/dt|_{t=0}$$

Where m is the mass of the cantilever, $\omega_0 = \sqrt{k/m}$ is the natural frequency of oscillation, k is the spring constant and φ_0 is the initial phase of oscillation. The first part in equation 10 describes the free oscillation, while the second part demonstrates the forced oscillation.

When an oscillated AFM tip approaches to the surface, the phase of the oscillation is disturbed due to the tip-sample interaction. This means the phase of the cantilever oscillation is no longer the same with that of the oscillator, due to the fact that some energy is transferred into the sample when the tip tapped it.

Since the feedback system will compensate this energy loss, the amplitude of the cantilever can be maintained, while the cantilever oscillation phase changes and it becomes different from the phase of the oscillator. This change is proportional to the force gradient and can be determined by equation 11:

$$\Delta\varphi \approx \frac{Q}{k} \frac{\partial F}{\partial z} \quad (11)$$

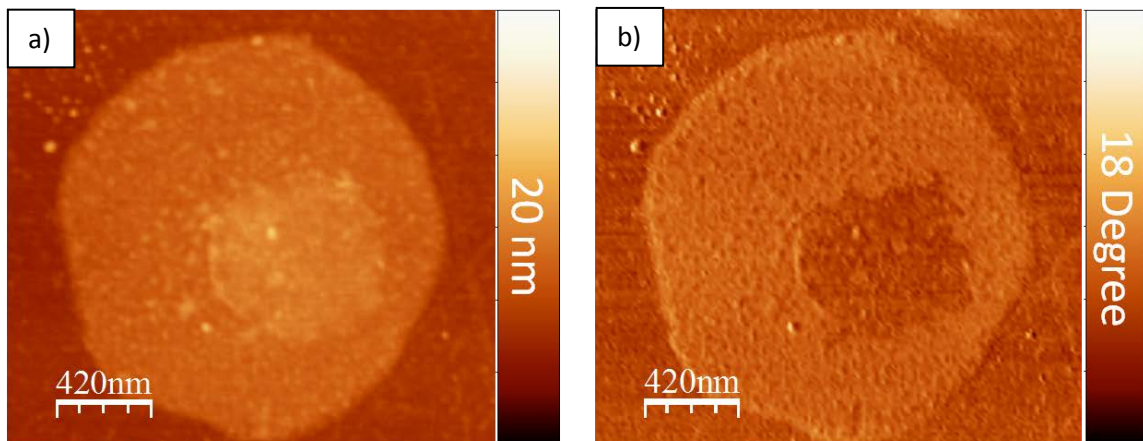
Where k is the cantilever stiffness, Q is the oscillating system Q-factor, F is the tip-sample interaction and z is the tip-sample separation. However, the amount of energy which is transferred into the sample depends on the surface property, especially the elastic nature of the sample surface. This means AFM phase image can be used to detect variation in composition, adhesion, viscoelasticity and perhaps other properties.

Tapping mode AFM can also be used for the amplitude-distance measurement. During the experiment, an oscillated tip approaches to the sample surface and the amplitude changes due to the tip-sample interaction, which is recorded by the AFM system. This curve can be used for the study of the surface property, which will be discussed in detail in Chapter 6.

For non-contact mode AFM, the oscillated cantilever hovers a few nanometers above the sample surface and never touches the surface, with a ~5nm oscillation amplitude.⁹⁴ The advantage of using non-contact mode is non-contacting, therefore, no deformation or damage to the sample, while the disadvantages are the poor imaging resolution and need for a special tip. Since the interaction between the AFM tip and sample surface is very weak in the non-contact mode

AFM, a flexible cantilever, which is very sensitive to this interaction, is needed. However, a flexible cantilever might be easily disturbed by the environmental vibration and trapped by the capillary force during the surface scanning.

Based on the above descriptions, three types of images can be formed. The first one is a topographical image, which records the vertical movements of AFM tip. The height information of objects can be obtained from this type of image. The second one is a frictional force image, which is used to determine the twisting behavior of the cantilever. The last one is a phase image, which reveals the elastic nature of the sample. Figure 2-7 demonstrates the examples of the topography, friction, and phase images captured by AFM. The color bar of the topography, phase, or friction image represents different height, phase or friction range. Low and high topography, hydrophobicity, or friction is respectively represented by bright and dark colors.



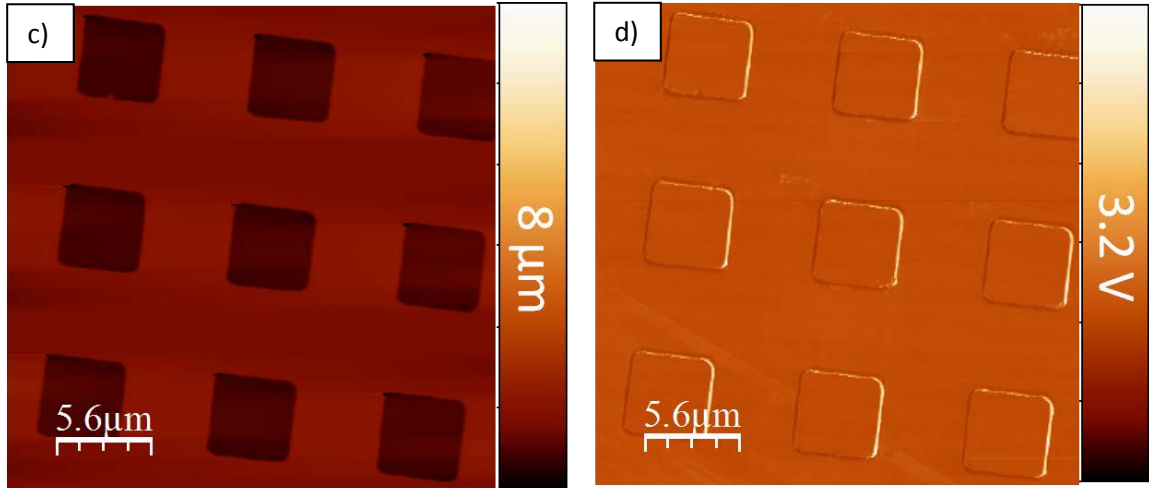


Figure 2-7 Examples of AFM images. (a) and (b) are the topography and phase images of CaM disk on the chemical pattern template, captured by AFM tapping mode. (c) and (d) are the topography and friction images of an AFM calibration standard made by tungsten, captured utilizing AFM contact mode.

2.5 AFM Tip Characterization

Determining the normal spring constant, torsional spring constant, and the tip radius of AFM is of fundamental importance in Lennar-Jones potential calculation, energy dissipation calculation, and tribological property study. All were addressed in our research and will be discussed in the later sections of this dissertation.

Normal spring constant, which is the spring constant for the cantilever in vertical direction/flexural deflection, is usually calculated based on the formulation developed by Sader et al.,¹⁰¹ which is expressed by:

$$k_f = 0.1906\rho_f b^2 L Q_f \Gamma_i(\omega_f) \omega_f^2 \quad (12)$$

Where, k_f is the normal spring constant; ρ_f is the density of the fluid, which is 1.18 kg/m³ during calculation; b and L are the width and length of the cantilever

respectively; Q_f is the quality factor; Γ_i is the imaginary components of the hydrodynamic function; ω_f is the fundamental mode resonant frequency.

Once the normal spring constant is obtained, torsional spring constant, which is the spring constant for the cantilever in lateral direction/torsional deflection, can be calculated by the following theoretical equation¹⁰²:

$$k_\varphi = k_f \frac{2L^2}{3(1+\nu)} \quad (13)$$

Where k_φ is torsional spring constant of cantilever; k_f is the normal spring constant of cantilever; ν is the Poisson ratio, which is 0.28 for SiO₂ made AFM cantilever.

The tip radius is usually measured by Scanning Electron Microscopy (SEM). The disadvantages of this approach are, firstly, that cantilever or probe might be damaged or contaminated during the operation; secondly, special software is needed for the curvature fitting in the data processing. Actually, AFM tip radius can be simply obtained by scanning any material with known size and geometry. This is because the AFM tip is not infinitely sharp, the image of an object is smeared out by the profile of tip as Figure 2-8 shows.⁹⁴ In this dissertation, tip radius is determined by scanning a graphene layer. As Figure 2-8 illustrated, AFM probe can be viewed as two basic geometries, a cone with an attached sphere. The following designations are introduced: w – the convolution of the actual surface topography, h – graphene thickness, R – curvature radius of the tip, and the orange colored line is the path of the tip apex movement. Calculation

of the AFM tip radius (R) is easily obtained using the equation shown underneath the scheme.

The tip-substrate contact area is another important parameter of AFM tip. The pressure under the tip at specific loading force can be obtained by using this value. There are three models for the estimation of the contact area. They are the Hertzian model, Derjaguin-Muller-Toporov (DMT) model and Johnson-Kendall-Roberts (JKR). Basically, DMT and JKR models are more complicated than the Hertzian model. Generally speaking, Hertzian model neglects the adhesion of the sample and can only be applied when the adhesion force is much smaller than the maximum load. While the JKR theory can be applied in the case of large tips and soft samples with a large adhesion and the DMT theory can be applied in the case of small tips and stiff samples with a small adhesion.⁹⁶

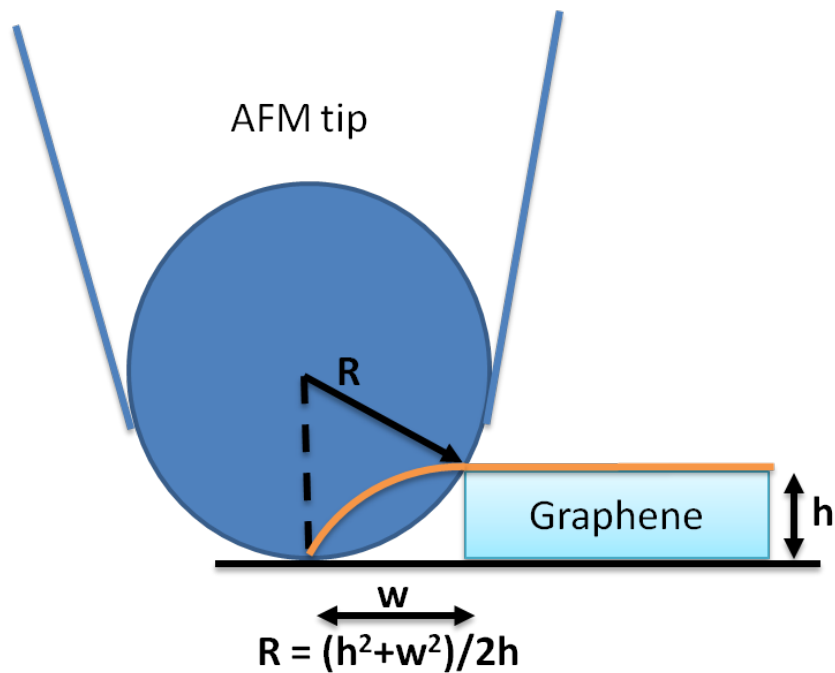


Figure 2-8 Measurement of the AFM tip radius.

2.6 Methodology

Figure 2-9 is the methodology of the projects in this dissertation. AFM was used to conduct the research. It has multiple roles. First, AFM was used as a fabrication tool. In the contact mode, conductive AFM tip was used to conduct the electrochemical oxidation to create a chemical pattern or conduct an electrowetting experiment. Then, AFM was used as a characterization tool in the tapping mode to characterize the surface structure, the thickness, as well as the surface potential. Also, AFM in the contact mode was used as a measurement tool to measure the tribological force properties of sample.

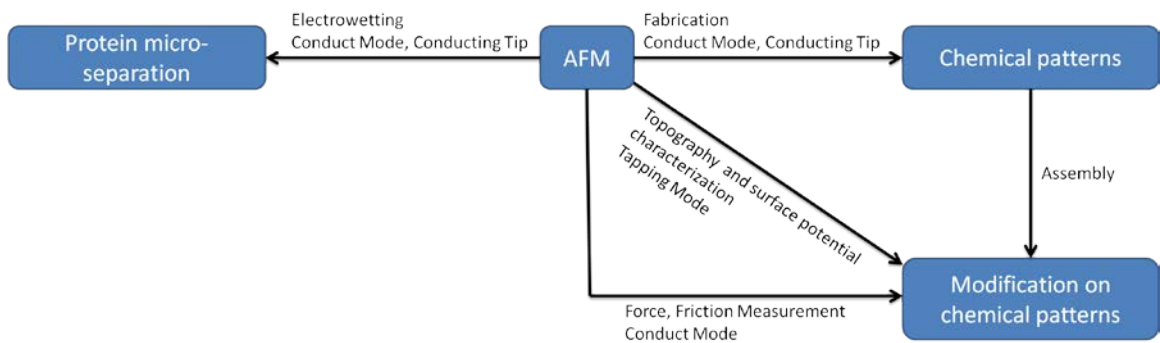


Figure 2-9 The flow chart of the methodology in this dissertation.

CHAPTER 3: SELF-ASSEMBLED MONOLAYERS (SAMS) FABRICATION AND AFM LOCAL OXIDATION LITHOGRAPHY

3.1 Introduction

Self-assembled monolayer (SAM) is formed by the spontaneous adsorption of the active organic molecules on the solid substrate. It was studied by Zisman et al.¹⁰³ in 1946, and has received more attention since the 1980s. Monolayer self-assembled on solid substrates plays a key role in nanoscience and nanotechnology for several reasons: 1) a variety of molecules can be easily stabilized on the surface with a fine chemical control; 2) surface property, such as wetting, adhesion, reactivity, and friction, can be modified in a molecular-level; 3) the monolayer can be used for surface protection or as an insulating film. The self-assembly is driven by the Van der Waals force and chemical bond formation. In order to minimize the free energy of the interface between the surface and the environment.¹⁰⁴ The adsorption kinetics of SAM can be expressed by Langmuir adsorption model:¹⁰⁵

$$k(1 - \theta) = \frac{d\theta}{dt} \quad (1)$$

Where the k is the rate constant, θ is the proportional amount of area deposited, and t is the reaction time. By increasing the time, three phase statuses can be achieved during the SAM formation. The first phase status is the low density phase/2-D gas phase, with random dispersion of molecules on the surface. After that, an intermediate density phase, 2-D liquid phase, with conformational disordered molecules or molecules lying flat on the surface can be formed. Finally, it transfers to a high density phase with close packed order and molecules stand normal to the substrate's surface.¹⁰⁶

Thiol-metal group, silane-hydrophilic surface group, alkene-Si-hyride group, alkane group, and phosphate/fatty acid group are five groups of widely used SAMs. Theoretically, SAM should provide highly ordered interface. However, because of the intrinsic or extrinsic reasons, such as the cleanliness of the substrate, methods for the substrate preparation, and the purity of the adsorbate solution, there might be some defects in SAM.¹⁰⁷

The organic self-assembled monolayer (SAM) coated wafers are widely used for studying the surface characteristics because people can easily design the desired physical and chemical properties on the required surface. The organic molecules can spontaneously assemble on the required surfaces after the substrate is immersed into a solution. Usually, the stable, homogeneous and functional monolayer has three parts as constituents seen in Figure 3-1. The first part is head group which owns specific, reversible affinity for different substrates by covalent bonding or electrostatic force. The other two parts are a tail (long alkyl chains) with a functional group at the terminal end. By varying these terminal groups, the interfacial characteristics of the monolayer can be changed significantly.

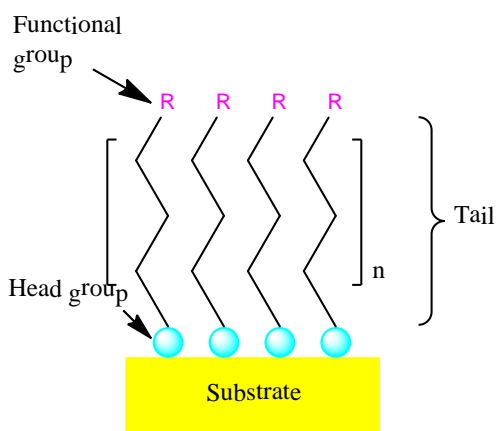


Figure 3-1 Representation of a SAM structure.

Scanning-probe lithography (SPL) is used for the generation of spatially defined nanostructures, since it can create precursor binding sites in the controlled shape, size and position at molecular level. Functionalized SAMs are good candidate for this fabrication with designable surface chemical properties.¹⁰⁸ For example, Octadecyltrichlorosilane (OTS) monolayer is an amphiphilic molecule consisting of a long-chain alkyl group ($C_{18}H_{37}$ -) and a polar head group ($SiCl_3$ -), which is the widely studied and used in academia and industry. It is known that OTS monolayer can be stabilized on various hydroxylated surfaces, like silicon oxide,^{109,110} aluminum oxide,¹¹¹ quartz,¹¹² glass,¹¹³ mica,¹¹⁴ and gold surface.¹¹⁵ In this dissertation, local oxidation lithography on OTS SAM is introduced as the patterning technique.¹¹⁶ Local oxidation lithography is one of the oxidative probe lithography techniques, but conducted in a 100% relative humidity environment. So, rather than the uncompleted oxidation, which only oxidizes the terminal group of silane film, or completed oxidation, which causes silane desorption from the substrate, the silane is partially degraded and stays on the surface after the

oxidation. Obviously, this is an ideal tool for nano-scale chemical pattern fabrication, which allows us to generate two-dimensional and three-dimensional chemically functionalized nanopatterns with a variety of functionalities on the surface.¹¹⁶

3.2 Experimental Set-up to Create Chemical Patterns on OTS

3.2.1 Instruments

The surface patterns were fabricated using Agilent PicoPlus 3000 Atomic Force Microscopy (AFM) in an environmental chamber. MikroMasch CSC17/Ti-Pt tips (12 kHz resonant frequency, 0.15 N/m force constant) were employed for pattern fabrication in contact mode. MikroMasch NSC14 tips (150 kHz resonant frequency, 5 N/m force constant) were used in sample characterization in tapping mode. All the AFM images were processed and rendered using WSxM.¹¹⁷ The SAM thickness on the silicon surface was examined by Angstrom Advance PhE 101 ellipsometer.

Ellipsometry is a non-destructive, non-contact measurement technique using the polarization of the laser light to determine the film thickness and the optical property of the sample. Basically, during the measurement, a linearly polarized laser light (helium/neon laser with 632.8 nm wavelength in our set-up), with a known orientation from the source, incidentally pound the surface of the substrate, and are reflected off the sample, become elliptically polarized. The polarization of the reflected light can be measured by the ellipsometer. By comparing with the orientation and the direction of polarization of the incident light, the relative phase change, Δ and the relative amplitude change, Ψ can be

calculated. The relationship between Δ and Ψ can be expressed by the Fresnel reflection equation:

$$\rho = \frac{R_p}{R_s} = \tan\Psi \exp(i\Delta) \quad (2)$$

Where ρ is the ratio that an ellipsometer measured, R_p and R_s are the Fresnel reflection coefficients for p- and s- polarized light. Combined with the established model and an iterative procedure, the thickness of the film can be obtained.

3.2.2 Chemicals and materials

Octadecyltrichlorosilane (OTS, 97%) was purchased from Gelest. Toluene (HPLC grade) was purchased from Sigma Aldrich. Silicon (100) wafers (Virginia Semiconductors, Nitrogen doped, 30 $\Omega\bullet\text{cm}$ resistivity) were polished to ultra-flat grade with a Root-Mean-Square (RMS) roughness smaller than 5 Å. All the solution was prepared with water from a Narnstead Nanopure Diamond lab water purification system with normal resistivity of 18.2 $\Omega\bullet\text{cm}$.

3.2.3 Octadecyltrichlorosilane (OTS) self-assembled monolayer preparation for pattern fabrication

The Si (100) wafer was cut into 1 cm x 1 cm pieces. Then, the wafer was boiled in the piranha solution (2 parts of 98% sulfuric acid and 1 part of 30% hydrogen peroxide) at 170 °C for 30 mins. At high temperature, the H_2O_2 was decomposed; $\text{O}\bullet$ and $\text{OH}\bullet$ are generated to remove all organic contaminants and also help to grow a thin oxide layer of silanol (Si-OH) on the surface. After that, the wafer was dipped into 5 mM OTS toluene solution for 8 hrs incubation. As shown in Figure 3-2, the precursor OTS molecule (Figure 3-2 a), reacted with the trace amount of water in the solution to form silanols, followed by the cross-linking and

condensation reactions. As a result, the silane molecules cross-linked together and anchored onto the surface via the Si–O–Si bond (Figure 3-2 d). Then, the as-prepared OTS film was incubated in a sealed vial at 40 °C, 100% relative humidity for 8 hours to get a pinhole-free OTS film (in this case, OTS molecules readjust their position and the surface intensity increase). Then the OTS-coated wafer was dipped into the OTS toluene solution again for another 8 hours. After three such cycles, the OTS film was stabilized, without a pinhole and capable of being used for the follow-up experiment.^{108,118-120}

Then, AFM was used to monitor the surface properties of OTS film, while the ellipsometer was used to determine the thickness of this film. AFM topography and phase image in Figure 3-3 show that OTS film is very flat and OTS molecules form a featureless and homogenous film on the top of the silicon wafer. The height variation between any two points within 20 μm^2 was less than 3 nm. The ellipsometry result demonstrates that the OTS film thickness was 2.6 ± 0.3 nm, which was consistent with the published results.¹²¹

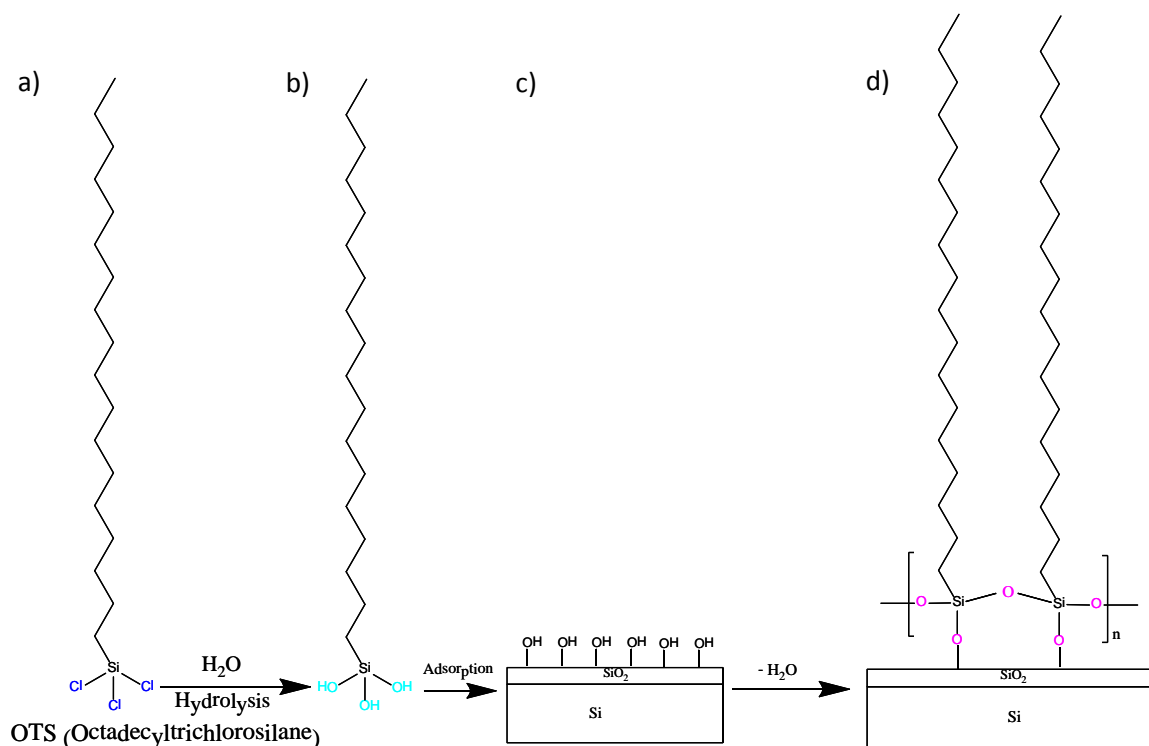


Figure 3-2 The formation of OTS film on Si (100) wafer.

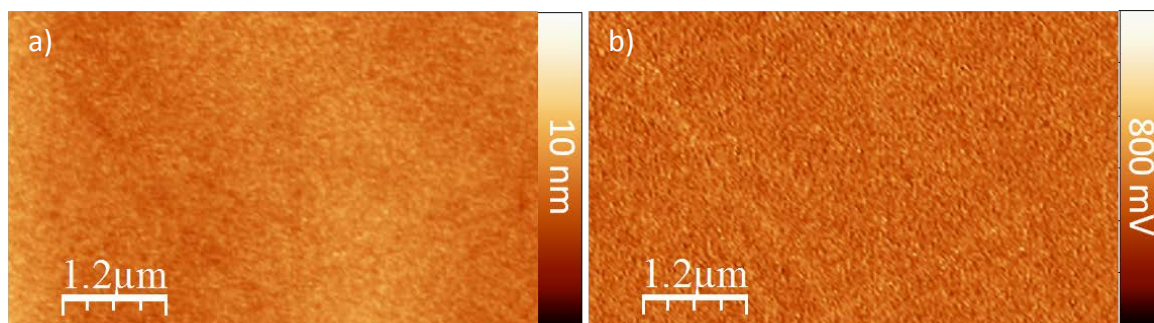


Figure 3-3 AFM (a) topographic and (b) phase image of a homogenous OTS film.

3.2.4 Fabrication hydrophilic chemical patterns on OTS by using local oxidation lithography

The chemical pattern was fabricated on the self-assembled monolayer of OTS by electrochemical writing using a conductive AFM probe in contact mode at a humid environment. With the help of the chemical patterns, we were able to modify surface with defined chemistry and topography with references in

positions and height. A Mikromasch Type CSC17 platinum–titanium-coated conductive AFM tip was used in the pattern fabrication process and was connected to the virtual ground. During fabrication, a 5 to 10 V DC bias was applied to the wafer. In this case, the Pt-Ti-coated tip acted as the cathode and the OTS wafer acted as the anode. Since the voltage applied is higher than the water electrolysis reaction needs (1.23 V), the water between the tip and the sample was electrolyzed, generating active oxygen species such as ozone, atomic oxygen, and hydroxyl radical, which can oxidize the methyl-terminated OTS film to carboxylic-terminated patterns. This partially degraded OTS pattern is called an OTSpd pattern.⁹⁹

Figure 3-4 shows a representative OTSpd pattern fabricated set-up using a stationary tip under the above controlled conditions. Because the formation of the OTSpd pattern is due to the diffusion of the active oxygen species, the size of the OTSpd pattern is actually in proportion to the dwell time of the bias voltage. After the active oxygen species are generated continually and have converted the hydrophobic OTS surface to hydrophilic OTSpd, a water film can cover the surface of the OTSpd pattern which is beneficial for the lateral diffusion of those active oxygen species. As the result, the new -COOH terminated surface is generated and the OTSpd pattern grows bigger and bigger. The size of the OTSpd pattern can range from ~25 nm to sub-millimeters.⁹⁹

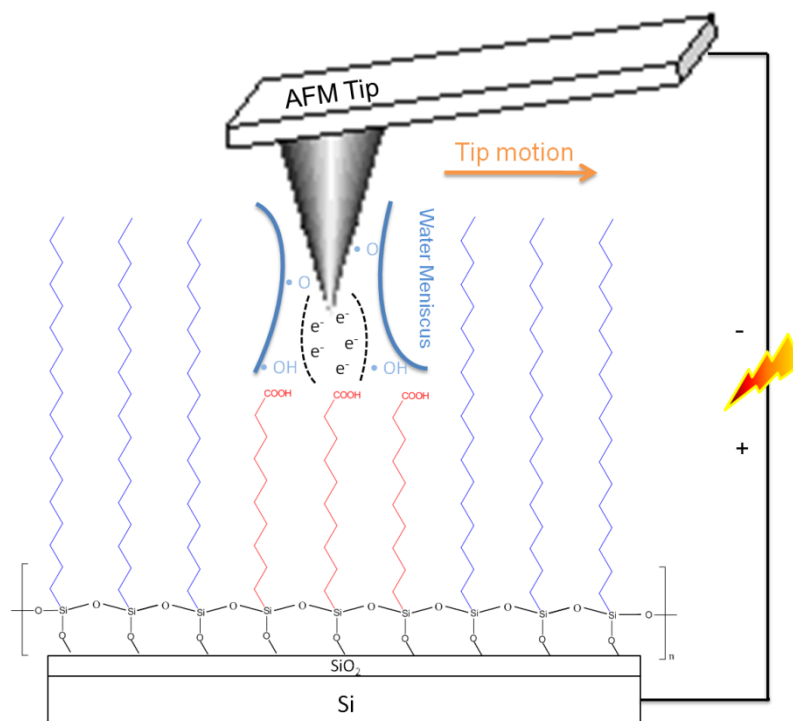


Figure 3-4 The experimental setup for the AFM probe oxidation lithography on OTS film.

The AFM image was acquired with the contact mode tip to overcome the topographic artifacts caused by the static charge during the AFM scanning in tapping mode. Figure 3-5 a is the topography image. It shows that there is a bright spot in the center of the OTSpd pattern. This peak is SiO₂ and it is formed due to the deep oxidation directly under the intense electric field. It can be proved by dipping the wafer in 1% HF solution for 30 s, the center peak disappears and it is changed into a deep hole whereas patterns remain intact. This HF etching test indicates that the center part is made of SiO₂.⁹⁹ The topography histogram in Figure 3-5b demonstrates the height distribution of the OTS background and the OTSpd pattern, which shows the visual impression of the distribution of the height of each pixel. It is an estimation of the probability distribution of a continuous variable. From the histogram, we know the apparent heights and standard deviation of OTS and OTSpd are 9.66±0.01 Å and 20.25±0.01 Å, respectively. The depth of OTSpd pattern can be calculated as¹²²

$$OTSpd_{Depth} = OTS_{ApparentHeight} - OTSpd_{ApparentHeight}$$

And the standard deviation of the OTSpd depth can be expressed as¹²²

$$\sigma_{OTSpdDepth} = \sqrt{\sigma_{OTSpdApparentHeight}^2 + \sigma_{OTSApparentHeight}^2}$$

Based on above calculation, the depth of the OTSpd pattern is $10.60 \pm 0.01 \text{ \AA}$ for the sample shown in Figure 3-5 a. Using the same approach, the depth of the OTSpd pattern was obtained for 30 different samples. The average value from these AFM measurements is $10.21 \pm 0.72 \text{ \AA}$. However, this height difference does not directly correspond to the degraded carbon number because two processes involved here. One is the degradation of the OTS film and another is the growth of SiO_2 underneath the film. Therefore, the final pattern height is the summation of the above two processes.

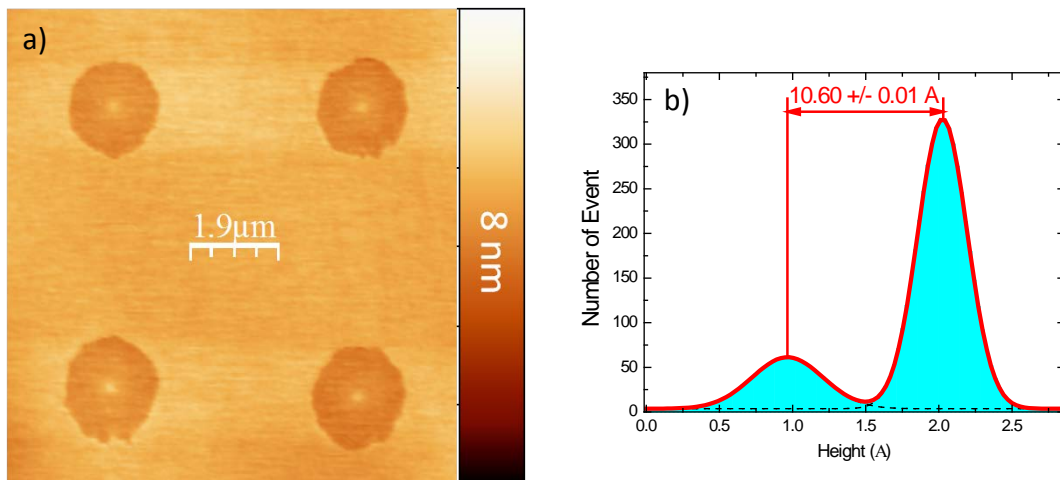


Figure 3-5 Measuring the depth of OTSpd pattern. (a) The topography image of an array of OTSpd pattern, acquired in contact mode immediately after the sample was prepared. (b) The histogram of the topography image, which indicates the depth of the OTSpd disk is $10.60 \pm 0.01 \text{ \AA}$ lower than the OTS background.

As mentioned before, the OTSpd is terminated with the carboxylic group ($-\text{COOH}$). This can be proved by using fluorescent probe 1-pyrenyldiazomethane (PDAM). PDAM is a small molecule, which can specifically react with the $-\text{COOH}$

group, so it can be used to detect the existence of-COOH.¹²³ The reaction is demonstrated in Figure 3-6, and the detailed procedure can be found in elsewhere written by our group.⁹⁹ The experimental result shows that PDAM molecules can couple with the carboxylic groups of the OTSpd surface, and emit fluorescent photons upon excitation. Therefore, the OTSpd is terminated with carboxylic group.

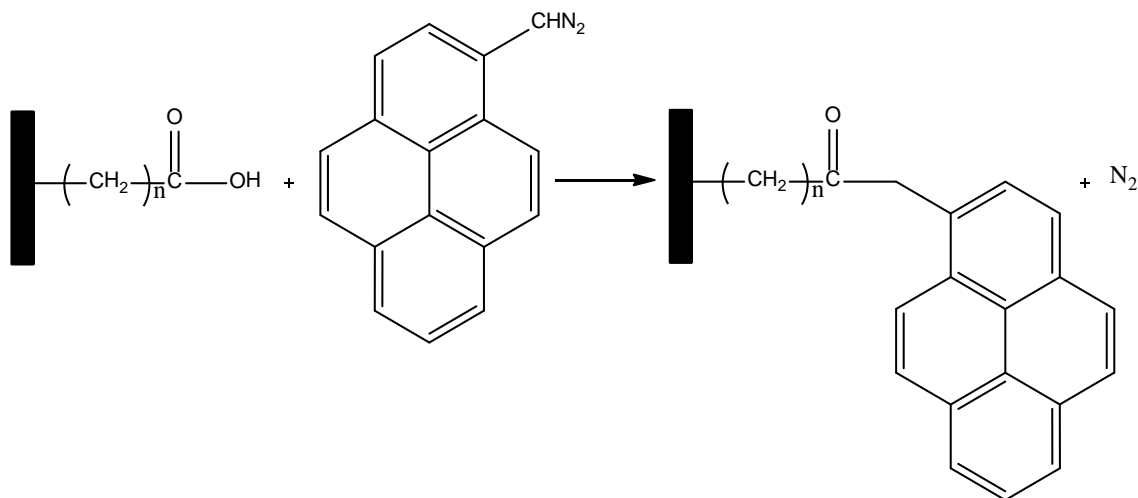


Figure 3-6 The reaction of PDAM and carboxylic acid-terminated surface.

3.3. Conclusion

A smooth OTS monolayer was obtained via chemically controlled self-assembly. The surface property and thickness of this film were studied from a combined AFM and ellipsometry study. Our experimental results demonstrate that this thin film is homogenous and about 2.6 nm thick. Then, AFM local oxidation lithography was used for the pattern creation on this OTS substrate. This method is a high-speed and direct approach to create surface patterns ranging from ~25 nm to sub-millimeter, which allow the growth of other molecular layers on their top in the future experiment.

CHAPTER 4: ATOMIC FORCE MICROSCOPY STUDY OF THE CONFORMATIONAL CHANGE OF IMMOBILIZED CALMODULIN

4.1 Introduction

Ligand binding in protein can lead to a wide range of conformational changes. Usually, this is the prerequisite for functional activity.¹²⁴ The characterization of these ligand induced structural modification is the first step to understand the conformation-function relationship of a protein.

Calcium plays key roles in a variety of biological processes, such as the blood-clotting process, metabolism and signal transduction. Lots of Ca^{2+} -dependent proteins exist in the cytoplasm of cells, calmodulin (CaM) is one of them, which is ubiquitous in almost all eukaryotic cells.¹²⁵ Calcium-bound CaM activates a series of kinases,¹²⁶⁻¹²⁸ these activated kinases are believed to mediate the effects of Ca^{2+} and play an essential role in vesicle fusion. Because of that, CaM is thought to be paramount important to the basic operation of neurons through synaptic communication¹²⁹ and important in various physiological processes such as movement, growth and proliferation.¹³⁰

CaM is a small (148 amino acid residues), acidic (PI=4.3), and heat-stable protein, which can be exposed to temperatures higher than 90 °C and remains stable. The calmodulin-calcium binding mechanism has been described since 1973.¹²⁵ Basically, calcium-bound CaM is dumbbell-shaped with two similar EF hands located at either end, each with two binding sites for Ca^{2+} binding. The EF hand is a helix-loop-helix structural domain, which is characterized by two α -helices connected by a flexible loop. Calcium is coordinated by ligands within this

12-residue loop, including seven oxygen atoms from the side chain carboxyl or hydroxyl group. In the solution, the Calcium-bound CaM molecule is about $6.5 \times 4 \times 2.5 \text{ nm}^3$ and after calcium binding, hydrophobic methyl groups from methionine residues become exposed on the protein via conformational change and allow for the interaction with target ligand (Figure 4-1a).¹³¹ After removing Ca^{2+} from CaM's EF hands, the dumbbell-shaped CaM changes to a bound shape (Apo-CaM) and the hydrophobic binding pocket becomes inaccessible to the ligands (Figure 4-1b).

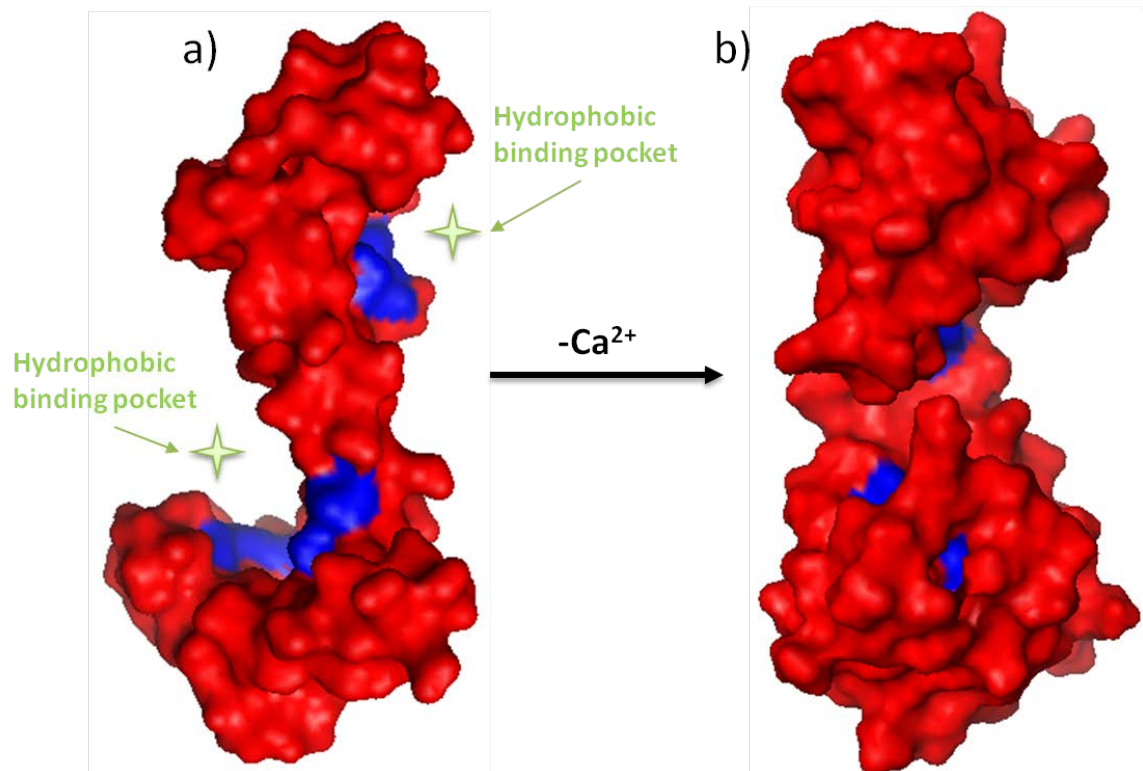


Figure 4-1 The main chain structure of (a) Ca^{2+} -CaM (PDB accession code 1CLL) and (b) Ca^{2+} -free CaM (Apo-CaM, PDB accession code 1CFD) (b) with respective N-terminal domains on bottom. Hydrophobic pockets in each of the two domains are shown in blue.

Protein patterning techniques in micro-scale have demonstrated their huge potential for the microarrays based bio-sensing and bio-analysis field.¹³²⁻¹³⁴ The

main advantages of these protein microarrays technologies include high detection sensitivity, low consumptions of reagent samples (nL level), and a few protein requirements.¹³⁵ However, immobilized proteins often behave differently from their solution-state counterparts. Although the conformational change of CaM had been well studied, its conformational change on the solid surface in immobilized state is still unclear. In this project, CaM was used as a model protein, and the AFM was utilized as a tool to investigate the conformational change of the protein on the molecular level since AFM image can provide structural and functional information.

In the experiment, CaM was purified using chitin beads from New England Biolabs and we demonstrated an experimental technique for 1-Cysteine-mutated calmodulin immobilization on a mercapto-terminated surface through cysteine-Hg-mercapto coupling. Our AFM characterization results revealed that dumbbell-shaped calmodulin was anchored on the chemical modified surface with its longest axis parallel to the surface. Upon conformational change results from the calcium releasing, the two termini of the dumbbell contract, making the immobilized calmodulin higher.

4.2 Experimental

4.2.1 Instruments

The fabrication and characterization of the chemical pattern were performed with an Agilent PicoPlus AFM in an environmental chamber. The software used for image processing was WSxM.¹¹⁷ The sample pattern was cleaned with a carbon dioxide snow cleaning system from Applied Surface Technologies. Patterns

characterizations were conducted in ac mode with MikroMasch NSC14 tips. Protein patterns were imaged in air at 75% relative humidity (at 25 °C). The imaging set point was maintained at 99% of the tip free oscillation amplitude in air. Under this setup, the tip tapped the protein surface under minimal force. Because the tip touched the protein surface in the humid environment, a possible electrostatic charge from the sample was dissipated after the tip touched the sample. Hence, the height measurement was not affected by the protein's electrostatic charge. The conducting high-aspect-ratio Ag₂Ga tip from the NaugaNeedles, LLC, was used for the topography and surface potential characterization conducted with the Veeco Multimode AFM (J scanner, working in the surface potential mode). The tip was held at 5 nm above the surface, with 10 V alternating current (AC) amplitude applied on the tip. A Nikon Eclipse 55C microscope was utilized for fluorescence imaging and measurement.¹²² The fluorescent images were acquired using a UV-2A filter and were analyzed using Nikon NIS elements BR software.

Fluorescence emission spectra were taken with a Perkin Elmer LS-55 fluorescence spectrometer (Perkin Elmer, Waltham, Massachusetts). Fluorescence spectroscopy allows the analysis fluorescence from a sample. Generally, the energy of molecules in the solution is on the ground-state energy level. The absorption of ultraviolet radiation causes an energy transfer from the ground state to the excited electronic state. With a series of rapid vibrational relaxations, the electronically excited molecules return to their lowest excited state. Finally, the transition from the lowest excited state to one of the vibrational

levels of the electronic ground state causes the fluorescence emission (Figure 4-2a). Figure 4-2b shows a configuration for our fluorometer. The light source is split into two beams. The upper sample beam passes through an excitation wavelength selector firstly and the radiation of the fluorescence emission wavelength is excluded. Then, the emitted radiations from the sample in all directions pass through an emission wavelength selector, which isolates the fluorescence emission. After that, the isolated radiation strikes a photon-transducer and an electrical signal is converted for measurement. For the lower reference beam, its power is attenuated to approximately that of the fluorescence radiation before striking the photon-transducer. At last, the electronics/computer data system calculates the ratio of the fluorescence emission intensity to the excitation source intensity to cancel the effect of source intensity fluctuations and produce the resulting spectrum. The fluorescence microscope method shares the same principle with fluorescence spectroscopy, but uses fluorescence emission to generate images.

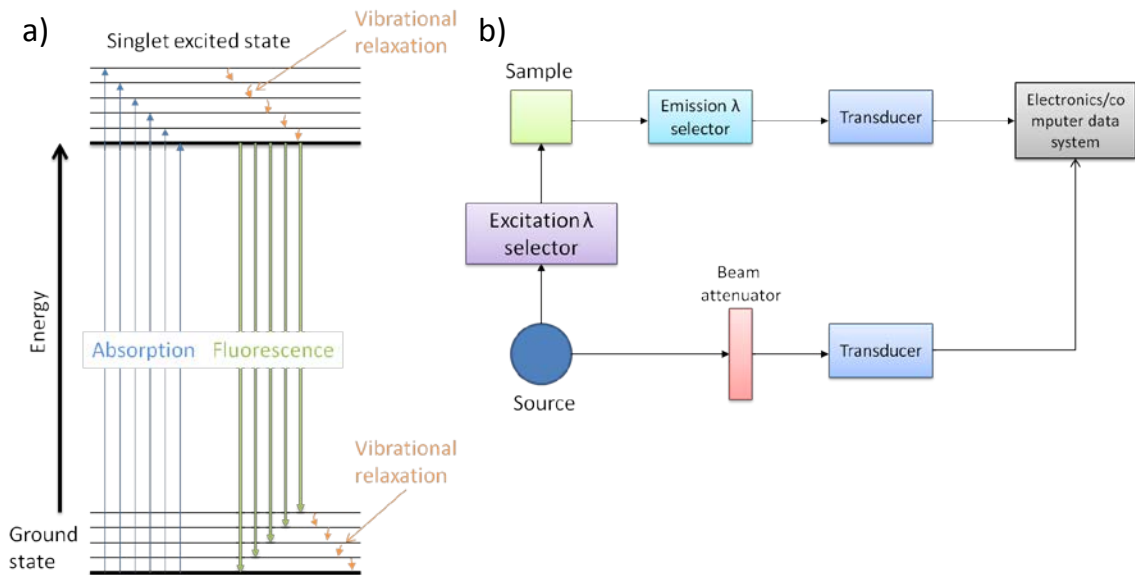


Figure 4-2 (a) Energy-level diagram for a fluorescence system and (b) components of a fluorometer.

In the experiment, surface potential characterization was conducted via Kelvin Probe Force Microscopy (KPFM). KPFM is a scanning probe microscopy technique which allows imaging of local sample surface potential. This technique was developed by Nonnenmacher et al.¹³⁶ and the principle of the technique originates from the macroscopic method developed by Lord Kelvin in 1898.¹³⁷ KPFM measures the contact potential difference (CPD) between a conductive AFM tip and a sample. The CPD can be expressed by¹³⁸:

$$V_{CPD} = \frac{\phi_{tip} - \phi_{sample}}{-e} \quad (1)$$

Where ϕ_{sample} and ϕ_{tip} are the work functions of the sample and tip; e is the electronic charge.

KPFM of Veeco Inc. is a two-pass system. On the first pass, the topography is measured. Then, on the second pass, the tip is lifted to follow the topography

profile measured in the first pass (so the tip was maintained at fixed distance from the surface); an oscillating AC voltage ($V_{AC} \sin(\omega t)$), at the frequency ω , plus a DC voltage (V_{DC}) are applied directly to the cantilever tip. Because of the $V_{AC} \sin(\omega t)$, an oscillating electrostatic force is generated between the tip and the sample surface, which has the following amplitude¹³⁸:

$$F_{es}(z) = -\frac{1}{2} \Delta V^2 \frac{dC(z)}{dz} \quad (2)$$

Where z is the direction normal to the sample surface; ΔV is the potential difference between V_{CPD} and the voltage applied to the AFM tip; $\frac{dC(z)}{dz}$ is the gradient of the capacitance between the tip and the sample surface. Since $V_{AC} \sin(\omega t) + V_{DC}$ are the voltages applied to the AFM tip, ΔV can be expressed by:

$$\Delta V = V_{tip} - V_{CPD} = V_{AC} \sin(\omega t) + V_{DC} - V_{CPD} \quad (3)$$

After substituting equation 3 in equation 2 and dividing the equation into three parts, we can get:

$$F_{DC} = -\frac{dC(z)}{dz} \left[\frac{1}{2} (V_{DC} - V_{CPD})^2 \right] \quad (4)$$

$$F_{\omega} = -\frac{dC(z)}{dz} (V_{DC} - V_{CPD}) V_{AC} \sin(\omega t) \quad (5)$$

$$F_{2\omega} = \frac{dC(z)}{dz} \frac{1}{4} V_{AC}^2 [\cos(2\omega t) - 1] \quad (6)$$

Equation 5 is used for the V_{CPD} measurement and a lock-in amplifier is employed to extract this electrical force component. When the applied V_{DC} equal to the V_{CPD} , the output signal of the lock-in amplifier is nullified and F_{ω} equals zero. At this

point, the V_{DC} will be the same as the sample surface potential and it is recorded by the KPFM system.

Equation 4 shows that the surface potential is a function of the capacitance between the AFM tip and the sample surface. While, the capacitance exists between the AFM probe and the area directly underneath the probe, and those areas close to the probe, which means the KPFM signal obtained by KPFM contains surface potential information not just from the place directly under the probe, but also the surface regions surrounding the tip. Therefore, the CPD value is convoluted, and this leads to a lower spatial resolution of KPFM.¹³⁹

Since a generic pyramid-shaped tip has large capacitances between the tip side planes and the sample surface, as Figure 4-3 demonstrated, we characterized the surface potential with an Ag_2Ga needle tip. The tip has a long and sharp Ag_2Ga needle attached at the end of the pyramid shaped probe, which minimizes the capacitances between the tip's side planes and surfaces surrounding the tip. Because the CPD signal contains mainly the local information directly under the tip, the resolution of the KPFM image is improved.

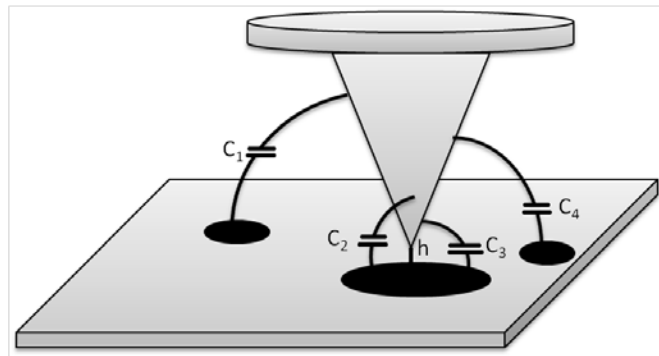


Figure 4-3 Capacitances formed between AFM pyramid-shaped conductive tip and sample surface.

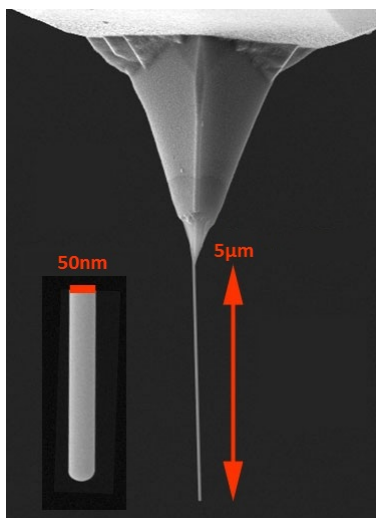


Figure 4-4 Scanning electron microscope (SEM) image of Ag_2Ga needle tip, from NaugaNeedles Inc.

4.2.2 Chemicals and materials

4.2.2.1 Chemicals for preparing the surface

OTS (octadecyltrichlorosilane, 97%) and mercaptoundecenyltrimethoxysilane (MUTMS) were purchased from Gelest. Chloroform (HPLC grade) was purchased from Mallinckrodt Baker. Toluene (HPLC grade) was from EMD. Silicon (100) wafers were purchased from KC electronics (nitrogen-doped, 5 $\Omega\cdot\text{cm}$ resistivity).¹²²

4.2.2.2 Chemicals for protein expression, purification, and reaction

Ethylenebis(oxyethylenitrilo)tetraacetic acid (EGTA), 4-(2-hydroxyethyl)-1-piperazineethanesulfonic acid (HEPES), tris(hydroxymethyl)aminomethane (Tris), isopropyl- β -dthiogalactopyranoside (IPTG), calcium chloride (CaCl_2), and β -mercaptoethanol (β -ME) were purchased from Sigma-Aldrich Corp. (St. Louis, MO). Luria–Bertani (LB) broth, used to grow the cell culture, was obtained from Difco Laboratories (Detroit, MI). CaM was purified using chitin beads from New

England Biolabs (Ipswich, MA). 2-Anilinonaphthalene-6-sulfonic acid (2,6-ANS) used for fluorescence experiments and SDS-PAGE used to confirm the expressed protein were obtained from Invitrogen Corporation (Carlsbad, CA). Immobilized tris(2-carboxyethyl) phosphine hydrochloride (TCEP) disulfide reducing gel was purchased from Pierce (Rockford, IL). Calmodulin - Dependent Protein Kinase I (299 - 320) Binding Domain were obtained from AnaSpec (Fremont, CA). The solution was prepared with water from a Narnstead Nanopure Diamond lab water purification system with normal resistivity of 18.2 Ω ·cm.

4.2.3 Methods

4.2.3.1 Protein purification

To monitor the conformational changes induced by Ca^{2+} -binding, one cysteine amino acid residue that is not directly involved in Ca^{2+} coordination needs to be introduced, so the CaM can be stabilized onto the chemical modified surface. The purification and expression of genetically engineered calmodulin with cysteine on the N-terminus is based on an instructional manual by New England Biolabs,¹⁴⁰ which involved the following process.

Firstly, the plasmid pTWIN2-CaM was transformed into *Escherichia coli* strain ER2566 for protein expression. The thawed cells were incubated with plasmid, then “heat-shock” at 37°C for 40 seconds (the cell wall split during the heat shock process and DNA is taken up by cells). At this step, 90% of *E. coli* died while 10% of them survived. Then, *E. coli* were transferred to nutrient broth and allow cells to recover for 50 mins. Sequentially, they were spread out on an agar plate. After

plate transformation reaction on LB (Luria-Bertani) agar, a single colony was grown at 37 °C in LB broth containing 100 µg/mL ampicillin for approximately 5 hrs, until the optical density (OD) of bacterial in liquid at a wavelength of 600 nm (OD₆₀₀) reached 0.5–0.7. At this OD value, the vast majority of cells were alive and healthy, which made them ideal for protein expression. After that, the bacteria were transferred into 250 mL of LB broth containing 100 µg/mL ampicillin at 37 °C until the OD₆₀₀ value was approximately 0.6. The culture was then induced with 1 mM Isopropyl β-D-1-thiogalactopyranoside (IPTG), which introduced the protein expression, for 3 hrs. The cells were harvested by centrifuging at 20°C for 5 mins at 5,000 g.

The harvested cell pellet was re-suspended in 20 ml of 10 mM imidazole buffer containing 5mM EDTA (pH 6.1) and 40 µl β-mercaptoethanol (β-ME). The cell suspension was sonicated on ice for lysing. The supernatant was collected via centrifuging at 20°C for 5 mins at 25,000 g. Then, CaCl₂ was placed in supernatant at final concentration of 10 mM. Sequentially, the solution was immersed in a water bath (80°C) for 20 mins and immediately submerged into ice slurry (0°C). Because the Calmodulin is a heat stable protein, it can stay in the solution while other proteins will be denatured and become immiscible with solution. Then, the agglutinated suspension was directly clarified by centrifugation (5 mins at 25,000 g).

In the experiment, CaM was also confirmed by SDS–PAGE (SDS-Polyacrylamide Gel Electrophoresis) analysis. SDS-PAGE is one of the most widely used biochemical method, which was firstly introduced by Shapiro et al. in

1967,¹⁴¹ for the protein separation and identification. In this approach, the sample to be analyzed was firstly mixed with sodium dodecyl sulfate (SDS), which denatures native proteins. Then, this protein mixture is heated to 100°C in the presence of SDS, and the detergent wraps around the polypeptide backbone. The detergent binds to polypeptides in a constant weight ratio of 1.4 g SDS per gram of polypeptide. This gives all polypeptide samples roughly the same charge-to-mass ratio. Also, SDS destabilizes the hydrogen-bonding which defines the 3D structure of protein, and this "denature" makes the protein more or less cylindrical in shape.

The SDS gel matrix is made by polyacrylamide, which are cross linked to each other by N,N-methylene bisacrylamide comonomers. Once the gel was polymerized, the protein mixture was loaded into the well of the gel by using the micropipettes, and then it was connected to a DC voltage which comes with the instrument. The electric field applied to the gel causes the negatively charged protein to migrate down to the gel. Since the electric force exerted on the charged source can be expressed by $F=E \cdot q$, where E is the electric field, q is the charge, and the charge-to-mass ratio of proteins is nearly the same, so the negatively charged proteins should own the same acceleration value ($a=E(q/m)$, where a is the acceleration, E is the electric field and q/m is the charge-to-mass ratio). This means those SDS-denatured polypeptides have a same electrophoretic mobility with time while the electrophoresis is running. Therefore, the protein mixture will be separated according to the size of various proteins. The smaller proteins move more quickly than the larger ones because they

experience less resistance when moving through the pores formed by the polyacrylamide molecules cross-linking.

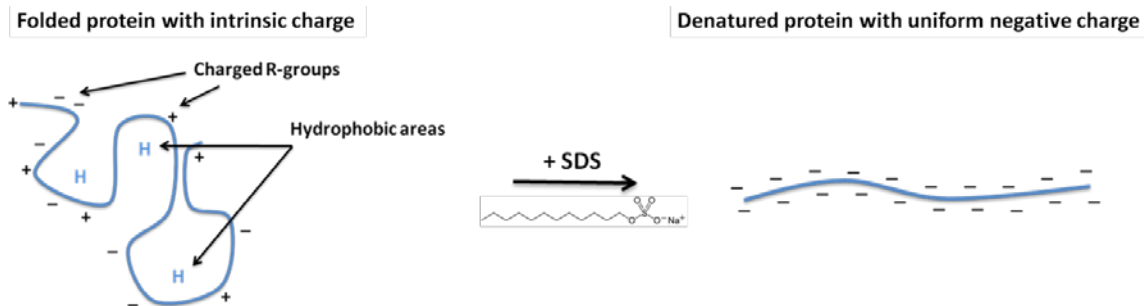


Figure 4-5 This cartoon depicts a protein (blue line) incubated in the SDS solution. After the gel running is complete, the thin film was stained with Coomassie blue dye, which can bind with proteins weakly and give blue color, so that the separated proteins are visible as distinct bands within the gel. Then, by comparing the distance travelled of the unknown protein with that of the molecular weight (MW) size marker, the approximate molecular mass of unknown proteins can be identified.

Figure 4-6 shows photography of our SDS-PAGE gel. The right side lane is the MW standard (Prestained Protein Molecular Weight Marker, Thermo Scientific; from top to bottom bands are 120, 85, 50, 35, 25 and 20), while the left side lane was loaded with purified CaM. Previous studies demonstrated that MW of CaM is around 17 kDa. Our SDS-PAGE analysis indicated that only one 17 kDa-band was observed, which suggested that CaM was successfully purified.

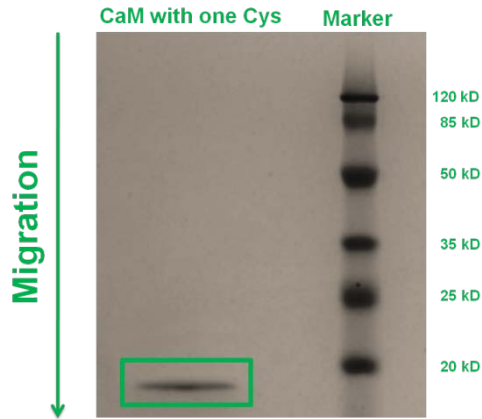


Figure 4-6 SDS gel electrophoresis of one Cys CaM.

Further confirmation can be performed by determine the protein's amino acid sequence. We extract the plasmid from the E.coli by using the DNA purification kits (IsoPure DNA Purification Kits, Denville Scientific INC.), which is a tool to provide a simple and efficient method for purification of DNA. The extracted DNA is selectively adsorbed in the silica gel-based column and other components are washed away. Then, the plasmid is eluted off the column. We obtained the amino acid sequence from the DNA sequence information, since DNA sequences correspond directly to mRNA sequences which in turn correspond to the amino acid sequences of proteins.¹⁴² Compared the sequence of our CaM with other known CaM sequence,¹⁴³ we ascertained that the protein we got was CaM. Based on amino acid sequence, we also knew that the Cys is located at the N-terminus as the second residues.

Sequence (One-Letter Code):

H₂N-

M**C**DQLTDEQIAEFKEAFSLFDKDGDTITTKELGTVMRS LGQNPTAELQDMIN

EVDADGNGTIDFPEFLNLMARKMKDSEELKEAFRVFDKDGNGFISAAELRH
VMTNLGEKLTDEEVDEMIREADV DGDGQVNYEEFVQVMMAKSGGGY-COOH

During the protein purification, we had introduced some unwanted chemical molecules, such as β -ME and EDTA which might interfere with subsequent steps in the experimental procedure. It was necessary to eliminate these substances via dialysis. Dialysis is a separation technique that uses a semi-permeable membrane, which contains various sized pores. During dialysis, molecules larger than the pores cannot pass through the membrane while the smaller ones can pass the pores freely.¹⁴⁰

During the experiment, we first pre-wetted the dialysis membrane (7000 molecular-weight cutoff), which retained 90% of the proteins having a molecular mass of 7 kDa or more. Then, we loaded the protein solution into dialysis tubing and dialyzed the protein mixture for 1-2 hours at room temperature in a buffer solution (10mM Tris-HCl with 1 mM CaCl_2 and 10 mM TCEP•HCl). To obtain better results, we increased the volume of the dialysis buffer 200-fold greater than the sample volume and dialyzed the protein solution overnight at 4°C.

It is known that Cys residues are able to crosslink proteins by disulfide bonds which could be formed by oxidation of the thiol groups of cysteine residues (Figure 4-7).¹⁴⁴ So, Tris (2-carboxyethyl) phosphine (TCEP) was applied as the disulfide bond reducing agent to prevent dimer formation.¹⁴⁵⁻¹⁴⁷ In an aqueous solution, TCEP reduces a disulfide group according to the reaction shown in Figure 4-8.^{144,148}

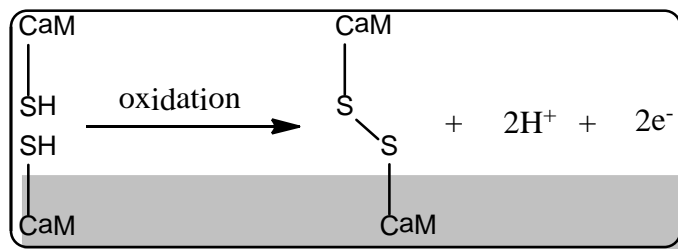


Figure 4-7 Formation of a disulfide bond.

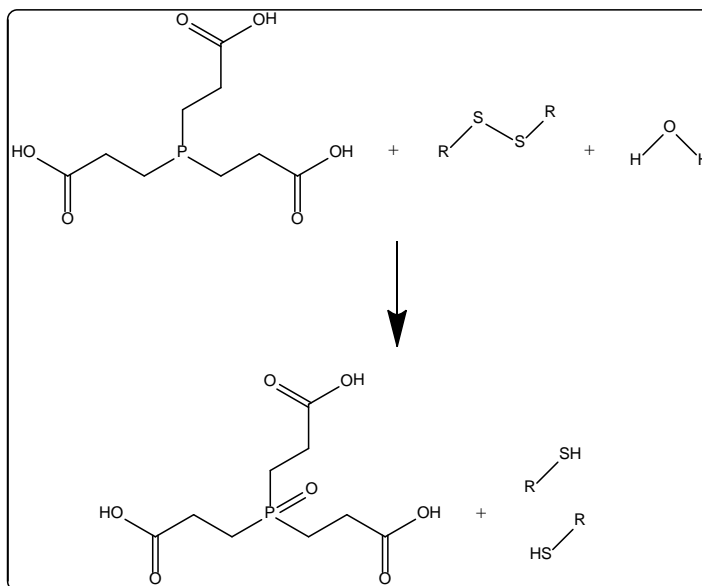


Figure 4-8 Reduction of disulfide bonds by using TCEP.

Since the reductive state of protein or peptide is characterized by the reactive sulfhydryl (-SH) groups and the mutant N-terminal Cys residue is very important for the later protein immobilization, an experiment need to be conducted to determine the existence of free -SH group. In the experiment, CaM containing a cysteine residue and CaM without cysteine residue (control experiment) were mixed with Maleimide (MAL), respectively. MAL can provide the functionality for labeling molecules that contain free sulfhydryl (-SH) groups. The mechanism of this reaction was demonstrated in Figure 4-9.¹⁴⁹ In this case, CaM with cysteine residue can be labeled with MAL according to conjugation reactions, while CaM

without Cys residue cannot. After labeling, the two protein mixture was treated with SDS-Page gel, the fluorescent image was acquired, which is shown in Figure 4-10. As we can see, there is a significant fluorescent band in the CaM with one cysteine lane (the center lane) while there is nothing in the CaM without cysteine lane (the right lane). This result demonstrated that the Cys residues in the CaM is active, which are not cross-linked with each other via disulfide bond in the protein.



Figure 4-9 Maleimide (MAL) dye is highly specific for cysteine residues.

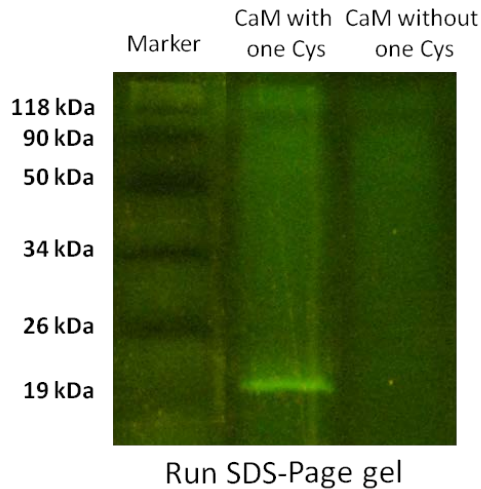


Figure 4-10 Specificity of thiol-reactive dyes for Cys proteins.

In our experiment, we also used the ANS fluorescent probe to test the bio-activity of the purified solution-state CaM upon Ca^{2+} binding. It is well established that solvent-exposed hydrophobic surfaces are formed upon Ca^{2+} binding to CaM and 2,6-anilinonaphthalene sulfonate (ANS) can serve as a fluorescent probe for

hydrophobicity.¹⁵⁰ ANS binds to proteins through polar interactions and can be monitored by the increase or decrease in fluorescence emission intensity, which demonstrates the activity of protein indirectly. Therefore, when Ca^{2+} is added to the solution, Apo-CaM change to CaM, this conformational change causes the exposure of the hydrophobic binding pocket. 2,6-ANS absorbs on the pocket and emits fluorescence. Hence, the fluorescence intensity from 2,6-ANS increases. When EDTA is added to the solution, Ca^{2+} is removed from CaM, CaM changes into Apo-CaM, and the hydrophobic binding pocket disappears. This conformational change causes the release of bound 2,6-ANS from CaM to the aqueous solutions. Hence, the fluorescence intensity from 2,6-ANS decreases. So, by monitoring the fluorescence intensity of 2,6-ANS-labeled CaM as a function of the amount of Ca^{2+} added to the solution, we can confirm the conformational change in calmodulin, which is an indication of viability.¹⁵¹

During the experiment, the protein was labeled with a 1:1 ratio of 2,6-ANS overnight at room temperature followed by dialysis against the same buffer. 1 μL increments 0.5 mM EDTA was added into the 400 μL CaM solution each time. The solution was excited at 310 nm, and emission spectra in the range from 400 to 500 nm were obtained. Figure 4-11 shows a sigmoidal shape of the binding curve which was observed by adding EDTA to CaM accumulatively. As expected, the increase of EDTA concentration led to a decreased in fluorescence signal intensity due to the release of 2,6-ANS by EDTA-induced conformational change. The intensity change of the fluorescence spectra indicates that our expressed

CaM was properly folded and was capable of changing its conformation in the solution state.

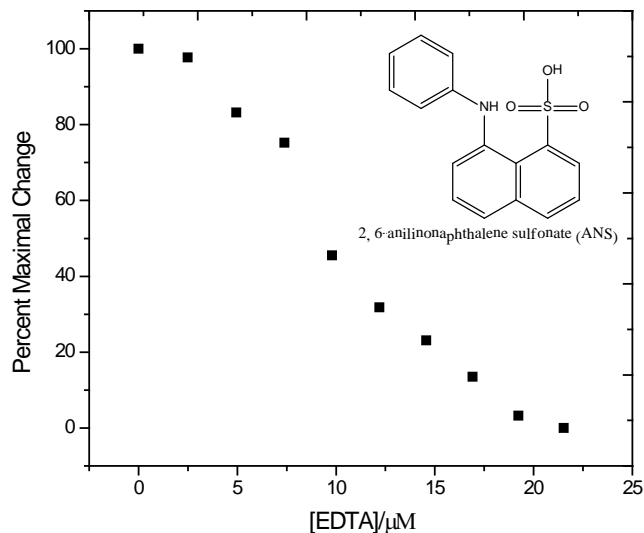


Figure 4-11 EDTA titrations of ANS labeled CaM monitored by ANS fluorescence emission measurement. The titration was performed by adding 1 μ L increments 0.5 mM EDTA with pipet to 400 μ L CaM solution. For purpose of comparison, all the fluorescence intensities were normalized to their respective 100% change.

4.2.3.2 Surface preparation and patterning

Silicon (100) wafers were cut into 1 \times 1 cm² pieces and cleaned using the piranha solution. After rinsing, samples were incubated in 5 mM OTS toluene solution overnight and an OTS monolayer was formed on the Si wafer.^{61,152}

Chemical patterns on the OTS coated samples were fabricated using deep oxidation lithography. During fabrication, a Pt-Ti-coated conducting AFM tip was used to contact the surface in a 100% relative humidity (at 25 °C) environment. A +10 V bias was applied to the sample. As a result, the OTS surface near the tip was oxidized into a partially degraded, carboxylic acid-terminated chemical

pattern (OTSpd pattern). A detailed description of the OTS film and the OTSpd pattern fabrication has been demonstrated in Chapter 3.

After the OTSpd pattern was fabricated, the wafer with OTSpd patterns was incubated in 10% hydrochloric acid for 10 mins and then cleaned with a CO₂ snow jet. As a result of these procedures, possible electrostatic charges and contaminants were completely removed. Then, the pattern was soaked in a 10 mM (11-mercaptopundecyl)trimethoxysilane (MUTMS) toluene solution overnight to convert the carboxylic acid-terminated OTSpd surface pattern to a mercapto-terminated pattern. The OTSpd surface is hydrophilic whereas the OTS background is hydrophobic. Once the sample is incubated in the MUTMS solution, MUTMS molecules react with the trace amount of water in the solution, forming silanols in the first step. Then the silanols cross-linked and selectively anchored on the hydrophilic OTSpd surface. After MUTMS incubation, the surface of the pattern was converted to a mercapto-terminated surface. The formation of MUTMS layer on OTSpd pattern is illustrated in Figure 4-12.

The pattern in Figure 4-13 is the MUTMS silane monolayer self-assembled on top of the OTSpd pattern. Figure 4-13 c is the corresponding height histogram, and the peak-fitting program in MicroCal Origin was used to fit the height histogram into two Gaussian-shaped peaks. The distance between these two peaks is the height of the pattern over the OTS background, which is 10.62 ± 0.02 Å. Since the OTSpd pattern is 10.60 ± 0.14 Å below the OTS background, the actual thickness of the MUTMS silane layer can be calculated as 20.12 ± 0.14 Å.

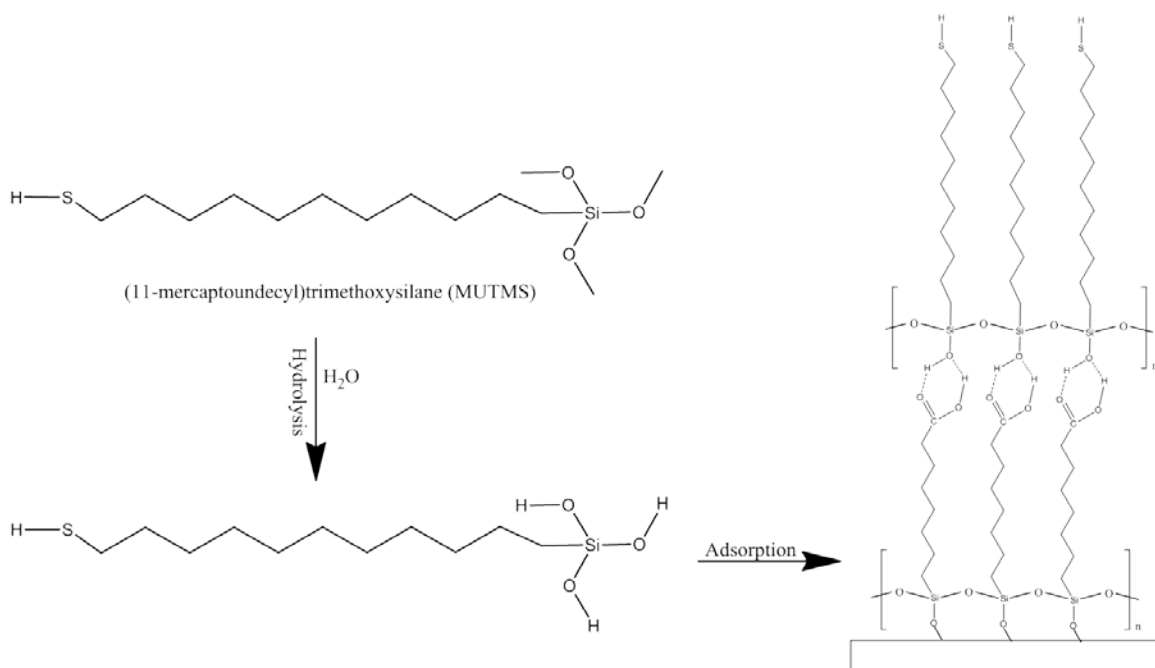


Figure 4-12 Schematic representation of the construction of a MUTMS monolayer on the OTSPd surface.

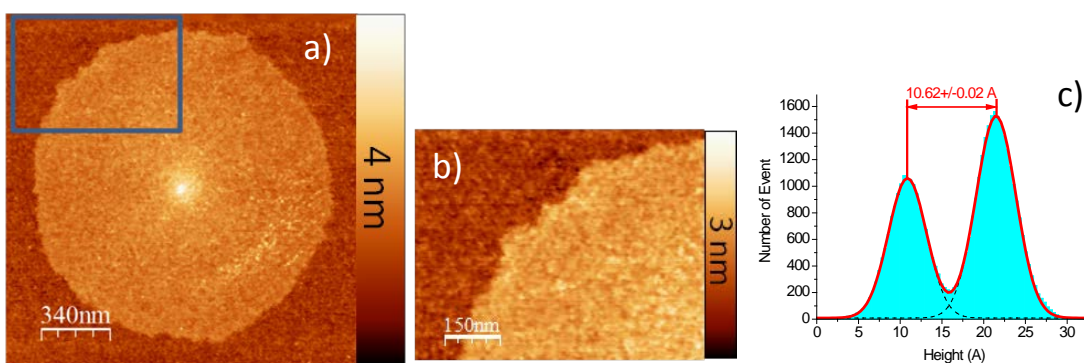


Figure 4-13 Panel a) is an AFM topography image of the MUTMS pattern. Panel b) is a zoom in view of the region in the cyan box in panel a), figure c) is the histogram corresponding to b). The distance between the two peaks in the histogram specifies the height of the pattern in the image.

Then, the sample with MUTMS patterns was incubated into 10 mM HgCl_2 solution for half an hour to form mercapto-Hg coupling, which will be used to immobilize cysteine-mutated CaM. To ascertain the S-Hg-S linking can be formed on the surface, we dipped the mercury ion stabilized wafer into 1 mM

dodecanethiol in butanol overnight. Figure 4-14 shows representative tapping mode AFM topography and phase images of a stabilized dodecanethiol layer on a mercury ion bound MUTMS pattern respectively. The topography image showed that the dodecanethiol islands sat on the MUTMS layer with OTS background, and the phase image demonstrated that the AFM phase signals for the OTS background and the dodecanethiol islands were the same within the same scan line. Phase image in AFM refers to the phase delay of cantilever oscillation, which is caused by its interaction with the surface. Since phase signal is sensitive to variations in composition, it can be used to characterize surface identity. The phase signals we compared here were obtained using the same tip, in the same scan line under the same instrumental settings. In phase image, the light brown-colored region in the left side is the OTS background, while the same color region in the right side of the phase image represents the dodecanethiol. The same phase signal revealed that the OTS surface and dodecanethiol surface had the same identity. The OTS is methyl-terminated, so the same phase signal indicates the dodecanethiol layer is also methyl-terminated and the dodecanethiol molecules stood upright with CH_3^- on the top, the SH group anchored to the Hg, as shown in Figure 4-15. The AFM phase characterization demonstrated that dodecanethiol could be stabilized on the MUTMS layer via mercapto-Hg-mercapto coupling. It also confirmed that S-Hg-S linkage can be formed on the chemical modified surface.

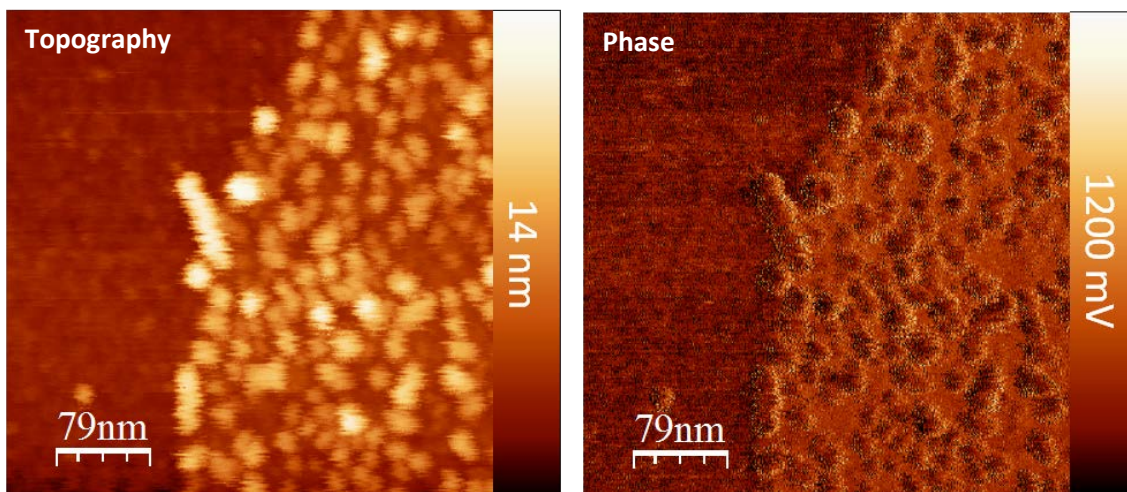


Figure 4-14 Representative AFM image of dodecanethiol islands on the MUTMS chemical pattern.

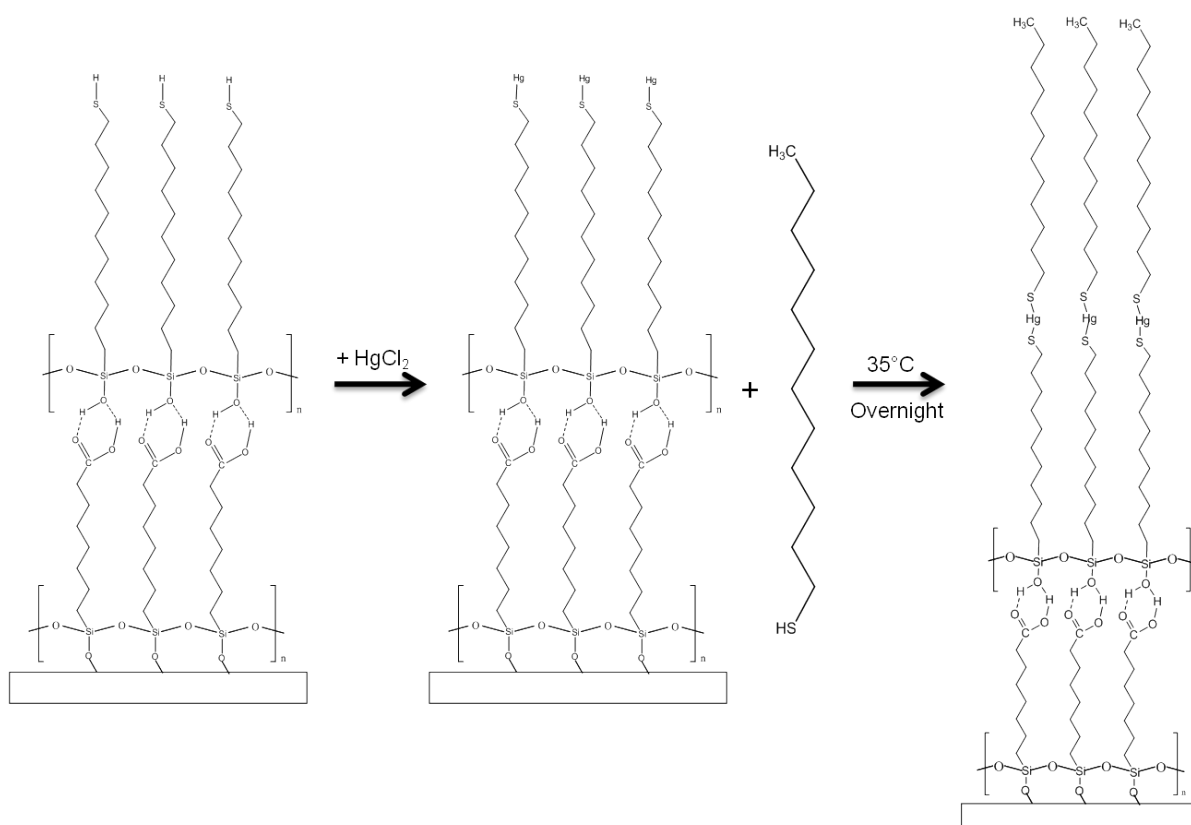


Figure 4-15 The structure and formation of dodecanethiol ($\text{CH}_3(\text{CH}_2)_{11}\text{SH}$) layers.

4.2.2.3 Protein immobilization and assay

The dumbbell shaped, genetically engineered CaM with one cysteine residue on the N-terminus was immobilized on a mercapto-terminated surface pattern through the cysteine-mercapto coupling reaction. 5µg/ml CaM with buffer solution (25 mM Tris-HCl, 1 mM CaCl₂, pH 8.0) was deposited onto the pattern area for 1 hour in freezer (-4°C). Then the sample surface was wiped with a piece of ChemWipe paper to remove the nonspecifically adsorbed protein on the OTS background, while those specifically adsorbed ones remained.⁶²

4.2.3.4 CaM conformational changes

Immobilized CaM was induced to undergo two types of conformational change. In the first test, immobilized CaM was incubated in an EDTA-containing buffer (2 mM EDTA, pH 8.0) at -4°C for 10 mins to remove the calcium ion from CaM, inducing CaM to change its conformation to Apo-CaM.

In the second test, immobilized CaM was soaked for 10 mins in a 1ug/ml CaM kinase I (CaM KI) tag solution at -4°C, leading CaM to change to its bound conformation. The experimental scheme was shown in Figure 4-16.

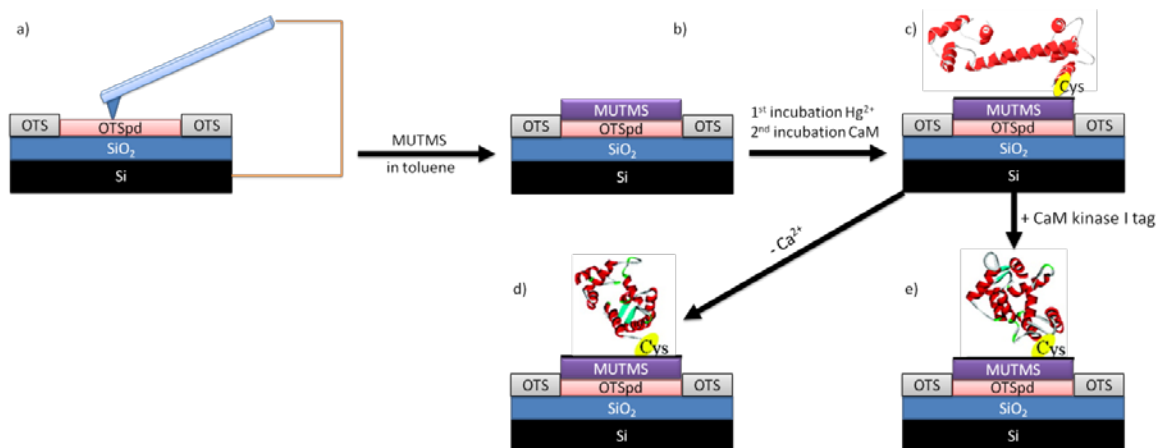


Figure 4-16 Experimental scheme. (a) OTSpd pattern fabrication. (b) Converting the OTSpd pattern into a mercapto-terminated surface by assembling an additional layer of MUTMS silane on top of the OTSpd pattern. (c) Immobilization of CaM on the MUTMS pattern through cysteine-Hg-SH coupling. (d) Reacting with EDTA, the Ca²⁺ bound to CaM was removed, which induced conformational change of CaM from the dumbbell shape to the Apo-CaM bound conformation. (e) Immobilized CaM in part c changed its conformation upon incubation in CaM kinase I (CaM KI) tag solution.

4.2.4 Characterization of conformational change of CaM

As stated before, this work utilized AFM to characterize the conformational change in calmodulin immobilized on a chemically modified surface to reveal protein's conformation–function relationship. To achieve this end, a MUTMS modified surface was used to immobilize cysteine-mutated CaM through Hg²⁺ coupling. AFM characterizations showed that after protein immobilization procedure, the height of the patterns changed to 3.00±0.03 nm above the OTS background (Figure 4-17), indicating that new materials were immobilized on the chemical pattern. The topography images show that immobilized calmodulin existed as a monolayer on the chemical patterns in most cases. No crystalline lattice structure was observed inside the calmodulin layer.

The immobilized CaM was induced to undergo a conformational change by dropping 2 mM EDTA solution (pH=8.0) onto the CaM pattern area for 10 mins at -4°C. Then the surface was rinsed with de-ionized water and probed with AFM. Since EDTA could sequester metal ions such as Ca^{2+} , it caused a conformational change of CaM to Apo-CaM. Figure 4-18 shows a representative immobilized Apo-CaM layer and the height histogram. Figure 4-18c indicates that the Apo-CaM disk is 3.41 ± 0.01 nm above the OTS background. The AFM characterization revealed that the height of immobilized CaM is 1.94 ± 0.03 nm whereas the height of immobilized Apo-CaM is 2.35 ± 0.01 nm. So, this EDTA induced conformational change corresponded to a 4.1 ± 0.3 Å increase in thickness of the immobilized CaM monolayer.

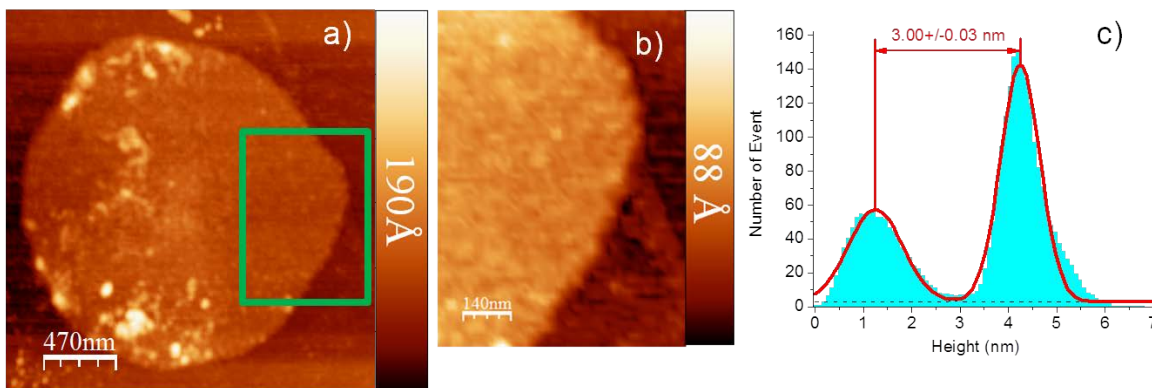


Figure 4-17 AFM topography image of the CaM (with Ca^{2+}) coated pattern. Panel b is a zoom in view of the region in the box in panel a, panel c is the height histogram corresponding to b. The distance between the two peaks in the histogram specifies the height of the pattern in the image.

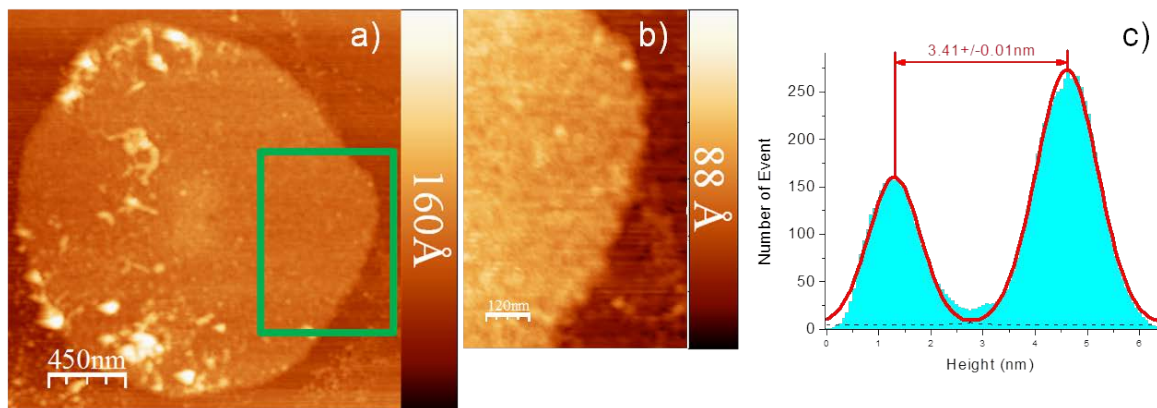


Figure 4-18 AFM topography image of the Apo-CaM (without Ca^{2+}) coated pattern. Panel b is a zoom in view of the region in the box in panel a, panel c is the height histogram corresponding to b. The distance between the two peaks in the histogram specifies the height of the pattern in the image.

The viability of immobilized CaM was also confirmed by fluorescence microscopy. We fabricated an immobilized CaM array on the OTS film, which has the structure shown in Figure 4-16 c. The immobilized CaM pattern was then labeled with 2,6-ANS. After rinsing with DI water, we acquired the fluorescent image of the immobilized CaM array under an ultrapure nitrogen environment. Next, the sample was incubated in 10 mM EDTA solution for 10 min, followed by rinsing in DI water three times. Because EDTA removed Ca^{2+} from the immobilized CaM, active immobilized CaM changed its conformation from the dumbbell shape (Figure 4-16 c) to the bound Apo-CaM form (Figure 4-16 d) and released 2,6-ANS, leading to a decrease in the fluorescence intensity.

Figure 4-19 shows the fluorescent images of an immobilized CaM pattern before (Figure 4-19 a) and after (Figure 4-19 b) EDTA treatment, which were acquired using the same setting and were rendered on the same x–y and intensity scales. In these fluorescent images, the blue represents no fluorescence and green

represents a fluorescence signal being emitted from ANS-labeled CaM. By software analysis, the fluorescence intensity of the immobilized CaM (Figure 4-19 a) is 59 counts whereas the intensity in Figure 4-19 b drops to 33 counts after EDTA treatment. The decrease in fluorescence intensity after EDTA treatment indicates that immobilized CaM can change its conformation, confirming the activity of the immobilized protein.

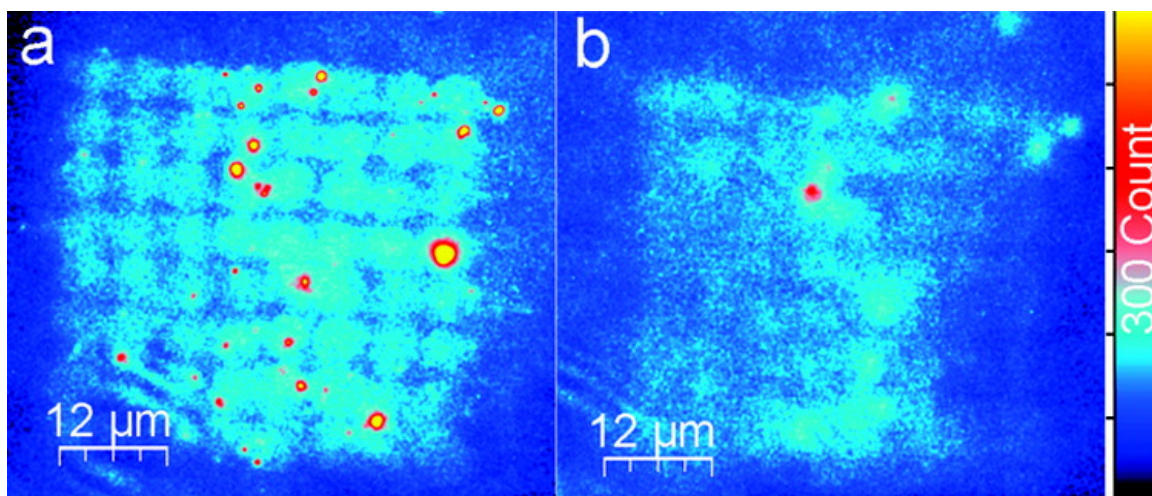


Figure 4-19 Fluorescent image of an immobilized ANS-labeled CaM array (a) before and (b) after EDTA incubation. The two fluorescence images were acquired using the same exposure time (135 s) and were rendered on the same x–y and intensity scales. After EDTA incubation, immobilized CaM changed its conformation from dumbbell-shaped to bound-shaped Apo-CaM. The fluorescence intensity of the array dropped from 59 counts to 33 counts.

Fluorescence intensity loss on the microscopic image of biological samples due to photobleaching has been recognized.¹⁵³ Photobleaching is a phenomenon when fluorophores permanently lose their ability to fluoresce due to interaction with another molecules or photon-induced chemical damage.¹⁵⁴ Although the lamp shutter was closed when fluorescence images were not being taken to limit

the exposure time of fluorophores to illumination, it is still necessary to confirm the intensity change did not result from photobleaching. To do so, fluorescence image was acquired at the same place twice, after the sample was incubated in EDTA solution. We found that the fluorescence intensity of the immobilized CaM is 32 counts for the second time captured fluorescence image, which is just 1 count lower than the previous one. This relative loss is smaller than the corresponding decrease in fluorescence intensity due to the CaM conformational change. This result indicates that the photobleaching effect is negligible under an ultrapure nitrogen environment.

In summary, the complementary AFM and fluorescence studies demonstrate that the 1-cysteine mutated CaM can be immobilized on chemical patterns through the cysteine-Hg-S linking. The immobilized CaM maintains its activity and can undergo conformational changes.

The multifunctional Ca^{2+} /CaM-dependent protein kinase I, also known as CaM kinase I (CaM KI) is a well-known effector of calcium- and CaM-mediated functions. It is found in many tissues, but in neurons it has especially high concentrations, and may be up to 2% of the total protein in some brain regions. This high abundance in the nervous system makes CaM KI an unusual enzyme.¹⁵⁵ Based on Dzhura's work, the CaM KI mediates phosphorylation and plays a fundamental part in triggering I_{Ca} facilitation, which responds to the intracellular Ca^{2+} concentration.^{156,157} For example, an external stimulus increases intracellular Ca^{2+} levels and increases the amount of Ca^{2+} -bound CaM. Ca^{2+} /CaM bind to the autoinhibitory domain of the CaM KI α -subunit, activating

CaM KI by causing the catalytic domain to dissociate from the autoinhibitory domain. The active CaM KI migrates to the post-synaptic density (PSD), phosphorylates α -amino-3-hydroxy-5-methyl-4-isoxazolepropionic acid receptors (AMPA receptors), which are ionotropic transmembrane receptors, and enhances their activity to decrease the Ca^{2+} level.¹⁵⁸

CaM KI binding domain is an amino acids 299 to 320 fragment of the calmodulin-dependent protein kinase I, which can independently bind CaM.¹⁵⁹ Calcium bound calmodulin can capture this fragment by wrapping tightly around it, inducing a calmodulin conformational change in the solution. Figures 4-20 a, b and Figures 4-21 a, b are the topography images of the CaM pattern before and after treatment with CaM KI tag solution. The results from histograms reveal that the CaM kinase binding domain caused the height of the CaM layer to increase $11.80 \pm 0.10 \text{ \AA}$. This result indicates that the immobilized CaM still maintained its activity to bind target protein.

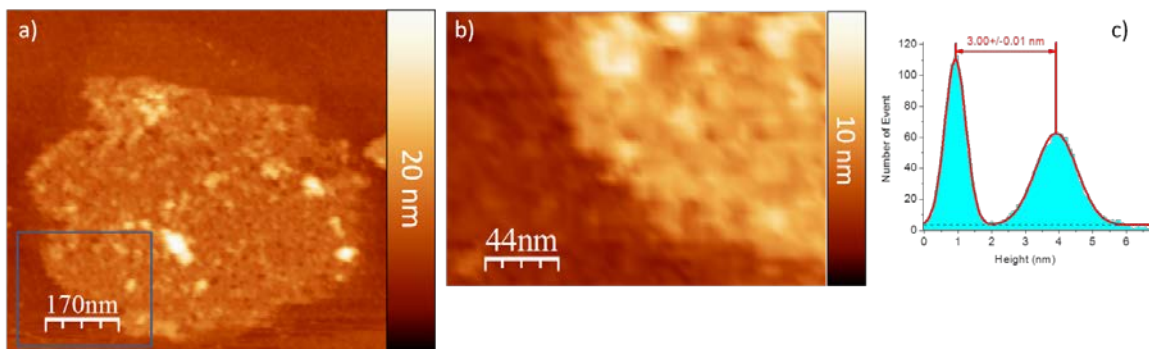


Figure 4-20 AFM topography image of the CaM (with Ca^{2+}) coated pattern. Panel b is a magnified view of the region in the box in panel a, panel c is the histogram corresponding to b. The distance between the two peaks in the histogram specifies the height of the pattern in the image.

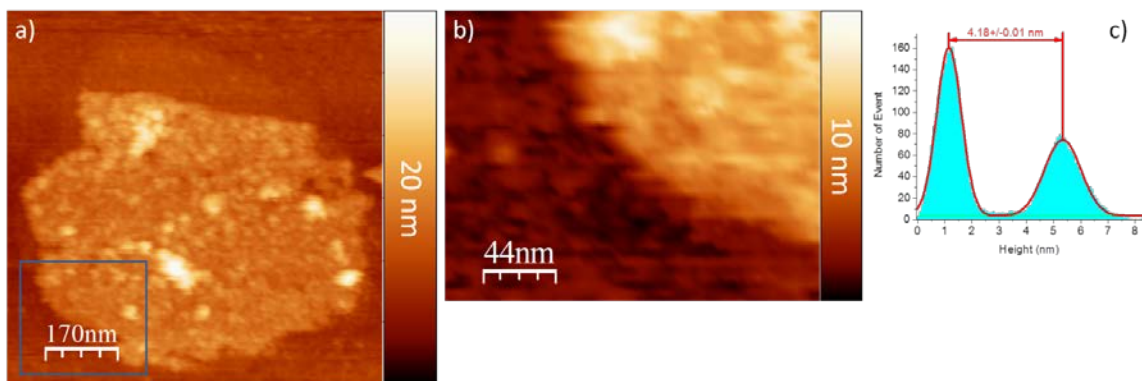


Figure 4-21 AFM topography image of CaM-CaM KI binding domain pattern. Panel b is a magnified view of the region in the box in panel a, panel c is the histogram corresponding to b. The distance between the two peaks in the histogram specifies the height of the pattern in the image.

Using the same approach, the heights of MUTMS, CaM and kinase-bound CaM patterns were obtained for different samples. The final results are summarized in Table 4-1.

Table 4-1 Height of the surface patterns.

	Apparent height above OTS (nm)	N
MUTMS	1.08±0.18	30
CaM	2.95±0.06	18
Apo-CaM	3.34±0.11	15
CaMKI binding domain-CaM	4.20±0.09	15

4.2.5 Analysis of the hydration on the exposed protein surface

The CaM to Apo-CaM conformational change also altered the amino acid residues' composition of the exposed protein surface, which affects the water molecules' distribution on the protein surface. Different surface hydration states might lead to different measured protein dimensions. We employed the tapping mode AFM phase signal to quantify the hydration state of CaM. The phase signal

reflects the energy dissipation during the tapping of an oscillation tip. Under our imaging condition (i.e., a humid air environment), the hydrophilicity determines the energy dissipation. For a more hydrophilic surface, more water molecules adsorb on the surface. Therefore, when a tip taps on such a surface, more energy is dissipated to overcome the surface tension and capillary forces between the tip and the surface. Therefore, a hydrophilic surface yields a high phase signal (a larger phase-lag angle). Theoretically, the phase signal φ (in term of the phase lag) is expressed by¹⁶⁰:

$$\sin\varphi = \frac{A}{A_0} - \frac{Q}{\pi k A A_0} E \quad (7)$$

where A and A_0 are the AFM tip's set oscillating amplitude and free oscillating amplitude, respectively, Q and k are the quality factor and the spring constant of the tip, respectively. E is the energy dissipation, which reflects the surface hydrophilicity. The equation shows that the phase signal is also a function of the imaging parameters (A and A_0) and the tip conditions (Q and k). Thus, the value of the phase signal cannot be directly used to assess the surface hydrophilicity (E in the equation). We use the chemical patterns to overcome this difficulty. We fabricated chemical patterns on the surface and deliberately imaged the protein surface and different chemical patterns in the same image. Here, the chemical patterns serve as an internal reference to quantify the surface hydrophilicity.

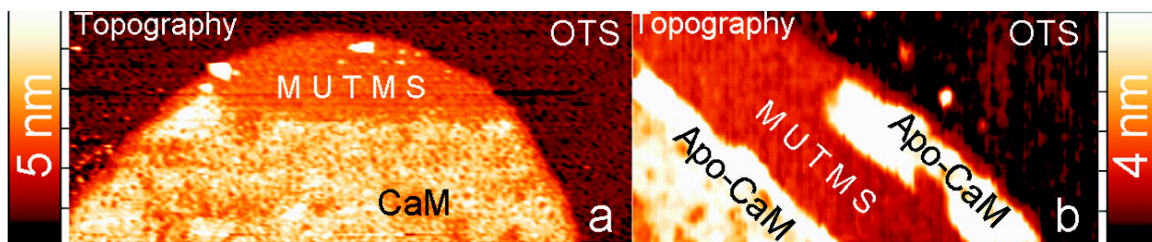


Figure 4-22 Partially covered protein patterns that reveal different surfaces. ac-mode topography images. (a) A partially covered immobilized CaM layer on the MUTMS pattern. (b) A partially covered immobilized Apo-CaM layer on the MUTMS pattern.

As shown in Figure 4-22, under 75% relative humidity (at 25 °C), we imaged a CaM and an Apo-CaM disk pattern with the same tip in the tapping mode. The protein films only partially covered the MUTMS disks. The images in Figure 4-22 show the surfaces of OTS, MUTMS, and protein at the same time. To characterize the hydrophilicity of the protein surface, we measured the average phase signals of the OTS, MUTMS, CaM, and Apo-CaM surfaces in the corresponding phase-channel images in Figure 4-22 a, b. These values are listed in Table 4-2.

Table 4-2 Phase Signals and Hydrophilicity Factors (H) of the Protein Surfaces in Figure 4-22.

	Sample a in Figure 4-22 (CaM)		Sample b in Figure 4-22 (CaM)	
	Phase signal (mV)	H	Phase signal (mV)	H
OTS	0 ± 10		4 ± 7	
MUTMS	431 ± 4		127 ± 8	
CaM	498 ± 9	1.16 ± 0.02		
Apo-CaM			139 ± 8	1.10 ± 0.06

We use the surface hydrophilicity factor H to quantify the hydrophilicity of the protein surface. The hydrophilicity factor H is defined as:

$$H \equiv \frac{\varphi_{\text{protein}} - \varphi_{\text{OTS}}}{\varphi_{\text{MUTMS}} - \varphi_{\text{OTS}}} \quad (8)$$

When φ is smaller than 10° , $\varphi \approx \sin \varphi$.

Thus, on the basis of eq 7,

$$H \equiv \frac{\sin \varphi_{\text{protein}} - \sin \varphi_{\text{OTS}}}{\sin \varphi_{\text{MUTMS}} - \sin \varphi_{\text{OTS}}} = \frac{\left(\frac{A}{A_0} - \frac{Q}{\pi k A A_0} E_{\text{protein}}\right) - \left(\frac{A}{A_0} - \frac{Q}{\pi k A A_0} E_{\text{OTS}}\right)}{\left(\frac{A}{A_0} - \frac{Q}{\pi k A A_0} E_{\text{MUTMS}}\right) - \left(\frac{A}{A_0} - \frac{Q}{\pi k A A_0} E_{\text{OTS}}\right)} = \frac{E_{\text{protein}} - E_{\text{OTS}}}{E_{\text{MUTMS}} - E_{\text{OTS}}} \quad (9)$$

Therefore, the H factor of a protein surface is independent of the tip status and imaging parameters. It is a function of only the energy dissipation of OTS, MUTMS, and the protein surface. Here, because the surfaces of OTS (methyl group terminated) and MUTMS (-SH group terminated) are stable, well ordered, and have the same roughness and packing density, $E_{\text{MUTMS}} - E_{\text{OTS}}$ can be used as a standard. Hence, using the known chemical patterns as standards, we can measure the phase signals over unknown surfaces (such as protein surfaces) and calculate the H factor, which is an indication of the protein hydrophilicity (E_{protein}). Using the measured values in Table 4-2, we get $H_{\text{CaM}} = 1.16 \pm 0.02$ and $H_{\text{Apo-CaM}} = 1.10 \pm 0.06$. Furthermore, the relative change can be calculated as

$$R = \frac{H_{\text{CaM}}}{H_{\text{Apo-CaM}}} = \frac{E_{\text{CaM}} - E_{\text{OTS}}}{E_{\text{Apo-CaM}} - E_{\text{OTS}}} = 1.05 \pm 0.06 \quad (10)$$

The R value reveals that the surface hydrophilicities of immobilized CaM and Apo-CaM do not have a statistically significant difference. Therefore, the observed height change for the CaM/Apo-CaM transition is not from the difference in water adsorption on the protein surfaces.

4.2.6 Possible orientations of the adsorbed protein

The dimensions of CaM and Apo-CaM can be measured from protein data bank (PDB), which are $6.7 \times 4 \times 2.5 \text{ nm}^3$ (Calmodulin structure 1CLL) and $5.7 \times 3 \times 3 \text{ nm}^3$ (Calmodulin structure 1CFD) respectively. Obviously, our observed protein heights for CaM ($1.94 \pm 0.03 \text{ nm}$) and Apo-CaM ($2.35 \pm 0.01 \text{ nm}$) are significantly different from the height of the orientation, in which CaM stands upright on the surface (the handle of the dumbbell is vertical to the surface). Based on our results, we conclude that the lying-down configuration would be the possible adsorption orientation for CaM where the handle of the dumbbell is parallel to the surface instead of the standing-up orientation.

Our observed AFM images show that the immobilized protein film is not a 2-D crystal. The observed heights of protein molecules have a statistical distribution. Hence, within the film, other orientations are also likely to occur. Our data indicate only that the laying-down orientation is the most probable adsorption orientation under our immobilization conditions.

In our case, CaM existed as a film and each immobilized CaM is embraced by neighboring immobilized CaM molecules. Since our AFM images were obtained under a humid environment, the surface of the immobilized protein was fully hydrated. As a result, the motion of the flexible parts within the protein molecules was limited. In similar studies conducted by other groups, a single biotinylated CaM molecule was immobilized on a crystalline streptavidin surface and the height measurement was conducted in buffer solution.¹⁶¹ Our approach should be more accurate because it is well known that protein imaged in humid air

usually have less mobility and flexibility, leading to a higher image resolution and better measurement accuracy,^{162,163} and the motions (such as standing up or wobbling) of the immobilized CaM molecules were suppressed, while in the solution, the CaM molecule has vast empty space around it and can rotate, wobble, or stand up freely. In that case, the observed height would be an average height corresponding to these possible orientations rather than that of the most probable adsorption orientation.

4.2.7 Friction Force Spectroscopy of immobilized CaM and Apo-CaM monolayers

AFM friction force microscopy is a special method for the study of the tribological properties of surfaces at the nanoscale.¹⁶⁴ In this work, friction force microscopy was applied to probe the calcium induced conformational change in surface-immobilized CaM and Apo-CaM. The purpose of this experiment is to determine if the AFM friction force microscopy is sensitive to the difference in the protein frictional properties, which originates from the different confirmation, as well as the exposed protein surface.

Before we measured the friction of the alkane layer, we let the CSC17 tip initially scan over the OTS surface for 30 mins to reach a stable and reproducible tip state. Then the tip was disengaged from the surface, and the AFM feedback loop was turned off. Then we measured the thermo drifting (non-equilibrium in thermo expansion/contraction) of the system to ensure that the error from the drifting was below the uncertainty of our measurement. All data presented were obtained using the same tip and obtained with the same scanning speed.

During the experiment, a well-calibrated MikroMasch CSC17 tip scanned over the sample surface in the contact operation mode with gradually increased loading forces at a constant tip velocity of $2\mu\text{m}\cdot\text{s}^{-1}$. The topographical and frictional signals were recorded in both the trace and retrace directions simultaneously for each scan. As Figure 4-23 shows, each zone between two green lines was scanned with different loading force. The scan mean friction force in nN was calculated via the following equation:

$$F_f = \frac{k_\varphi \cdot \varphi}{H} \cdot \frac{\Delta V_{Lateral}}{2} \quad (11)$$

Where φ is the torsional deflection. To obtain this value, force curve was acquired while the tip pressed against an OTS coated silicon surface firstly. Then, the ratio of piezo displacement to cantilever deflection, which can be obtained from the force curve, was divided by the length of the cantilever. k_φ is the torsion spring constant of the cantilever, which is determined by using the methods developed by Sader and co-workers, which was mentioned in Chapter 2.^{101,102} H is the effective height of the AFM probe. $\frac{\Delta V_{Lateral}}{2}$ is the average difference in the friction signal between the trace and retrace over all the scanning lines.

After converting the unit of the total normal force applied on the sample from V to nN by multiplying a ratio k_z , a friction v.s. load curve was obtained (Figure 4-24). Here, k_z can be calculated from the product of the normal spring constant.

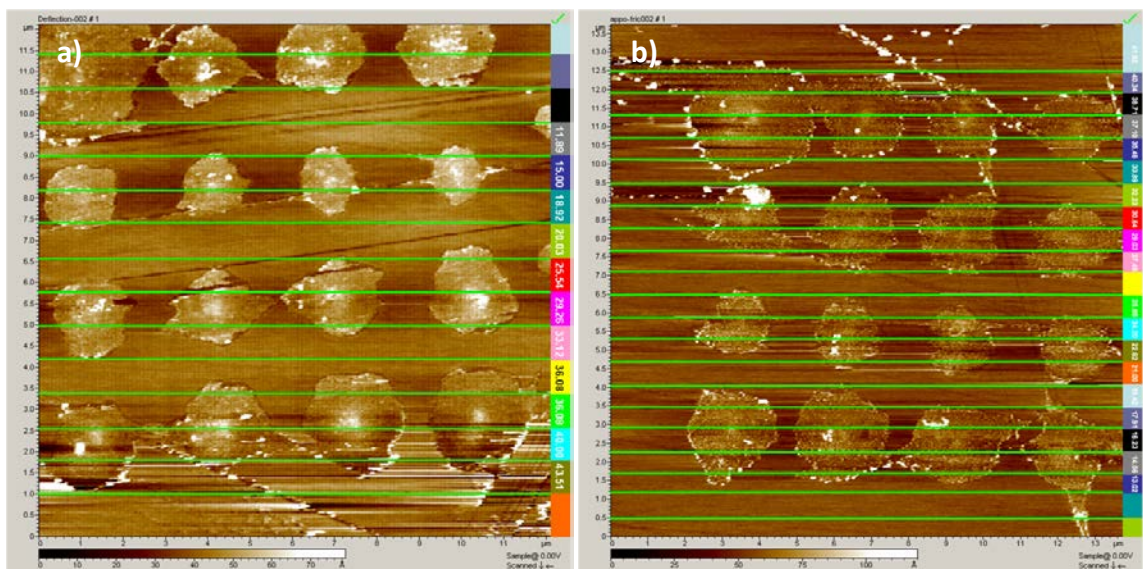


Figure 4-23 Panel a and panel b are the topography image obtained during the contact mode scanning for the CaM and Apo-CaM patterns with different loading forces respectively. The numbers in the frame in panels a and b show the loading force (in nN) used to scan between two green lines.

As figure 4-24 shows, the slopes of the friction curve for both CaM (the red line) and Apo-CaM (the dark cyan line) increase with load, but they show a different frictional response. We found that there is one critical value, which is 18 nN. When the loading force is below 18 nN, the friction loading force response from the Apo-CaM patterns is slightly larger than that from CaM patterns. This means the tip endures more resistance when it slid on the Apo-CaM surface. However, when the tip loading force increased above 18 nN, the CaM surface had a larger friction response than the Apo-CaM surface gradually. We speculate that when the tip's loading force was lower than 18 nN, the tip scanned over the top of the protein surface, which resisted the tip's scanning. When we studied the CaM and Apo-CaM surface roughness, we found that the CaM exhibited a more homogeneous surface structure (RMS roughness= 0.245 ± 0.027 , N=15) than Apo-

CaM did (RMS roughness= 0.517 ± 0.053 , N=18). Thus, when the tip loading force is below 18 nN, the tip actually scans over the top of the protein surface. In this case, the friction force is mainly from the surface roughness. Therefore, the friction force acted upon the Si tip/Apo-CaM interface would be larger for that on the Si tip/CaM interface, which corresponds to the friction response of Apo-CaM is slightly larger than that of CaM.

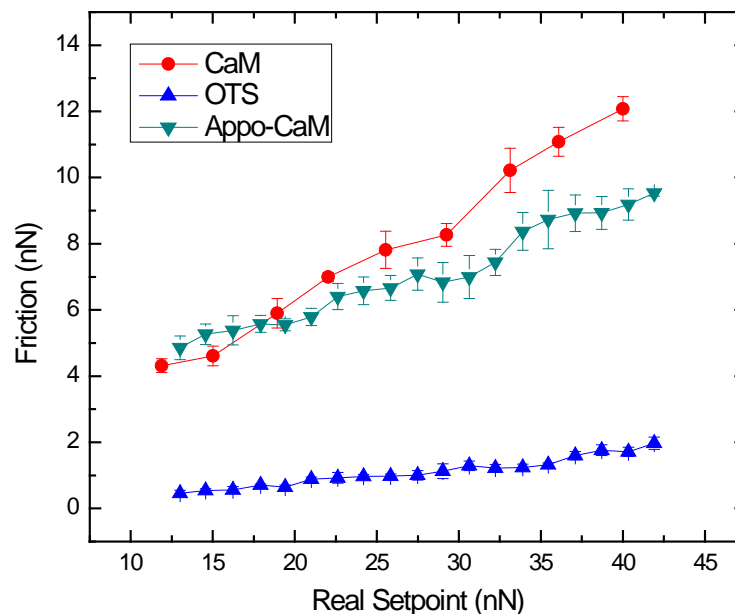


Figure 4-24 Comparisons of frictional behavior were made among the following three interfaces: a Si tip sliding on an OTS-coated Si wafer (Si-on-OTS), the same Si tip sliding on CaM (Si-on-CaM) and Apo-CaM (Si-on-Apo-CaM).

However, when the loading force is larger than 18nN, the friction over the CaM surface becomes higher than that of the Apo-CaM surface. We speculated that when the tip's loading force is higher than 18 nN, the CaM molecules adsorbed on MUTMS patterns underwent a conformational change, resulting in a friction response on CaM that is larger than that of Apo-CaM. Here, our data indicate that the friction of protein layer is determined by its structure and adsorption

orientation. We hope that the AFM study on the frictional properties of CaM/Apo-CaM will help further quantize the surface properties of immobilized protein.

4.2.8 Label-free detection of the Ca²⁺ binding on CaM patterns using Kelvin Probe Force Microscopy (KPFM)

Kelvin probe force microscopy (KPFM) measures the spatial distribution of surface potential.^{165,166} Other research has revealed that KPFM has some advantages as a bio-molecular detection technique.^{165,167} Firstly, it can be operated under ambient conditions rather than in the specialized vacuum or fluid cell. Then, since it is non-contact, KPFM can characterize the nano-scale electronic/electrical properties not only metal/semiconductor surfaces, but also biological material without damage.¹⁶⁷ Finally, the KPFM is a powerful tool for measuring surface potential variations over a substrate of interest with a reasonably high resolution.¹⁶⁷ Previous KPFM experiments have demonstrated that single-stranded DNA and double-stranded DNA can be distinguished.¹⁶⁷ Also, the research results of our group showed that the aptamer-protein binding at nanometer scale could be detected by KPFM.¹³⁹ The above works have demonstrated the power and potentials of KPFM in the bio-molecular detection. Here, we hope to use KPFM to detect the conformational change of CaM molecule and the binding behavior between CaM and CaM KI binding domain.

Figure 4-25 a) and b) are the surface potential profiles of the same protein pattern before and after EDTA solution treatment. In Figure 4-25 c), we plot the cross-sectional profiles of the surface potential (cyan line) for CaM and Apo-CaM pattern together. Here, because the surface of OTS (methyl-group-terminated) is

stable, well-ordered, and have the same roughness and packing density, it serves as an internal reference to quantify the surface potential.⁶³ Figure 4-25 a) shows that CaM surface is positively charged and the surface potential of CaM disk is higher than that of OTS by 180.13 ± 1.78 mV. Figure 4-25 b) is the surface potential image of the same immobilized calmodulin layer that was incubated in EDTA solution for 10 mins and rinsed with DI-H₂O. The images were taken at the same scanning speed and scan height to maintain the signal fidelity.^{167,168} Since EDTA could sequester Ca²⁺, it can cause calmodulin to change its conformation from the dumbbell shape to the Apo-CaM bound conformation. The cross-sectional profiles reveal that the CPD of Apo-CaM complex is 190 ± 3 mV above that of the OTS background. Since the two profiles correspond to the same position in the image, we can conclude that the Ca²⁺-induced conformational change corresponds to approximately 10 mV surface potential increase.

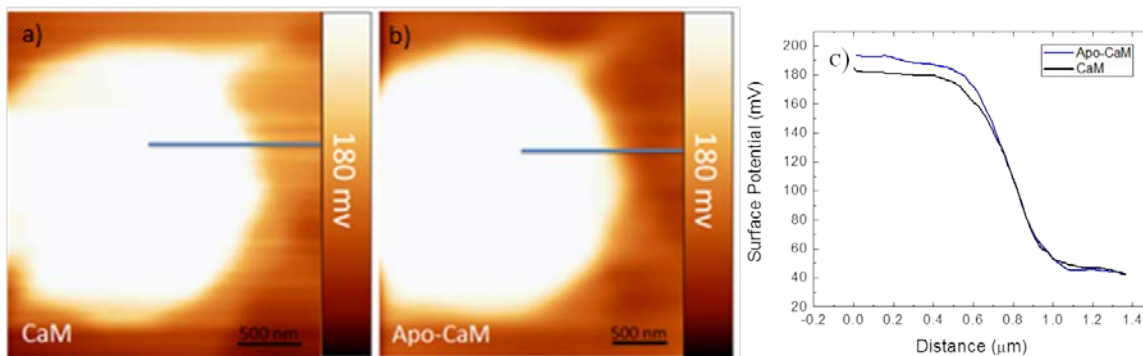


Figure 4-25 The surface potential (a, b) images of the tightly packed CaM pattern before and after incubation with the EDTA solution. The surface potential channel cross-sectional profiles corresponding to the cyan lines were shown in c). The images were acquired by the Veeco Multimode AFM with the same Ag₂Ga tip in tapping mode and are rendered in the same surface potential scale (180 mV).

The surface potential of the kinase bound CaM pattern was also investigated by applying KPFM. In this experiment, the same tip as before was used to

investigate whether KPFM is capable of detecting the CaM kinase binding domain binding on the CaM pattern area. Figure 4-26 a) is the surface potential image of a CaM KI binding domain-bound CaM pattern. The surface potential of protein pattern areas was compared with the OTS background. We found that the surface potential of protein pattern was about 104.8 ± 0.8 mV. It was much higher than that of the OTS background, which was approximately 76 mV lower than that of the CaM pattern and 85 mV lower than that of the Apo-CaM pattern.

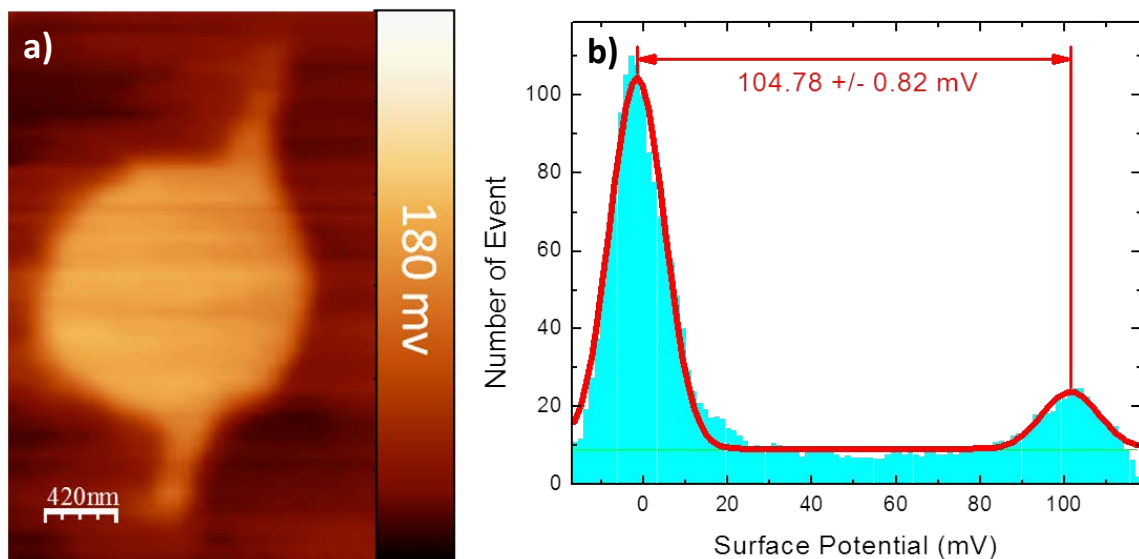


Figure 4-26 Panel a is the KPFM image of a CaM KI binding domain-bound CaM pattern. Panel b is the histogram corresponding to a. The distance between the two peaks in the histogram specifies the surface potential of the pattern in the image.

In summary, our results demonstrate that KPFM is capable of detecting the Ca^{2+} and CaM kinase binding domain induced CaM conformational change without any form of labeling. Since the key issue in the array technology is how to transduce the recognition events to readable signals,¹³⁹ our results indicate that KPFM could be used in the practical biosensor development.

4.2.9 CaM orientational difference detected by KPFM

Protein patterning techniques in micro-scale has demonstrated its huge potentials in the bio-sensing and bio-analysis field.¹³²⁻¹³⁴ The main advantages of protein microarrays technologies include high detection sensitivity, low consumptions of reagent samples (nL level), and a few amount of protein requirement.¹³⁵ However, the geometric orientation of absorbed protein molecules might be different due to the inherently asymmetric distribution in physical/chemical properties and bio-functional sites on the protein surface.¹⁶⁹ This protein orientational difference might have a notable influence on the efficiency and robustness of biosensors, which had been observed experimentally.¹⁷⁰⁻¹⁷⁶ For example, the antigen binding activity of an immobilized antibody with the active sites facing the substrate loses a lot.¹⁷⁷ Another drawback of the protein orientational difference is that it increases the background noise of the bio-analysis system. Consequently, the development of techniques that can discriminate the protein orientation on a solid support accurately and quickly is highly important for the construction of highly efficient biosensors. In this study, the KPFM surface potential signal was employed and combined with phase signal to examine the orientational difference of immobilized CaM monolayer. To the best of our knowledge, this is the first work which employs KPFM in protein orientation discrimination.

Figure 4-27 shows the calmodulin monolayer immobilized on the chemical pattern. From the topography image, the entire CaM area is well immobilized on the MUTMS pattern. However, by comparing the topographic image (Figure 4-

27a) together with the corresponding phase image (Figure 4-27b) and the surface potential map (Figure 4-27c), it was found the phase and CPD signal over this pattern have quite different contrasts. It was hypothesized that this observed difference results from different CaM orientations.

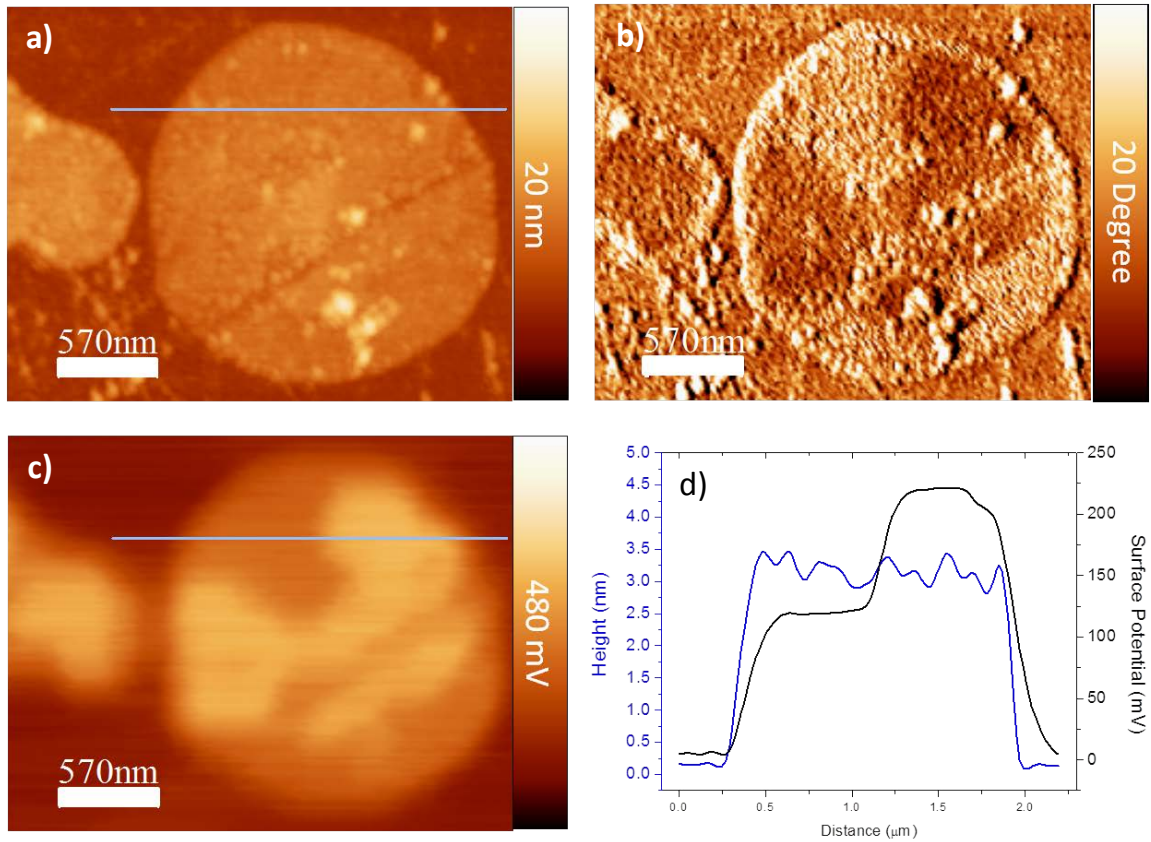


Figure 4-27 (a) The topography image for the tightly packed CaM pattern. (b) The phase image corresponding to the topography image in a). (c) The surface potential map corresponding to the topography image in a). (d) The topography (black line) and surface potential (blue line) channel cross-sectional profiles corresponding to the cyan lines shown in a) and c). The images were acquired by Veeco Multimode AFM with the same Ag_2Ga tip in tapping mode.

In the phase image (Figure 4-27b) corresponding to the topography image shown in Figure 4-27a, the phase signals over the CaM complex are different, revealing

that this pattern contained two different domains - One domain with a higher phase contrast than OTS background and it appeared as brighter in the phase image; and another domain with a reversed situation. The phase signal difference can originate from the topography change or the variations in physical property of the surface. The black line in Figure 4-27d is the height cross-sectional profile along the cyan line in Figure 4-27a. From the plot, it is obvious that the height signal difference is smaller than the noise level. Since the height signal was acquired during the same scanning line and under the same instrumental set-ups, we can conclude that the CaM surface had a same height value, 2.99 ± 0.16 nm. This film thickness indicates that the CaM molecules adopted a lying-down configuration, which was mentioned in our previous work.⁶³ Consequently, the observed phase signal difference should result from the physical property of the surface rather than the topography. For bio-molecules, this physical property depends on the polarity of the side chain, which determined by various amino acids residues of protein. Therefore, the phase signal difference could reflect the physical orientation of CaM molecules on the chemical pattern.

Besides the phase signal difference, it was also observed that there was a surface potential difference over the same pattern as Figure 4-27c shows. This difference can be further quantitatively illustrated by the surface potential cross-sectional profile along the cyan line, which is plotted in Figure 4-27d. In the plot, the surface potential difference between the two different domains is 97 ± 7 mV. Since the charge state of the molecule reflects in its isoelectric point and directly

correlated with the measured surface potential,^{165,167} we concluded that this surface potential difference is relative to different orientation of the immobilized CaM on the chemical pattern. It is also worth pointing out that the surface potential image and the corresponding phase image match exactly. So, the complementary phase and surface potential signal indicate that the 1-Cysteine mutated CaM anchored on the chemical pattern with two different orientations. Our study provides the first evidence to indicate that KPFM can be used to probe the orientation of the peptide.

Previous work to detect the orientation of proteins on surfaces has been investigated mainly by methods such as fluorescence spectroscopy, X-ray photoelectron spectroscopy (XPS), ellipsometry, surface plasmon resonance (SPR), and neutron reflectivity.¹⁷⁸⁻¹⁸⁶ Recently, more powerful instrumentations with the ability to analyze protein orientation have been developed. For example, Loren and colleagues successfully use a combination of time-of-flight secondary ion mass spectrometry (ToF-SIMS), sum frequency generation (SFG) vibrational spectroscopy, and near-edge X-ray absorption fine structure (NEXAFS) spectroscopy to characterize the orientation of surface-immobilized Protein G B1.¹⁸⁷ Compared with the above techniques, we believe that our approach offers shorter detection time, lower unit cost, and is able to transduce the orientational difference to readable signals. Furthermore, our results show that KPFM is capable of detecting the orientational difference down to the nanometer scale.

Next, the immobilized calmodulin with two types of orientations was incubated in EDTA aqueous solution for 10 minutes. Figure 4-28a shows a representative

tightly packed CaM pattern before EDTA solution incubation. At first glance, the pattern appears uniform. However, by analyzing the topography image (Figure 4-28a) together with the corresponding phase image (Figure 4-28b), we find that the well distributed CaM pattern has two different domains. Figure 4-28c shows the phase images of the same region of CaM pattern after the EDTA solution incubation. After the incubation, most of the hydrophobic patches on the protein area disappeared. We suspect that this is because the hydrophobic binding pocket exposed CaM changed its conformation to Apo-CaM with inaccessible hydrophobic binding pocket.

In Figure 4-28d, we plotted the height cross-sectional profile, which correspond to the same place of the cyan line in Figure 4-28c before and after EDTA solution treating. From the height cross-sectional profile, the calmodulin disk is 2.98 ± 0.16 nm above the OTS background. After incubating the CaM pattern with a 10 mM EDTA solution for 10 minutes, the height of the CaM pattern changed to 3.34 ± 0.11 nm. The height increase is consistent with our published data.⁶³ Since the cross-sectional profile crosses two different CaM domains, it illustrates details about the surface height variation over both CaM domains with different orientations. From the height cross-sectional profile, no significant height difference was observed for these two different CaM domains and the average height increases about 3 Å for both of them after EDTA solution treatment. Therefore, two CaM domains behaved similarly and demonstrated the same binding preference when reacted with calcium ions.

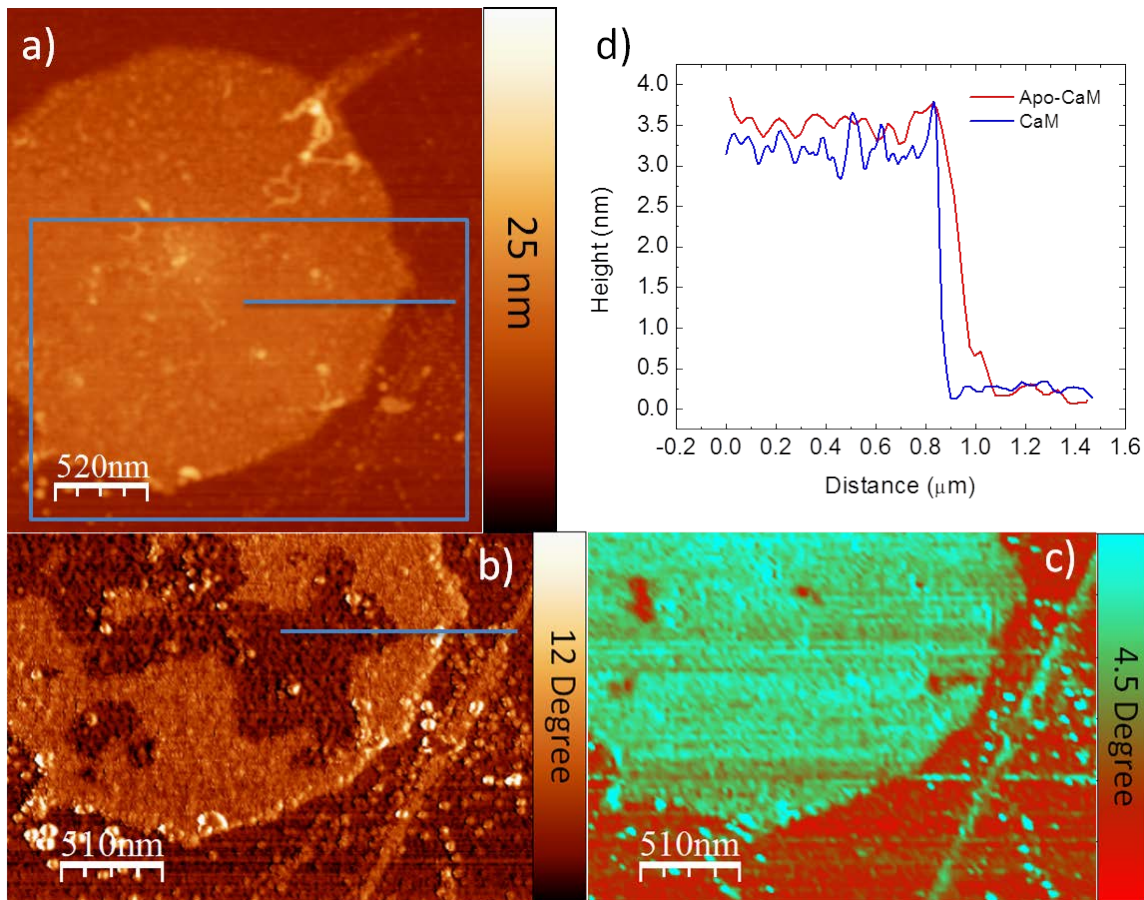


Figure 4-28 (a) is the representative AFM topography image of the proteins on the chemical pattern template. (b) and (c) are the phase images of protein pattern before and after EDTA solution incubation, which correspond to the zone of the cyan box in (a). The height cross-sectional profile corresponding to the cyan lines were plotted in (d).

It is necessary to conduct a control experiment to confirm that the phase change was not induced by the AFM tip scanning, although the probe only gently “tapped” on the sample surface during scanning. In the experiment, an AFM tapping mode tip immediately performed a scan over the sample surface in an environmental chamber with 100% relative humidity (RH) after the sample was ready. Figure 4-29 (a) and (b) are the AFM phase images taken at first and second scanning. Then, Figure 4-29 (a) was laid over Figure 4-29 (b). The combined image in Figure 4-29 (c) demonstrates that these two AFM phase images match exactly.

Therefore, this phase difference shown in Figure 4-28 (b) and Figure 4-28 (c) was induced by the Ca^{2+} removing due to EDTA solution incubation, rather than the AFM tip scanning.

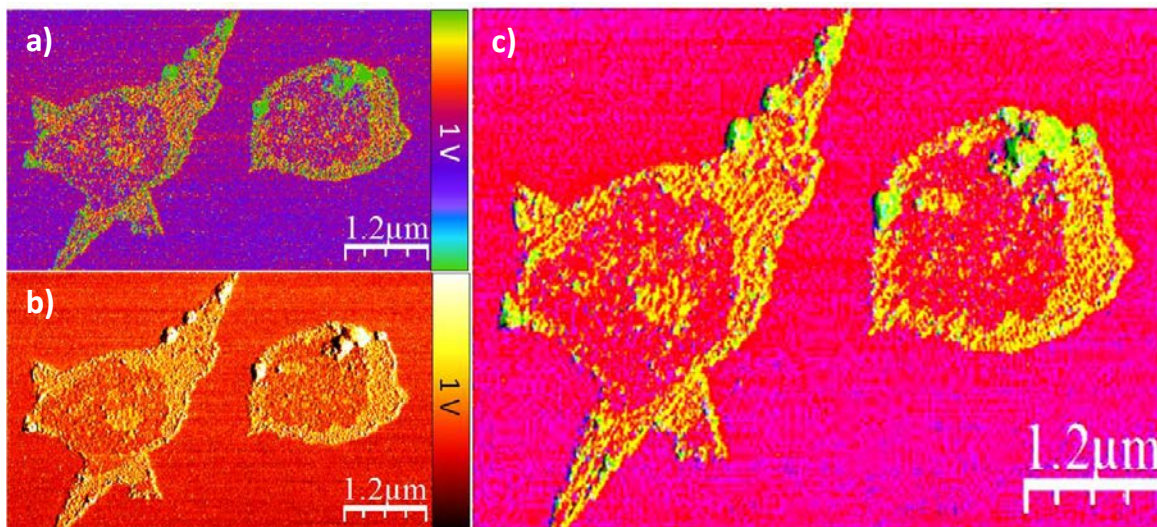


Figure 4-29 AFM phase images of protein patterns at (a) the first and (b) second time scanning, and (c) an (a)–(b) combined image (a is rendered in an artificial multicolor gradient scale and b is rendered in the gradient scale).

To investigate the stability of these two differently orientated CaM patterns under the same pressure, an AFM contact mode tip was used to scan over the pattern surface for 3 hours in an environmental chamber with 100% relative humidity (RH). Figure 4-30 (a) and (b) are the AFM phase images taken before and after 3 hour's scanning using contact mode. The phase signal difference was confirmed by overlaying Figure 4-30 (a) and (b) together, as shown in Figure 4-30 (c). In Figure 4-30 (c) the difference of the hydrophobic patch on the protein pattern was rendered on the pink color, the protein pattern was rendered on yellow color, while the exactly matched area was rendered on the dark color. Obviously, the hydrophobic patches still exist on the pattern area but cannot overlap with one

another exactly. Compared with Figure 4-30 (a), the area of the hydrophobic patch in Figure 4-30 (b) shrinks a little bit. Considering the scanning force, it can be concluded that the orientation of the hydrophobic patched CaM can be changed under certain scanning force.

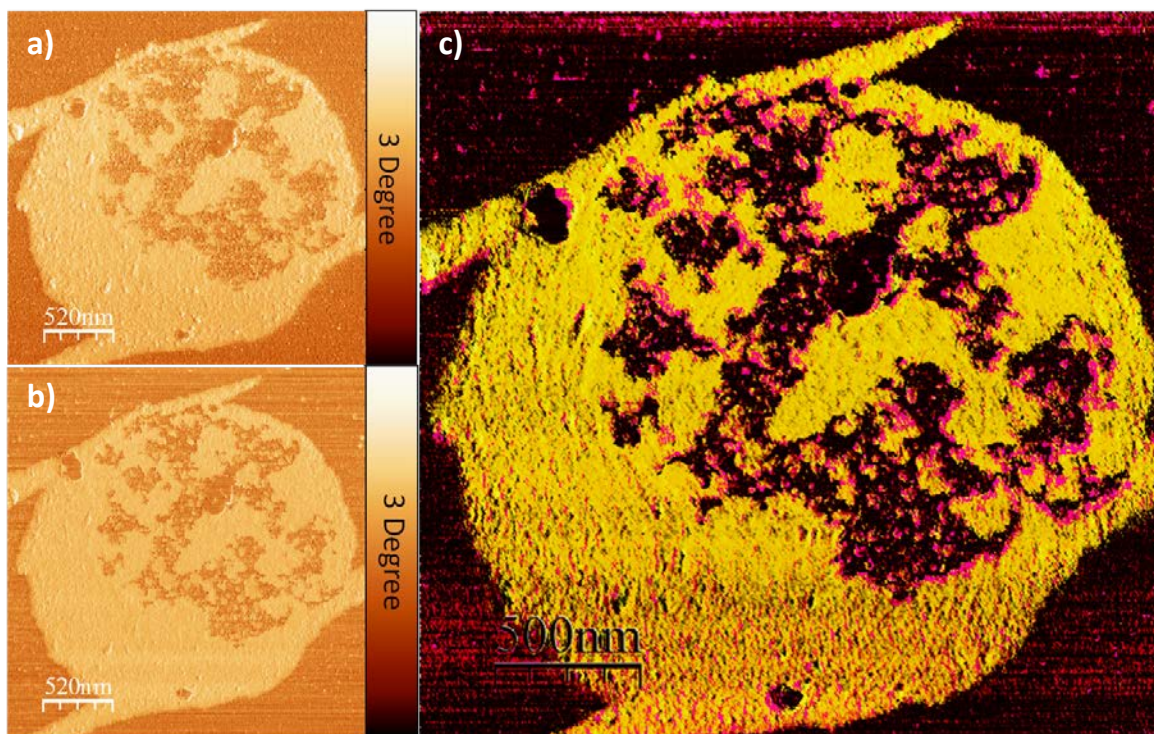


Figure 4-30 The phase image of the same protein pattern (a) before and (b) after the sample was subjected to 3 hours scanning, and (c) is an (a)–(b) combined image.

A second protein layer was also found during our experiment (Figure 4-31a). AFM phase image (Figure 4-31c) demonstrated that this second layer is a hydrophobic surface formation on a hydrophilic surface. The topography measurement (the cyan line in Figure 4-31a) shows that an extra CaM layer attached on the protein pattern, which is about 1.9 nm higher than the Cys-Hg-S bonded CaM monolayer. This film thickness is consistent with the height of the calmodulin layer observed in our previous work.⁶³ The KPFM measurement indicated that the surface potential of the second layer CaM is 99 ± 3 mV higher

than the CaM Cys-Hg-S bounded monolayer. This value is roughly the same as that of the hydrophobic CaM layer (97 ± 7 mV). When cumulatively considering the similarity of the phase, topography, as well as the CPD signals of the second layer CaM with those of hydrophobic CaM layer, we proposed that orientation of the CaM second layer is similar to that of the hydrophobic CaM.

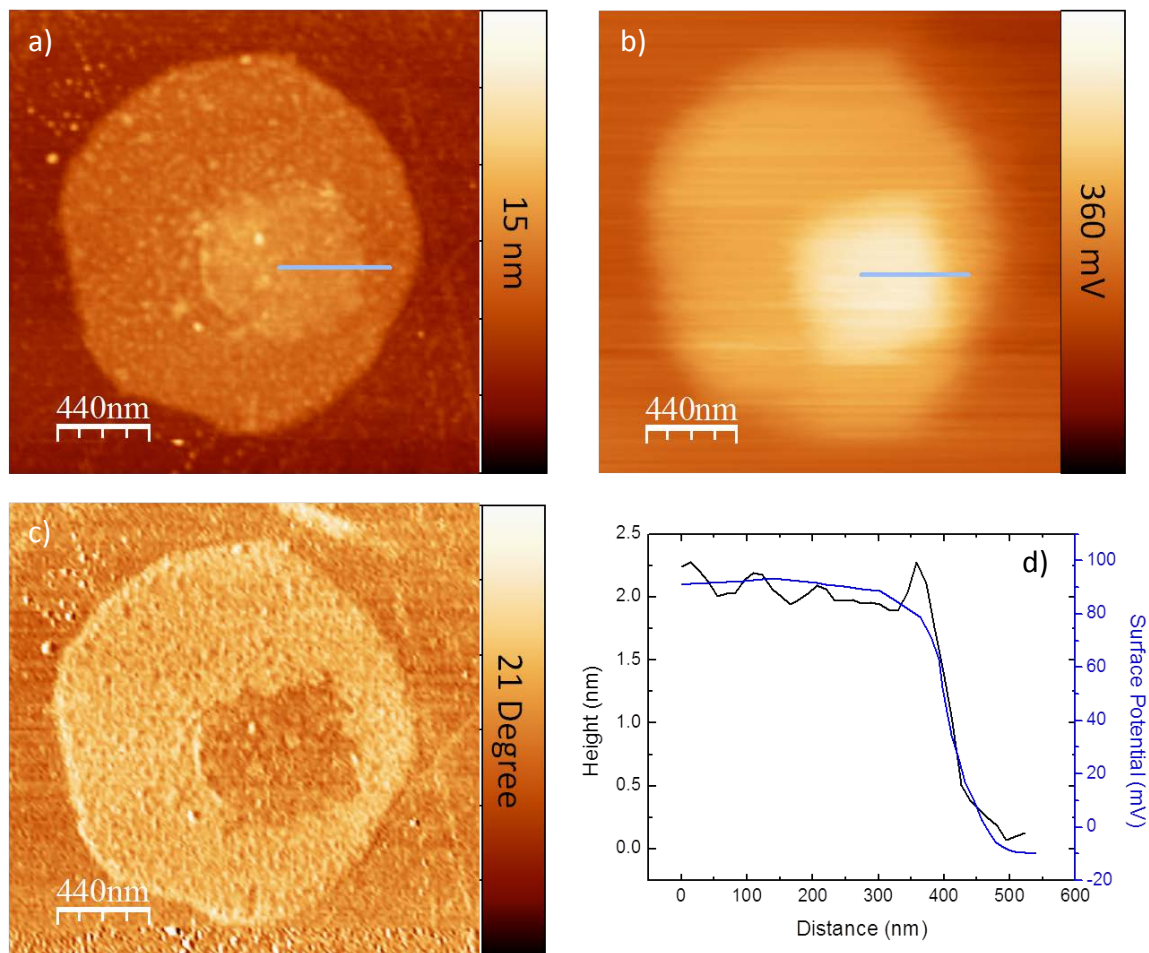


Figure 4-31 a) AC mode topography image for CaM patch with double layer on it. b) The surface potential map corresponding to the topography image in a). c) The phase image corresponding to the topography image in a). d) The topography (black line) and surface potential (blue line) channel cross-sectional profiles corresponding to the cyan lines shown in a) and b).

4.3 Conclusion

Our results show that the immobilization of CaM on a solid support does not interfere with its ability to bind with calcium, changing its shape from dumbbell-shaped conformation to bound conformation. Moreover, immobilized CaM retains its activity, which is proven by binding CaM KI binding domain. We found that the dumbbell-shaped CaM adsorbed on the surface with its handle parallel to the surface. Upon conformational change to the bound-shaped Apo-CaM or CaM KI binding domain-bound CaM, the apparent height of the CaM molecule increased.

In addition, we demonstrated that KPFM was capable of detecting conformational change induced by the calcium and CaM KI binding domain. Our results also show that the immobilized CaM demonstrated two different orientations, which can be identified through KPFM combining with AFM phase signal straightforwardly. Those differently orientated CaM experienced a same height increase after treated with EDTA solution, indicating both retained the same bio-activity for calcium binding. Finally, by comparing the phase, topography, as well as the CPD signals of the second layer CaM with those of hydrophobic domain within first CaM layer, we proposed that the CaM second layer and the hydrophobic domain within first CaM layer have a similar orientation.

Furthermore, our protein immobilization method requires a terminal cysteine group to anchor it to the SH-terminated surface. Most proteins can be prepared through this established procedure to engineer a terminal cysteine group. Therefore, our method would be helpful in research and assay work involving engineered proteins.

CHAPTER 5: OCTADECYLTRICHLOROSILANE (OTS)-COATED IONIC LIQUID DROPS: MICRO-REACTORS FOR HOMOGENOUS CATALYTIC REACTIONS AT DESIGNATED INTERFACES

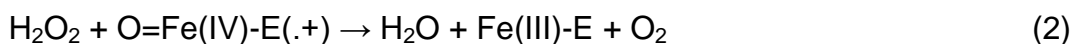
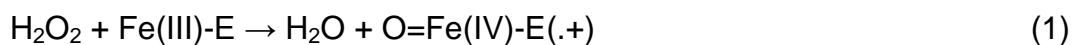
5.1 Introduction

Some reactions like transesterification and amide synthesis require an anhydrous solvent as reaction medium to restrain those unwanted hydrolytic side reactions.¹⁸⁸ Enzymes working in anhydrous solvents could play critical roles in these reactions. In recent years, ionic liquids (IL) were considered as an anhydrous medium and used in biocatalytical transformations. In comparison with conventional organic solvents, ILs are low temperature melting salts with low vapor pressure, and possess tunable properties by changing the cation and anion part. Of course, improving reaction rate or productivity is the major driving force and the most desired aim for ILs used as a medium in biocatalytical transformations.¹⁸⁸ Significant reaction rate enhancements and improvements in ionic liquid reaction media had already been reported. Park S et al. found that *Candida Antarctica lipase* (CaLB) catalysed esterification of glucose reaction in IL [MOEMIm][BF₄] is 100 times faster than when this reaction is conducted in acetone.¹⁸⁹ Lozano P et al. found that the final product concentration of the enzyme-catalyzed transesterification and stabilization of N-acetyl-L-tyrosine ethyl ester reaction increased in IL reaction medium due to the increased enzyme stability.¹⁹⁰

ILs can be recycled and re-used by removing products and unconverted reactant from the mixture. In enzymatic reaction conducted by Erbeldinger et al., the IL was recycled and reused several times after extracting the remaining substrates

out by using water.¹⁹¹ Moreover, some products could be collected via simple evaporation method due to the negligible volatility of ILs. This case was shown in the reduction of prochiral ketones in [Bmim][PF₆] by baker's yeast, the reductions produced alcohols was distilled from the IL under high vacuum.¹⁹² Also, because the solubility of ILs could be adjusted by changing a cation or anion, it makes the two-phase enzymatic reaction possible. In Lozano et al.'s work, a specific IL, which is immiscible with supercritical CO₂, is synthesized. Because of this insolubility, the enzyme can stay in IL phase, while reactants and products can be kept in the supercritical CO₂ phase, and a continuous biphasic biocatalysis reaction can be initiated.¹⁹³

At the preliminary stage of this research, catalase was used as a model protein molecule to study the catalytic activity of protein in ILs. Catalase is a very important enzyme in living cells that can decompose H₂O₂ to O₂ and H₂O for the oxygen level control. It is very efficient since each catalase molecule can decompose 83000 hydrogen peroxide molecules per second.¹⁹⁴ Catalase is also widely used in industry. For example, it has been used to remove the H₂O₂ from fabrics in the textile industry.¹⁹⁴ The mechanism of the reaction of catalase for the decomposition reaction of hydrogen peroxide is believed to be possible in the two stages as follows:



Where Fe(III)-E indicates the enzyme, Fe(IV)-E(.+) represents an activated transition state of catalysis. In the first step, one H₂O₂ molecule binds to Fe³⁺, then, breaks apart with one O atom attached to the Fe³⁺ and the release of one H₂O. In the second step, another H₂O₂ binds to Fe atom, releasing O₂ and H₂O.¹⁹⁵

Based on previous research by past member of Cai's research group, catalase molecules can be immobilized on the OTSpd pattern via adhesion force. The activity of the immobilized protein was maintained and hydrogen peroxide could be decomposed.⁶² To provide a chance to study the activity of the catalase in IL, the catalase was mixed with [Bmim]Cl and [Bmim]Tf₂N ILs respectively to see whether the reaction rate can be improved further. Another aim of this experiment is to provide a method to preserve the catalytic activity of catalase in the room temperature due to the low volatility of the ILs. By observing the generation of oxygen bubbles, we can prove the bioactivity of the catalase in the ILs. Since FeCl₃ is a homogenous catalyst for the decomposition reaction of H₂O₂,¹⁹⁶ it was also mixed with [Bmim]Cl and [Bmim]Tf₂N respectively as control experiments.

The micro-reactor attracts lots of focus due to advantages such as portability, reduced reactant consumption, and minimized waste production. However, a number of the reactions executed in such systems involved a reagent phase that are mutually immiscible, like aqueous-organic liquid micro-systems and gas-liquid micro-systems.⁶⁹ Therefore, if the catalytic activity of the catalase in IL can be preserved, we will try to use this active mixture to build up a model micro-

reactor, which is suitable for the miscible reagent phase and allows chemical reactions to occur at the designated interfaces.

Based on our results, no bubbles were observed when 30% H_2O_2 solution was added into the $[\text{Bmim}]\text{Cl}/[\text{Bmim}]\text{Tf}_2\text{N}$ IL contained catalase mixture, while the H_2O_2 decomposition reaction occurred in the mixture of ILs contained FeCl_3 and 30% H_2O_2 solution. This difference means the catalase lost its catalytic activity, while the catalytic activity of FeCl_3 was still maintained when it was around by $[\text{Bmim}]\text{Cl}$ or $[\text{Bmim}]\text{Tf}_2\text{N}$. Since the ultimate purpose of this project is to build a micro-reactor for two miscible reagent phases, we hypothesized we could use FeCl_3 substitute catalase as reagent. After all, FeCl_3 is also an important chemical, which can be used in wastewater treatment¹⁹⁷ or as a catalyst for organic synthesis.¹⁹⁸

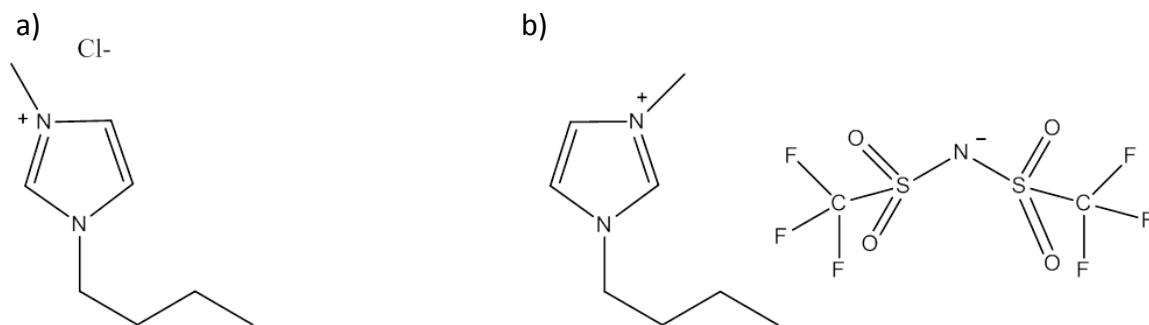


Figure 5-1 The structures of a) 1-butyl-3-methylimidazolium chloride ($[\text{Bmim}]\text{Cl}$) and b) 1-butyl-3-methyl-imidazolium bis(trifluoromethanesulfonyl)imide ($[\text{Bmim}]\text{Tf}_2\text{N}$)

In this experiment, a homogenous catalyst (FeCl_3) was dissolved in $[\text{Bmim}]\text{Cl}$ and assembled together on the chemical patterns, we found that the chemical patterns can control the shape, size and position of the IL on surface. Then it was encapsulated with an OTS coating as Figure 5-2 illustrates. We discovered that

the pinhole defects on the OTS coating layer provided spaces for the catalyst inside the capsule and reactants outside the capsule to react. Hence, the coating IL drops enabled the interfacial chemical reactions.



Figure 5-2 Octadecyltrichlorosilane (OTS)-coated ionic liquid/FeCl₃ drop.

5.2 Experimental

5.2.1 Instruments

The chemical pattern fabrication and characterization were conducted by the Agilent PicoPlus 2500 environmental AFM. The optical examination of the surface was conducted using a Nikon Eclipse 55c microscope.

5.2.2 Chemicals and materials

Octadecyltrichlorosilane (OTS, 97%) was purchased from Gelest. 1-butyl-3-methylimidazolium chloride ([Bmim]Cl) was purchased from Sigma Aldrich. 1-butyl-3-methylimidazolium bis(trifluoromethylsulfonyl) imide ([Bmim][Tf₂N]) was donated by Dr. De-en Jiang of Oak Ridge National Laboratory. Silicon (100) wafers (KC electronics, Nitrogen doped, 30 Ω•cm resistivity) were polished to ultra-flat grade with a Root-Mean-Square (RMS) roughness smaller than 5 Å. All

the solution was prepared with water from a Narnstead Nanopure Diamond lab water purification system with normal resistivity of 18.2 M Ω •cm.

5.2.3 Coating IL on OTSpd patterns

After an ultra-flat, pinhole-free, featureless film being prepared, several 8 x 8 OTSpd disc arrays were fabricated on the OTS film by the scanning probe deep oxidation lithography. The detailed set-up and procedure have been described in Chapter 3. The size of the array was 50 x 50 μm^2 . Then, 10g [Bmim]Cl powder was heated to 120°C and then cooled to room temperature in a sealed vial. After cooling, [Bmim]Cl in the vial existed as a viscous super-cooled liquid at 25°C. A drop of liquid [Bmim]Cl was placed on the patterned area, a pipette was used to remove the IL drop from the sample surface (The OTSpd pattern is a high energy, lyophilic surface whereas the OTS background is a methyl-terminated low energy, lyophobic surface). Based on the wetting-driven assembly approach,¹⁹⁹ [Bmim]Cl can be assembled on the OTSpd patterns as drops due to the contrast in surface energy. [Bmim]Tf₂N assembly is the same mechanism, but without heating before placing it on the patterned area since it is in a liquid phase already.

Unlike conventional molecular liquids, there is no existence of individual molecule in the IL liquid. Also, ILs are not diluted electrolyte solutions. So far, no existing theory and model can precisely describe the behavior of ILs, especially at the IL interfaces. Therefore, it is necessary to study the IL interfacial properties for further developments of IL-based applications. A Veeco Multimode AFM described previously was used to perform surface potential measurements. KPFM maps the surface potential distribution over the surface, as we mentioned

in Chapter 4, which could determine how the ions are arranged at the interface.²⁰⁰ Figure 5-3 reveals that the surface potential of [Bmim]Cl droplets and [Bmim]Tf₂N droplets sit on the OTSpd pattern. The [Bmim]Cl droplets and [Bmim]Tf₂N droplets have a surface potential of -514 ± 27 and -482 ± 14 mV with respect to the background, respectively. The above results revealed how the ions of these two types of ILs are structured at the interface - the cation groups are more likely pointed toward the bulk while the anion groups are more possibly present on the surface.

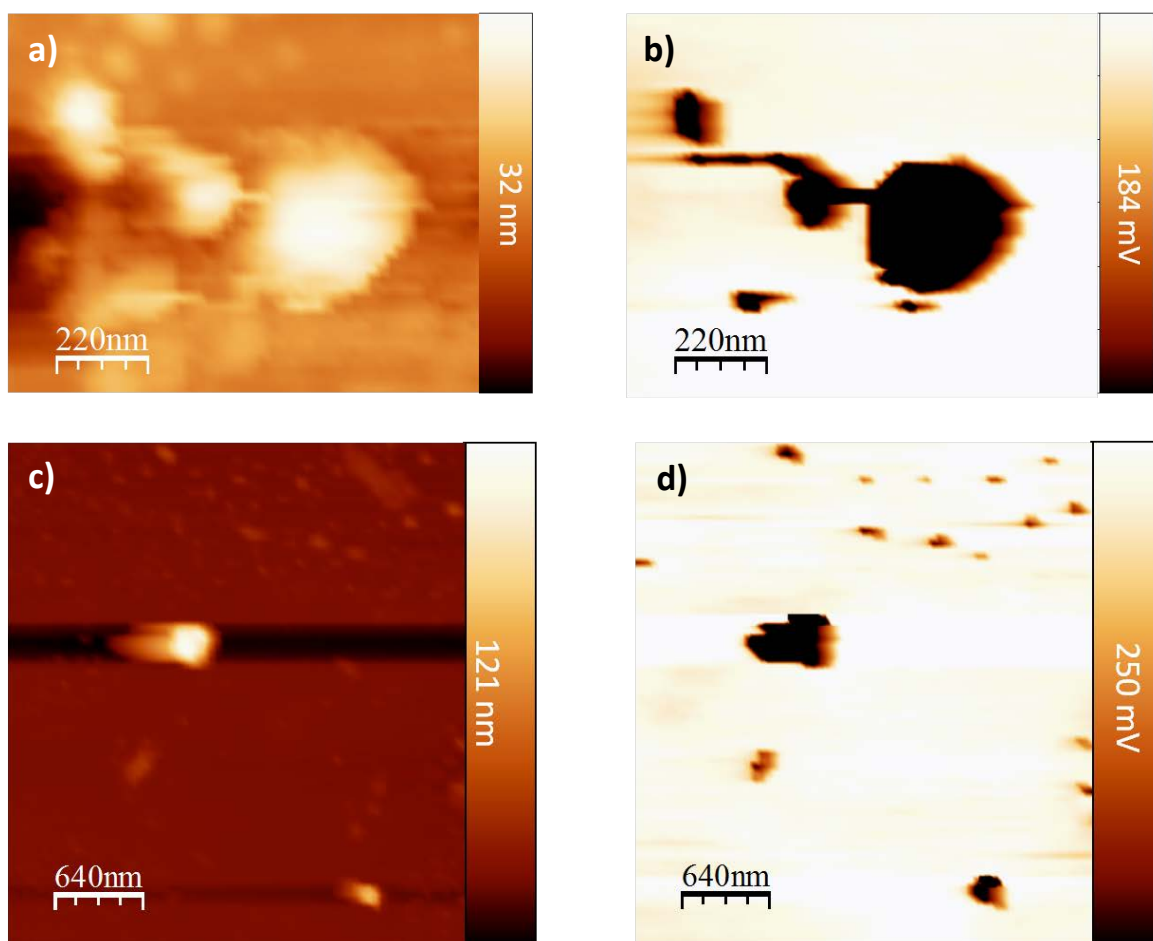


Figure 5-3 AFM topography images and surface potential images of the ILs droplets on OTSpd pattern. (a) Topography image of [Bmim]Cl droplets on OTSpd. (b) Surface potentials of [Bmim]Cl droplets on OTSpd. (c) Topography image of [Bmim]Tf₂N droplets

on OTSpd. (d) Surface potentials of [Bmim]Tf₂N droplets on OTSpd. The two images were acquired using the same condition.

Samples with IL drops assembled were placed in a sealed vial with 33 μ L OTS liquid. The vial was placed in an oven at 55°C for 2 hrs. The OTS molecules from the vapor formed a layer at the IL drop surface. During this process, silane molecules reacted with water to form silanols, which subsequently cross-linked with each other using the Si–O–Si covalent bonds and formed a polymer network.^{121,196} Such a silane network is mechanically stable and chemically inert. When silane molecules reacted with hydrophilic IL drop surfaces, a self-assembled silane layer formed on its surface.

5.2.4 AFM and optical microscope characterization

After the IL was assembled on the chemical pattern, the sample surface was then characterized using an optical microscope and Agilent PicoPlus AFM in tapping mode with a MikroMasch NSC14 tip (150 kHz resonance frequency, 5 N/m force constant). All images were processed using the WSxM software.¹¹⁷

As Figure 5-4 illustrated, the OTSpd disc array was fabricated on the OTS film via scanning probe deep oxidation lithography. After a liquid [Bmim]Cl drop rolling over the OTSpd pattern area, an AFM image was taken again as Figure 5-4b shown. From Figure 5-4a to Figure 5-4b, we found that the IL micro-drop arrays were selectively deposited on the high surface energy OTSpd chemical patterns. Then, an optical microscope was used to capture the image of the sample surface. As Figure 5-4c illustrated, the IL drop arrays were assembled on OTSpd patterns. Each dark spot is an IL micro-drop and the background is the

smooth OTS film. The regions shown in Figure 5-4a and 5-4b are highlighted within the red box in Figure 5-4c.

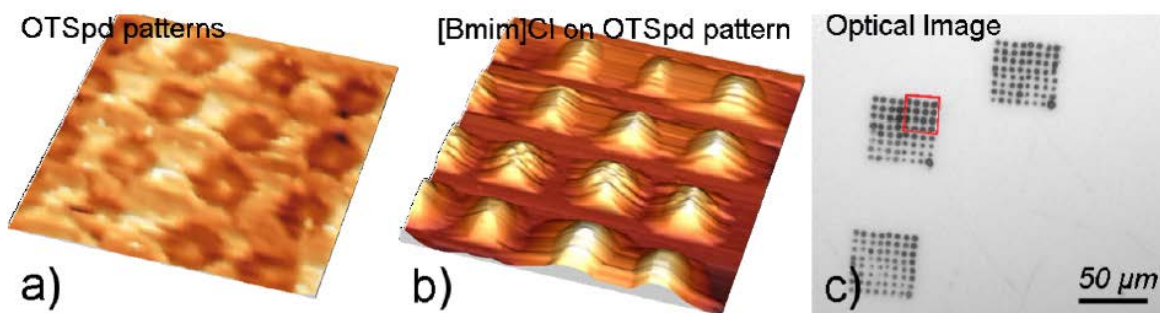


Figure 5-4 [Bmim]Cl assemblies on the OTSpd pattern. a) OTSpd discs fabricated by scanning probe deep oxidation lithography on OTS film. Topography image. The center-to-center distance between two neighboring discs is $\sim 5 \mu\text{m}$. b) The same area after [Bmim]Cl was coated on the sample. [Bmim]Cl selectively assembled on the lyophilic OTSpd discs. Topography image. c) Optical image of [Bmim]Cl assembled on the OTSpd patterns. The light background is the OTS film. The red box is the zone shown in a) and b). In this optical image, each IL drop assembled on an OTSpd disc appears as a dark dot.

The optical image (Figure 5-4c) reveals that the amount of IL assembled on each OTSpd disc are similar but not identical. The darker the discs appear, the more the IL was assembled on the discs. For the AFM topography image, this difference can be reflected to the height variation of each disc, from 250 nm to 800nm. The AFM image reveals more details about the shape of the IL droplet assembled on the OTSpd discs. Figure 5-5 is a representative high-resolution AFM image, which shows that the IL is not a hemispherical drop that covers the whole OTSpd disc. Instead, the shape of the IL drop is a Mexican hat - a partial drop sitting on top of a hydrophobic solid-like layer, which can be viewed from the Figure 5-5b, the AFM phase image. The green line marks the positions of the

hydrophobic solid-like layer. The partial drop covers the central part of the OTSpd disc and is typically 250-800 nm high. The central drop is surrounded by a rim, which extends out and covers the remaining part of the OTSpd disc. Our experimental results indicate that the IL sitting on the OTSpd has two parts: one is the central partial drop and the other is the solid-like IL layer. Yasuyuki Yokota et al. applied AFM to various IL/Solid interfaces in the fluid ILs and directly observed the step-terrace structures at the IL/solid interfaces with negligible IL mobility.²⁰¹ They thought the formation of this tight packing film was because of the strong Coulombic interactions between the ions and the charged confining surfaces.^{202,203} To proof the droplets sitting on the pattern area are IL, the sample was dipped into the water. Since [Bmim]Cl is miscible with water, all IL micro-droplets on the patterned area disappeared instantaneously after the sample was immersed in water, indicating that those droplet arrays were made of [Bmim]Cl.

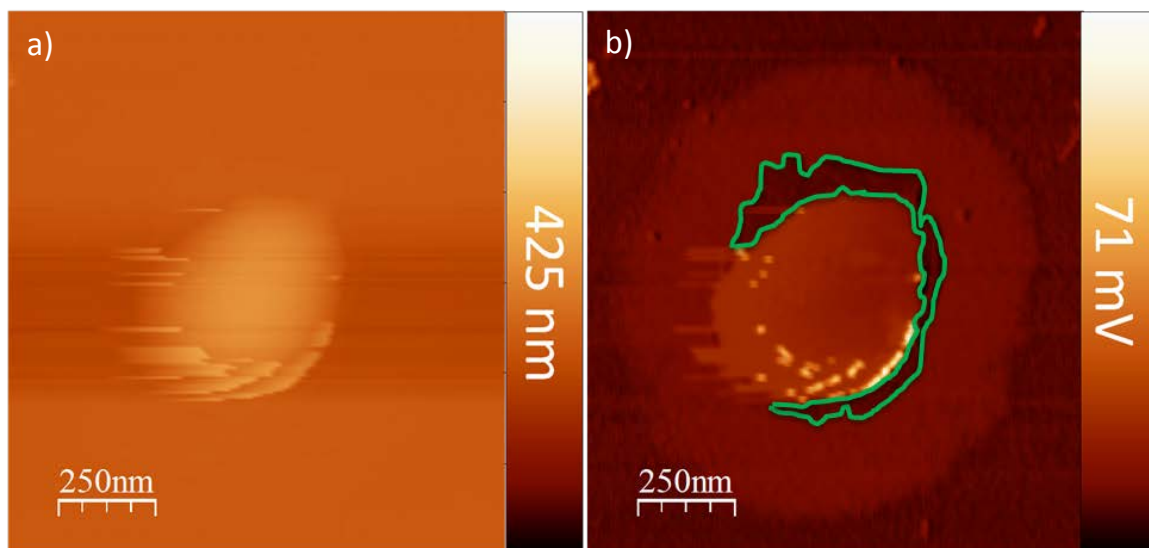


Figure 5-5 Tapping mode image of an representative [Bmim]Cl drop on OTSpd pattern. The green line marks the position of the precursor layer.

Figure 5-6a is a representative phase image of the [Bmim]Cl IL sit on the OTSpd chemical pattern, which shows that OTS and the drop surface have different phase signals. The corresponding histogram in Figure 5-6b indicates that the drop surface is 1.1 V above the OTS background for this image.

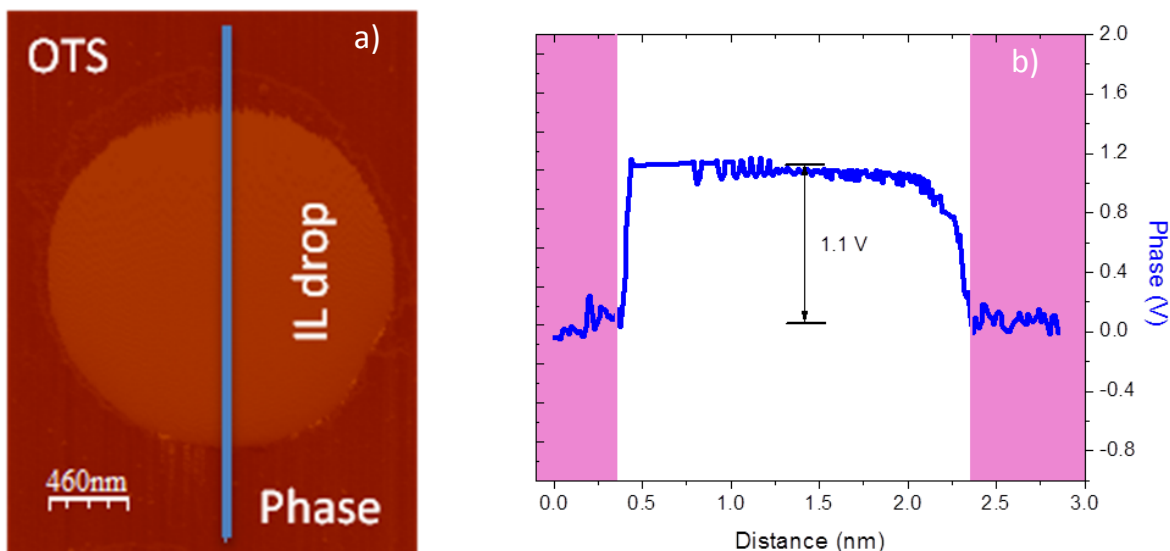


Figure 5-6 a) A representative [Bmim]Cl drop on the OTSpd pattern before OTS coating. Tapping mode phase image. b) The phase (blue line) channel cross-sectional profiles corresponding to the cyan lines shown in a). The pink zones indicate that the phase signal is from the OTS background while the cyan line in the white zone represents the phase signal from [Bmim]Cl drop.

Figure 5-7 indicates that an OTS layer covered the IL drop surface, forming a capsule that encapsulated the IL inside. The height cross-sectional profile along the cyan line in the AC mode topography image (Figure 5-7a) is plotted in Figure 5-7d (black line), which reveals that the drop in Figure 5-7a is 300 nm in height. Figure 5-7b is an optical image of the OTS-coated [Bmim]Cl drop array. The image was produced under water after 1 h of incubation. Under the optical microscope, interfaces separating the drop and the water can be clearly

observed. In contrast, in the control experiment for those IL drops assembled on OTSpd disc without OTS coating, after water was applied to the patterned area, the un-coated IL drops were instantaneously miscible with water, and thereby disappeared. Based on this control experiment, we concluded that the coating separated [Bmim]Cl inside the capsule and the water outside the capsule.

Figure 5-7c is the phase image corresponds to the topography image shown in Figure 5-7a. It is found that the phase signals over the OTS coated IL drop and the OTS background are the same. Compared with the phase signal difference between [Bmim]Cl IL droplet and OTS background shown in Figure 5-6b, this similarity in phase signal reveals that additional material coated on the IL drop. This can be further quantitatively illustrated by the phase cross-sectional profile along the cyan line in Figure 5-7a, which is plotted as the blue line in Figure 5-7d. In the plot, the phase signal difference between the drop surface (central white region in Figure 5-7d) and the OTS film (pink regions in Figure 5-7d) is smaller than the noise level. Thus, we conclude that OTS and the drop surface have the same phase signal. The phase signal acquired during the same scanning line and under the same instrumental set-ups represents the surface identity. Since the OTS background is methyl-terminated, we conclude that the vapor treated [Bmim]Cl drop is also covered with a layer of methyl-terminated OTS silane.

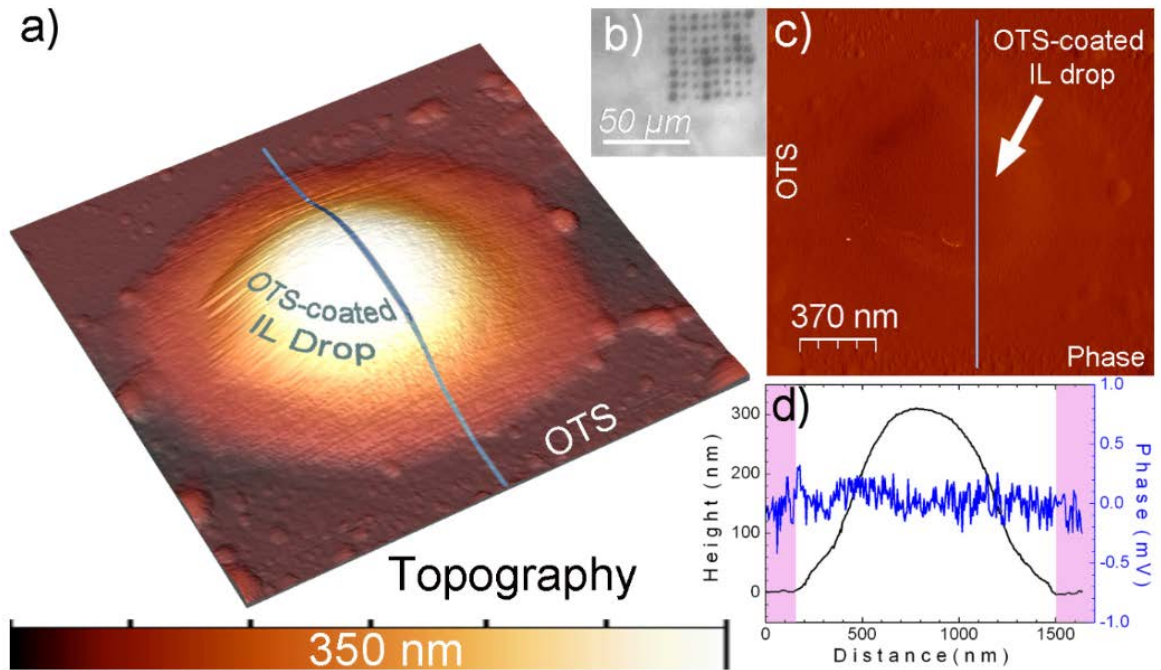


Figure 5-7 a) A representative OTS-coated [Bmim]Cl drop on the OTSpd pattern. Tapping mode topography image. b) Optical image of OTS-coated [Bmim]Cl drops on the OTSpd disc array. The imaged was acquired under water. c) The phase image corresponding to the topography image in a). d) The topography (black line) and phase (blue line) channel cross-sectional profiles corresponding to the cyan lines shown in a) and c). The topography cross-section profile reveals that the drop height is 300 nm. The phase cross-section profile indicates that the phase signal of the OTS regions (pink zones in d) and the phase signal of the OTS-coated drop surface are the same because their difference in phase signal is smaller than the noise level.

During the tapping mode imaging, we also varied the tapping amplitude set point in order to examine how the encapsulated IL responded to different external tapping intensities. At a high amplitude set point (99.5% of the free oscillation amplitude), the tip tapped the OTS-coated drop gently. A smooth topography profile of the drop was acquired. In contrast, at a low set point (95% of the free oscillation amplitude), the tip tapped the OTS-coated drop hard, with a high force. Phase signal oscillations were observed when the tip scanned over the drop, as

shown in the Figure 5-8b. The oscillation at a low set point indicates that the drop was disturbed when the tip tapped it hard, which caused the IL inside to oscillate. Hence, the IL inside the capsule was still fluidic. In comparison, under the same low set point, the AFM scan lines over the OTS film background did not show any oscillation because the OTS film was in solid phase. Hence, this control reveals that the oscillation we observed over the drop is the true physical oscillation of the IL inside the drop rather than the electronic oscillation originated from the AFM feedback loop. Therefore, from this experiment we conclude that the coated silane layer only formed at the surface of the IL drop.

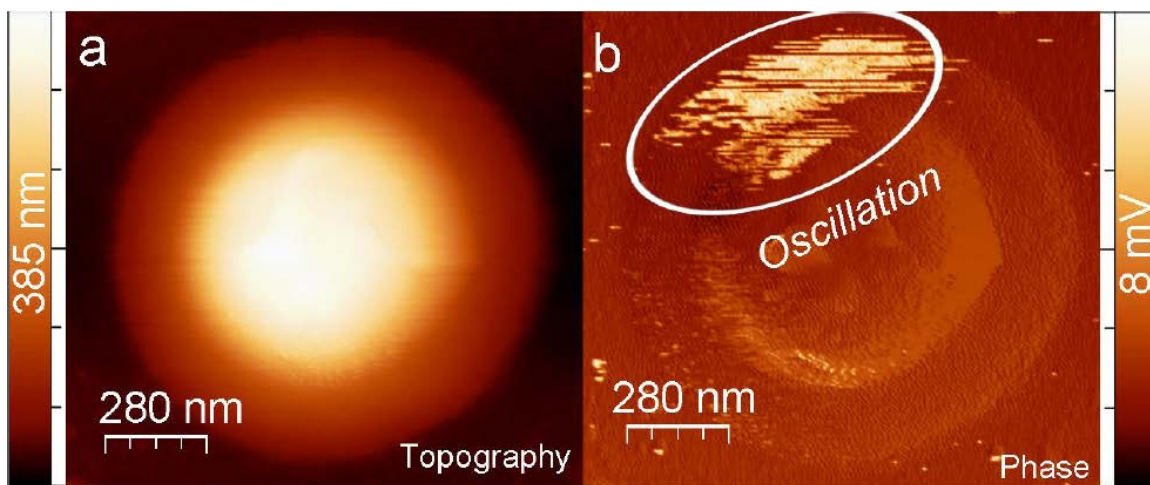


Figure 5-8 AC mode image of an representative OTS-coated [Bmim]Cl drop. During imaging, the imaging amplitude set point was intentionally varied. When we scanned the upper part of the image b), the amplitude set point was lowered, which led to the tip tap harder on the OTS-coated drop and interacted strongly with the OTS-coated IL drop. As a result, oscillations were observed as highlighted in the white circle in b) Once the set point was increased, the tip tapped the surface gently; the oscillation disappeared, indicating the tip did not disturb the OTS-coated IL drop.

5.2.5 Reaction of the OTS-coated IL capsules

Pinholes widely exist in the silane film that was prepared without stabilization.²⁰⁴ Tohru Nakagawa et. al.²⁰⁵ demonstrated that OTS molecules form a monolayer on the surface arranged perpendicularly, but contain some pinholes ranging from several nanometers to about 100 nanometers based on different substrate. The origin of the pinholes might be attributed to several reasons. The first may be the substrate contamination, which was proposed by Barrat et al.²⁰⁶ The second one may be the imperfections of the OTS network, as the OTS molecules cannot always bind to their neighbor molecules perfectly, caused by steric effect of the long chain groups $-(\text{CH}_2)_{17}\text{CH}_3$ in OTS molecules. Based on Xiang et al.'s research,²⁰⁷ the long chains form an array dotted on the surface during the OTS SAM formation, which causes a steric effect. This steric effect can obstruct the adsorption of more OTS molecules on the substrate. This means the coverage of OTS SAM cannot be improved by increasing incubation time without stabilization in a humid environment.

In our case, when the “unstabilized” OTS film was imaged using a MikroMasch ultra-sharp AFM tip (~1 nm in tip diameter), no pinholes could be resolved. On the other hand, when the unstabilized OTS film is incubated in (11-mercaptoundecyl)trimethoxysilane toluene solution, the (11-mercaptoundecyl)trimethoxysilane molecules can fill the pinholes in the OTS film, leaving the terminal –SH groups on top. The –SH group can subsequently bond to gold nanoparticles and immobilize them on the surface. Hence, we infer that the size of the pinhole would be around 0.5–1 nm, which cannot be resolved by

AFM probes in x-y dimension. We proposed that these pinholes provide spaces for reactions/encounters between the materials encapsulated inside the drop and reactants in the external solvent.

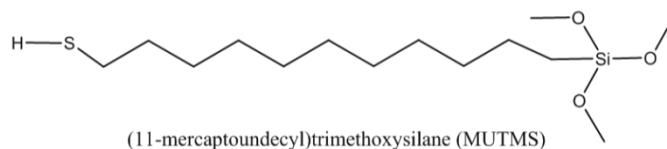


Figure 5-9 The molecular structure of (11-mercaptoundecyl)trimethoxysilane.

Figure 5-10 is the optical microscope images for the OTS-coated [Bmim]Cl drop arrays. The IL inside drops contained 30% (w/w) of FeCl_3 . The sample was incubated under 30% H_2O_2 solution at 25 °C. FeCl_3 is a homogenous catalyst for the decomposition reaction of H_2O_2 .²⁰⁸ When FeCl_3 was added in H_2O_2 solution, the H_2O_2 decomposed and oxygen bubbles were generated in the solution as the decomposition product. In our experimental set-up, the FeCl_3 was dissolved in IL solution, which was encapsulated by the OTS coating and existed as the immobilized capsules arrays on the designated places. We applied one drop (30 μL) 30% H_2O_2 solution onto the surface to cover the OTS-coated FeCl_3/IL arrays. The Fe^{3+} inside the IL was slowly released from the pinholes on the OTS film. The released Fe^{3+} catalyzed the decomposition reaction of H_2O_2 , which generated O_2 bubbles. The reaction was monitored by the optical microscope in real time. As Figure 5-10 shows, after immersion, oxygen bubbles were observed on the patterned area immediately (within 0.5 s after the H_2O_2 drop was applied onto the sample). Under the optical microscope, the smallest bubble that can be resolved is around 600 nm in size, which is at the resolution limit of our

microscope. At the beginning, these small bubbles randomly appeared at the surface of the IL capsules. However, nearby oxygen bubbles fused together to form large bubbles. The size of the bubbles increased with time. Upon further growth, the fused bubbles took off from the surface and the patterned area became clean. Then, new bubbles appeared at the interfaces of the OTS-coated IL drops. These new bubbles may not have always originated from exactly the same spot in the array as the previous bubbles. However, the bubbles always started from the OTS-coated IL drops in the arrays. The overall decomposition reaction lasted for ~12 h, until all H_2O_2 was consumed. After the H_2O_2 decomposition reaction, H_2O_2 droplet was removed and the sample was rinsed with DI- H_2O . Our optical microscope and AFM image demonstrated that OTS coating is still there without demolished (Figure 5-11).

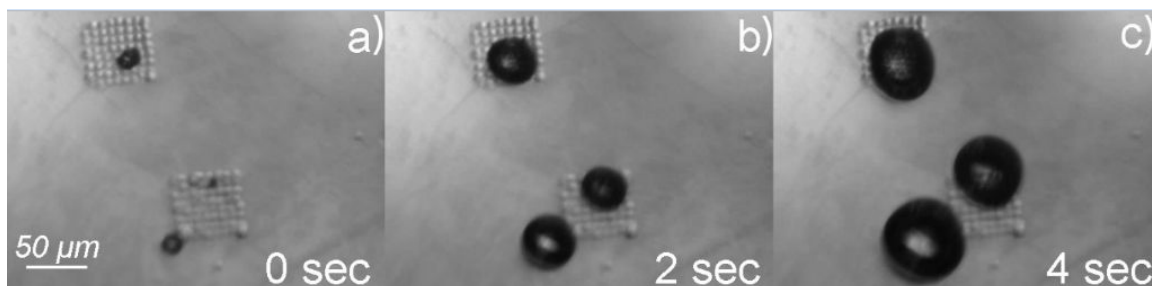


Figure 5-10 H_2O_2 decomposition reaction catalyzed by FeCl_3 . The process was recorded by the optical microscope under 30% H_2O_2 solution. The FeCl_3 [Bmim]Cl solution were assembled on two 8×8 OTSpd disc arrays. The IL drops were protected by a layer of OTS film coating. a), b), c): The same region with two OTS-coated IL arrays were immersed under 30% H_2O_2 solution and recorded at 0, 2, and 4 seconds, respectively. The observed oxygen bubbles (black spots) grew with time, indicating that the H_2O_2 decomposition reaction was proceeding.

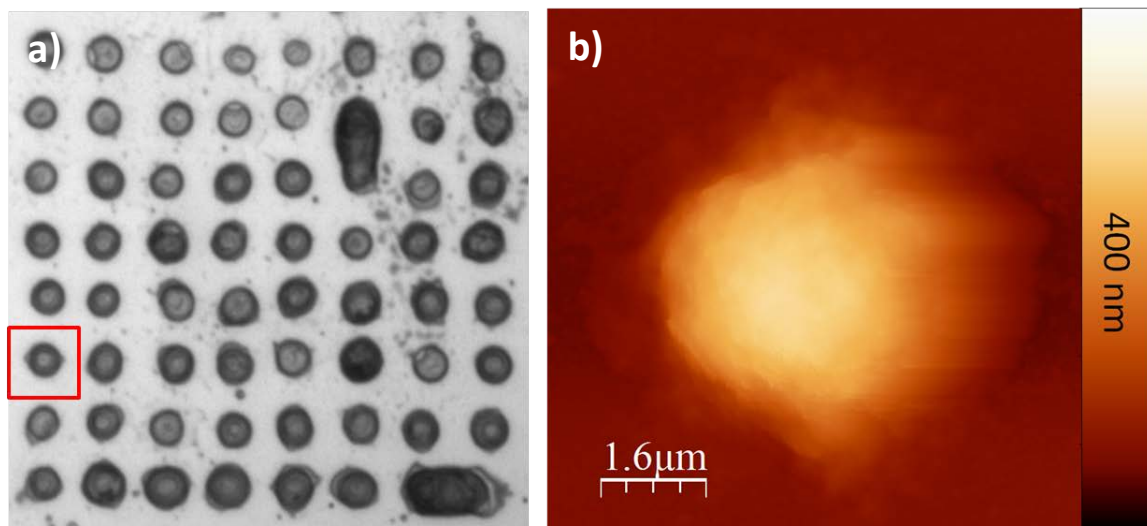


Figure 5-11 OTS-coated capsules after the H_2O_2 decomposition reaction. a) Optical image. b) AFM topographic image. The red box is the zone shown in b).

The potential leaking of IL into solution was assessed through the following experiment: as the first step, we fabricated one 8×8 OTSpd disc array on a $1 \times 1 \text{ cm}^2$ OTS sample. In total, we fabricated three such samples (sample A, sample B and sample C). Within the array, each OTSpd disc has a diameter of $3.5 \mu\text{m}$. For sample A, IL was assembled on the OTSpd discs firstly, then they were coated a layer of OTS silane in OTS vapor. After AFM characterization, AFM images were imported into the analysis software WSxM software to calculate the volume of each capsule through the flooding analysis using a manually set threshold. The manual setting of the threshold is the most efficient way of eliminating the background from the calculated volume.²⁰⁹ On average, the volume for each capsule was about $8 \mu\text{m}^3$. Then, we put one drop ($10 \mu\text{L}$) of deionized water over the 8×8 OTS-coated IL capsule array for 2 hrs. Next, we transferred the drop to sample B and let this drop cover on the 8×8 OTSpd disc array on sample B. This drop evaporated in air within 30 min. If the IL leaked out

from the capsule during the previous 2 hrs long incubation over sample A, the dissolved IL would be transferred to sample B. Since the IL would not evaporate with the water, IL would be deposited on sample B. Furthermore, because this IL ([Bmim]Cl) does not wet the OTS film, as demonstrated in Figure 5-4c, the deposited IL would be selectively concentrated on the high-energy 8 × 8 OTSpd disc array on sample B. Therefore, we can use AFM to characterize the 8 × 8 OTSpd disc array to reveal how much IL was deposited. Figure 5-12 shows a representative image of one OTSpd disc after the drop evaporated over the OTSpd disc array. From this image, we computed that the volume of the IL deposition on this OTSpd disc was 0.044 μm^3 . We used AFM to characterize all 64 OTSpd discs in the array and computed the IL deposition volume, which yielded an average IL deposition volume of 0.04 μm^3 /disc. AFM scan also revealed that no IL was deposited on the OTS surface. In the control experiment, we put one drop (10 μL) of deionized water over the 8 × 8 OTSpd array for 2 hrs on sample C. After the drop evaporated in air, we characterized the 8 × 8 OTSpd array on sample C. No deposit was found, and the OTSpd arrays did not change (Figure 5-13). Hence, we conclude that the material deposited on OTSpd disc on sample B is the leaked IL. It was concluded that after a two hours long incubation, only 0.5% (v/v) IL inside OTS-coated capsule was slowly released to water. The OTS coating led to the slow release of the IL.

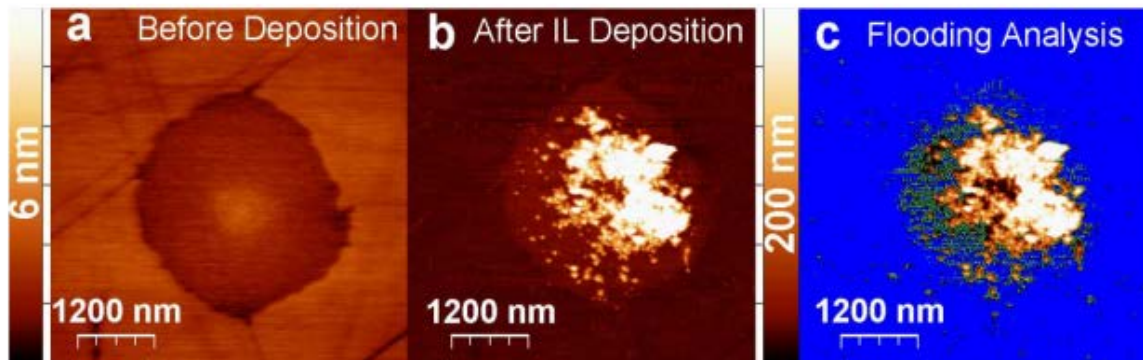


Figure 5-12 Assessment of IL leaking from the OTS-coated capsule. a) A representative clean OTSpd disc. After a 10 μL drop of water covering the OTS-coated IL capsule for two hours, this drop was transferred onto the clean OTSpd array surface (a) and let this drop to evaporate. b) After evaporation, the IL dissolve in water was deposited on this OTSpd disc. c) Flooding analysis reveals that the volume of the deposited IL is $0.04 \mu\text{m}^3$. The green line marks the positions of the IL deposits. The blue region is the flooded area.

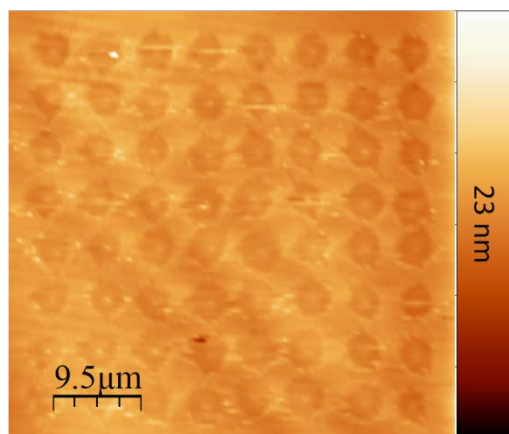


Figure 5-13 The AFM topography image of OTSpd pattern after a 10 μL drop of water covering the pattern area.

The potential leaking of Fe^{3+} from the OTS-coated IL capsule was also studied. We put one drop (30 μL) 30% H_2O_2 solution onto the surface to cover the OTS-coated FeCl_3/IL arrays to initiate the reaction. After 1 h, while the reaction was still proceeding, we used a pipette to transfer the solution onto another clean OTS-coated wafer surface. At this stage, if a large amount of Fe^{3+} was released into the bulk solution phase, the Fe^{3+} would have been transferred onto the clean

OTS-coated wafer surface as well. Then, we injected additional 30 μL 30% H_2O_2 solution into this drop. Since Fe^{3+} is the catalyst in the decomposition reaction, it will not be consumed. On the contrary, it would continue to catalyze the decomposition reaction. Nevertheless, we did not observe any oxygen bubbles generated within this drop (Figure 5-14). Figure 5-15 is an illustrated representation of this experiment. This fact suggests that the concentration of Fe^{3+} within this 60 μL drop was just too low to initiate the decomposition reaction of hydrogen peroxide. The Fe^{3+} concentration in the original 30 μL drop was just twice as high as that of in the 60 μL drop. Therefore, the Fe^{3+} concentration in the original 30 μL drop would be low as well. Our data show that the OTS coating on the IL drop surface effectively suppressed the diffusion of Fe^{3+} into the external solution.

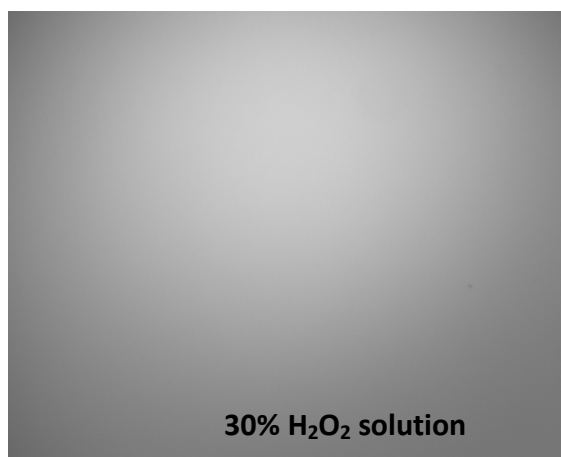


Figure 5-14 No oxygen bubble was observed inside the droplet, when two 30 μl 30% H_2O_2 solution drops were mixed together.

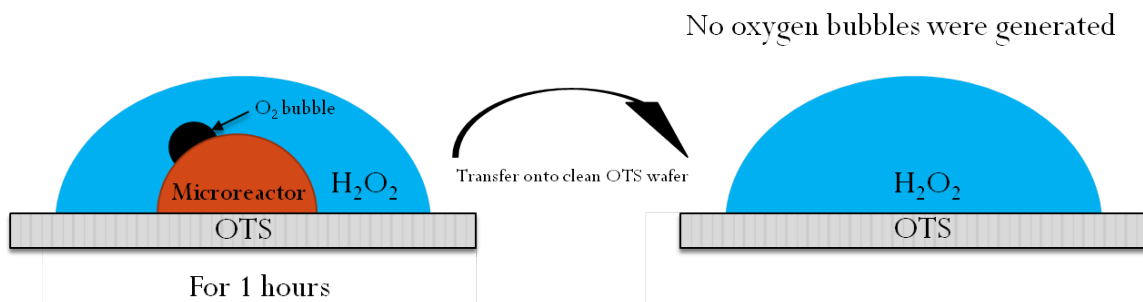


Figure 5-15 The OTS coating on the IL drop surface effectively suppressed the diffusion of Fe^{3+} into the external solution.

To prove that the decomposition reaction of hydrogen peroxide is due to the leaking of Fe^{3+} , a separated control experiment was conducted, and OTS-coated FeCl_3 -free IL drops were incubated with H_2O_2 solution. No oxygen bubbles were generated (Figure 5-16), indicating that Fe^{3+} was responsible for the decomposition of H_2O_2 . From these experimental results we conclude that the H_2O_2 decomposition reaction occurred at the IL–OTS–water interface. The reaction occurred either because the Fe^{3+} ions diffused out of or the H_2O_2 molecules diffused into the IL capsules through pinholes in the OTS film.

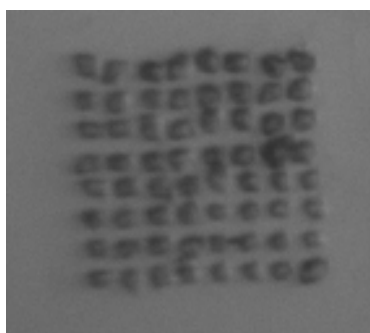


Figure 5-16 The $[\text{Bmim}]\text{Cl}$ solution was assembled on a 8×8 OTS pd disc array. The IL drops were protected by a layer of OTS film coating. No oxygen bubbles were observed.

5.3 Conclusion

We found that the carboxylic acid-terminated OTSpd chemical pattern can direct the assembly of the IL on the OTS film surface. The chemical pattern can control the position, size and shape of the IL on the surface. The IL drops assembled on the chemical patterns can be coated with a protective layer of silane which encapsulates the IL and the solute within the IL and protects the IL drops from being instantaneously dissolved by other solutions. Therefore, the coated IL drops can stably exist in other solvents that are miscible with the IL. Pinholes in the silane coating layer enable a slow material exchange between both sides of the protective silane layer.

Our experiments show that the FeCl_3 catalyst encapsulated within the IL drop can still catalyze the decomposition reaction of the hydrogen peroxide at the IL–OTS coating–water interface when the coated IL drops were immersed in hydrogen peroxide solution. Therefore, the coated IL drop may allow homogenous catalytic reactions to proceed in a heterogeneous fashion at the designated places with a controlled reaction time. This capability helps facilitate the subsequent product separation procedures.

CHAPTER 6 SURFACE PROPERTIES OF IONIC LIQUID (IL) ADSORBATE LAYER ON DIFFERENT CHEMICAL PATTERNS

6.1 Introduction

In Chapter 5, we observed IL solid-like layer through AFM characterization (Figure 5-5). Other studies also revealed the existence of IL layers at the liquid-solid interface,^{201,203,210,211} which suggest that the improvements of interface properties are related to the IL interfacial layers. For instance, it had been known by Liu et al. that IL interfacial layer can reduce the Debye ionic screen length to a few angstroms, and makes the measured capacitance nearly equal to the real quantum capacitance in surface electrochemistry.^{212,213} Certain solid-like IL interfacial layers possess ultrahigh capacitance, which can also be used as the key components in transistors^{214,215} In addition, an ultrathin dual-layer film was fabricated successfully on a silicon substrate by Wang's research group,²¹⁶ which showed the improved surface tribological properties. Of course, before these applications, we need to characterize the IL interfacial layer and understand the detailed interface structure of IL ions, including the adsorption, configuration, distribution, as well as orientation. Presently, the properties of the IL interfacial layer are not fully understood. As revealed by earlier AFM and X-ray studies, the IL layer on the solid surface has its own structure and properties, which can be understood neither through extrapolating data from liquid-phase IL nor from the structures of the underneath solid surface. Obviously, the correlations between ion structural arrangements and physical properties are only beginning to be ascertained.²¹⁷ Further developments of IL-based applications require a more thorough understanding of the IL interfacial layers.

It is known that the substrate plays a key role in determining ionic liquid interfacial structure, as it templates the first layer of ions, which then directs the second layer of ions and so on.²¹⁷ Recent experiments indicate that imidazolium family ILs has a preferential adsorption orientation, and the relative position of the anions/cations with respect to the cations/anions depends on different surface properties. For instance, the local order in thin films of 1-alkyl-3-methylimidazolium ionic liquids on Si (111) was studied by Carmichael's research group²¹⁸ via X-ray reflectivity measurement in air. The experimental results demonstrated that the layered structure adopted a multilayer stack of inter-digited amphiphilic layer with charged layers at the silicon and air interfaces. In another work, Cremer et al.²¹⁹ studied the surface properties of an ultrathin [Emim][Tf₂N] film on a glass substrate in vacuum by using X-ray photoelectron spectroscopy (XPS). They found that the [Emim]⁺ cations preferred direct contact with the glass surface, while the [Tf₂N]⁻ anions were located at the vacuum side. The structure suggested by these experiments is also consistent with the simulation studies.²²⁰⁻
²²³ Recent simulation studies pointed out that ions could form dense layers over a charged surface and the properties of the ion layers such as capacitance depend on the surface charge polarities.²²⁰⁻²²³ In particular, the density functional theory (DFT) simulation result from the Jiang group predicted that the IL could form alternating cation and anion layers on a charged surface, which hints that the IL adsorbate layer properties might be different for cation or anion layers.²²⁴

In this project, IL adsorbate layer was fabricated on chemical patterns with opposite dipoles directly via vapor phase adsorption. Then, their surface

properties were studied in four aspects using scanning probe microscopy (SPM). We used [Bmim]Cl as a model molecule in our study, because [Bmim]Cl have been widely used and thoroughly studied, and also has characteristic asymmetric L-shaped cations of imidazolium family ILs, whereas the butyl chain is not in the same plane of the imidazolium ring.^{225,226} We speculated that the dipole of the chemical pattern can direct the adsorption and assembly of the IL adsorbate. As the ions of ILs also have their distinct charges and dipoles, and the charge/dipole of the ion would interact with the dipole of a different chemical pattern. The charge–dipole and dipole–dipole interactions are directional.

6.2 Experimental

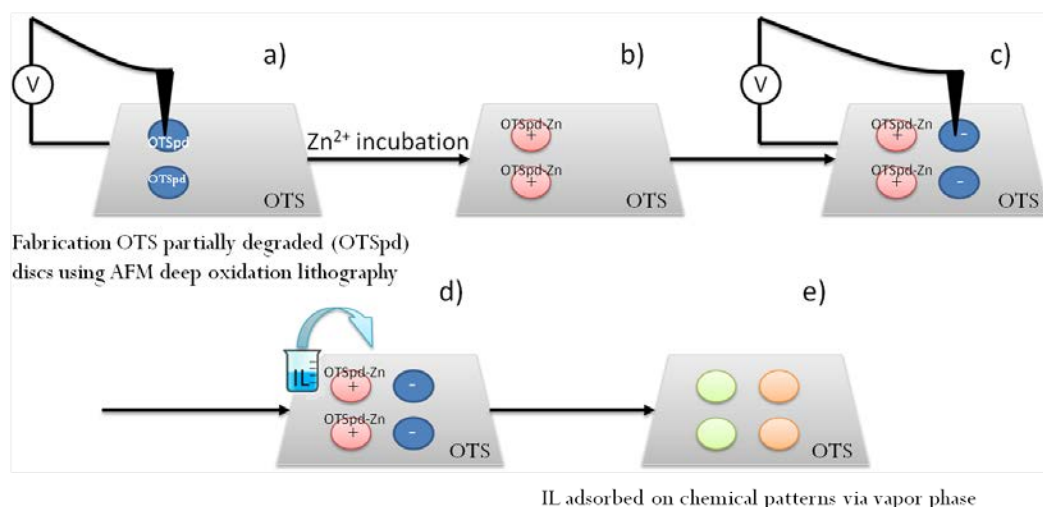
6.2.1 Instruments and chemicals

The Agilent PicoPlus 2500 environmental AFM was used for the chemical patterns creation, and AFM force curve/energy dissipation/friction measurement. The Veeco Multimode AFM was used for the surface potential characterization. Other instrumentations and chemicals are the same as described previously. All AFM images were processed and rendered using WSxM.¹¹⁷

6.2.2 Coating IL on OTSpd patterns

The procedures were shown in Scheme 6-1. After an ultra-flat, pinhole-free, featureless film was prepared, several OTSpd disc arrays were fabricated on the OTS film by the scanning probe deep oxidation lithography. The detailed experimental set-up and procedure have been described in Chapter 3. Then, the sample with OTSpd patterns was dipped into a 10 mM ZnCl₂ solution. Since Zn²⁺ is divalent, the surface charges and dipole direction were changed when Zn²⁺

ions were bound on the carboxylic acid-terminated OTSpd surface. The mechanism is similar to the process for converting a negatively charge mica surface into a positively charged surface in order to capture negatively charged DNA strands on a flat mica surface.²²⁷ After conversion of the chemical pattern to Zn-bound OTSpd, AFM deep oxidation lithography was used again to fabricate additional OTSpd discs near the OTSpd–Zn patterns. After this step, the sample with both OTSpd and OTSpd–Zn patterns was incubated in a sealed vial with 2 g of [Bmim]Cl placed on the bottom. The vial was heated to 100 °C for 10 min. After heating, [Bmim]Cl was vaporized and the space of the vial was full of the [Bmim]Cl molecules. Since the carboxylic acid-terminated OTSpd pattern and Zn-bound OTSpd patterns are a hydrophilic high-energy surface, whereas the OTS background is a methyl-terminated low energy, lyophobic surface. [Bmim]Cl molecules can be adsorbed on the chemical pattern specifically due to the contrast in surface energy.



Scheme 6-1 Preparation of different chemical patterns on the OTS surface and subsequent vapor-phase IL adsorption on the chemical patterns. (a) Fabrication OTSpd discs (blue discs) on the OTS film using AFM deep oxidation lithography. (b) Incubating the carboxylic acid-terminated OTSpd discs into a 10 mM ZnCl_2 solution and converting discs into the Zn^{2+} -bound pattern (pink discs). (c) AFM deep oxidation lithography was used again to fabricate another OTSpd disc pattern near the OTSpd-Zn disc patterns. (d) [Bmim]Cl IL was incubated together with the sample. (e) [Bmim]Cl IL vapor adsorbed on high-energy OTSpd and OTSpd-Zn discs, forming adsorbate layers on these two chemical patterns. Nevertheless, the adsorbate layer on OTSpd (green discs) and adsorbate layer on OTSpd-Zn (orange discs) are different.

6.2.3. Characterization of IL adsorbed layer on chemical patterns

The IL-coated chemical patterns were characterized by Kelvin Probe Force Microscopy (KPFM) and force-distance spectroscopy to compare the surface properties of the same OTSpd and OTSpd-Zn discs before (Scheme 6-1c) and after (Scheme 6-1e) these patterns were incubated in IL vapor. Both AFM topography characterization (Figure 6-1) and force-distance spectroscopy reveal that IL vapor did not adsorb on the low-energy OTS surface. Thus, we used the surface properties of OTS as internal references for comparison of the surface

properties of different chemical patterns before and after vapor incubation. The results are summarized in Table 6-1.

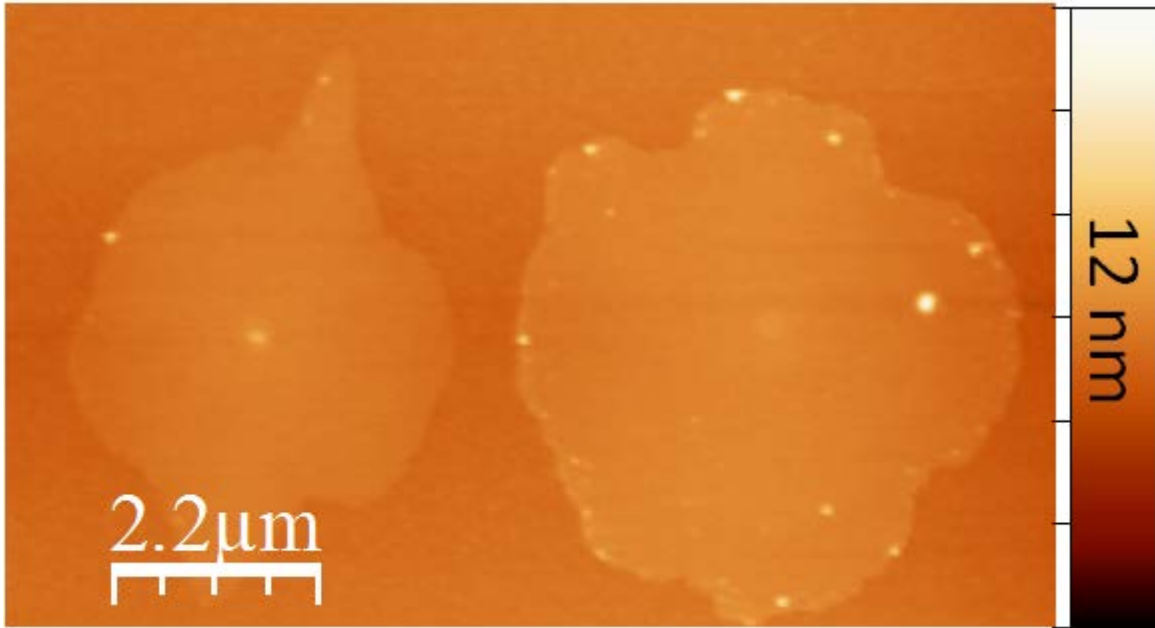


Figure 6-1 AFM topography image of OTSpd-IL disc (left) and OTSpd-Zn-IL disc (right) on OTS film background.

Table 6-1 The surface properties of OTSpd and OTSpd-Zn patterns before and after the IL vapor adsorption.

	OTS	Before Vapor Adsorption		After Vapor Adsorption	
		OTSpd	OTSpd-Zn	OTSpd-IL	OTSpd-Zn-IL
Surface potential (mV, with respect to OTS)		-53±14	62±8	7±11	167±16
Lennar-Jones Potential (1×10⁻¹⁸ J)	37.3±3.5	18.7±1.0	10.3±0.9	7.7±0.5	5.8±0.9
N	80	60	80	80	70

KPFM maps the surface potential distribution over the surface. The surface potential is a direct indicator of the surface dipole.²²⁸ Figure 6-2 reveals that the surface potential of clean OTSpd and OTSpd-Zn patterns changed after they were incubated in IL vapor. The clean OTSpd and OTSpd-Zn pattern have a surface potential of -53 ± 14 and 62 ± 8 mV with respect to the background OTS film, respectively. After incubation in IL's vapor, the surface potential over the same OTSpd and OTSpd-Zn patterns changed to 7 ± 11 and 167 ± 16 mV with respect to OTS background, respectively. The change in surface potential reveals that additional material adsorbed on the clean chemical patterns. A control experiment was conducted in order to investigate other potential factors that could lead to the change in surface potential for the same experimental procedures. The clean OTSpd and OTSpd-Zn patterns were incubated in the sealed vial under the same condition without the presence of IL. Subsequent KPFM characterization revealed that the surface potential did not change. Therefore, the observed surface potential change was due to the IL's vapor adsorption on the high-energy chemical patterns.

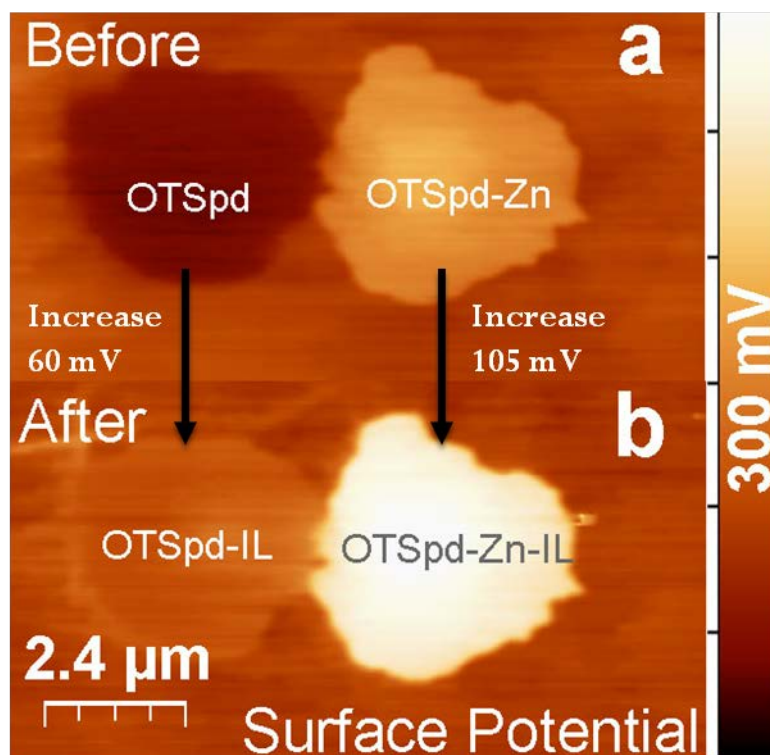


Figure 6-2 Surface potentials of the same clean OTSpd and OTSpd–Zn patterns before and after incubation in IL vapor. (a) Surface potentials of clean OTSpd and OTSpd–Zn pattern. (b) Surface potentials of the same patterns after incubation in IL vapor. Background is the OTS film. Two KPFM images are rendered in the same surface potential scale.

As a complementary method, we acquired AFM force–distance spectra over the OTSpd and OTSpd–Zn patterns before and after IL vapor incubation using a well-calibrated MikroMasch CSC17 SiO₂ tip (4.7 nm in radius with a spring constant of 0.182 N/m). The spring constant of the AFM tips was measured using Sader’s method,^{102,229} which was discussed in Chapter 2. Our AFM cantilever has an 8° tilting angle. The sample’s tilting angle was carefully adjusted to match the tiling of the cantilever in order to ensure that the applied loading force is perpendicular to the sample. Before measurement, pure nitrogen was used to purge the AFM chamber at 50 mL/s for 1 hour, and subsequent amplitude-phase-

distance (APD) curve ensured that no water film existed on the sample surface, which will be discussed later in this chapter. All measurements were conducted under a nitrogen environment.

From the force–distance spectra we calculated the Lennard–Jones (L-J) potential between the tip and the surface by integrating the attractive van der Waals force over the tip’s displacement. The Lennard-Jones potential is a mathematical approximation that illustrates the energy of interaction between two nonbonding atoms or molecules based on the distance of their separation.²³⁰ Here, a hemisphere-plane L-J potential is used to model the tip–surface interactions. During our measurement over different surfaces we always used the same tip. Therefore, the Lennard–Jones potentials obtained from the AFM force–distance curves correspond to the substrate surface property. A representative force–distance curve on the OTSpd–Zn disk after IL vapor incubation (denoted as OTSpd–Zn–IL) is plotted in Figure 6-3. The purple-shaded area corresponds to the Lennard–Jones potential when the two surfaces touched with no force acted on the cantilever. Under our experimental condition, the AFM tip and surface interaction can be modeled as a hemispherical surface approaching a flat surface. Then the Lennard–Jones potential can be expressed according to formula 1,²³¹⁻

233

$$V = \int_{\infty}^{D_0} F dD \quad (1)$$

$$F = -\frac{HR}{6D^2} \quad \text{and} \quad H = \pi^2 C \rho_1 \rho_2$$

where F is van der Waals force, R is the radius of the tip, D_0 is the tip-surface distance at which there's no interaction between tip and surface, D is the tip-surface distance, H is the Hamake constant, ρ_1 and ρ_2 are the number of atoms per unit volume in the two bodies, and C is the coefficient in the atom-atom pair potential. Since we always use the same tip during the measurement, the value of the Lennard-Jones potentials, which obtained from the AFM force-distance curve, could reflect the surface property of the substrate.

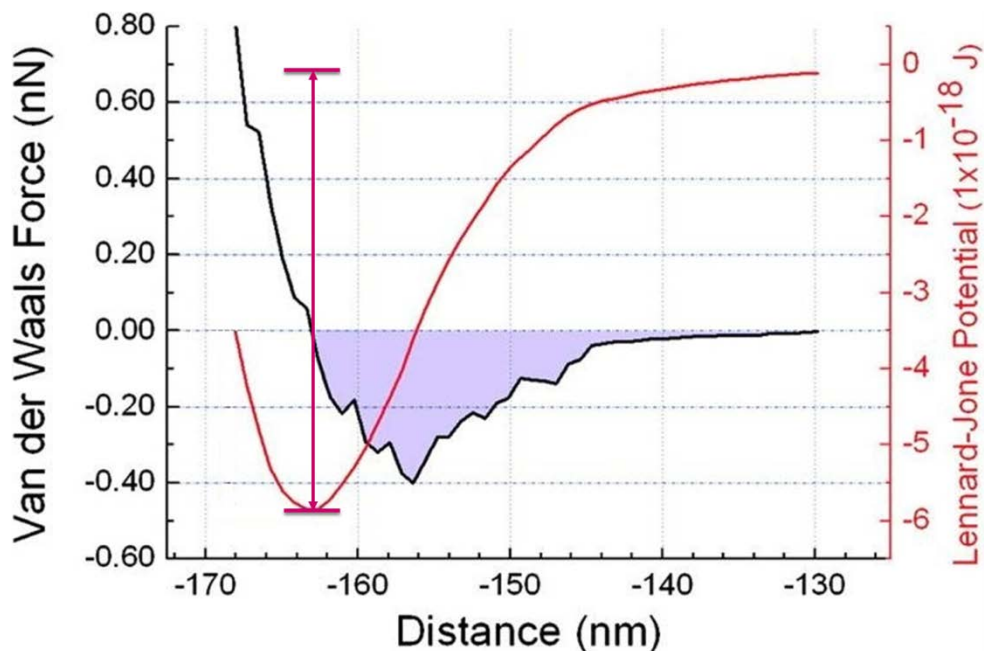


Figure 6-3 Representative AFM force v.s. distance curve for the OTSpd-Zn-IL surface. Force-distance curve (black line) was acquired when the tip was approaching the substrate surface. Lennard-Jones potential curve (red line) was calculated from the AFM force v.s. distance curve. Calculated Lennard-Jones potential listed in Table 1 corresponds to the area of the blue-shaded region on the force curve or the depth of the well on the red curve. Data were obtained using a calibrated MikroMasch CSC17 tip, which has a SiO_2 surface and a radius of 4.7 nm.

As Table 6-1 shows, the Lennard-Jones potential for the tip-OTS surface was $(37.5 \pm 3.5) \times 10^{-18}$ J, which did not change before and after the IL vapor

incubation. On clean OTSpd and OTSpd–Zn chemical patterns the Lennard–Jones potentials were $(18.7 \pm 1.0) \times 10^{-18}$ and $(10.3 \pm 0.9) \times 10^{-18}$ J, respectively. After the patterns were incubated in IL vapor, the Lennard–Jones potentials over OTSpd and OTSpd–Zn chemical patterns changed to $(7.7 \pm 0.5) \times 10^{-18}$ and $(5.8 \pm 0.9) \times 10^{-18}$ J, respectively. In contrast, a control experiment shows that the Lennard–Jones potential over the OTSpd patterns did not change after incubating the sample in the sealed vial without IL vapor. On the basis of the Lennard–Jones potential data, we conclude that IL adsorbed on the OTSpd and OTSpd–Zn chemical patterns, which is in agreement with the conclusion from AFM surface potential characterization.

In summary, our results reveal that the vapor of the IL can adsorb on chemical patterns with high surface energy and form an adsorbate layer with distinct surface properties. Because of its very low vapor pressure, the role of IL's vapor has been generally ignored during the studies of IL and solid interface interactions. Nevertheless, the vapor of ILs has its role in certain applications. For example, certain imidazolium ILs can be distilled, which makes recycling and purifying these IL possible.²³⁴ Our results indicate that for some popular ILs (such as imidazolium family ILs), vapor can adsorb on charged surfaces and form a stable layer. Since vapor always coexists with liquid, and ions in the vapor travel faster than liquid's diffusion and spreading, the stable adsorbate layer originated from the vapor would exist preceding any direct liquid–solid interaction. As a result, the liquid–solid interface properties such as wetting, spreading, and

charge density would be influenced by the structure and properties of this interfacial layer.

6.2.4 Surface properties of IL adsorbate layers depend on the surface dipole of the underneath chemical pattern

As table 6-1 demonstrates, the surface potential of clean OTSpd and OTSpd-Zn patterns are quite different. Since the surface potential signals are obtained by using the same long and sharp Ag_2Ga needle attached at the end of the pyramid shaped probe under the same condition, the difference in surface potential indicates that they have different surface dipoles.²²⁸ Because ions of ILs also have their distinct charges and dipoles, the charge-dipole and dipole-dipole interactions might induce different adsorption orientations of IL ions on the different chemical patterns with distinct charges and dipoles.

In our experiment, the IL layers were adsorbed on OTSpd and OTSpd-Zn chemical pattern as Scheme 6-1 illustrates. Then the surface properties of OTSpd-IL and OTSpd-Zn-IL were measured in the following three aspects: surface potential, Lennard-Jones potential, and tribological behavior. Our experimental data demonstrate that the surface properties of OTSpd-IL and OTSpd-Zn-IL are different in those three aspects.

6.2.4.1 Difference in surface potential

Because the surface of OTS (methyl-group-terminated) is stable, well ordered, and has the same roughness and packing density, it can be used as an internal reference during the measurement. As Figure 6-2 and Table 6-1 show, the surface potentials over OTSpd-IL and OTSpd-Zn-IL adsorbate layers are 7 ± 11

and 167 ± 16 mV, respectively. In contrast, before IL adsorbate layer formed, the clean OTSpd and OTSpd–Zn patterns have surface potentials of -53 ± 14 and 62 ± 8 mV, respectively. Hence, formation of the IL adsorbate layer caused a 60 mV increase over the OTSpd pattern and a 105 mV increase over the OTSpd–Zn pattern. The difference in the surface potential increase indicates that the IL adsorbate layers over the OTSpd surface and OTSpd–Zn surface are distinct. They have different dipoles.

6.2.4.2 Difference in Lennard-Jones potential

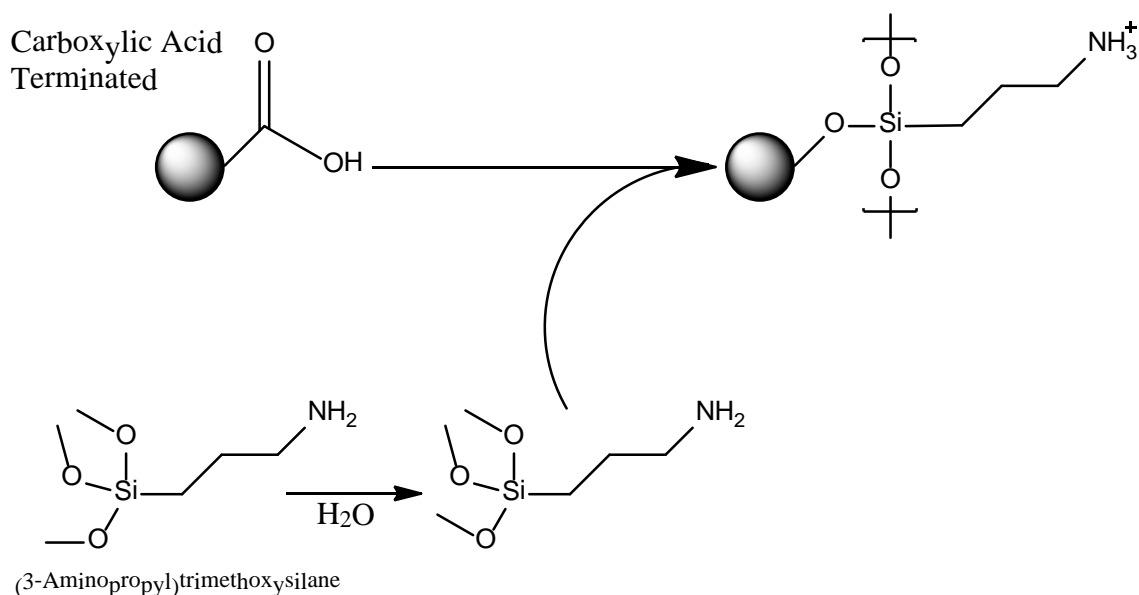
On the basis of the formula of Lennard-Jones potential, it is a function of the contact area (tip radius R in our case), tip-surface distance (D), and Hamaker constant (H), which is determined by the surface properties of the substrate surface and the tip surface. Since we used the same tip, both R and D should be the same during the force curve measurements. The Lennard–Jones potential difference for OTSpd–IL ($(7.7 \pm 0.5) \times 10^{-18}$ J) and OTSpd–Zn–IL ($(5.8 \pm 0.9) \times 10^{-18}$ J) surfaces reflects that these two surfaces have different Hamaker constants and the different Hamaker constants indicate that the OTSpd–IL and OTSpd–Zn–IL surface are different.

We also investigated the Lennard-Jones potential of the IL adsorbate layer on an amine-terminated surface by using the same experimental set-up under the same condition. Here, (3-Aminopropyl)trimethoxysilane (APTMS) molecules were immobilized on the OTSpd pattern by incubating OTSpd surface into 10 mM APTMS toluene solution for 30 mins. In this step, APTMS molecules reacted with the trace amount of H_2O in the solution, forming silanols first. Then, they were

cross-linked and selectively anchored on the hydrophilic OTSpd surface (Scheme 6-2). After that, the sample was wiped by Chemwipe paper to remove those nonspecific adsorbed APTMS molecules and left an amine group exposed surface on the OTSpd pattern. Since the pKa of alkyl-aminium group is about 10.6, under neutral conditions (the pH of pure water is 7), amino groups of APTMS were protonated, and the modified surface was positively charged.²³⁵ Next, the sample with OTSpd-APTMS patterns were incubated in [Bmim]Cl vapor using the same procedure for the OTSpd-IL or OTSpd-Zn-IL preparation. The amine-terminated surface was chosen because we wanted to investigate the impact of different surface but with the same surface charge property on the interfacial properties of the IL adsorbate layer. By comparing the Lennard-Jones potential of the [Bmim]Cl adsorbate layer on the APTMS surface (Table 6-2) with that on the OTSpd-Zn surface, we found our conclusion holds for OTSpd-APTMS surface as well. First, IL vapor can adsorb on OTSpd-APTMS positively charged surface and form a stable layer; Second, the Hamaker constants for OTSpd-IL and OTSpd-APTMS-IL surfaces are different, indicating that the OTSpd-IL and OTSpd-APTMS-IL surface are different. Additionally, by comparing the Lennard-Jones potential of OTSpd-APTMS-IL with that of OTSpd-Zn-IL, we found that OTSpd-APTMS-IL and OTSpd-Zn-IL surfaces are different as well, which indicates that the adsorption orientations or adsorption density of IL ions on the different chemical patterns with distinct charges and dipoles might also be distinct.

Table 6-2 The surface properties of OTSpd-APTMS patterns before and after the IL vapor adsorption.

	OTSpd-APTMS	OTSpd-APTMS-IL
Surface potential (mV, with respect to OTS)	63±6	180±10
Lennard-Jones potential (1×10^{-18} J)	9.184±0.559	11.576±0.315
N	60	60



Scheme 6-2 Carboxylic acid terminated surface plus (3-Aminopropyl)trimethoxysilane (APTMS) cross linking reaction scheme.

6.2.4.3 Difference in tribological properties

We measured the friction of the OTSpd-IL and OTSpd-Zn-IL as a function of the loading force via a well-calibrated OTS-coated tip. OTS-coated tip was used here since it is demonstrated that the magnitude of the adhesive force at the OTS-coated tip-sample interface (hydrophobic) reduced significantly during the friction measurement.²³⁶ From our results (Figure 6-4), the linear fitting of the friction vs. loading curve yields that coefficient of friction (COF) for OTS is 0.066 ± 0.003 ,

which is similar to published results.²³⁷ The black line and red line in Figure 6-4 show the friction responses of OTSpd-IL and OTSpd-Zn-IL surfaces, respectively. The friction v.s. loading curves for these two surfaces have a similar shape, but they are not identical. The linear fitting yields that the COF for OTSpd-Zn-IL and OTSpd-IL is 0.185 ± 0.005 and 0.231 ± 0.019 , respectively. When the loading force is small, the friction on the OTSpd-Zn-IL surface is smaller than the OTSpd-IL surface. However, when the loading force increased above 6nN, the friction v.s. loading curves for these two surfaces gradually became the same, which yields a COF of 0.185 ± 0.005 .

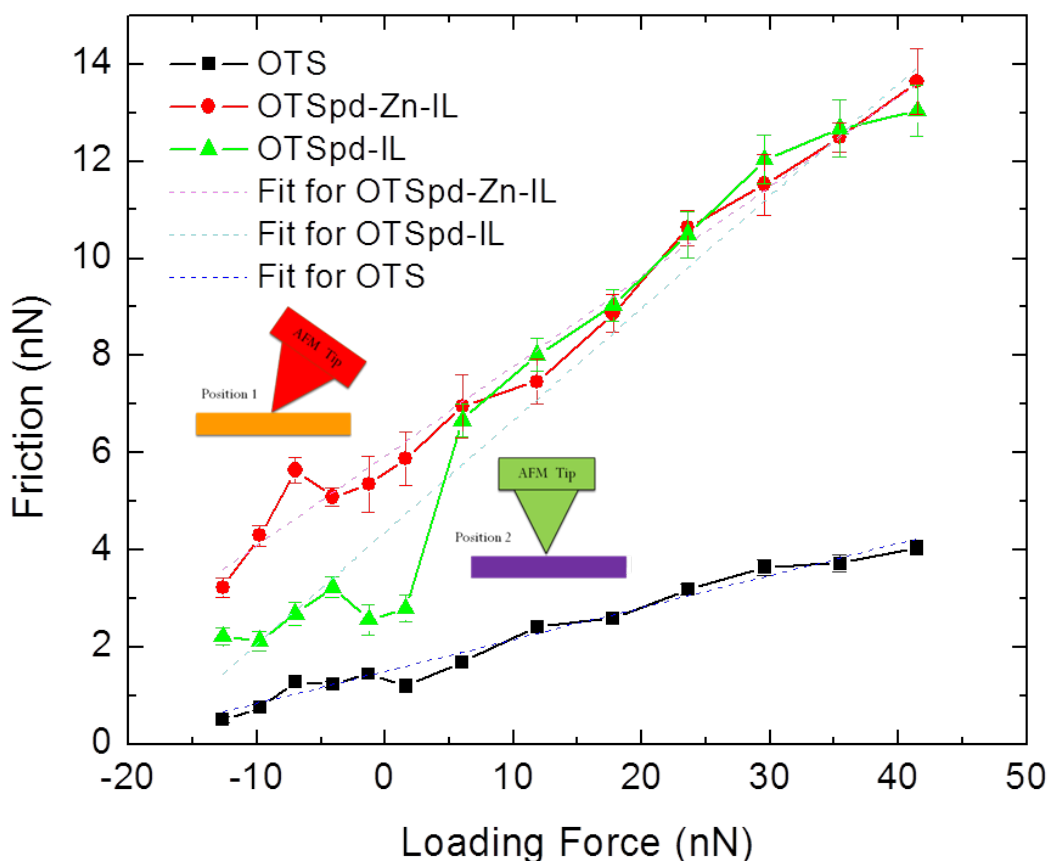


Figure 6-4 The friction v.s. loading curves for OTS surface (black), OTSpd-IL surface (green) and OTSpd-Zn-IL surface (red). These data are measured using an OTS-coated SiO₂ tip. The dash lines are the linear fitting of the loading curves.

In summary, the vapor of IL ([Bmim]Cl) can adsorb on high energy chemical patterns and form distinctive layers. Three independent experiments all confirmed that the surface properties of interfacial IL layers are determined by the surface dipole of the underneath chemical patterns.

We have also investigated the surface potentials of two additional ILs (1-butyl-3-methylimidazolium bis(trifluoromethylsulfonyl) imide, [Bmim][Tf₂N] and 1-decyl-3-methylimidazolium chloride, [C₁₀mim]Cl) by using the same KPFM experimental set-up. These two ILs were selected because we wanted to examine how the interfacial property varies with the anion and cation. By comparing the surface potentials of the [Bmim]Cl adsorbate layer with that of [Bmim][Tf₂N], we reveal the impact of the anion. Similarly, the surface potential difference between [Bmim]Cl and [C₁₀mim]Cl adsorbate layers revealed the impact of cation. Our KPFM characterization results (Figure 6-5 and 6-6 and Table 6-3) from these additional studies reveal that the surface potential for the ILs adsorbate layers on the OTSpd pattern was not the same as the adsorbate layer on the OTSpd-Zn pattern. The conclusion that the chemical patterns with different surface dipoles lead to different surface potentials of IL adsorbate layer holds for [Bmim]Cl, [Bmim][Tf₂N], as well as [C₁₀mim]Cl.

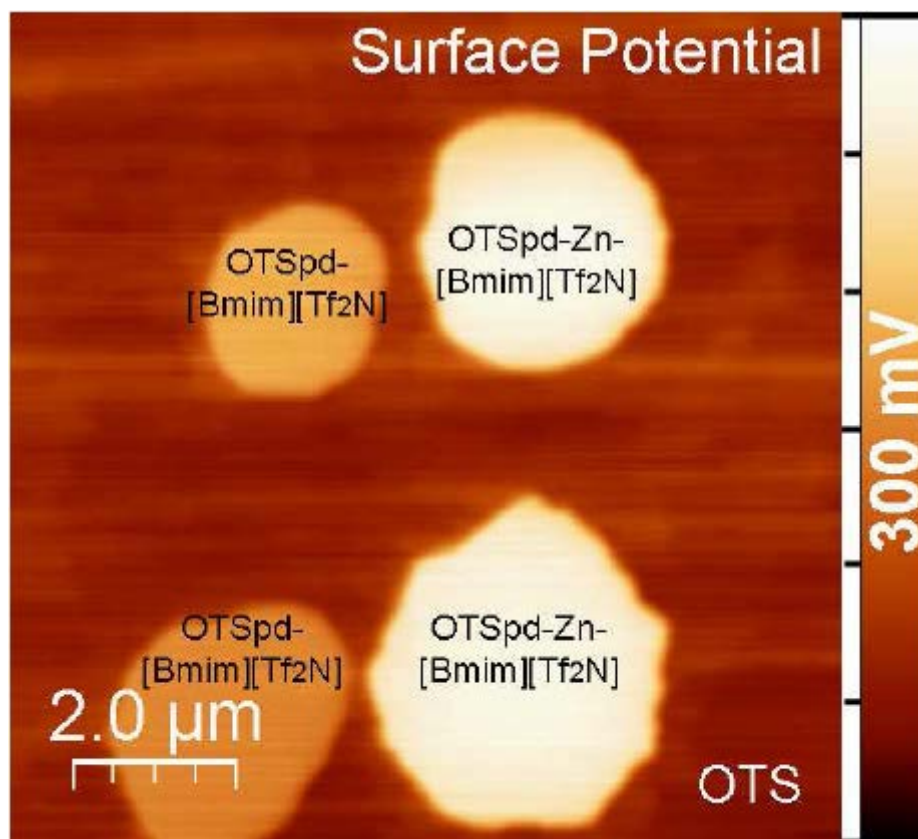


Figure 6-5 The surface potential image of adsorbate layer of 1-butyl-3-methylimidazolium bis(trifluoromethylsulfonyl) imide ([Bmim][Tf₂N]) on OTSpd (left two discs) and on OTSpd-Zn (right two discs) chemical patterns. The images were obtained using the same condition as the Figure 6-2.

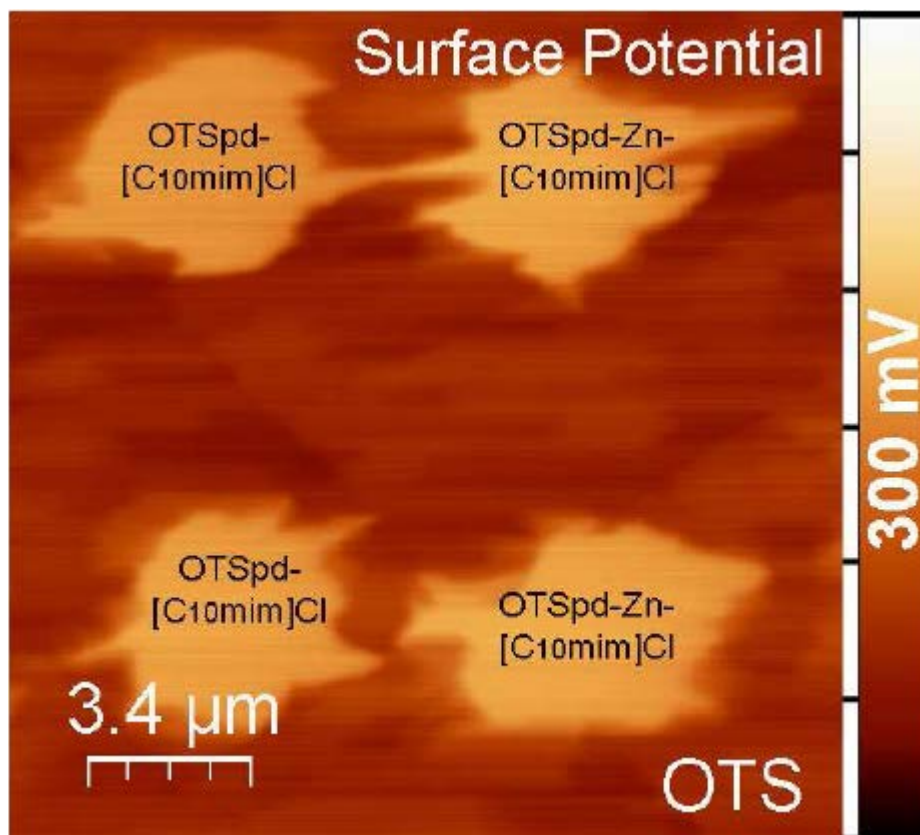


Figure 6-6 The surface potential image of adsorbate layer of 1-decyl-3-methylimidazolium chloride ($[C_{10}mim]Cl$) on OTSpd (left two discs) and on OTSpd-Zn (right two discs) chemical patterns. The images were obtained using the same condition as the Figure 6-2.

The surface potential of the $[Bmim]Cl$ adsorbate layer on APTMS was also investigated with the same KPFM experimental scheme. By comparing the surface potential of the $[Bmim]Cl$ adsorbate layer on APTMS pattern with that on Zn^{2+} pattern we reveal the impact of the surface dipole of the chemical pattern on the IL adsorbate layer. As Figure 6-7 demonstrated, the KPFM characterization shows that the surface potential for the IL adsorbate layer on positively charged APTMS (180 ± 10 mV) was not the same as the adsorbate layer on the OTSpd-Zn pattern (167 ± 16 mV). This result confirms that the surface properties of the IL adsorbate layer depend on the dipole of the underneath chemical patterns.

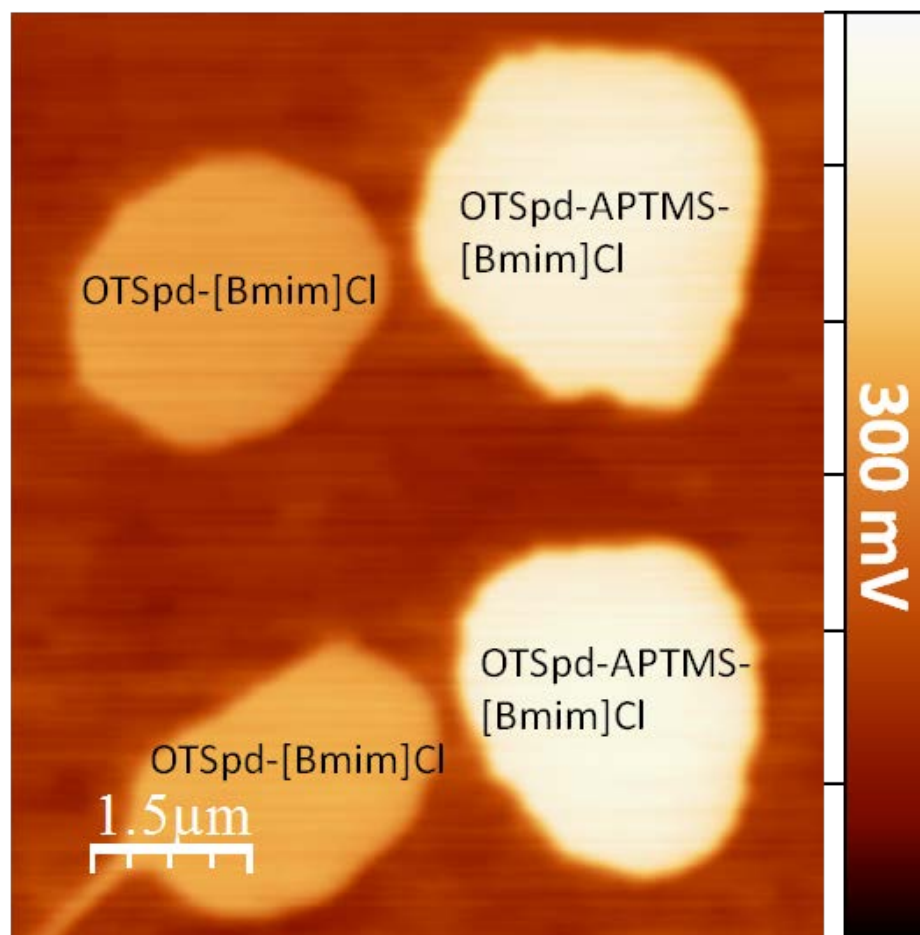


Figure 6-7 The surface potential image of adsorbate layer of 1-butyl-3-methylimidazolium chloride ([Bmim]Cl) on OTSpd (left two discs) and on OTSpd-APTMS (right two discs) chemical patterns. The images were obtained using the same condition as the Figure 6-2.

Table 6-3 The surface potentials of OTSpd, OTSpd-Zn and OTSpd-APTMS patterns before and after the IL vapor adsorption. The surface potentials of the IL surfaces were calculated through the corresponding histograms of Figure 6-5, 6-6 and 6-7. After subtracting the surface potentials of the clean OTSpd, OTSpd-Zn and OTSpd-APTMS backgrounds, the surface potentials of individual IL adsorbate layers were obtained. The data show that the surface potentials of [Bmim][Tf₂N] adsorbate layer on OTSpd and OTSpd-Zn surfaces are different. Similarly, the surface potentials of [C₁₀mim]Cl adsorbate layer on OTSpd and OTSpd-Zn surfaces are not the same as well. Additionally, the surface potentials of [Bmim]Cl adsorbate layer on OTSpd-APTMS and OTSpd-Zn surfaces are different.

	Surface	Surface Potential with respect to OTS (mV)	Surface Potential of IL Adsorbate Layer (mV)
Clean Background Before IL Adsorption	OTSpd	-53±14	-
	OTSpd-Zn	62±8	-
	OTSpd-APTMS	63±6	-
After [Bmim]Cl Adsorption	OTSpd-[Bmim]Cl	7±11	60±18
	OTSpd-APTMS-[Bmim]Cl	180±10	117±12
After [Bmim][Tf ₂ N] Adsorption	OTSpd-[Bmim][Tf ₂ N]	116±14	169±20
	OTSpd-Zn-[Bmim][Tf ₂ N]	194±25	132±26
After [C ₁₀ mim]Cl Adsorption	OTSpd-[C ₁₀ mim]Cl	98±24	151±28
	OTSpd-Zn-[C ₁₀ mim]Cl	108±23	46±24

6.3 Discussion

The tip's energy dissipation over IL adsorbate layers on different chemical patterns was investigated quantitatively by recording the amplitude-phase-distance (APD) curves (Figure 6-8), where the amplitude and phase of the oscillating cantilever are measured while the distance between tip and sample is

continuously reduced or increased.²³⁸⁻²⁴¹ From this curve, the cantilever can be viewed as a simple harmonic oscillator when there is a large separation between tip and substrate. As the tip-sample distance is reduced, the interaction of tip with the substrate leads an almost linear reduction of the amplitude.^{242,243} However, if there is a thin film of water covering both tip and sample, a capillary neck can be formed between tip and sample when the AFM cantilever comes close to the sample surface.²⁴⁴ A jump to a higher amplitude can be observed due to the hysteresis caused by the water meniscus formation and break based on Zitzler's results.²⁴³ Because of this, APD curves can also be used for checking the existence of the water film on the sample surface.

Before the experiment, both cantilevers and samples were mounted to the AFM and allowed to equilibrate for half hour. The experiments were carried out at the resonance frequency of the free cantilever.²⁴³ Each APD curve was recorded by gradually reducing the distance between tip and sample, until that the measured oscillation amplitude A was reduced to 10% of the free amplitude A_0 . Figure 6-8 shows two typical experimental APD curves for a Si tip on a hydrophobic OTS surface. The data presented in Figure 6-8 do not show any signature (jump) that can be attributed to the presence of an adsorbed water film, which indicates no water film existed in the N_2 -filled environmental chamber.

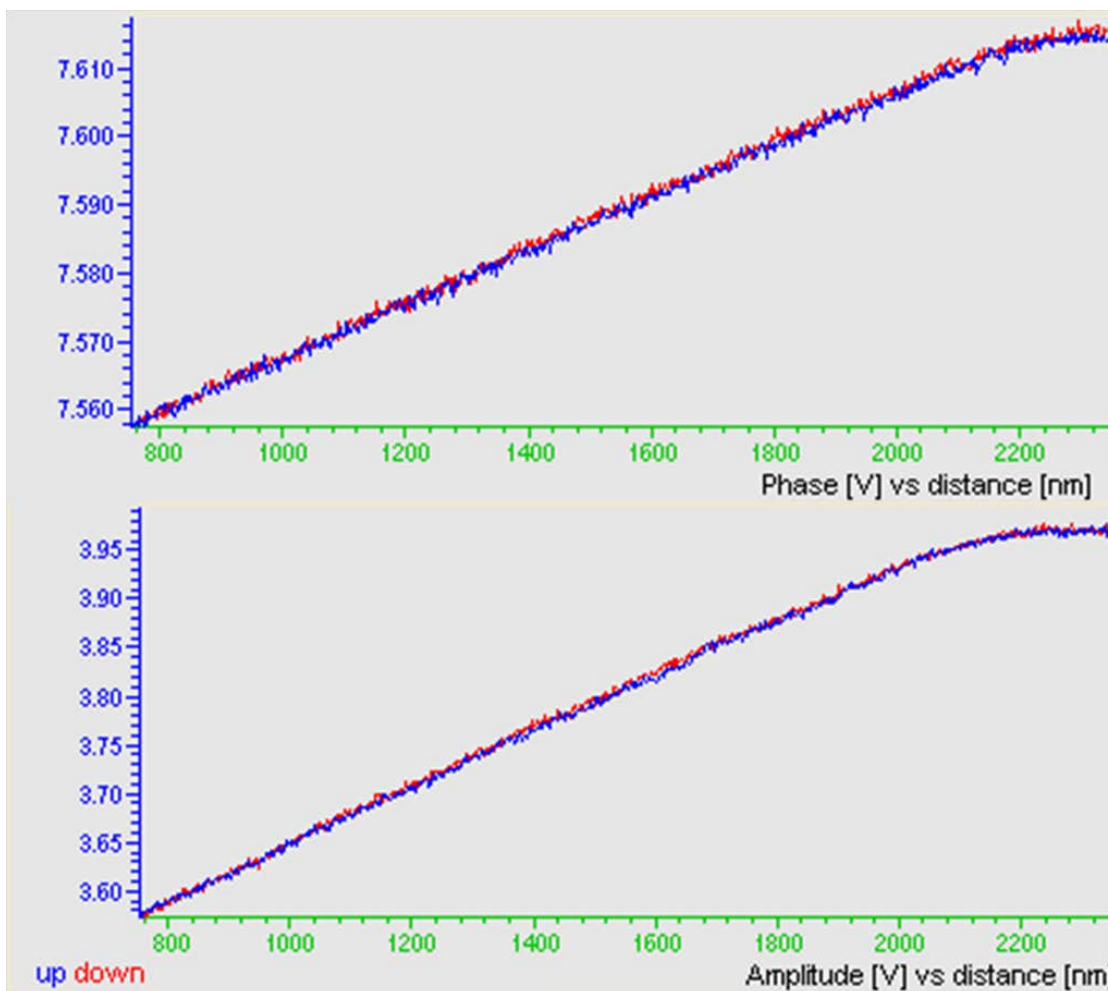


Figure 6-8 Amplitude-phase-distance curves with AFM probe and OTS coated Si wafer.

To calculate the tip's energy dissipation over surfaces, we also need to ascertain the mechanical properties and geometry of the tip. The MikroMasch NSC14 tip we used has a spring constant of 15.5 N/m, natural frequency of 177.20 kHz, and quality factor of 276. The tip radius is 3.7 nm, which is obtained through scanning the tip over the monatomic step edge of a piece of a graphene sheet. With the tip's mechanical parameters in hand, the tip's energy dissipation can be calculated in one tapping cycle over the OTSpd and OTSpd-Zn surfaces before and after IL ([Bmim]Cl) adsorption through the following equation²⁴⁵

$$E = \frac{k_z \pi A^2}{Q} \left(\frac{A_0}{A} \sin \varphi - 1 \right) \quad (3)$$

, where k_z is the tip's spring constant, Q is the tip's quality factor, A_0 is the tip's free oscillation amplitude, A is the actual set oscillation amplitude, and φ is the phase shift angle. The tapping intensity is defined as

$$I \equiv A_0 - A \quad (4)$$

The energy dissipation as function of tapping intensity of clean OTS surface, clean OTSpd, clean OTSpd-Zn, OTSpd-IL, and OTSpd-Zn-IL is plotted in Figure 6-9.

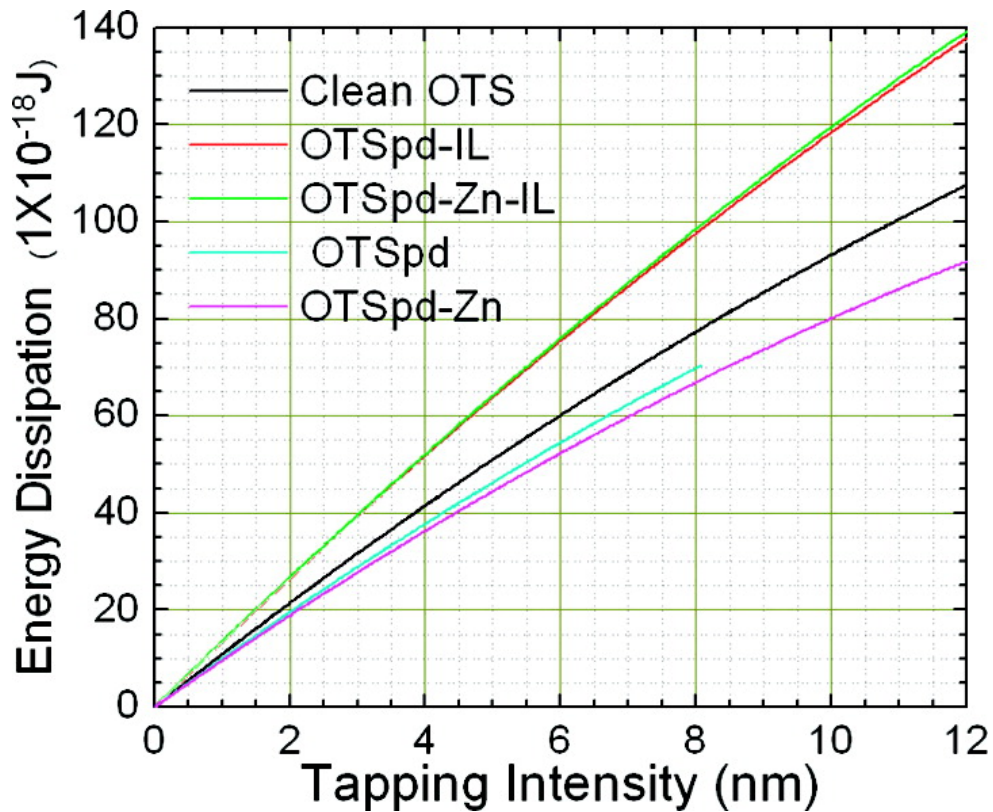


Figure 6-9 Energy dissipation of a NSC14 tip during one cycle of tapping over different surfaces. Tapping intensity is defined as the difference between the tip's free oscillation amplitude in air and the actual tapping amplitude on the surface.

During one tapping cycle, the tip is subjected to three types of forces²⁴³:

$$F_{tip}(z) = F_{vdW}(z) + F_{elastic+inelastic}(z) + F_{cap}(z) \quad (4)$$

where $F_{vdW}(z)$ is the van der Waals force, $F_{elastic+inelastic}(z)$ is the repulsive elastic and inelastic forces acted on the tip, which are from the deformation of the surface, and F_{cap} is the capillary force from the water meniscus between the tip and surface. Then, the energy dissipation of the tip during one cycle of tapping can be calculated by

$$E = \int_A^0 F_{vdW}(z)dz + \int_0^A F_{vdW}(z)dz + \int_A^0 F_{elastic+inelastic}(z)dz + \int_0^A F_{cap}(z)dz \quad (5)$$

where A is the amplitude of the tip's oscillation. Because the van der Waals force is a conservative force, we have $\int_A^0 F_{vdW}(z)dz = -\int_0^A F_{vdW}(z)dz$. Before ac mode imaging, N_2 gas was purged into AFM chamber for 1 hour to remove the moisture, so that the relative humidity inside the chamber approached to 0%. This ensured that no water film existed on the hydrophobic OTS surface and no capillary condensation occurred. Because $\int_0^A F_{cap}(z)dz = 0$, the term E could be finally expressed as:

$$E = \oint F_{tip}(z)dz = \int_A^0 F_{elastic+inelastic}(z)dz \quad (5)$$

Here, E becomes repulsive energy, in which the tip dissipates energy to the surface, causing the molecules on the surface to have elastic change and inelastic permanent structural deformation under our experimental condition. As Figure 6-9 demonstrates, the tip always consumed more energy on the OTSpd surface than on the OTSpd-Zn surface during the compression of the IL adsorbates. Hence, the OTSpd-Zn surface is stiffer than the OTSpd surface. In

contrast, when IL layers adsorbed on these two chemical patterns, the tip consumed more energy on the OTSpd-Zn-IL layer than on OTSpd-IL layer at the same tapping intensity. Thus, as a composite surface, the OTSpd-IL is stiffer than the OTSpd-Zn-IL layer. By cumulative consideration, we conclude that the IL adsorbate layer on the OTSpd surface is stiffer than the IL layer adsorbed on the OTSpd-Zn surface. Since Young's modulus is a measure of the stiffness of an elastic material and is a quantity used to characterize materials,²⁴⁶ we can also conclude that the IL layer adsorbed on OTSpd has a higher Young's modulus than the IL layer adsorbed on OTSpd-Zn. For the same tapping intensity, the IL adsorbate layer on OTSpd deformed less than the IL adsorbate layer on OTSpd-Zn. The tip dissipated more energy to compress the IL layer adsorbed on OTSpd-Zn than the IL layer on OTSpd-IL layer.

This conclusion from the phase analysis can explain the observed tribological difference for OTSpd-IL and OTSpd-Zn-IL as well. As Figure 6-3 shows, below 6 nN loading force, the OTSpd-Zn-IL surface has a lower friction than the OTSpd-IL surface. Above 6 nN loading force, the two curves become almost identical. Such difference can be understood through the difference in contact area for these two surfaces under the same loading force. The tip's contact area A on the surface can be estimated using the Hertzian model²⁴⁷

$$A^{3/2} = \frac{3}{4} \left(\frac{1 - \nu_1^2}{E_1} + \frac{1 - \nu_2^2}{E_2} \right) \pi^{3/2} RL$$

where the R is the tip radius, L is the loading force, E_1 and E_2 are the Young's moduli of the tip and the IL layer, and ν_1 and ν_2 are the Poisson numbers of the

tip and IL layer, respectively. Since the IL layer on OTSpd-Zn has a lower young's modulus than the IL layer on OTSpd surface, the tip's contact area on OTSpd-Zn-IL surface would be larger than that on the OTSpd-IL surface. Large tip-surface contact area yields stronger van der Waals force, which corresponds to a larger friction when the tip moves across the surface.²⁴⁸ Therefore, due to different stiffness, under the same loading force, the friction force acted upon the AFM tip would be larger for on the softer OTSpd-Zn-IL surface. We speculate that when the tip's loading force is higher than 6 nN, the IL ions adsorbed on OTSpd patterns underwent a conformational change, adopting the same conformation as the adsorbates on OTSpd-Zn pattern. Therefore, when the loading force is above 6nN, the frictional response on OTSpd-IL and OTSpd-Zn-IL become identical. Previous studies on the tribological properties of imidazolium IL film on solid surfaces have demonstrated that different anions, different IL film thickness yield different COFs.^{202,249} Here, our data indicate that the friction of an IL interface layer is also determined by its structure, adsorption orientation and the loading force.

6.4 Conclusion

The properties of the ionic liquid–solid interface formed by vapor adsorption play a key role in most IL applications. In this study, we investigated the surface properties of these IL–solid interfaces. We found that the IL ions can adsorb on high-energy surfaces. Therefore, for applications involving the IL's wetting, dewetting, spreading, extraction on surface, and applications involving repetitive liquid–solid contact/disengagement, the role of vapor-phase adsorption has to be considered, even if the vapor pressure of IL is low.

Furthermore, our study reveals that different surface chemistry will affect the orientation of the ions adsorbed on the surface, which was consistent with those previous studies; this is because the ions of IL are usually large and have a directional charge/dipole distribution. We reveal that for the representative [Bmim]Cl, even under the same vapor exposure level, the IL adsorbate layer on the OTSpd–Zn pattern is softer, has a higher friction under low loading force (6 nN) than that on the OTSpd chemical pattern. Our discoveries could provide experimental data for further theoretical studies.

CHAPTER 7 ULTRA-LOW VOLTAGE ELECTROWETTING ON SOLID-LIKE IONIC LIQUID DIELECTRIC LAYER

7.1 Introduction

The spreading and contact angle reduction of a liquid drop on a solid can be electrically induced, a phenomenon known as electrowetting.²⁵⁰⁻²⁵³ Examples for electrowetting within 20-500V include variable-focus liquid lenses,²⁵⁴ optical displays,^{86,255} mirrors,²⁵⁶ electrical,²⁵⁷ and thermal switches,²⁵⁸ a tensiometer,²⁵⁹ rheometers^{260,261} and many digital microfluidic devices for bioanalysis.²⁶²⁻²⁶⁴ So far, the high driving voltage is the main obstacle for further developments and wider application of electrowetting-based devices. Consequently, decreasing the driving voltage is a crucial motivation for scholars to explore in the field of electrowetting. In the past several years, EW voltage has been reduced from 200 V to 20 V.^{87,265-267} Electrowetting-on-Dielectric (EWOD), which describes a configuration in which an insulating layer separates the working liquid and actuation electrodes,²⁶⁸⁻²⁷¹ is the preferred arrangement over the traditional direct electrowetting on a conductor due to (i) insulators can protect working fluids from electrodes, and (ii) the contact angle hysteresis is small, so that the reversibility and easy movement of the working fluids become possible.²⁷² In 1993, Berge first experimentally showed that the voltage-induced contact angle reduction could also be observed on an insulating surface covering a conductor.²⁶⁹ Since then, various EWOD configurations and platforms have been reported. Table 7-1 lists benchmark achievements in the technology of EWOD. Figure 7-1(a) demonstrates a conductive droplet sitting on a flat dielectric-coated electrode with a voltage applied between the liquid and the electrode.

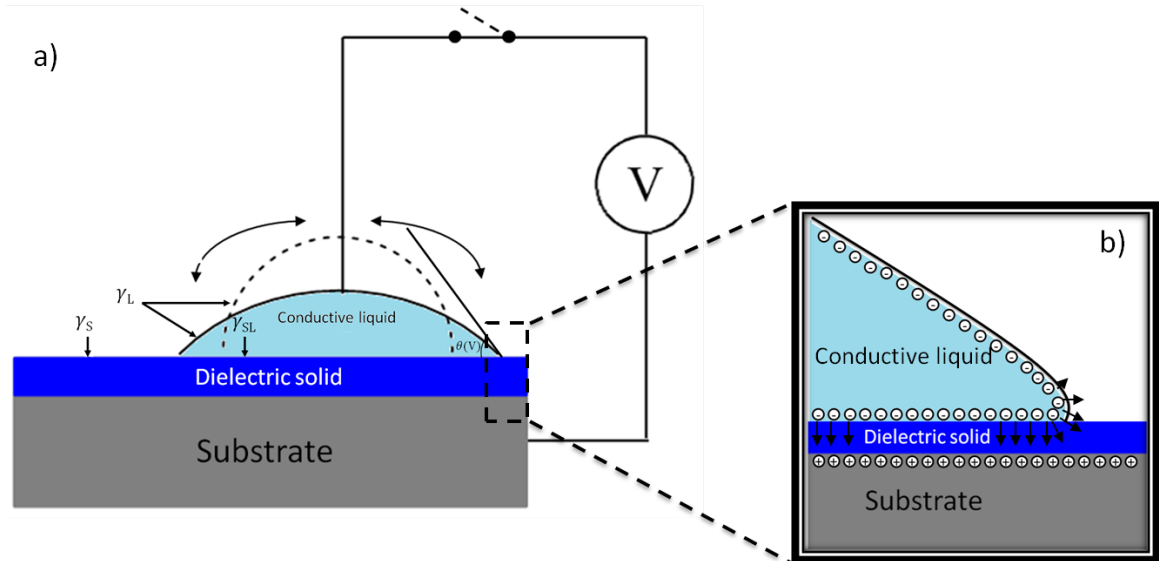


Figure 7-1 (a) A conductive liquid sits on a EWOD surface with and without voltage applying. (b) The boxed drawings enlarged for the contact line region.

Table 7-1 Benchmark achievements in EWOD.

Year	Achievement	Reference
1996	Spreading of aqueous droplet by EWOD	Vallet <i>et al.</i> ²⁵¹
1998	Electrostatic transport of liquid droplets for microreactor applications	Washizu ²⁷³
2000	Liquid droplets transport in oil medium	Pollack <i>et al.</i> ²⁶⁶
2002	Liquid droplets handling in air	Lee <i>et al.</i> ²⁶⁸
2002	Low voltage electrowetting in air (15 V)	Moon <i>et al.</i> ²⁷¹
2003	Creating, transporting, cutting, and merging liquid droplets by electrowetting	Cho <i>et al.</i> ²⁷⁴

Based on the equations in Chapter 1, we can see that the voltage applied to the liquid (V) is a function of contact angle (θ):

$$V = \pm \sqrt{\frac{2(\gamma_L \cos \theta + \gamma_{SL}^0 - \gamma_S)}{C}} = \pm \sqrt{\frac{2d(\gamma_L \cos \theta + \gamma_{SL}^0 - \gamma_S)}{\epsilon_0 \epsilon_r A}} \quad (1).$$

The electrowetting equation in the form of equation (4) indicates that the driving voltage can be reduced by simply increasing the capacitance between the liquid and the substrate through decreasing the dielectric layer thickness or employing

a high dielectric constant coating. It can also be minimized by decreasing the term $(\gamma_{SL}^0 - \gamma_S)$ and the interfacial energy of liquid (γ_L), usually through using an immiscible oil bath.^{275,276} At the current stage, the first approach can reduce the driving voltage down to ~15V by employing thin fluoropolymer coating.^{271,277} If combined with the oil bath approach, the observable electrowetting can be achieved at less than 3V.²⁷⁸ Nevertheless, the oil bath approach is not compatible with digital micro-fluidics. The need for two immiscible liquids with desirable interfacial tensions also greatly limits the scope of electrowetting applications. At present, without the help of oil bath, 15-200 V driving voltage for electrowetting is an obstacle for the further development of electrowetting applications.

Here, we found that IL molecules can form a solid-like ionic liquid film on the top of the surface either by directly contact or vapor deposition. This IL film can serve as the electric double layer (EDL) due to its high charge carrier density and stable structures. Also, previous studies have demonstrated such IL EDL has an ultrahigh capacitance density, which has been used for super-capacitors.^{214,279} Based on equation 1, which was discussed previously, we proposed this solid-like IL EDL was able to reduce the driving voltage significantly due to a larger capacitance. Since the ions in IL EDL at the interface would not diffuse into liquid on top of it, this approach was hoped to employ for Lab-on-chip experiments, like protein mixture separation.

7.2 Experimental

7.2.1 Surface preparation

The surface used for electrowetting in this chapter was the octadecyltrichlorosilane (OTS)-coated silicon wafer and the COOH terminated C₁₀ silane (referred to in the following as UTS_{ox}) film coated silicon wafer. The route for the OTS-coated silicon wafer is the same with our previous description. However, the OTS film at here is the unstablized OTS, which was not annealed in the humid chamber for 10 hours and re-incubated in OTS Toluene solution. The unstabilized OTS has many pinholes inside the film. The OTS monolayer is 26 Å thick, hydrophobic, which provides a hydrophobic coating on the electrode. However, because of the existence of pinhole defects, water, ions, small organic silane molecules can fill into the defect sites. Therefore, it is not an insulating layer.

For the preparation of the UTS_{ox} coated silicon wafer, the silicon (100) wafers (nitrogen doped, 1-40 Ω·cm resistivity, ultra-flat with a root mean square roughness < 5Å) were cleaned with pirahna solution and rinsed with deionized water firstly. Then, the wafers were incubated in a 5 mM 10-undecenyltrichlorosilane (UTS) toluene solution at 20°C overnight in order to form an UTS monolayer silane coating on the silicon surface. This UTS coated surface appeared hydrophobic with a water contact angle of 99±2°. ²⁸⁰ Next, the sample was dipped into a solution containing 5×10⁻⁴M KMnO₄ and 0.02 M NaIO₄ and incubated at 40 °C for 10 h to convert the UTS terminal double bond to -COOH. To remove remnant permanganate or MnO₂, the wafer was rinsed in a 1

mM hydrazine solution for 1 min followed by rinsing in 10% HCl solution for 1 min. The step-by-step scheme is illustrated in Figure 7-2. This prepared surface was incubated in the ionic liquid vapor immediately for 2 hours. We used [Bmim][Tf₂N] vapor to coat the UTSox surface. Due to the surface dipole of the carboxylic-terminated UTSox, an electric double layer (EDL) formed on top of the UTSox. The IL-coated UTSox wafers have surface structures shown in Figure 7-3.

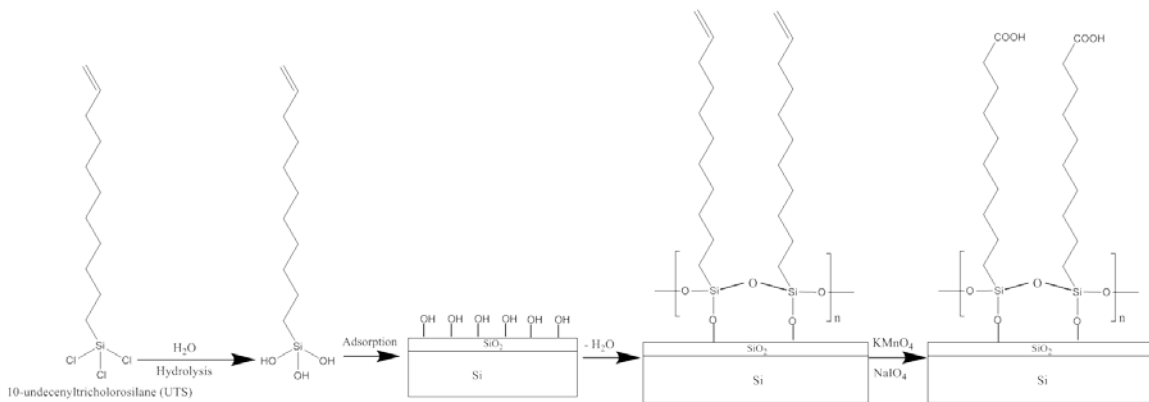


Figure 7-2 The formation of UTSox film on Si (100) wafer.

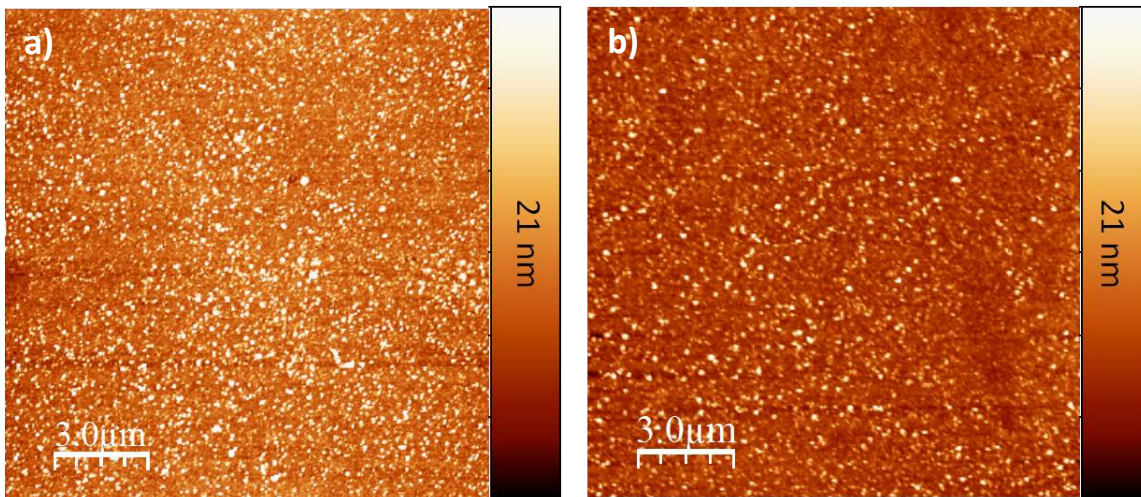


Figure 7-3 Representative AFM image of a) [Bmim]Cl and b) [Bmim][Tf₂N] vapor coated UTSox wafer.

7.2.2 Electrowetting setup and measurement of contact angle

The electrowetting experiment was set up according to Figure 7-4. The experiment was conducted inside the environmental chamber of our Agilent PicoPlus 3000 AFM. The wafer was mounted on the AFM sample holder and grounded. A drop was placed on the sample surface. The bias voltage was applied through a conducting AFM probe to the drop. During the electrowetting experiment, the laser on AFM was turned off. The drop could be viewed and the shape varies was recorded from the top through the attached video camera of PicoPlus 3000 AFM. Liquid 1-butyl-3-methylimidazolium chloride ([Bmim]Cl) was used in the electrowetting. [Bmim]Cl has a melting point of 73°C. When heated, [Bmim]Cl melted and existed as a viscous super-cooled liquid at room temperature. For the electrowetting test of water drop on surface, the relative humidity (RH) inside environmental chamber was maintained at 100% in order to prevent the water drop from evaporation during the experiment. The applied DC voltage was generated by a voltage-biased conducting AFM tip manipulated by AFM feedback system, while the applied AC voltage was produced by a function generator (FG-7002C SWEEP/FUNCTION GENERATOR).

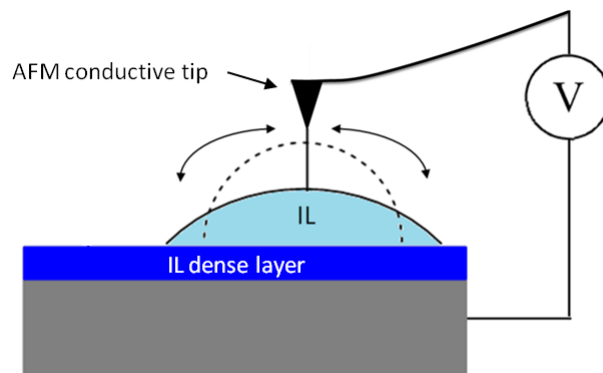


Figure 7-4 Scheme of the experimental setup with cross sectional view.

The drop's contact angle was calculated from the diameter and the height of the drop, since in our experimental setup, only the top-view of the drop could be obtained. The drops used in the experiment were about 100 μm in diameter and 90 μm in height (2.4×10^{-4} μL in volume). Based on the previous analysis,²⁸¹ the use of a drop volume of 1 up to 10 microliters has no influence of gravity on contact angle values measurement. The gravity's influence on the shape of drops in our experiment is negligible. Therefore, we used a spherical cap model (Figure 7-5) to calculate the geometry of the drop, as shown in equation 2. From the drop diameter and the height, we can obtain the contact angle. During experiment, we varied the voltage applied to the drop and recorded the corresponding changes in drop size. The actual contact angles were obtained from the recorded video files.

$$h = R \cdot \left[\frac{1}{\sin\theta} (1 - \cos\theta) \right] = R \cdot \tan\frac{\theta}{2} \quad (2)$$

where R is the radius of the sphere, and h is the height of the cap and θ is the contact angle.

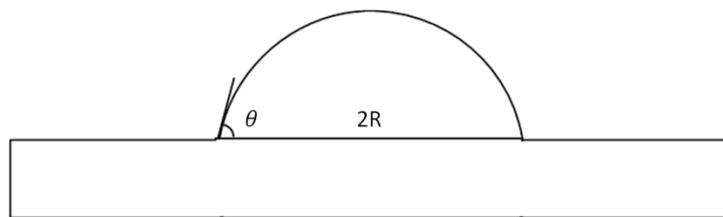


Figure 7-5 Illustration of model for the theoretical calculation.

7.3 Low Voltage EW and Its Application

Figure 7-6 shows a representative image of a [Bmim]Cl drop on the OTS surface without voltage applied to it (Figure 7-6a) and the same drop with -6 volts applied

(Figure 7-6b) in a pure N₂ environment. The top views of the drop (Figure 7-6a/b) indicate that the drop's contact line advanced after voltage was applied. Since the volume of the drop did not change, the contact line advancement corresponded to the decreasing of contact angle, demonstrating the electrowetting effect. In Figure 7-7, we plotted the contact angle as a function of the applied voltage for [Bmim]Cl drop on OTS surface. The contact angles decreased rapidly at voltage of -5V for [Bmim]Cl. As a reference, on fluoropolymer surface, the contact angle of [Bmim]Cl drop decreased 18° at 50V.²⁸² Figure 7-7 reveals that the low voltage electrowetting was achieved for [Bmim]Cl on OTS surface.

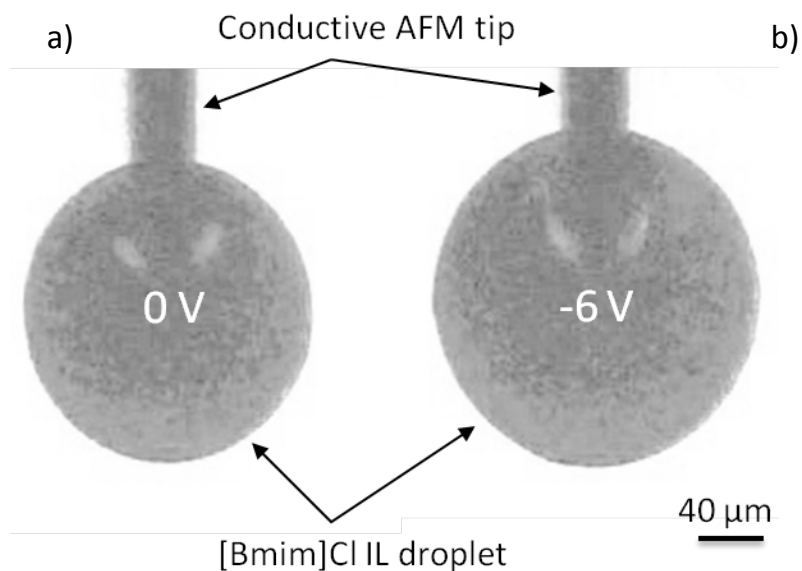


Figure 7-6 Optical microscope images for voltage dependence of the shape of the [Bmim]Cl IL droplet.

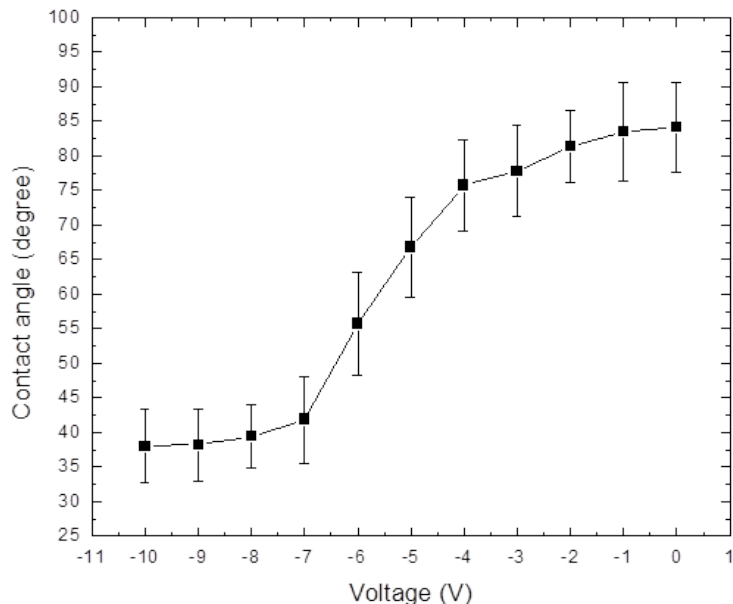


Figure 7-7 The contact angle of a [Bmim]Cl drop on OTS surface as a function of the applied voltage. The sample was grounded. The voltage was applied to the drop through the conducting AFM probe. The electrowetting experiment was conducted in a pure N₂ environment.

When a 8 V square-wave shaped pulse was applied to the [Bmim]Cl drop, we also observed the feature of drop oscillation in electrowetting, which indicated that the low voltage electrowetting was reversible, reproducible and responsive. This electrowetting phenomenon results from the force concentrated on the three-phase contact line (TCL) induced by the AC voltage, while, the time-dependent component of this force is expected to be related to the drop oscillations. Because the force exerted on the TCL is proportional to the square of the applied voltage, it is always positive (in the outward direction respect to the TCL). However, its amplitude changes with the time (Figure 7-8).²⁸³ This droplet oscillation that accompanies AC EWOD actuation has led to interesting experiments, such as exploring the frequency dependence of flow inside a droplet in electrowetting,²⁸⁴ or the source of the generation of the fluid flow,^{285,286}

as well as novel device demonstrations, such as droplet mixers,²⁸⁷ micro-bubble tweezers,²⁸⁸ and a wiper-free windscreen.²⁸⁹

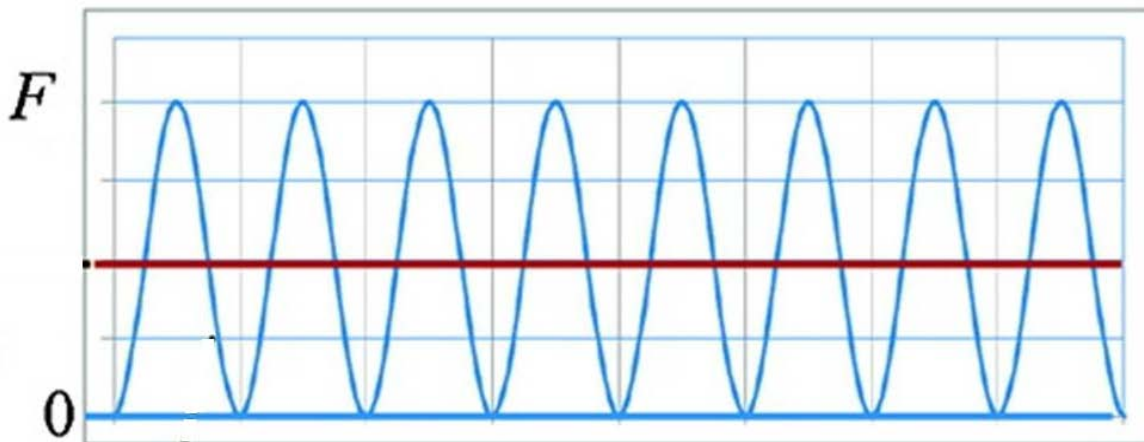


Figure 7-8 Conceptual description of ac electrowetting.

After the electrowetting experiment, we used a stream of nitrogen to blast the IL drop off the surface and characterize the surface by AFM. AFM images in Figure 7-9 show the edge of the drop. The left side of the image is OTS surface, which was outside of the drop and never contacted with IL; whereas the right part is previously under the IL drop. The topography image (Figure 7-9a) shows that the right part is higher than the left part. Specifically, the height histogram of the topography (inset in Figure 7-9b) reveals that this layer is 6.4\AA higher than the OTS surface. In addition, the phase image (Figure 7-9b) corresponding to the topography indicates that the right part has a higher phase signal than the OTS surface, indicating that the tip dissipated more energy tapping over this surface than over OTS. Based on observed differences in both the topography and phase channels, it is concluded that the right part of the surface is a [Bmim]Cl layer adsorbed on the OTS surface. Furthermore, this adsorbed layer formed at

the liquid-OTS interface when the IL drop sat on OTS. In the topography image, “green” droplet-like features can be seen. The left height scale indicates that these green features are on top of the [Bmim]Cl adsorbate layer and 5-8 nm higher than it. In the corresponding phase image, these green features have significant higher phase signal than the [Bmim]Cl adsorbate layer. When we slightly decreased the tapping amplitude set point, *i.e.* tap the surface harder, oscillations occurred over these green features. Such behavior is characteristic of liquid.²⁹⁰ Oscillations indicated that the tip tapped into the liquid and induced perturbation inside the drop. Therefore, these green features are the remaining droplet of liquid phase of [Bmim]Cl on the [Bmim]Cl adsorbate layer. Furthermore, since the phase image reveals that the [Bmim]Cl adsorbate layer and the [Bmim]Cl droplet have different phase contrast, they are in different phases. The [Bmim]Cl droplet cannot wet or dissolve the [Bmim]Cl adsorbate layer.

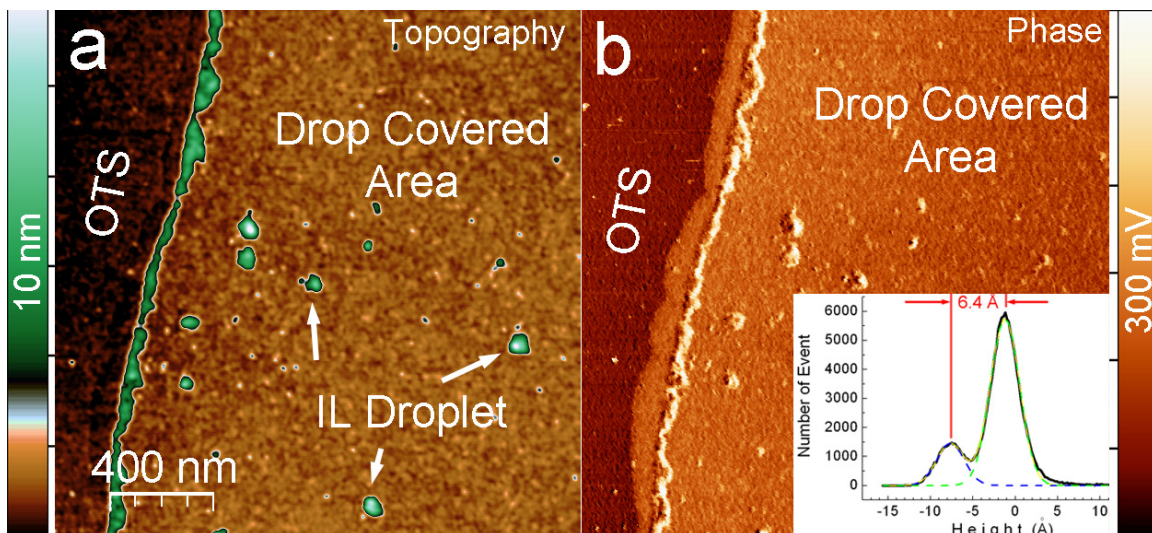


Figure 7-9 AFM image of the edge of the drop after the IL drop was blasted off. a) Topography. The green features are the liquid phase [Bmim]Cl remaining on the surface. The green line is the position of the drop edge. The left side of the edge is the clean OTS surface, which was outside of the drop. The right side of the edge is the surface

previously under the IL drop. b) The phase image. The green features in the topography appear as white spots, indicating the tip dissipating huge energy tapping over them. The high phase signals of these white spots in the phase image reveal that they are in liquid phase. The inset in b is the histogram of the topography image, which indicates the surface under the drop is 6.4 Å higher than clean OTS.

ILs have been known to form layers at the liquid-solid interface when the IL contacts either charged surface or neutral surface.^{201,202,221,224,291-294} It is known that the first layer at the interface is the tightly packed and solid-like, whereas the order of other layers above gradually decrease and the IL layers gradually change into an orderless liquid phase. Our AFM results in Figure 7-9 reveal that upon the contact of OTS, [Bmim]Cl forms a solid-like adsorbate layer, which is consistent with published results on other ILs.

It is also known that the IL interfacial layer has very high charge carrier density and ultra-high capacitance density. Experimental results have shown that the capacitance density of the IL interfacial layer is on the level of 0.01-0.1F/m².^{224,279,295} Hence the solid-like IL adsorbate layer can serve as the dielectric layer with ultra-high capacitance density. When [Bmim]Cl liquid drop contacted OTS surface, the solid-like [Bmim]Cl dielectric layer formed at the liquid-OTS interface. Liquid [Bmim]Cl drop sat on top of the [Bmim]Cl dielectric layer. The electrowetting system is the electrowetting on dielectrics (EWOD), as shown in Figure 7-4.

It was suggested that the ultra-high capacitance of the IL dielectric layer is the reason for the observed low voltage electrowetting. In a control experiment, we conducted scanning probe local oxidation on a clean OTS-coated silicon wafer

using a conducting SPM probe. The probe is ground and 10V bias was applied to the wafer for 10 seconds. Subsequent AFM characterization revealed the OTS film was partially degraded and formed a carboxylic-terminated OTSpd chemical pattern. In this oxidation process, a current was detected, indicating that the OTS film was not a dielectric layer. Rather, the OTS-coated silicon substrate was the electrode for the EWOD system. Therefore, the functioning dielectric layer was the solid-like IL adsorbate layer at the ionic liquid-OTS interface.

Besides the application for low voltage electrowetting in IL on a solid-like IL dielectric layer system, the solid-like IL dielectric layer may work for low voltage electrowetting of other liquids. Once the IL dielectric layer formed, other liquids should also achieve similar low voltage electrowetting effect due to the high capacitance of the dielectric layer. The electrowetting on [Bmim][Tf₂N] dielectric layer is an example. A drop of [Bmim][Tf₂N] was put on the OTS-coated sample and let the drop cover the whole sample surface. After conducting an electrowetting test on this [Bmim][Tf₂N] drop, we then removed the [Bmim][Tf₂N] drop and placed a water drop on the sample surface. Since [Bmim][Tf₂N] is immiscible with water, the water drop would not remove the [Bmim][Tf₂N] dielectric layer adsorbed on OTS. We observed the same low voltage electrowetting on the water drop as well.

An electrowetting experiment was also conducted on [Bmim][Tf₂N] vapor coated UTS_{ox} surface. To demonstrate the [Bmim][Tf₂N] molecules could form a stable dielectric layer on the charged surface, we conducted an experiment using an IL layer adsorbed on charged OTSpd chemical patterns. We fabricated a

carboxylic-terminated OTSpd pattern on the OTS surface using scanning probe local oxidation. The OTSpd surface has the same surface chemistry as the UTS_{ox} surface. Hence we used an OTSpd chemical pattern to study how IL adsorbs on surface with a large surface dipole. Figure 7-10 shows a representative OTSpd pattern after incubated in IL vapor for 2 hours according to the same vapor coating Scheme described in Chapter 6. Figure 7-10a is the topography image and 7-10b is the corresponding phase image. In Figure 7-10a, the apparent height on the OTSpd pattern has changed from $10.2 \pm 0.7 \text{ \AA}$ below the OTS to 5.4 \AA above OTS (Figure 7-10c). From the difference, we can derive that the IL adsorbate on the OTSpd is 15.6 \AA thick. On top of this layer, another layer can be identified. The cross-sectional profile shows that the thickness of this layer is 35.4 \AA (Figure 7-10d). In the corresponding phase image, layers 1 and 2 have different phase contrast. The background OTS film is methyl-terminated and has a low surface energy, which can be used as a reference to compare the phase signal here. Layer 1 has a high phase contrast, whereas layer 2 has the same phase contrast as the OTS background. Therefore, layer 1 is more hydrophilic and layer 2 has a hydrophobic surface. Finally, droplets are sitting on top of layer 1 and 2. The topography shows that the drop surface is smooth and featureless. The corresponding phase signal over the drop is high, which indicates that the tip dissipated more energy while tapping the drop surface. When the tapping amplitude set point was slightly decreased, *i.e.* tapped the surface harder, oscillations occurred. This characteristic shows that the drop is in liquid phase. Oscillations in topography indicated that the tip tapped into the liquid. Thus, the

tapping induced perturbation inside the drop. Therefore, the analyses on the AFM image in Figure 7-10 reveal that IL liquid on the charged surface had multiple phases.

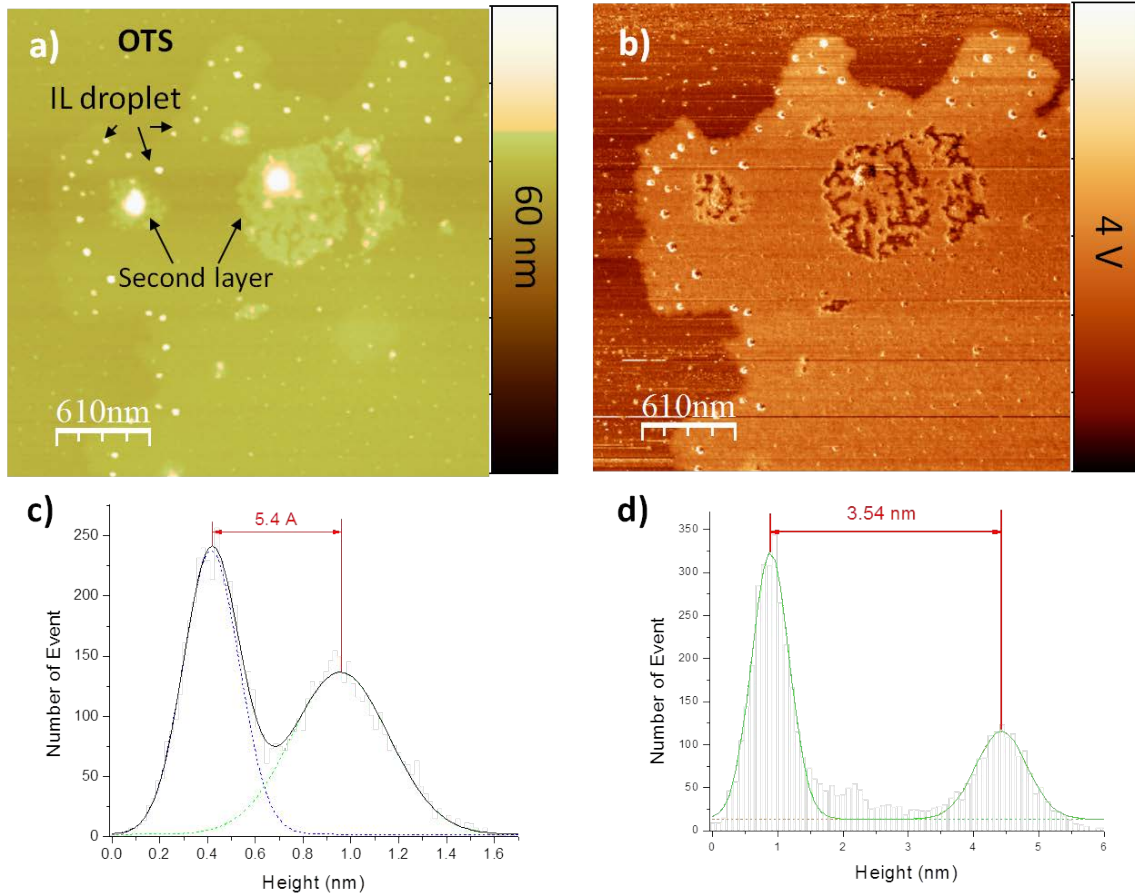


Figure 7-10 AFM image of the OTS pattern after incubated in $[Bmim][Tf_2N]$ vapor for 2 hours. a. topography. The bright white features are the liquid phase $[Bmim][Tf_2N]$ remaining on the surface. b. The phase image. The features in the phase appear as white spots, indicating that the tip dissipated huge energy tapping over them. The high phase signals of these white spots in the phase image reveal that they are in liquid phase. c is the histogram of the topography image of layer 1, which indicates the pattern surface is 5.4 \AA higher than clean OTS. d is the histogram of the topography image of layer 2, indicating layer 2 is 35.4 \AA higher than clean layer 1.

The structure revealed in Figure 7-10 suggests that if we apply voltage to the IL drop, layer 1 and 2 would serve as the IL dielectric layer, even though they are

not in the same phase. As a result, the dielectric layer will lead to the low voltage electrowetting of the IL drop on top of it. Based on the same rationale, if the liquid on top of layer 1 and 2 are other liquids, as long as the dielectric layer still exists, the same low voltage electrowetting will occur as well.

[Bmim][Tf₂N], which is immiscible with water, was used in this experiment. Therefore, other ILs such as [Bmim]Cl and water will not affect the structure of [Bmim][Tf₂N] dielectric layer already coated on UTS_{ox} surface. In fact, they all demonstrated electrowetting effects at low driving voltage during the experiment.

Besides the observation of contact angle change with low driving voltage, the contact line of the droplet was found to become unstable, leading to the ejection of small satellite droplets from the edge of the main droplet under either DC voltage or AC voltage (see Figure 7-11). Based on Mugele and Herminghaus's observation,²⁹⁶ the mother and satellite droplet remain connected by a thin liquid bridge (see Figure 7-11). Qualitatively, this instability associated with two important time scales, the charging time of the solid-liquid interface T_{charge} and the period of the applied voltage T_{applied} . In the DC voltage case, $T_{\text{charge}} \ll T_{\text{applied}}$, the liquid phase boundary will acquire a net charge while voltage is applied, shielding the liquid bulk from the electric field. Beyond certain voltage, the repulsion of like charge at the contact line cause an unbalance between the surface tension and the electrostatic force, this leads to the emission of satellite droplets. Alternatively, when an AC voltage is applied onto a conductive liquid drop, $T_{\text{charge}} \gg T_{\text{applied}}$ (at certain frequencies), the liquid boundary will not acquire a net charge as quickly as the voltage is applied, and the electric field will be distributed within the liquid

bulk phase. However, because of the electrical force, the droplet will change its shape which can maximize the amount of capacitive energy, like enlarging contact area by pulling the satellite droplets along the outward direction.^{84,272}

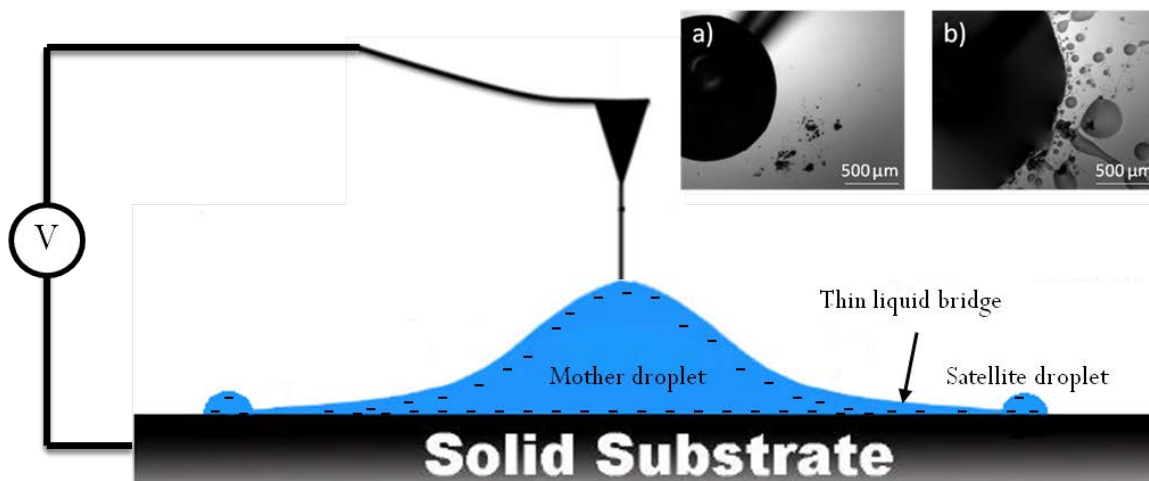


Figure 7-11 Schematic diagram of a small satellite droplet connected to the reservoir drop. Inset a) and b) are the illustrations of a water droplet before and after the ejection of satellite droplets.

An experiment was designed to determine the thickness of this thin liquid channel. A 10 μL drop of sodium chloride saturated solution was transferred onto a [Bmim][Tf₂N] coated UTSox wafer and let this drop to spread under a applied voltage. After evaporation, the NaCl dissolve in water was deposited on the surface. Flooding analysis reveals the volume and the surface area of the deposited NaCl solid. Since the solubility of NaCl in saturated NaCl solution is 35.7g per 100 ml water at 20 °C,²⁹⁷ we can easily calculate the thickness of the liquid film between the main droplet and satellite droplets is about 100 nm.

In another experiment, two types of nanospheres, with particle sizes of 240 nm and 500 nm, were employed. Firstly, these two different particles were mixed

with H₂O respectively, and one droplet of the mixture suspension was sat on the [Bmim][Tf₂N] IL dielectric layer coated UTSox sample surface. Then, this droplet was pumped by EWOD and satellite droplets were ejected from the edge of the main droplet on sample surface. We supposed that the nanosphere would be pushed out with the ejected droplet. After evaporation of solution media, the nanospheres deposited on the surface and from the distribution of the nanosphere density, we can tell the scenario of the liquid flow. As Figure 7-12 demonstrated, a ring, which is composed of millions of nanospheres, was observed outside of the main droplet, when the 240 nm nanosphere was employed. Whereas, nothing was deposit into a circle further from the main droplet when 500 nm nanosphere was used. This phenomenon indicated that 240 nm nanospheres can pass through the thin liquid bridge freely while 500 nm nanospheres cannot; indicating the ability to spray nano particles according to their size using EWOD.

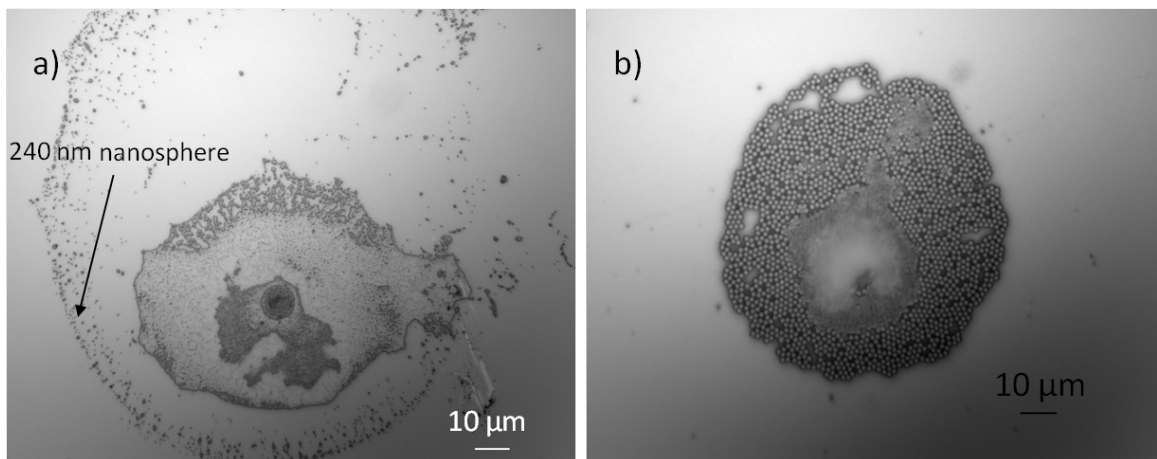


Figure 7-12 a) 240 nm nanospheres were distributed through the thin liquid bridge while b) 500 nm nanospheres maintain within the main droplet.

Using this property, the protein mixture was separated successfully based on their molecular weight. The smaller proteins can move further with respect to the mother droplet than the larger ones, because they experience less resistance when moving over the surface. Figure 7-13 shows the ability to separate streptavidin (60 kDa) from green fluorescence protein (GFP, 26.9kDa). The initial sample contains 1 μ g/ml fluorescently stained streptavidin, mixed with 1 μ g/ml GFP. On introduction of a voltage, we expect GFP moves to the outer side, leaving mostly streptavidin close to the center of the droplet, due to the smaller hysteresis they experience.

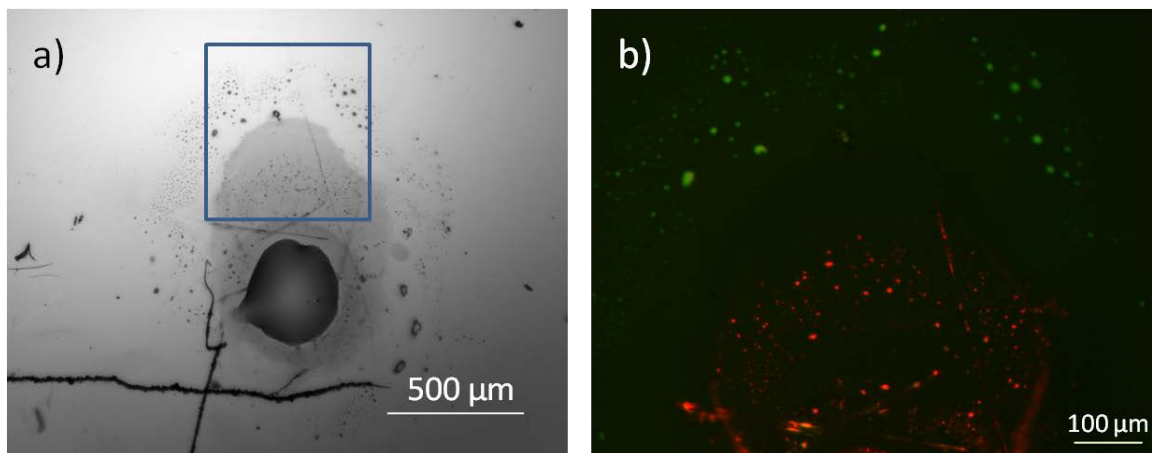


Figure 7-13 Optical microscope image of protein mixture after the introduction of voltage. The cyan box is the zone shown in (b). (b) a fluorescence combined image.

The sample surface was imaged by using Nikon fluorescence microscopy combining two different filters, G-2A filter and GFP filter, after EW. The G-2A filter combination is configured as the standard green filter block, with a wide excitation pass band for application to a large number of fluorophores activated by green wavelengths. The long pass emission filter permits detection of all fluorescence wavelengths longer than the yellow spectral region. The GFP filter

permits 450-490 nm excitation wavelength pass through, while only detect 500-550 nm emission fluorescence wavelengths.²⁹⁸ The fluorescence image captured by G-2A filter and that captured by GFP filter were laid over and the combined image was demonstrated in Figure 7-13b. In that image, the red features are the fluorescence emission from streptavidin stained with AF680, captured by using G-2A filter. While, the green features are the fluorescence emission from green fluorescent protein, captured by using GFP filter. As Figure 7-13 demonstrated, two proteins were separated successfully. By comparing two fluorescence signals, the green ones (the protein with smaller MW) come from the regions located further from the central part of the droplet, which proves our hypothesis. Our study proposed a technique for the protein mixture separation, which was pumped by EWOD.

7.3 Conclusion

A new approach to realize low voltage electrowetting without help of oil bath was reported in this chapter. By coating surface with ionic liquid, liquid drops on the IL coating demonstrate electrowetting effect at driving voltage as low as 1 volt in nitrogen environment. AFM studies reveal that IL formed a solid-like thin film, which is immiscible with liquid IL or other aqueous solutions and serves as the dielectric layer between the liquid and electrode in electrowetting. Our data suggest that the ultra-high capacitance density of the IL dielectric layer leads to the low voltage electrowetting. After that, we successfully demonstrated the streptavidin and GFP proteins separation by EWOD force.

Our method to realize low voltage electrowetting provides a new approach to simplify the digital micro-fluidic design, and enables new studies on micro-separation, micro-pumps, liquid lens and e-ink display, since the liquids drops on the surface can be manipulated by electrowetting effect without oil bath. Furthermore, since the voltage need for electrowetting could be lower than 5V, most electrowetting experiments can be directly driven by digital integrated circuit chip, or computer output ports (such as RS-232, printer port, or GPIB port). Therefore, the technical impediments to study and develop electrowetting applications would be drastically reduced.

CHAPTER 8 CONCLUSIONS AND FUTURE PROJECTS

8.1 Summary

This dissertation first summarizes the development and current knowledge of nanolithography, microreactor, and electrowetting, and explains the theoretical knowledge of atomic force microscopy. Then it provides systematic description of the design and observations of our experiments.

In our first project, we fabricated a tightly packed CaM pattern on the -SH terminated chemical pattern, which was created by using AFM local oxidation lithography method. The AFM characterization results show that the immobilization of CaM on a solid support does not interfere with the ability of the protein to bind calcium. Furthermore, our AFM phase and KPFM surface potential signals demonstrate that the immobilized CaM have two different orientations.

To preserve the activity of catalase in the room temperature, a novel ionic liquid based micro-reactor was build up. Although the experimental results indicate the failure of this attempt, the FeCl_3 catalyst encapsulated micro-reactor was proved that it can catalyze the decomposition reaction of the hydrogen peroxide at the IL-OTS coating-water interface, when the micro-reactors were immersed in hydrogen peroxide solution. This is because the pinholes in the silane coating layer enable a slow material exchange between both sides of the protective silane layer. Therefore, the coated IL drop may allow homogenous catalytic reactions to proceed in a heterogeneous fashion at the designated places with controlled reaction time.

We observed solid-like IL layer through AFM characterization in the micro-reactor experiment. The properties of this ionic liquid–solid interface was studied with AFM and KPFM in four aspects, which are surface potential, Lennard-Jones potential, energy dissipation, and tribological properties. Our study reveals that the surface properties of the IL adsorbate layer depend on the dipole of the underneath chemical patterns. Therefore, characterization and measurements of the IL interfacial properties must be conducted under the pretext that the charge/dipole of the substrate is known.

Finally, this ionic liquid interfacial layer was used as a dielectric layer to reduce the driving voltage of electrowetting. Drops on the IL dielectric layer demonstrated electrowetting effect at voltage as low as 70 mV. The IL film in this experiment serves as the electric double layer (EDL) due to its high charge carrier density and stable structures. This low voltage electrowetting technique was successfully employed in the protein mixture separation.

8.2 Future work

Strategies to study the conformational change in immobilized calmodulin, surface properties of IL interfacial layer, as well as the electrowetting have been presented in this dissertation. In this section, some important future issues raised from our experimental results are outlined:

1. In CaM experiment part, we know that AFM phase signal and KPFM surface potential signal are powerful for protein orientation distribution measurement in molecular level. A related issue is whether the variation in

orientation would affect the activity or binding ability of CaM. An experiment or a technique is needed to estimate and quantify their difference in activity.

2. By changing the cation and anion, ILs can possess tunable properties. Hence an ionic liquid with compatible property for specific enzyme can be designed; this specifically designed IL would be used as a medium in our micro-reactor for biocatalytic reactions.
3. The protein mixture with two different sized fluorescently stained proteins was used in our EW work. Developing a more complex protein mixture, which contains 3 or more proteins with different sizes, is another interesting challenge for future research.

Reference

- (1) Bucknall, D. G. *Nanolithography and patterning techniques in microelectronics*; Woodhead Pub., CRC Press: Cambridge, Boca Raton, FL, 2005.
- (2) Wouters, D.; Schubert, U. S. *Angew Chem Int Edit* **2004**, *43*, 2480-2495.
- (3) Xia, Y. N.; Rogers, J. A.; Paul, K. E.; Whitesides, G. M. *Chem Rev* **1999**, *99*, 1823-1848.
- (4) Gates, B. D.; Xu, Q. B.; Stewart, M.; Ryan, D.; Willson, C. G.; Whitesides, G. M. *Chem Rev* **2005**, *105*, 1171-1196.
- (5) Saavedra, H. M.; Mullen, T. J.; Zhang, P. P.; Dewey, D. C.; Claridge, S. A.; Weiss, P. S. *Rep Prog Phys* **2010**, *73*.
- (6) Service, R. F. *Science* **1996**, *274*, 1834-1836.
- (7) Ngunjiri, J.; Garno, J. C. *Anal Chem* **2008**, *80*, 1361-1369.
- (8) Okazaki, S. *J Vac Sci Technol B* **1991**, *9*, 2829-2833.
- (9) Switkes, M.; Kunz, R. R.; Rothschild, M.; Sinta, R. F.; Yeung, M.; Baek, S. Y. *J Vac Sci Technol B* **2003**, *21*, 2794-2799.
- (10) Mulkens, J.; Flagello, D.; Streefkerk, B.; Graeupner, P. *J Microlith Microfab* **2004**, *3*, 104-114.
- (11) Owa, S.; Nagasaka, H. *J Microlith Microfab* **2004**, *3*, 97-103.
- (12) Hoffnagle, J. A.; Hinsberg, W. D.; Sanchez, M.; Houle, F. A. *J Vac Sci Technol B* **1999**, *17*, 3306-3309.
- (13) Owa, S.; Nagasaka, H.; Ishii, Y.; Hirakawa, O.; Yamamoto, T. *Solid State Technol* **2004**, *47*, 43-+.
- (14) Switkes, M.; Rothschild, M. *J Vac Sci Technol B* **2001**, *19*, 2353-2356.
- (15) Campbell, S. A. *The science and engineering of microelectronic fabrication*; 2nd ed.; Oxford University Press: New York, 2001.
- (16) Pimpin, A. *Engineering Journal* **2012**, *16*.
- (17) Brainard, R. L.; Cobb, J.; Cutler, C. A. *J Photopolym Sci Tec* **2003**, *16*, 401-410.
- (18) Golovkina, V. N.; Nealey, P. F.; Cerrina, F.; Taylor, J. W.; Solak, H. H.; David, C.; Gobrecht, J. *J Vac Sci Technol B* **2004**, *22*, 99-103.
- (19) Talin, A. A.; Cardinale, G. F.; Wallow, T. I.; Dentinger, P.; Pathak, S.; Chinn, D.; Folk, D. R. *J Vac Sci Technol B* **2004**, *22*, 781-784.
- (20) Toriumi, M.; Ishikawa, T.; Kodani, T.; Koh, M.; Moriya, T.; Yamashita, T.; Araki, T.; Aoyama, H.; Yamazaki, T.; Furukawa, T.; Itani, T. *J Vac Sci Technol B* **2004**, *22*, 27-30.
- (21) Kubena, R. L. *Mater. Res. Soc. Symp. Proc.* **1993**, *279*.
- (22) Wang, D., Georgia Institute of Technology, August 2010.
- (23) Spatz, J. P. *Angew Chem Int Edit* **2002**, *41*, 3359-3362.
- (24) Golzhauser, A.; Eck, W.; Geyer, W.; Stadler, V.; Weimann, T.; Hinze, P.; Grunze, M. *Adv Mater* **2001**, *13*, 806-+.
- (25) Pease, R. F.; Chou, S. Y. *P IEEE* **2008**, *96*, 248-270.
- (26) Binning, G.; Rohrer, H.; Gerber, C.; Weibel, E. *Phys Rev Lett* **1982**, *49*, 57-61.
- (27) Ringger, M.; Hidber, H. R.; Schlogl, R.; Oelhafen, P.; Guntherodt, H. J. *Appl Phys Lett* **1985**, *46*, 832-834.
- (28) Eigler, D. M.; Schweizer, E. K. *Nature* **1990**, *344*, 524-526.
- (29) Crommie, M. F.; Lutz, C. P.; Eigler, D. M. *Science* **1993**, *262*, 218-220.
- (30) Liu, J. F.; Cruchon-Dupeyrat, S.; Garno, J. C.; Frommer, J.; Liu, G. Y. *Nano Lett* **2002**, *2*, 937-940.
- (31) Liu, G. Y.; Xu, S.; Qian, Y. L. *Accounts Chem Res* **2000**, *33*, 457-466.

- (32) Rolandi, M.; Suez, I.; Dai, H. J.; Frechet, J. M. J. *Nano Lett* **2004**, *4*, 889-893.
- (33) Garno, J. C.; Yang, Y. Y.; Amro, N. A.; Cruchon-Dupeyrat, S.; Chen, S. W.; Liu, G. Y. *Nano Lett* **2003**, *3*, 389-395.
- (34) Nakamura, Y.; Mera, Y.; Maeda, K. *Phys Rev Lett* **2002**, *89*.
- (35) Heinrich, A. J.; Lutz, C. P.; Gupta, J. A.; Eigler, D. M. *Science* **2002**, *298*, 1381-1387.
- (36) Piner, R. D.; Zhu, J.; Xu, F.; Hong, S. H.; Mirkin, C. A. *Science* **1999**, *283*, 661-663.
- (37) Hong, S. H.; Zhu, J.; Mirkin, C. A. *Science* **1999**, *286*, 523-525.
- (38) Mirkin, C. A. *Mrs Bull* **2000**, *25*, 43-54.
- (39) Mirkin, C. A. *Inorg Chem* **2000**, *39*, 2258-2272.
- (40) Hong, S. H.; Zhu, J.; Mirkin, C. A. *Langmuir* **1999**, *15*, 7897-7900.
- (41) Maynor, B. W.; Li, Y.; Liu, J. *Langmuir* **2001**, *17*, 2575-2578.
- (42) Rozhok, S.; Piner, R.; Mirkin, C. A. *J Phys Chem B* **2003**, *107*, 751-757.
- (43) Schwartz, P. V. *Langmuir* **2002**, *18*, 4041-4046.
- (44) Jang, J. Y.; Schatz, G. C.; Ratner, M. A. *Phys Rev Lett* **2004**, *92*.
- (45) Jang, J.; Schatz, G. C.; Ratner, M. A. *Phys Rev Lett* **2003**, *90*.
- (46) Jang, J. Y.; Hong, S. H.; Schatz, G. C.; Ratner, M. A. *J Chem Phys* **2001**, *115*, 2721-2729.
- (47) Lee, K. B.; Park, S. J.; Mirkin, C. A.; Smith, J. C.; Mrksich, M. *Science* **2002**, *295*, 1702-1705.
- (48) Su, M.; Dravid, V. P. *Appl Phys Lett* **2002**, *80*, 4434-4436.
- (49) Dobisz, E. A.; Marrian, C. R. K.; Shirey, L. M.; Ancona, M. *J Vac Sci Technol B* **1992**, *10*, 3067-3071.
- (50) Majumdar, A.; Oden, P. I.; Carrejo, J. P.; Nagahara, L. A.; Graham, J. J.; Alexander, J. *Appl Phys Lett* **1992**, *61*, 2293-2295.
- (51) Marrian, C. R. K.; Perkins, F. K.; Brandow, S. L.; Koloski, T. S.; Dobisz, E. A.; Calvert, J. M. *Appl Phys Lett* **1994**, *64*, 390-392.
- (52) Stockman, L.; Neuttiens, G.; Vanhaesendonck, C.; Bruynseraede, Y. *Appl Phys Lett* **1993**, *62*, 2935-2937.
- (53) Voicu, R.; Boukherroub, R.; Bartzoka, V.; Ward, T.; Wojtyk, J. T. C.; Wayner, D. D. M. *Langmuir* **2004**, *20*, 11713-11720.
- (54) Aizenberg, J.; Black, A. J.; Whitesides, G. M. *Nature* **1999**, *398*, 495-498.
- (55) Kim, S. O.; Solak, H. H.; Stoykovich, M. P.; Ferrier, N. J.; de Pablo, J. J.; Nealey, P. F. *Nature* **2003**, *424*, 411-414.
- (56) Black, C. T.; Guarini, K. W.; Milkove, K. R.; Baker, S. M.; Russell, T. P.; Tuominen, M. T. *Appl Phys Lett* **2001**, *79*, 409-411.
- (57) Brockman, J. M.; Frutos, A. G.; Corn, R. M. *J Am Chem Soc* **1999**, *121*, 8044-8051.
- (58) Unger, M. A.; Chou, H. P.; Thorsen, T.; Scherer, A.; Quake, S. R. *Science* **2000**, *288*, 113-116.
- (59) Joachim, C.; Gimzewski, J. K.; Aviram, A. *Nature* **2000**, *408*, 541-548.
- (60) Loo, Y. L.; Lang, D. V.; Rogers, J. A.; Hsu, J. W. P. *Nano Lett* **2003**, *3*, 913-917.
- (61) Gao, P.; Cai, Y. G. *Langmuir* **2008**, *24*, 10334-10339.
- (62) Gao, P.; Cai, Y. G. *Ultramicroscopy* **2009**, *109*, 1023-1028.
- (63) Trajkovic, S.; Zhang, X. N.; Dauner, S.; Cai, Y. G. *Langmuir* **2011**, *27*, 10793-10799.
- (64) Kubena, R. L. *Materials Research Society Symposium Proceeding* **1993**.
- (65) Doku, G. N.; Haswell, S. J. *Anal Chim Acta* **1999**, *382*, 1-13.

- (66) Greenway, G. M.; Haswell, S. J.; Petsul, P. H. *Anal Chim Acta* **1999**, *387*, 1-10.
- (67) Reyes, D. R.; Iossifidis, D.; Auroux, P. A.; Manz, A. *Anal Chem* **2002**, *74*, 2623-2636.
- (68) Auroux, P. A.; Iossifidis, D.; Reyes, D. R.; Manz, A. *Anal Chem* **2002**, *74*, 2637-2652.
- (69) Doku, G. N.; Verboom, W.; Reinhoudt, D. N.; van den Berg, A. *Tetrahedron* **2005**, *61*, 2733-2742.
- (70) Skelton, V. A.; Henderson, K.; Liu, C. *Eur J Anaesth* **2000**, *17*, 390-394.
- (71) Greenway, G. M.; Haswell, S. J.; Morgan, D. O.; Skelton, V.; Styring, P. *Sensor Actuat B-Chem* **2000**, *63*, 153-158.
- (72) Brivio, M.; Fokkens, R. H.; Verboom, W.; Reinhoudt, D. N.; Tas, N. R.; Goedbloed, M.; van den Berg, A. *Anal Chem* **2002**, *74*, 3972-3976.
- (73) Fletcher, P. D. I.; Haswell, S. J.; Pombo-Villar, E.; Warrington, B. H.; Watts, P.; Wong, S. Y. F.; Zhang, X. L. *Tetrahedron* **2002**, *58*, 4735-4757.
- (74) Burns, J. R.; Ramshaw, C. *Chem Eng Res Des* **1999**, *77*, 206-211.
- (75) Hisamoto, H.; Saito, T.; Tokeshi, M.; Hibara, A.; Kitamori, T. *Chem Commun* **2001**, 2662-2663.
- (76) Doku, G. N.; Haswell, S. J.; McCreedy, T.; Greenway, G. M. *Analyst* **2001**, *126*, 14-20.
- (77) Loscertales, I. G.; Barrero, A.; Guerrero, I.; Cortijo, R.; Marquez, M.; Ganan-Calvo, A. M. *Science* **2002**, *295*, 1695-1698.
- (78) Ganan-Calvo, A. M.; Gordillo, J. M. *Phys Rev Lett* **2001**, *87*.
- (79) Ganan-Calvo, A. M. *Phys Rev Lett* **1998**, *80*, 285-288.
- (80) Fox, R. W.; McDonald, A. T. *Introduction to fluid mechanics*; 3rd ed.; Wiley: New York, 1985.
- (81) Mills, P. L.; Chaudhari, R. V. *Catal Today* **1997**, *37*, 367-404.
- (82) Pollack, M. G.; Shenderov, A. D.; Fair, R. B. *Lab Chip* **2002**, *2*, 96-101.
- (83) Lippmann, G. *Ann. Chim. Phys.* **1875**, *5*.
- (84) Mugele, F.; Baret, J. C. *J Phys-Condens Mat* **2005**, *17*, R705-R774.
- (85) Huh, D.; Tkaczyk, A. H.; Bahng, J. H.; Chang, Y.; Wei, H. H.; Grothberg, J. B.; Kim, C. J.; Kurabayashi, K.; Takayama, S. *J Am Chem Soc* **2003**, *125*, 14678-14679.
- (86) Hayes, R. A.; Feenstra, B. J. *Nature* **2003**, *425*, 383-385.
- (87) Berge, B.; Peseux, J. *Eur Phys J E* **2000**, *3*, 159-163.
- (88) Shapiro, B.; Moon, H.; Garrell, R. L.; Kim, C. J. *J. Appl. Phys.* **2003**, *93*, 5794-5811.
- (89) Quinn, A.; Sedev, R.; Ralston, J. J. *J. Phys. Chem. B* **2005**, *109*, 6268-6275.
- (90) Binnig, G.; Quate, C. F.; Gerber, C. *Phys Rev Lett* **1986**, *56*, 930-933.
- (91) Skoog, D. A.; Holler, F. J.; Crouch, S. R. *Principles of instrumental analysis*; 6th ed.; Thomson Brooks/Cole: Belmont, CA, 2007.
- (92) Liu, B. H.; Chen, C. H. *Ultramicroscopy* **2011**, *111*, 1124-1130.
- (93) Chen, G. J.; Ning, X. G.; Park, B.; Boons, G. J.; Xu, B. Q. *Langmuir* **2009**, *25*, 2860-2864.
- (94) Morris, V. J.; Kirby, A. R.; Gunning, A. P. *Atomic force microscopy for biologists*; 2nd ed.; Imperial College Press ; Distributed by World Scientific Pub.: London Singapore ; Hakensack, NJ, 2010.
- (95) Cappella, B.; Dietler, G. *Surf Sci Rep* **1999**, *34*, 1-+.
- (96) Butt, H. J.; Cappella, B.; Kappl, M. *Surf Sci Rep* **2005**, *59*, 1-152.
- (97) Adamson, A. W. *Physical chemistry of surfaces*; 5th ed.; Wiley: New York, 1990.

- (98) Eastman, T.; Zhu, D. M. *Langmuir* **1996**, *12*, 2859-2862.
- (99) Bhushan, B. *Scanning probe microscopy in nanoscience and nanotechnology*; Springer: Berlin, 2010.
- (100) Schmitz, I.; Schreiner, M.; Friedbacher, G.; Grasserbauer, M. *Anal Chem* **1997**, *69*, 1012-1018.
- (101) Sader, J. E.; Chon, J. W. M.; Mulvaney, P. *Rev Sci Instrum* **1999**, *70*, 3967-3969.
- (102) Green, C. P.; Lioe, H.; Cleveland, J. P.; Proksch, R.; Mulvaney, P.; Sader, J. E. *Rev Sci Instrum* **2004**, *75*, 1988-1996.
- (103) Bigelow, W. C.; Pickett, D. L.; Zisman, W. A. *J Coll Sci Imp U Tok* **1946**, *1*, 513-538.
- (104) Adamson, A. W.; Gast, A. P. *Physical chemistry of surfaces*; 6th ed.; Wiley: New York, 1997.
- (105) Karpovich, D. S.; Blanchard, G. J. *Langmuir* **1994**, *10*, 3315-3322.
- (106) Ulman, A. *Chem Rev* **1996**, *96*, 1533-1554.
- (107) Love, J. C.; Estroff, L. A.; Kriebel, J. K.; Nuzzo, R. G.; Whitesides, G. M. *Chem Rev* **2005**, *105*, 1103-1169.
- (108) Maoz, R.; Cohen, S. R.; Sagiv, J. *Adv Mater* **1999**, *11*, 55-61.
- (109) Gun, J.; Iscovici, R.; Sagiv, J. *J Colloid Interf Sci* **1984**, *101*, 201-213.
- (110) Wasserman, S. R.; Tao, Y. T.; Whitesides, G. M. *Langmuir* **1989**, *5*, 1074-1087.
- (111) Miller, C. J.; Widrig, C. A.; Charych, D. H.; Majda, M. *J Phys Chem-US* **1988**, *92*, 1928-1936.
- (112) Despotopoulou, M. M.; Frank, C. W.; Miller, R. D.; Rabolt, J. F. *Macromolecules* **1996**, *29*, 5797-5804.
- (113) Superfine, R.; Guyotsionnest, P.; Hunt, J. H.; Kao, C. T.; Shen, Y. R. *Surf Sci* **1988**, *200*, L445-L450.
- (114) Britt, D. W.; Hlady, V. *J Colloid Interf Sci* **1996**, *178*, 775-784.
- (115) Ulman, A.; Tillman, N. *Langmuir* **1989**, *5*, 1418-1420.
- (116) Cai, Y. G.; Ocko, B. M. *J Am Chem Soc* **2005**, *127*, 16287-16291.
- (117) Horcas, I.; Fernandez, R.; Gomez-Rodriguez, J. M.; Colchero, J.; Gomez-Herrero, J.; Baro, A. M. *Rev Sci Instrum* **2007**, *78*.
- (118) Maoz, R.; Frydman, E.; Cohen, S. R.; Sagiv, J. *Adv Mater* **2000**, *12*, 725-+.
- (119) Hoepfener, S.; Maoz, R.; Cohen, S. R.; Chi, L. F.; Fuchs, H.; Sagiv, J. *Adv Mater* **2002**, *14*, 1036-+.
- (120) Liu, S. T.; Maoz, R.; Schmid, G.; Sagiv, J. *Nano Lett* **2002**, *2*, 1055-1060.
- (121) Wasserman, S. R.; Whitesides, G. M.; Tidswell, I. M.; Ocko, B. M.; Pershan, P. S.; Axe, J. D. *J Am Chem Soc* **1989**, *111*, 5852-5861.
- (122) Cai, Y. G. *Langmuir* **2009**, *25*, 5594-5601.
- (123) Yan, B.; Liu, L.; Astor, C. A.; Tang, Q. *Anal Chem* **1999**, *71*, 4564-4571.
- (124) Frimurer, T. M.; Peters, G. H.; Iversen, L. F.; Andersen, H. S.; Moller, N. P. H.; Olsen, O. H. *Biophys J* **2003**, *84*, 2273-2281.
- (125) Vogel, H. J. *Calcium-binding protein protocols*; Humana Press: Totowa, N.J., 2002.
- (126) Chin, D.; Means, A. R. *Trends Cell Biol* **2000**, *10*, 322-328.
- (127) Swindells, M. B.; Ikura, M. *Nat Struct Biol* **1996**, *3*, 501-504.
- (128) Osawa, M.; Swindells, M. B.; Tanikawa, J.; Tanaka, T.; Mase, T.; Furuya, T.; Ikura, M. *J Mol Biol* **1998**, *276*, 165-176.
- (129) Hudmon, A.; Schulman, H. *Annu Rev Biochem* **2002**, *71*, 473-510.

- (130) Comella, J.; Egea, J.; Soler, R. M.; Dolcet, X.; Espinet, C. *Method Find Exp Clin* **2000**, *22*, 395-396.
- (131) SchauerVukasinovic, V.; Cullen, L.; Daunert, S. *J Am Chem Soc* **1997**, *119*, 11102-11103.
- (132) Cahill, D. J. *J Immunol Methods* **2001**, *250*, 81-91.
- (133) Zhu, H.; Snyder, M. *Curr Opin Chem Biol* **2003**, *7*, 55-63.
- (134) Blawas, A. S.; Reichert, W. M. *Biomaterials* **1998**, *19*, 595-609.
- (135) Lee, Y.; Lee, E. K.; Cho, Y. W.; Matsui, T.; Kang, I. C.; Kim, T. S.; Han, M. H. *Proteomics* **2003**, *3*, 2289-2304.
- (136) Nonnenmacher, M.; Oboyle, M. P.; Wickramasinghe, H. K. *Appl Phys Lett* **1991**, *58*, 2921-2923.
- (137) *Kelvin probe force microscopy*; Springer: New York, 2011.
- (138) Melitz, W.; Shen, J.; Kummel, A. C.; Lee, S. *Surf Sci Rep* **2011**, *66*, 1-27.
- (139) Gao, P.; Cai, Y. G. *Anal Bioanal Chem* **2009**, *394*, 207-214.
- (140)
- (141) Shapiro, A. L.; Vinuela, E.; Maizel, J. V. *Biochem Bioph Res Co* **1967**, *28*, 815-&.
- (142) Garrett, R.; Grisham, C. M. *Biochemistry*, 3rd ed.; Thomson Brooks/Cole: Belmont, CA, 2005.
- (143) Sharma, B.; Deo, S. K.; Bachas, L. G.; Daunert, S. *Bioconjugate Chem* **2005**, *16*, 1257-1263.
- (144) Jocelyn, P. C. *Methods in Enzymology* **1987**, *143*, 246-256.
- (145) Burns, J. A.; Butler, J. C.; Moran, J.; Whitesides, G. M. *J Org Chem* **1991**, *56*, 2648-2650.
- (146) Tiwari, A.; Hayward, L. J. *J Biol Chem* **2003**, *278*, 5984-5992.
- (147) Lykkesfeldt, J. *Anal Biochem* **2000**, *282*, 89-93.
- (148) Pliska, V.; Marbach, P.; Vasak, J.; Rudinger, J. *Experientia* **1977**, *33*, 367-369.
- (149) Tyagarajan, K.; Pretzer, E.; Wiktorowicz, J. E. *Electrophoresis* **2003**, *24*, 2348-2358.
- (150) Means, A. R.; Dedman, J. R. *Nature* **1980**, *285*, 73-77.
- (151) Crivici, A.; Ikura, M. *Annu Rev Bioph Biom* **1995**, *24*, 85-116.
- (152) Cai, Y. G. *Langmuir* **2008**, *24*, 337-343.
- (153) Bernas, T.; Robinson, J. P.; Asem, E. K.; Rajwa, B. *J Biomed Opt* **2005**, *10*.
- (154) Nikon; Vol. 2012.
- (155) Marley, P. D.; Thomson, K. A. *Biochem Bioph Res Co* **1996**, *221*, 15-18.
- (156) Zuhlke, R. D.; Pitt, G. S.; Deisseroth, K.; Tsien, R. W.; Reuter, H. *Nature* **1999**, *399*, 159-162.
- (157) Dzhura, I.; Wu, Y. J.; Colbran, R. J.; Balsler, J. R.; Anderson, M. E. *Nat Cell Biol* **2000**, *2*, 173-177.
- (158) Chazin, W. J., Spring 2002; Vol. 2012.
- (159) AnaSpec, I.
- (160) Anczykowski, B.; Gotsmann, B.; Fuchs, H.; Cleveland, J. P.; Elings, V. B. *Appl Surf Sci* **1999**, *140*, 376-382.
- (161) Yamamoto, D.; Nagura, N.; Omote, S.; Taniguchi, M.; Ando, T. *Biophys J* **2009**, *97*, 2358-2367.
- (162) Chen, C. H.; Clegg, D. O.; Hansma, H. G. *Biochemistry-U S* **1998**, *37*, 8262-8267.
- (163) Yermolenko, I. S.; Lishko, V. K.; Ugarova, T. P.; Magonov, S. N. *Biomacromolecules* **2011**, *12*, 370-379.

- (164) Sotres, J.; Lindh, L.; Arnebrant, T. *Langmuir* **2011**, *27*, 13692-13700.
- (165) Laoudj, D.; Guasch, C.; Renault, E.; Bennes, R.; Bonnet, J. *Anal Bioanal Chem* **2005**, *381*, 1476-1479.
- (166) Palermo, V.; Palma, M.; Samori, P. *Adv Mater* **2006**, *18*, 145-164.
- (167) Sinensky, A. K.; Belcher, A. M. *Nat Nanotechnol* **2007**, *2*, 653-659.
- (168) Park, J.; Yang, J.; Lee, G.; Lee, C. Y.; Na, S.; Lee, S. W.; Haam, S.; Huh, Y. M.; Yoon, D. S.; Eom, K.; Kwon, T. *Acs Nano* **2011**, *5*, 6981-6990.
- (169) Edmiston, P. L.; Lee, J. E.; Cheng, S. S.; Saavedra, S. S. *J Am Chem Soc* **1997**, *119*, 560-570.
- (170) Tarlov, M. J.; Bowden, E. F. *J Am Chem Soc* **1991**, *113*, 1847-1849.
- (171) Cullison, J. K.; Hawkrige, F. M.; Nakashima, N.; Yoshikawa, S. *Langmuir* **1994**, *10*, 877-882.
- (172) Chang, I. N.; Herron, J. N. *Langmuir* **1995**, *11*, 2083-2089.
- (173) Lin, J. N.; Chang, I. N.; Andrade, J. D.; Herron, J. N.; Christensen, D. A. *J Chromatogr* **1991**, *542*, 41-54.
- (174) Seong, S. Y.; Choi, C. Y. *Proteomics* **2003**, *3*, 2176-2189.
- (175) Spinke, J.; Liley, M.; Guder, H. J.; Angermaier, L.; Knoll, W. *Langmuir* **1993**, *9*, 1821-1825.
- (176) Muller, W.; Ringsdorf, H.; Rump, E.; Wildburg, G.; Zhang, X.; Angermaier, L.; Knoll, W.; Liley, M.; Spinke, J. *Science* **1993**, *262*, 1706-1708.
- (177) Lin, J. N.; Andrade, J. D.; Chang, I. N. *J Immunol Methods* **1989**, *125*, 67-77.
- (178) Kowalczyk, D.; Slomkowski, S.; Wang, F. W. *J Bioact Compat Pol* **1994**, *9*, 282-309.
- (179) Soderquist, M. E.; Walton, A. G. *J Colloid Interf Sci* **1980**, *75*, 386-397.
- (180) Ivarsson, B. A.; Hegg, P. O.; Lundstrom, K. I.; Jonsson, U. *Colloid Surface* **1985**, *13*, 169-192.
- (181) Jonsson, U.; Lundstrom, I.; Ronnberg, I. *J Colloid Interf Sci* **1987**, *117*, 127-138.
- (182) Buijs, J.; Norde, W.; Lichtenbelt, J. W. T. *Langmuir* **1996**, *12*, 1605-1613.
- (183) Malmsten, M.; Lindstrom, A. L.; Warnheim, T. *J Colloid Interf Sci* **1995**, *173*, 297-303.
- (184) Vasquez, R. P.; Margalit, R. *Thin Solid Films* **1990**, *192*, 173-180.
- (185) Su, T. J.; Lu, J. R.; Thomas, R. K.; Cui, Z. F.; Penfold, J. *Langmuir* **1998**, *14*, 438-445.
- (186) Lu, J. R.; Su, T. J.; Thirtle, P. N.; Thomas, R. K.; Rennie, A. R.; Cubitt, R. *J Colloid Interf Sci* **1998**, *206*, 212-223.
- (187) Baugh, L.; Weidner, T.; Baio, J. E.; Nguyen, P. C. T.; Gamble, L. J.; Slayton, P. S.; Castner, D. G. *Langmuir* **2010**, *26*, 16434-16441.
- (188) van Rantwijk, F.; Lau, R. M.; Sheldon, R. A. *Trends Biotechnol* **2003**, *21*, 131-138.
- (189) Park, S.; Kazlauskas, R. J. *J Org Chem* **2001**, *66*, 8395-8401.
- (190) Lozano, P.; de Diego, T.; Guegan, J. P.; Vaultier, M.; Iborra, J. L. *Biotechnol Bioeng* **2001**, *75*, 563-569.
- (191) Erbedinger, M.; Mesiano, A. J.; Russell, A. J. *Biotechnol Progr* **2000**, *16*, 1129-1131.
- (192) Howarth, J.; James, P.; Dai, J. F. *Tetrahedron Lett* **2001**, *42*, 7517-7519.
- (193) Lozano, P.; de Diego, T.; Carrie, D.; Vaultier, M.; Iborra, J. L. *Chem Commun* **2002**, 692-693.
- (194) Chelikani, P.; Fita, I.; Loewen, P. C. *Cell Mol Life Sci* **2004**, *61*, 192-208.
- (195) Jones, P.; Suggett, A. *Biochem J* **1968**, *110*, 617-8.

- (196) Sagiv, J. *J Am Chem Soc* **1980**, *102*, 92-98.
- (197) Aslanidou S, L.-S. N., Kotsifaki C, Pentari D, Katsivela E *PROTECTION 2008 Conference* **2008**.
- (198) Chanda, M.; Roy, S. K. *Plastics technology handbook*; 4th ed.; CRC Press/Taylor & Francis Group: Boca Raton, FL, 2007.
- (199) Chowdhury, D.; Maoz, R.; Sagiv, J. *Nano Lett* **2007**, *7*, 1770-1778.
- (200) Martinez, I. S.; Baldelli, S. *J Phys Chem C* **2010**, *114*, 11564-11575.
- (201) Yokota, Y.; Harada, T.; Fukui, K. I. *Chem. Commun.* **2010**, *46*, 8627-8629.
- (202) Perkin, S.; Albrecht, T.; Klein, J. *Phys Chem Chem Phys* **2010**, *12*, 1243-1247.
- (203) Atkin, R.; Warr, G. G. *J Phys Chem C* **2007**, *111*, 5162-5168.
- (204) Zeira, A.; Chowdhury, D.; Hoepfener, S.; Liu, S. T.; Berson, J.; Cohen, S. R.; Maoz, R.; Sagiv, J. *Langmuir* **2009**, *25*, 13984-14001.
- (205) Nakagawa, T.; Ogawa, K.; Kurumizawa, T. *Langmuir* **1994**, *10*, 525-529.
- (206) Barrat, A.; Silberzan, P.; Bourdieu, L.; Chatenay, D. *Europhys Lett* **1992**, *20*, 633-638.
- (207) Xiang, J. H.; Zhu, P. X.; Masuda, Y.; Koumoto, K. *Langmuir* **2004**, *20*, 3278-3283.
- (208) Kozlov, Y. N.; Nadezhdi, A.; Pourmal, A. P. *Int J Chem Kinet* **1974**, *6*, 383-394.
- (209) Kad, N. M.; Myers, S. L.; Smith, D. P.; Smith, D. A.; Radford, S. E.; Thomson, N. H. *J Mol Biol* **2003**, *330*, 785-797.
- (210) Tamam, L.; Ocko, B. M.; Reichert, H.; Deutsch, M. *Phys Rev Lett* **2011**, *106*.
- (211) Mezger, M.; Schramm, S.; Schroder, H.; Reichert, H.; Deutsch, M.; De Souza, E. J.; Okasinski, J. S.; Ocko, B. M.; Honkimaki, V.; Dosch, H. *J Chem Phys* **2009**, *131*.
- (212) Liu, H. T.; Liu, Y.; Li, J. H. *Phys Chem Chem Phys* **2010**, *12*, 1685-1697.
- (213) Xia, J. L.; Chen, F.; Li, J. H.; Tao, N. J. *Nat Nanotechnol* **2009**, *4*, 505-509.
- (214) Quinn, A.; Sedev, R.; Ralston, J. *J. Phys. Chem. B* **2003**, *107*, 1163-1169.
- (215) Ye, J. T.; Inoue, S.; Kobayashi, K.; Kasahara, Y.; Yuan, H. T.; Shimotani, H.; Iwasa, Y. *Nat Mater* **2010**, *9*, 125-128.
- (216) Pu, J. B.; Wang, L. P.; Mo, Y. F.; Xue, Q. J. *J Colloid Interf Sci* **2011**, *354*, 858-865.
- (217) Plechkova, N. V.; Seddon, K. R. *Ionic liquids uncoiled : critical expert overviews*; Wiley: Hoboken, N.J., 2012.
- (218) Carmichael, A. J.; Hardacre, C.; Holbrey, J. D.; Nieuwenhuyzen, M.; Seddon, K. R. *Mol Phys* **2001**, *99*, 795-800.
- (219) Cremer, T.; Killian, M.; Gottfried, J. M.; Paape, N.; Wasserscheid, P.; Maier, F.; Steinrueck, H. P. *Chemphyschem* **2008**, *9*, 2185-2190.
- (220) Reed, S. K.; Lanning, O. J.; Madden, P. A. *J Chem Phys* **2007**, *126*.
- (221) Kislenko, S. A.; Samoylov, I. S.; Amirov, R. H. *Phys Chem Chem Phys* **2009**, *11*, 5584-5590.
- (222) Ghatee, M. H.; Zolghadr, A. R.; Moosavi, F.; Ansari, Y. *J Chem Phys* **2012**, *136*.
- (223) Vatamanu, J.; Borodin, O.; Bedrov, D.; Smith, G. D. *J Phys Chem C* **2012**, *116*, 7940-7951.
- (224) Wu, J. Z.; Jiang, T.; Jiang, D. E.; Jin, Z. H.; Henderson, D. *Soft Matter* **2011**, *7*, 11222-11231.
- (225) Saha, S.; Hayashi, S.; Kobayashi, A.; Hamaguchi, H. *Chem Lett* **2003**, *32*, 740-741.

- (226) Holbrey, J. D.; Reichert, W. M.; Nieuwenhuyzen, M.; Johnston, S.; Seddon, K. R.; Rogers, R. D. *Chem Commun* **2003**, 1636-1637.
- (227) Hansma, H. G.; Revenko, I.; Kim, K.; Laney, D. E. *Nucleic Acids Res* **1996**, *24*, 713-720.
- (228) Lu, J.; Delamarche, E.; Eng, L.; Bennewitz, R.; Meyer, E.; Guntherodt, H. *J. Langmuir* **1999**, *15*, 8184-8188.
- (229) Green, C. P.; Sader, J. E. *J Appl Phys* **2002**, *92*, 6262-6274.
- (230) Naeem, R.; UCDAVIS CHEMWIKI, 2012; Vol. 2012.
- (231) Hamaker, H. C. *Physica* **1937**, *4*, 1058-1072.
- (232) Dzyaloshinskii, I. E.; Lifshitz, E. M.; Pitaevskii, L. P. *Adv Phys* **1961**, *10*, 165-209.
- (233) Lee, S. W.; Sigmund, W. M. *Colloid Surface A* **2002**, *204*, 43-50.
- (234) Earle, M. J.; Esperanca, J. M. S. S.; Gilea, M. A.; Lopes, J. N. C.; Rebelo, L. P. N.; Magee, J. W.; Seddon, K. R.; Widegren, J. A. *Nature* **2006**, *439*, 831-834.
- (235) Zhang, W. X.; Tong, L.; Yang, C. *Nano Lett* **2012**, *12*, 1002-1006.
- (236) Alley, R. L.; Komvopoulos, K.; Howe, R. T. *J Appl Phys* **1994**, *76*, 5731-5737.
- (237) Flater, E. E.; Ashurst, W. R.; Carpick, R. W. *Langmuir* **2007**, *23*, 9242-9252.
- (238) Kopp-Marsaudon, S.; Leclere, P.; Dubourg, F.; Lazzaroni, R.; Aime, J. P. *Langmuir* **2000**, *16*, 8432-8437.
- (239) Chen, X.; Davies, M. C.; Roberts, C. J.; Tendler, S. J. B.; Williams, P. M.; Burnham, N. A. *Surf Sci* **2000**, *460*, 292-300.
- (240) Ouyang, Q.; Ishida, K.; Okada, K. *Appl Surf Sci* **2001**, *169*, 644-648.
- (241) Winkler, R. G.; Spatz, J. P.; Sheiko, S.; Moller, M.; Reineker, P.; Marti, O. *Phys Rev B* **1996**, *54*, 8908-8912.
- (242) Spatz, J. P.; Sheiko, S.; Moller, M.; Winkler, R. G.; Reineker, P.; Marti, O. *Nanotechnology* **1995**, *6*, 40-44.
- (243) Zitzler, L.; Herminghaus, S.; Mugele, F. *Phys Rev B* **2002**, *66*.
- (244) Colchero, J.; Storch, A.; Luna, M.; Gomez-Herrero, J.; Baro, A. M. *Langmuir* **1998**, *14*, 2230-2234.
- (245) Cleveland, J. P.; Anczykowski, B.; Schmid, A. E.; Elings, V. B. *Appl Phys Lett* **1998**, *72*, 2613-2615.
- (246) Wong, E. W.; Sheehan, P. E.; Lieber, C. M. *Science* **1997**, *277*, 1971-1975.
- (247) Carpick, R. W.; Agrait, N.; Ogletree, D. F.; Salmeron, M. *Langmuir* **1996**, *12*, 3334-3340.
- (248) Mazyar, O. A.; Jennings, G. K.; McCabe, C. *Langmuir* **2009**, *25*, 5103-5110.
- (249) Zhao, W. J.; Zhu, M.; Mo, Y. F.; Bai, M. W. *Coll. Surf. A* **2009**, *332*, 78-83.
- (250) Beni, G.; Hackwood, S. *Appl Phys Lett* **1981**, *38*, 207-209.
- (251) Vallet, M.; Berge, B.; Vovelle, L. *Polymer* **1996**, *37*, 2465-2470.
- (252) Beni, G.; Tenan, M. A. *J Appl Phys* **1981**, *52*, 6011-6015.
- (253) Darhuber, A. A.; Troian, S. M. *Annu Rev Fluid Mech* **2005**, *37*, 425-455.
- (254) Crassous, J. G., C.; Liogier, G.; Berge, B. *Proc. SPIE* **2004**, *5639*, 143-148.
- (255) Heikenfeld, J.; Steckl, A. J. *Appl Phys Lett* **2005**, *86*.
- (256) Kang, H. K., J. In *Proc. Int. Conf. MEMS: Istanbul, Turkey, 2010*; pp 742-745.
- (257) Sen, P.; Kim, C. J. *J Microelectromech S* **2009**, *18*, 990-997.

- (258) Gong, J. C., G.; Ju, Y. S.; Kim, C.-J In *Proc. IEEE Int. Conf. MEMS: Tucson, AZ, 2008*; pp 848-851.
- (259) Banpurkar, A. G.; Nichols, K. P.; Mugele, F. *Langmuir* **2008**, *24*, 10549-10551.
- (260) Nelson, W. K., P.; Kim, C.-J In *Proc. Int. Conf. MEMS: Hong Kong, China, 2010*; pp 75-78.
- (261) Banpurkar, A. G.; Duits, M. H. G.; van den Ende, D.; Mugele, F. *Langmuir* **2009**, *25*, 1245-1252.
- (262) Hua, Z. S.; Rouse, J. L.; Eckhardt, A. E.; Srinivasan, V.; Pamula, V. K.; Schell, W. A.; Benton, J. L.; Mitchell, T. G.; Pollack, M. G. *Anal Chem* **2010**, *82*, 2310-2316.
- (263) Luk, V. N.; Wheeler, A. R. *Anal Chem* **2009**, *81*, 4524-4530.
- (264) Moon, H.; Wheeler, A. R.; Garrell, R. L.; Loo, J. A.; Kim, C. J. *Lab Chip* **2006**, *6*, 1213-1219.
- (265) Prins, M. W. J.; Welters, W. J. J.; Weekamp, J. W. *Science* **2001**, *291*, 277-280.
- (266) Pollack, M. G.; Fair, R. B.; Shenderov, A. D. *Appl Phys Lett* **2000**, *77*, 1725-1726.
- (267) Seyrat, E.; Hayes, R. A. *J Appl Phys* **2001**, *90*, 1383-1386.
- (268) Lee, J.; Moon, H.; Fowler, J.; Schoellhammer, T.; Kim, C. J. *Sensor Actuat a-Phys* **2002**, *95*, 259-268.
- (269) Berge, B. *Cr Acad Sci li* **1993**, *317*, 157-163.
- (270) Dahms, H. *J Electrochem Soc* **1969**, *116*, 1532-8.
- (271) Moon, H.; Cho, S. K.; Garrell, R. L.; Kim, C. J. *J Appl Phys* **2002**, *92*, 4080-4087.
- (272) Nelson, W. C.; Kim, C. J. *J Adhes Sci Technol* **2012**, *26*, 1747-1771.
- (273) Washizu, M. *Ieee T Ind Appl* **1998**, *34*, 732-737.
- (274) Cho, S. K.; Moon, H. J.; Kim, C. J. *J Microelectromech S* **2003**, *12*, 70-80.
- (275) Chevalliot, S.; Heikenfeld, J.; Clapp, L.; Milarcik, A.; Vilner, S. *J Display Tech.* **2011**, *7*, 649-656.
- (276) Zhang, S. G.; Hu, X. D.; Qu, C.; Zhang, Q. H.; Ma, X. Y.; Lu, L. J.; Li, X. L.; Zhang, X. P.; Deng, Y. Q. *ChemPhysChem* **2010**, *11*, 2327-2331.
- (277) Vallet, M.; Vallade, M.; Berge, B. *Eur. Phys. J. B* **1999**, *11*, 583-591.
- (278) Berry, S.; Kedzierski, J.; Abedian, B. *J. Colloid and Interface Sci.* **2006**, *303*, 517-524.
- (279) Ye, J. T.; Inoue, S.; Kobayashi, K.; Kasahara, Y.; Yuan, H. T.; Shimotani, H.; Iwasa, Y. *Nat. Mater.* **2010**, *9*, 125-128.
- (280) Cai, Y. G.; Ocko, B. M. *Langmuir* **2005**, *21*, 9274-9279.
- (281) Kranias, S. *KRÜSS Surface Science Newsletter* **2004**.
- (282) Nanayakkara, Y. S.; Moon, H.; Payagala, T.; Wijeratne, A. B.; Crank, J. A.; Sharma, P. S.; Armstrong, D. W. *Anal. Chem.* **2008**, *80*, 7690-7698.
- (283) Oh, J. M.; Ko, S. H.; Kang, K. H. *Langmuir* **2008**, *24*, 8379-8386.
- (284) Ko, S. H.; Lee, H.; Kang, K. H. *Langmuir* **2008**, *24*, 1094-1101.
- (285) Garcia-Sanchez, P.; Ramos, A.; Mugele, F. *Phys Rev E* **2010**, *81*.
- (286) Ko, S. H.; Lee, S. J.; Kang, K. H. *Appl Phys Lett* **2009**, *94*.
- (287) Mugele, F.; Baret, J. C.; Steinhauser, D. *Appl Phys Lett* **2006**, *88*.
- (288) Chung, S. K. Z., Y.; Yi, U.-C.; Cho, S.-K. In *Pro. Int. Conf. MEMS: Kobe, Japan, 2007*.
- (289) 't Mannetje, D. J. C. M.; Murade, C. U.; van den Ende, D.; Mugele, F. *Appl Phys Lett* **2011**, *98*.
- (290) Zhang, X. N.; Cai, Y. G. *Beilstein J Nanotech* **2012**, *3*, 33-39.

- (291) Atkin, R.; Warr, G. G. *J. Phys. Chem. C* **2007**, *111*, 5162-5168.
- (292) Tamam, L.; Ocko, B. M.; Reichert, H.; Deutsch, M. *Phys. Rev. Lett.* **2011**, *106*, 197801.
- (293) Bovio, S.; Podesta, A.; Lenardi, C.; Milani, P. *J. Phys. Chem. B* **2009**, *113*, 6600-6603.
- (294) Romero, C.; Baldelli, S. *J. Phys. Chem. B* **2006**, *110*, 6213-6223.
- (295) Yuan, H. T.; Shimotani, H.; Ye, J. T.; Yoon, S.; Aliah, H.; Tsukazaki, A.; Kawasaki, M.; Iwasa, Y. *J. Am. Chem. Soc.* **2010**, *132*, 18402-18407.
- (296) Mugele, F.; Herminghaus, S. *Appl Phys Lett* **2002**, *81*, 2303-2305.
- (297) Potter, R. W.; Clyne, M. A. *J Chem Eng Data* **1980**, *25*, 50-51.
- (298) Schwartz, A. S. a. S.; Nikon MICROSCOPYU, 2000-2012; Vol. 2012.

VITA

Xiaoning Zhang

PLACE OF BIRTH

CHONGQING, P.R. CHINA

EDUCATION

M.S., Environmental Science, Chongqing University, Chongqing, P. R. China
2009

B.S., Pharmacy, Chongqing University, Chongqing, P. R. China
2008

RESEARCH EXPERIENCE

Department of Chemistry, University of Kentucky, 2009 to 2013

Department of Chemistry, Chongqing University, 2007 to 2009

TEACHING EXPERIENCE

2010-13 Teaching Assistant: General Chemistry Lab, Department of Chemistry,
University of Kentucky. (2 semesters)

Physical Chemistry Lab, Department of Chemistry,
University of Kentucky. (2 semesters)

SCHOLASTIC AND PROFESSIONAL HONORS

10/2012 3rd Place of 2012 Graduate Research Competition Awards in 98th
Kentucky Academy of Science (KAS) Annual Meeting, Richmond, Kentucky

6/2012 EPSCoR Fellowship, Oak Ridge National Laboratory, Oak Ridge,
Tennessee

8/2011-8/2012 Kentucky Opportunity Fellowship, University of Kentucky, Lexington,
Kentucky

ABSTRACTS AND PRESENTATIONS

4/2013 Sun, Y.; Heidary, D.; **Zhang, X. N.**; Cai, Y. G.; and Glazer, E., Mechanistic
Studies of Light-activated Ruthenium Polypyridyl Compounds as Potential Anti-cancer
Drugs. Naff Symposium-The Origin of Life, Lexington, Kentucky

4/2013 **Zhang, X. N.** and Cai, Y. G., Kelvin Probe Force Microscopy (KPFM)
Study of the Conformational Change and Orientational Difference in Immobilized
Calmodulin (CaM). 245th American Chemical Society (ACS) National Meeting, New
Orleans, Louisiana.

11/2012 **Zhang, X. N.** and Cai, Y. G., Surface Properties of Ionic Liquid Adsorbate Layer Are Influenced by the Dipole of the Underneath Substrate. 2012 Southeastern Regional Meeting of the American Chemical Society (ACS), Raleigh, North Carolina.

10/2012 **Zhang, X. N.** and Cai, Y. G., Octadecyltrichlorosilane (OTS)-coated Ionic Liquid Drops: Micro-reactors for Homogenous Catalytic Reactions at Designated Interfaces. 2012 Kentucky Academy of Science (KAS) Annual Meeting, Richmond, Kentucky.

6/2012 **Zhang, X. N.** and Cai, Y. G., Atomic Force Microscopy Study of the Orientational Difference in Immobilized Calmodulin. Neutrons in Structural Biology Symposium. Oak Ridge National Laboratory, Oak Ridge, Tennessee.

5/2012 **Zhang, X. N.** and Cai, Y. G., Orientation and Calcium-induced Structural Change of Calmodulin (CaM) Characterized by Atomic Force Microscopy (AFM) and Kelvin Probe Force Microscopy (KPFM). Naff Symposium-Metals and Proteins, Lexington, Kentucky.

4/2011 **Zhang, X. N.** and Cai, Y. G., Probing the Calmodulin Conformational Change with Atomic Force Microscopy (AFM). Naff Symposium-Biochemistry at Interfaces, Lexington, Kentucky.

1/2010 Yang, Y. N.; Zhang, Y. H.; Xiao, P.; **Zhang, X. N.**; Lu, L.; Li, L., Synthesis of Ni/TiO₂ nanocomposite by loading TiO₂ nanotubes with Ni nanoparticles. Nanoelectronics Conference (INEC), 2010 3rd International, Hong Kong.

1/2010 Li, L.; Zhang, Y. H.; Xiao, P.; Yang, Y. N.; Lu, L.; **Zhang, X. N.**; Preparation and photocurrent response of ZnO/TiO₂ nanotubes composite. Nanoelectronics Conference (INEC), 2010 3rd International, Hong Kong.

PUBLICATIONS

1. Hu, H. M.; Guo, Y. M.; Sun, X. M.; Chen, X. C.; **Zhang, X. N.**; Liu, Q.; Xu, C. X., Determination of Chlorobenzenes in Water Samples by Solid Phase Disk Extraction and Gas Chromatography-electron Capture Detection. *Journal of Chromatographic Science* (Accepted).

2. **Zhang, X. N.** and Cai, Y. G., Ultra-Low Voltage Electrowetting on Solid-like Ionic Liquid Dielectric Layer. *Angewandte Chemie International Edition* 2013, 52 (8), 2289–2292.

3. Hu, H. M.; Sun, X. M.; Zhong, Z., Chen, X. C.; **Zhang, X. N.**; Guo, Y. M., Determination of Chlorobenzenes in Pure, Tap, and Sea Water by Static Headspace

- Gas Chromatography–Electron Capture Detection. *Journal of Separation Science* 2012, 35, 2922-8.
4. **Zhang, X. N.**; Lu, L. B.; Cai, Y. G., Surface Properties of Ionic Liquid Adsorbate Layer Are Influenced by the Dipole of Underneath Substrate. *Langmuir* 2012, 28 (25), 9593-9600.
 5. **Zhang, X. N.** and Cai, Y. G., Octadecyltrichlorosilane (OTS)-coated Ionic Liquid Drops: Micro-reactors for Homogenous Catalytic Reactions at Designated Interfaces. *Beilstein Journal of Nanotechnology* 2012, 3, 33-39.
 6. **Zhang, X. N.**; Trajkovic, S.; Dauner, S.; Cai, Y. G., Atomic Force Microscopy Study of the Conformational Change in Immobilized Calmodulin. *Langmuir* 2011, 27 (17), 10793-10799.
 7. Fang, J.; **Zhang, X. N.**; Cai, Y. G.; Wei, Y. N.; Chai, Q.; William, C. H., Noncovalent Interactions in YajC-CT Fibrillation and Gelation—Effects of Detergent, Urea, Salt, and Glycerol. *Journal of Biological Research* 2012, 1.
 8. Fang, J.; **Zhang, X. N.**; Cai, Y. G.; Wei, Y. N., Small Globular Protein Motif Forms Particulate Hydrogel under Various pH Conditions. *Biomacromolecules* 2011, 12 (5), 1578-1584.
 9. Lu, L.; Zhang, Y. H.; Xiao, P.; **Zhang, X. N.**; Yang, Y. N., Aggregation of TiO₂ Nanotubes as Recyclable Catalyst for Photocatalytic Degradation of Methylene Blue. *Environmental Engineering Science* 2010, 27 (3), 281-286.
 10. Yang, Y. N.; Zhang, Y. H.; Xiao, P.; **Zhang, X. N.**; Lu, L.; Lu, L., Preparation of Ni Nanoparticle-TiO₂ Nanotube Composite By Pulse Electrodeposition. *Materials Letters* 2009, 63, 2429–2431.
 11. Li, Y. L.; Lv, S. Y.; Li, J. H.; Qi, Q. Q.; **Zhang, X. N.**, The Statistical Analysis of Research Articles Published By Chongqing University in EI Compendex Database. *Journal of Chongqing University of Arts and Sciences (Natural Science Edition)* 2010, 29 (2), 105-108.
 12. Yang, Y. N.; Zhang, Y. H.; Xiao, P.; **Zhang, X. N.**, Progress in Preparation Methods and Applications of Metal/TiO₂ Nanocomposite Materials. *Materials review* 2009, 23 (14), 157-160.
 13. Hu, Y. Z.; Zhang, Y. H.; Xiao, P.; Cao, L. J.; Lu, L.; **Zhang, X. N.**, Application of Improved Grey Neural Network Model to Water Quality Prediction. *Journal of Natural Science of Helongjiang University* 2009, 26 (5), 657-661.

14. Lu, L.; Zhang, Y. H.; Xiao, P.; **Zhang, X. N.**; Yang, Y. N., Recent Developments in Photocatalytic Water-splitting Using TiO₂ Nanotubes for Hydrogen Production. *Chemical Industry and Engineering Progress* 2009, 28 (11), 1913-1916.

Xiaoning Zhang

04-20-2013